CANADIAN THESES ON MICROFICHE

THÈSES CANADIENNES SUR MICROFICHE

National Library of Canada
Collections Development Branch

Canadian Theses on
Microfiche Service

Ottawa, Canada
K1A 0N4

Bibliothèque nationale du Canada
Direction du développement des collections

Service des thèses canadiennes
sur microfiche

NOTICE

The quality of this microfiche is heavily dependent upon the quality of the original thesis submitted for microfilming. Every effort has been made to ensure the highest quality of reproduction possible.

If pages are missing, contact the university which granted the degree.

Some pages may have indistinct print especially if the original pages were typed with a poor typewriter ribbon or if the university sent us an inferior photocopy.

Previously copyrighted materials (journal articles, published tests, etc.) are not filmed.

Reproduction in full or in part of this film is governed by the Canadian Copyright Act, R.S.C. 1970, c. C-30. Please read the authorization forms which accompany this thesis.

AVIS

La qualité de cette microfiche dépend grandement de la qualité de la thèse soumise au microfilmage. Nous avons tout fait pour assurer une qualité supérieure de reproduction.

S'il manque des pages, veuillez communiquer avec l'université qui a conféré le grade.

La qualité d'impression de certaines pages peut laisser à désirer, surtout si les pages originales ont été dactylographiées à l'aide d'un ruban usé ou si l'université nous a fait parvenir une photocopie de qualité inférieure.

Les documents qui font déjà l'objet d'un droit d'auteur (articles de revue, examens publiés, etc.) ne sont pas microfilmés.

La reproduction, même partielle, de ce microfilm est soumise à la Loi canadienne sur le droit d'auteur, SRC 1970, c. C-30. Veuillez prendre connaissance des formules d'autorisation qui accompagnent cette thèse.

THIS DISSERTATION
HAS BEEN MICROFILMED
EXACTLY AS RECEIVED

LA THÈSE A ÉTÉ
MICROFILMÉE TELLE QUE
NOUS L'AVONS REÇUE

Canada

NL 339 (r. 86/09)

Dynamic Behavior of Rotor Systems with a Comprehensive Model for the Hydrodynamic Bearing Supports Using Modal Analysis and Testing

Rajagopal Subbiah

A Thesis

in

The Department

of

Mechanical Engineering

Presented in Partial Fulfillment of the Requirements
for the Degree of Doctor of Philosophy at
Concordia University
Montréal, Québec, Canada

August 1985

ABSTRACT

Dynamic Behavior of Rotor Systems with a Comprehensive Model for the Hydrodynamic Bearing Supports Using Modal Analysis and Testing

Rajagopal Subbiah, Ph.D.
Concordia University, 1985

Rotors in many applications are mounted on fluid film bearing supports. Their dynamic characteristics such as the critical speeds, unbalance response, instability threshold speeds and the change of whirl direction must be known in order to design a rotor system for safe operation. In order to understand completely the dynamic behavior of complex rotor systems, appropriate analytical and experimental studies are carried out and the results are reported and discussed in this thesis. The rotor system is modeled using the finite element formulation and the modal analysis technique is used for analysis. Since the fluid film bearing properties are nonsymmetrical, biorthogonality relations are used to uncouple the equations of motion. Modal reduction techniques are adopted to reduce the size of system matrices. The effect of dissimilar bearing clearances on the dynamic behavior of simple rotors mounted on two fluid film bearings is studied. The conditions for backward whirl in such rotors are derived and verified experimentally. Rotational stiffness and damping coefficients in fluid films when the journal is operating under misaligned conditions are computed by solving the appropriate Reynolds equations using a finite difference approach. The behavior of rotor systems under randomly varying pedestal-base excitation is also investigated. Modal testing is carried out on rotor systems to identify the left and the right eigenvectors as well as other relevant parameters and the results agree in a qualitative sense with the

analytical results. Suggestions for future work are given.

DEDICATED TO MY PARENTS, MENTORS AND MY TEACHERS

ACKNOWLEDGEMENTS

The author expresses his indebtedness to his thesis supervisor Dr. R.B. Bhat for his excellent guidance, help and encouragement during the development of this thesis. His patience, understanding nature and technical excellence were the constant source of inspiration to the author throughout the course of the work. The author also expresses his sense of gratitude to the thesis co-supervisor Dr. T.S. Sankar who exposed the author to various technical problems in the field. Also, the discussions and the support provided by him are deeply appreciated.

Helpful review and fruitful discussions of the work by Dr. B.S. Prabhu is gratefully appreciated. The valuable assistance rendered by Mr. P. Canzano in the author's experimental work, the impeccable typing of the manuscript by Ilana Crawford and Patricia Stewart, and the excellent drawings by Messrs. Victor Woo and C. Voisard are acknowledged with gratitude.

The financial support provided by the department of Mechanical Engineering of Concordia University and the Natural Sciences and Engineering Research Council of Canada is acknowledged.

Sincerest thanks are due to my friends for their valuable help and emotional support.

This work would not have been possible but for the abundant emotional support and understanding of the author's wife Kala and daughter Suki, throughout the course of this investigation. They were a constant source of strength and the author is grateful to them.

TABLE OF CONTENTS

LIST OF FIGURES

LIST OF TABLES

NOMENCLATURE

a	disk eccentricity
$[c]$	system damping matrix
c_1, c_2	clearances at the left and right end bearings
c_α, c_β, c_γ	shaft damping at the disk locations
c_{yy}^{tt}, c_{zz}^{tt}, c_{yz}^{tt}, c_{zy}^{tt}	collinear end cross coupled fluid film damping coefficients due to translational velocity of the journal
c_{yy}^{rr}, c_{zz}^{rr}, c_{yz}^{rr}, c_{zy}^{rr}	collinear and crosscoupled fluid film damping coefficients due to rotational velocity of the journal
c_{yy}^{tr}, c_{zz}^{tr}, c_{yz}^{tr}, c_{zy}^{tr} c_{yy}^{rt}, c_{zz}^{rt}, c_{yz}^{rt} c_{zy}^{rt}	coupled damping coefficients of the fluid film
$\bar{c}_{yy}$, $\bar{c}_{zz}$, $\bar{c}_{yz}$, $\bar{c}_{zy}$	nondimensional fluid film damping co-efficients
c_{p_y}, c_{p_z}	damping of the pedestal structure
e	eccentricity of the journal
$\{f\}$	exciting force vector
$[g]$	gyroscopic matrix of the element
h	resultant oil film thickness
h_o	oil film thickness due to static displacement of the journal
j	$\sqrt{-1}$
$[k]$	system stiffness matrix
k_{yy}^{tt}, k_{zz}^{tt}, k_{yz}^{tt}, k_{zy}^{tt}	collinear and cross coupled fluid film stiffness coefficients due to translational displacement of the journal

$k_{yy}^{tr}, k_{zz}^{tr}, k_{yz}^{tr}, k_{zy}^{tr}$ $k_{yy}^{rt}, k_{zz}^{rt}, k_{yz}^{rt}, k_{zy}^{rt}$	coupled stiffness coefficients of the fluid film
$\bar{k}_{yy}, \bar{k}_{zz}, \bar{k}_{yz}, \bar{k}_{zy}$	nondimensional fluid film stiffness coefficients
k_B^e	bending stiffness of the element
k_{p_y}, k_{p_z}	stiffness of the pedestal structure
ℓ	total length of the rotor shaft
ℓ_1, ℓ_2	distances to the disk from the left and right ends of the bearings
$[m]$	system mass matrix
$[m_r], [m_t]$	rotary and translational inertia matrices
m_d	mass of the disk
m_p	mass of the pedestal structure
p	oil film pressure
p_o	static pressure of the fluid
p_y, p_z	fluid film pressures due to the displacement of the journal
$p_{\dot{y}}, p_{\dot{z}}$	fluid film pressures due to the velocity of the journal
$\bar{p}_y, \bar{p}_z$	nondimensional pressures
$\{q\}$	generalized displacement vector
q_b	generalized support displacements
q_1	generalized displacement at the bearing supports
q_r	generalized relative displacements
q_y, q_z	fluid film presssures due to the bending of the journal at Y and Z axes
$q_{\dot{y}}, q_{\dot{z}}$	fluid pressures due to velocity of the journal in bending about Y and Z axes
r	maximum unbalance response of rotor

r_d	unbalance response at the disk location
t	time
x	axial coordinate of the journal
y_o, z_o	deflections of the rotor at the disk locations
y_1, y_2, z_1, z_2	displacement of the rotor at the bearing locations
y_p, y_b, z_p, z_b	pedestal and base displacements
$A_{\phi i}$, $\bar{A}_{\phi i}$	i-th forward and backward modal displacement vectors
$[C]$	overall system damping matrix
D	bearing diameter
$\bar{D}$	dissipation function
E	Young's modulus
E_p	error function
$E_{\phi i}$, $\bar{E}_{\phi i}$	i-th forward and backward modal force vectors
$\{F\}$	overall exciting force vector
F_Y, F_Z	bearing oil film forces along Y and Z directions
F_{yo}, F_{zo}	fluid film forces along Y and Z directions under static equilibrium conditions
H	nondimensional fluid film thickness
$H(j\omega)$	complex frequency response function
$[I]$	identity square matrix
I_o	M.I. of the cross section of the shaft
I_d, I_{ds}	transverse mass moment of inertia of disk and shaft elements
I_p, I_{ps}	polar mass moment of inertia of disk and shaft elements
$I_{p_{xx}}$, $I_{p_{yy}}$	pedestal mass moment of inertia about X and Y directions
$[K]$	overall system stiffness matrix

L	bearing length
$\bar{L}$	Lagrangian
$[M]$	overall system mass matrix
M_Y, M_Z	bearing fluid film moments about Y and Z axes
N	speed of the rotor
N_1 and N_2	shape functions
$\{Q\}$	overall displacement vector
R	radius of the bearing
R_e	radius of the cross section of the element
S	Sommerfeld number = $(\Omega NDL/W)\left(\frac{R}{C}\right)^2$
S_F	input power spectral density
S_R	output power spectral density
T	transpose of
$\bar{T}$	kinetic energy
U	translational displacement of the element of the rotor shaft in Y direction
V	translational displacement of the element of the rotor shaft in Z direction
$\bar{V}$	potential energy
W	static load at the bearing
X,Y,Z	coordinates of the rotor system
α, β, γ	shaft stiffnesses at the disk location
α	force per unit displacement
α^*	$\alpha + j\omega c_\alpha$
β	moment per unit displacement
$\bar{\beta}$	angular coordinate of the journal
β_1	attitude angle of the journal
β_2	$(\bar{\beta} - \beta_1)$

γ	force per unit angular displacement
Δ	whirl ratio $\frac{\nu}{\omega}$
ε	$\frac{e}{c}$, eccentricity ratio
η_i	i-th modal displacement
θ	angular displacement of the shaft about Y
θ_p, θ_b	pedestal and base angular displacements
θ_y, θ_z	local deviational angles at the disk
λ_i	i-th eigenvalue
λ_i'	$-\omega (1 - \xi_i^2)^{\frac{1}{2}}$
μ_i	i-th generalized mass
μ_1	mass of the uniform beam element/unit length
ρ_i	i-th complex eigenvector of the transposed system
σ_i	i-th generalized force vector of the nonsymmetric system
ϕ	angular displacement of the shaft about Z
ϕ_p, ϕ_b	pedestal and base angular displacements
$\{\phi_i\}$	i-th complex eigenvector of the original system
ψ	angular displacement of the shaft about X
ω	frequency
ζ	structural damping
Ω	co-efficient of viscosity of oil
$\mathscr{C}_i$	i-th generalized damping
$\mathscr{F}_i$	i-th generalized force of the symmetric system
κ_i	i-th generalized stiffness
Δy, Δz	small perturbations of the journal in Y and Z axes

$\Delta\varphi$, $\Delta\Psi$	perturbations of the journal about Y and Z axes

Superscripts

*	complex conjugate of
d	of disk location
e	of element

CHAPTER 1

OBJECTIVES AND LITERATURE REVIEW

1.1 General Objectives

Rotors are used in all machinery, whenever power is transmitted from one point to another. Rotors are rotating shafts with concentrated masses such as disks, impellers etc., supported on stationary structures called bearings. These bearings can be either rolling element type such as ball or roller bearings or journal bearings with a fluid film separating the annular area between the journal and the bearing surfaces. The rotor systems are mainly classified as (i) light rotors and (ii) heavy rotors depending upon the applied loads and the type of operation they are subjected to. Again, on the basis of the geometrical configurations, they are further classified as simple systems and large rotor systems. Heavy rotor systems such as generator rotors are generally supported on fluid film bearings. With the increasing trend towards the concept of lighter weight components in structures, the weight of the rotor can be reduced either by resorting to different geometrical configurations or by adopting different materials. When all other geometrical parameters of a rotor remain the same, reduction in weight of a rotor will make it flexible and thereby brings down the critical speed of the system.

The design of a rotor system must consider several aspects such as critical speeds, peak unbalance response, regions of change of whirl directions and instability. The hydrodynamic bearings, on which the rotors are supported, exhibit asymmetric cross-coupled stiffness and damping properties which vary with the speed of operation. Such

properties influence the dynamic behavior of rotors significantly. Even though, other aspects of rotors such as rotating inertia, shear deformation and hysteresis damping etc., influence the dynamic behavior of high speed rotors, the major design parameters are in fact, controlled by the support suspension and hence play a dominant role in the design of rotor systems irrespective of their classifications.

Because the fluid film bearings influence the dynamic behavior of the rotor system, it is highly essential to have a realistic rotor-bearing support model for analysis. Fluid film bearings, in fact are nonlinear in nature and the resulting nonlinear model is most involved. However, the nonlinear model is meaningful if the dynamic behavior of the rotor systems is required at or near the critical regions. Most of the practical rotors operate well beyond these critical regions and the response behavior in these regions can be predicted using a linear model. Hence, it is reasonable to proceed with the linear model of the bearing support to analyze the rotor system behavior.

The response analysis by most of the researchers was carried out assuming the linear bearing model with fluid film translational stiffness and damping co-efficients. When the rotor is flexible or when the support span is large, the tilted or inclined journal provides rotational stiffness and damping effects in the fluid film about transverse axes of the rotor. Hence, it is important to include the rotational springs and dampers along with translational springs and dampers in order to represent an accurate bearing support model.

The fluid film bearings which support the rotor, are in turn mounted on support structures such as pedestals which possess definite

stiffness and damping properties. A support model is complete if it includes the pedestal properties also. The response of rotors arising out of unbalance excitations can be predicted using a deterministic analysis. In some situations, the excitations to the system come through the supports and they may not always be deterministic. Under such circumstances, the deterministic method of evaluation of response is not sufficient and hence statistical methods must be employed.

The objective of the present investigation is to obtain a comprehensive model for the fluid film bearing supports so as to include it in the finite element model of rotor system to study its dynamic behavior. For a large rotor system, the size of the system matrices become very large and hence they are reduced using a modal reduction technique. The resulting equations are solved by a modal analysis procedure which provides all the relevant system parameters.

1.2 Literature Review

Several studies on the dynamic behavior of rotors supported on fluid film bearings are reported in literature. Those contributions which are pertinent to the present investigation are discussed in Sections 1.2.1 to 1.2.3.

Section 1.2.1 deals with the different modelling and solution methodologies adopted to predict the dynamic behavior of rotors supported on identical and dissimilar hydrodynamic bearings, the investigations about backward whirl, different procedures involved on the evaluation of dynamic fluid film co-efficients in inclined journal bearings and the stability analysis of rotor systems. The section 1.2.2 covers the various experimental contributions in the area of rotor dynamics. It

deals with the conventional methods as well as the modal testing techniques in order to determine the dynamic parameters of the rotor-bearing systems. The section 1.2.3 is devoted to the stochastic response of rotors subjected to random base excitations.

1.2.1 Rotors on Flexible Supports

The rotor system consists of several subsystems such as bearings, mechanical couplings, impellers, detachable rigid or flexible disks and support pedestals etc. Each subsystem has a definite influence on the dynamic behavior of rotor systems. Hence, accurate modelling and proper articulation of subsystems are essential to achieve better results. Accordingly, there are quite a few modelling methods available depending upon the type of rotor systems, such as (i) Jeffcott rotor model which is essentially a single mass mounted on a shaft supported on bearings, (ii) lumped parameter model and (iii) finite element model with distributed system properties. Similarly, there are different solution procedures available to solve the resulting equations obtained by different models. The solution procedures are: (i) direct method, (ii) transfer matrix method and (iii) modal analysis. The review covers various modelling methods and the solution procedures.

One of the earlier works on the prediction of critical speeds of rotors introducing a simple model was by Jeffcott [1]. In his work, the rotor system was modelled as a single mass mounted on a shaft supported on identical bearings and the resulting equations of motion were solved by the direct method. Prohl [2] extended this method to calculate the critical speeds in flexible rotors based on a technique developed by Myklestad [3] to calculate the torsional natural frequencies of airplane

wings. Bishop and Gladwell [4] studied the behavior of simple rotors using a lumped mode. This rotor model was improved upon by Green [5] to include the gyroscopic effects on the critical speeds of simple rotor systems. Eshleman and Eubanks [6] studied the effect of shaft phenomena such as axial torque, gyroscopic moments and transverse shear on critical speeds of rotor systems. Their contribution is basically an extension of work carried out by Tondl [7].

Unbalance response of rotors was studied by several researchers. Yamamoto, Ota and Kono [8] obtained the unbalance response and critical speeds using a simple rotor with unsymmetrical mass properties at the disk. An asymmetrically mounted rotor on dissimilar fluid film bearings was investigated by Ardayfio and Frohrib [9]. However, the cross-coupled stiffness and damping of the fluid film were not included in the bearing model. Rao [10], Rao, Bhat and Sankar [11] employed the Jeffcott rotor model to obtain simple expressions for the unbalance response and critical speeds of rotors mounted on fluid film bearings and solved them by the direct method.

The earliest work using transfer matrix method on the rotor system was by Myklestad [3] for finding out the unbalance response and critical speeds. He used cantilever beam theory in his approach to formulate the point and field transfer matrices. Later, Kramer [12] used this technique to study the dynamic response of rotor systems. Lund [13] also followed this approach to determine the dynamic parameters of flexible rotor system. Kikuchi [14] solved a multi disk rotor problem resorting to the transfer matrix technique. Recently, Rao [15] has analyzed the rotor systems using time marching transfer matrix technique.

Modal analysis is another solution procedure which is widely used by several investigators to study the behavior of rotor systems. Gunter, Choy and Allaire [16] used the planar modes of the undamped rotor systems ignoring the effects of disk gyroscopics and cross-coupled bearing properties. Also, Berthier, Ferraris and Lalanne [17] employed modes of the rotor at rest to study the behavior of rotors using a finite element model. Due to the presence of significant damping in bearings, the modes are not planar and due to the nonsymmetry in stiffness and damping matrices of rotors supported on fluid film bearings, the modes are not orthogonal to each other. Hence, a biorthogonality relation between the modes of the original system and those of a transposed system is essential to uncouple the equations of motion. Lund [18], Saito and Azuma [19] used this technique to study dynamic behavior of flexible rotor systems. Childs [20,21] developed a modal simulation model for flexible asymmetric rotors in order to evaluate the dynamic characteristics of rotor systems. Glasgow and Nelson [22] adopted a component mode method in conjunction with complex mode analysis. Bhat [23] employed the modal analysis technique for simple rotor systems with no damping. He showed that even in the absence of physical damping, the rotor exhibits a pseudo damping when one of the cross-coupled bearing stiffnesses becomes negative. Bhat, Subbiah and Sankar [24] developed a rotor model and employed modal analysis in order to get the dynamic responses of a rotor supported on dissimilar hydrodynamic bearings. The dissimilarity was obtained by having different clearances and by having different loads at the bearings. They also obtained rotor whirl response at the bearings and showed that it is important to see that the rotor response at the bearing must be much smaller than the

bearing clearance in order to validate the analytical predictions obtained using a linear model. If not, the nonlinear fluid film co-efficients must be employed in the study of the rotor dynamic behavior.

Finite element techniques are convenient to model complex rotor systems consisting of several disks, impellers or mechanical couplings etc. Ruhl and Booker [25] and Nelson and McVaugh [26] used finite element methods to evaluate the dynamic characteristics of rotors. In their approach, the rotor was discretized into rigid disk elements, shaft elements and bearing elements. The resulting equations are solved by a direct method. Subsequent studies [17,27,28,29] included the effects of internal damping, axial torque and hysteresis damping etc. of the rotor in mofelling the rotor systems using finite elements. The resulting equations obtained from the model, form large size matrices and are difficult to handle in digital computers. Nelson and McVaugh [26], Craig and Bampton [30] and Rouch and Kao [31] employed reduction techniques to reduce the matrix sizes as proposed by Guyan [32]. More recently, Ookuma and Nagamatsu [33] developed a multiple mode synthesis method to reduce large matrices of a symmetric structure with less memory size than used in a component mode synthesis. However, the system damping is not included in their approach. In the present investigation, the method of Ookuma and Nagamatsu is extended to reduce large rotor-bearing system matrices by means of modal reduction procedure.

The industrial rotors that are mostly supported on hydrodynamic bearings, sometimes exhibit a change of rotor whirl direction depending on the variable bearing parameters and the operating conditions. Consequently, the direction of whirl changes from a forward whirl to a backward whirl. This change of whirl in the

operating speed range is not desirable for safe operation of rotor systems. Hence, a proper design of the rotor systems should take this factor into account in order that the operating range do not fall in the region of whirl change. Earlier work on this aspect was by Green [5]. Yamamoto [34] presented a major contribution to the study of critical speeds in which the phenomena of forward and backward whirl due to gyroscopic effect was reported. Other excellent contributions [35-37] on the whirl aspects were due to shear deformation and disk flexibility etc., of the rotor systems. For a simple rotor supported on hydrodynamic bearings, Glienicke [38] experimentally proved that the critical speed of the rotor in the synchronous whirl region is often split up into two critical speeds. Kellenberger [39] also developed an analysis to corroborate Glienicke's results and found that in certain configurations of the rotor, the backward synchronous whirl mode was excited in between the split criticals. Rao [40] derived the conditions for a forward or a backward whirl in a simple rotor supported on fluid film bearings. However, conditions for the occurrence of backward whirl are not clear and such a study has not been carried out exclusively. Hence, in the present investigation, the conditions of occurrence of backward whirl are developed analytically to observe backward whirl in specific configurations of practical rotor systems.

Another important parameter to be analyzed in rotors supported on hydrodynamic bearings is the self-excited instabilities. The literature contains numerous work carried out on this aspect of instability of rotors arising from various causes. A few of them which are relevant to the present work is referred to in [41]. In the earlier reports, Newkirk [42] found the shaft disturbances due to fluid film in journal bearings.

He explained the cause of half-frequency whirl in rotors. Morrison and Patterson [43] presented an approach to describe the stability threshold of symmetrical two-bearing flexible rotors. Other notable publications on instability of rotors due to oil film are by Hagg [44], and Robertson [45]. The above works were frequently referred to and the various effects that lead to rotor instability were presented by Gunter [46]. Rao [47], Reiger [48] and Lund [49] adopted different methodologies to arrive at the threshold speed of instability in rotors. More recently, a series of works by Iwatsubo and Kawai [50] is reported on stability evaluation of a multi rotor system supported by oil film bearings using energy concepts. In the present work, an instability study is carried out for a simple rotor on hydrodynamic bearings along the lines of Rao [47] and Reiger [48] in order to verify the threshold speed of instability obtained before by the modal analysis method.

In rotor dynamics, most of the analyses were carried out assuming aligned conditions and considering only the linear force stiffness and damping co-efficients in the hydrodynamic bearings [51-53]. These dynamic co-efficients are obtained by solving the appropriate Reynolds equations [54,55]. When the rotor shaft is flexible or when the support span is large, journal tilt at the bearing supports is inevitable and hence it is essential to include the moment stiffness and damping co-efficients about transverse axes at the bearing locations due to the time varying inclination of the journal at the bearings. This leads to an improved model of the rotor system by including the rotational springs and dampers together with the translational springs and dampers at the bearing supports. Kikuchi [14] evaluated the rotational fluid film co-efficients of the plain cylindrical bearings using a short bearing

approximation. Bannister [56] calculated 28 fluid film co-efficients making use of the experimentally determined tilt ratios for 120° partial arc journal bearings. He studied the influence of nonlinearity of the oil film on the response of the rotor system by introducing the misalignment only in the vertical plane. Hashish [57] developed a non-linear bearing model using finite elements in order to evaluate the bearing dynamic co-efficients. The response behavior of flexible rotor systems with nonlinear stiffness characteristics had been investigated by Black and Brown [58]. They found that the effect of nonlinear hydro-dynamic forces is to reduce only the peak mid-span response to 30% compared with linear predictions. At all other regions, except the critical region, the responses obtained by both linear and nonlinear models are almost the same. Hence, in rotor-bearing analysis, it is essential to identify the critical regions and avoid them. A linear analysis is good enough to provide this information with simple analytical procedures. Mukherjee and Rao [59] evaluated the stiffness and damping film co-efficients due to the inclined journal by solving the appropriate Reynolds equations using Fedor's proportionality hypothesis. A comparison of their results with those by Capriz [60] obtained for a finite bearing showed considerable discrepancy for higher eccentricities. Pafelias [61] evaluated 32 fluid film stiffness and damping co-efficients for misaligned partial arc journal bearing.

In the present investigation, a simplified approach is carried out in order to evaluate the collinear and cross-coupled translational and rotational fluid film co-efficients for small perturbations around the mean position of the journal using a finite bearing model. The resulting equations are formulated using finite difference mesh [55] and solved by the

column method [62,63]. The linearized model for the bearing is thus improved by including the properties of rotational springs and dampers along with the translational springs and dampers.

1.2.2 Experimental Work on Rotor Systems

Compared to the several analytical studies available for the rotor-bearing system in the literature, very few experimental investigations are reported. One of the earlier reports on the response of rotors using both analytical and experimental methods was by Yamamoto [34]. He studied the vibrations of a rotor system supported on ball bearings. Downham [64] verified experimentally that there were two critical speeds in asymmetrically supported rotor systems. He found that the lubricant had a stiffness effect with a consequent increase in critical whirling speed. Hull [65] investigated whirls of round and flattened shafts whereas Lund and Orcutt [66] conducted a combined analytical and experimental study of the test rotor, a uniform flexible shaft with disks, supported in two silicone fluid-lubricated tilted pad bearings. They found that peak vibration response did not always occur at the calculated damped critical speed. Cunningham [67] presented the experimental data for the unbalance response of a flexible, ball bearing supported rotor. He compared the values of squeeze film damping co-efficients obtained from measured data to those of theoretical values. In the present investigation, the unbalance response and critical speeds of a simple rotor obtained by the analytical method compare very well with the corresponding experimental results obtained for a laboratory model rotor supported on hydrodynamic bearings.

Recent developments in the measurement techniques and computing technology make the evaluation of dynamic parameters simple by resorting to modal testing methods and turn the conventional experimental methods obsolete. The modal testing of a structure is carried out by measuring the relevant gross parameters of the structure by experiments and using them in a different mathematical model called "modal model". This method provides reliable characteristics of the structure. Even though numerous studies have been carried out on symmetrical stationary structures using modal testing procedure, very little work has been reported regarding non-symmetric or rotating structures. Klosterman [68] identified the modal parameters of stationary beam structures. More recently, Nordmann [69,70] identified the modal parameters of an elastic shaft supported on fluid film bearings. In the present work, a comparative study is carried out between the analytically obtained natural frequencies of the system and those obtained by modal testing procedures for a simple rotor supported on identical as well as dissimilar bearings.

1.2.3 Response due to Base Excitations

When the excitation considered in the rotor systems is due to mass unbalance, it is a single frequency excitation and the response is large in the vicinity of critical speeds. However, when the excitation is from outside sources, such as in the case of support excitations, it can be a single frequency type or random, involving several frequencies. If it happens to be random with considerable power distributed at several frequencies, the system will also respond at those frequencies. Particularly, if one of the system natural frequencies of the rotor coincides with the excitation frequencies, the resulting response may be quite significant and of concern. Ruhl, Conry and Steger [71] developed an

elastic half space soil model of the rotor-pedestal-foundation system and analyzed the deterministic characteristics of the rotor. Bhat [23] used modal analysis to study the response of an undamped simple rotor mounted on fluid film bearings and subjected to deterministic excitations at the supports. Some other notable works of support motions are reported in [72,73]. But, base motions occuring in nature are not always deterministic. For example, structures installed in regions of low or moderate seismological activity are subjected to base/ground excitations which are random in nature [74,75]. Hence, the response of rotors subjected to random base motions is of considerable importance. Boyce, Kozik and Parzen [76] developed probabilistic design criteria for a class of unbalanced rotors subjected to foundation forces. Lund [77] carried out response spectral density analysis of rotor systems due to stationary random excitations of the base, considering excitations only in the vertical direction. Further, Tessarzik, Chiang and Badgley [78] conducted experiments on turbo-rotor system subjected to support random excitations. When base excitations are random in nature, statistical methods must be used to evaluate the response of such rotor systems. In the present work, the power spectral densities of rotor response are obtained when random support excitations in various degrees of freedom of support structure are input to the rotor system.

Some of the works reported in this investigation are published and they are reported in References [79-81].

1.3 Scope of the Present Investigation

The objectives of the present investigation are:

(i) To develop a comprehensive support model for rotor-bearing-pedestal systems by introducing the rotational springs and dampers in the hydrodynamic bearing model.

(ii) To obtain the unbalance response and the response due to random base excitations using the finite element model of the rotor.

(iii) To carry out modal testing of the rotor mounted on fluid film bearings, and compare the resulting modal parameters with those of the analytical results.

(iv) To study the stability aspects of rotor mounted on fluid film bearings.

In Chapter 2, a mathematical model of a simple rotor system is developed as a Jeffcott rotor with linear bearing fluid film stiffness and damping co-efficients. The system of equations is solved by a direct method and the unbalance response and critical speeds of the rotor are obtained. The orbital diagrams are used to study the whirl pattern of the rotor and also, to verify the journal amplitude at the bearing location not to exceed the bearing clearance values. The experimentally obtained unbalance response and critical speeds of a simple laboratory rotor are compared with those obtained through theoretical analysis. The experimental results show a good qualitative agreement with theoretical results validating the mathematical model of the rotor system. Also, equations are developed to predict the conditions of the occurrence of backward whirl and are verified by experiments.

Chapter 3 deals with the modal analysis technique used to study the

dynamic behavior of rotor systems. The procedure provides stability information of the rotor system in addition to the unbalance response and critical speeds. Moreover, modal testing is performed on the simple rotor system to extract the modal parameters. For a particular configuration of the rotor, the threshold speed of instability condition is obtained.

The mathematical model is developed for simple rotor-bearing systems in Chapter 4, using the finite element method and the resulting equations are solved by modal analysis. The response plots obtained earlier using the Jeffcott model of the rotor are compared with those obtained using a finite element model. They bear good qualitative agreement. However, the finite element model provides a higher value of the response. Since, the finite element model leads to large size systems matrices, they are reduced using a modal reduction procedure. Also, threshold speed of instability of the rotor system is determined using a simple analytical procedure.

The bearing fluid film properties thus far used in the analysis of rotor systems, were eight linearized film stiffness and damping co-efficients. When the shaft is flexible or the support span is large, the inclined journal produces moments in addition to forces in the fluid film. Consequently, the moment effects in the fluid film can be modelled by including the rotational springs and dampers in the bearings. Chapter 5 deals with the evaluation of these rotational fluid film properties and their associated coupled properties by solving the appropriate Reynolds equations for the fluid film. These rotational fluid film stiffness and damping co-efficients of the finite cylindrical bearing are compared with those obtained using a short bearing theory. An excellent qualitative agreement is seen between the two. In general, it is observed

that the effect of rotational fluid film properties on the prediction of the dynamic behavior of rotors is more pronounced in the case of large rotor systems compared with the simple systems.

In Chapter 6, excitation of the rotor through the bearing support structure is considered. The rotor bearing structure supported on board vehicles or installed at places of seismological activity, are subjected to excitations of the bearing supports also. These excitations are in general random in nature. Hence, a statistical method is necessary to analyze the dynamic behavior of such systems. The base excitations are assumed to be a Gaussian and a stationary process and power spectral density approach is used to evaluate the response power spectral densities of the system. The influence of excitations due to the rotational degrees of freedom on the response of rotors in the translational degrees of freedom is also studied.

The results of the work so far achieved in all the previous chapters are summarized in Chapter 7. Also, the discussions of results are presented along with the recommendations for future work.

CHAPTER 2

DYNAMIC BEHAVIOR OF A SIMPLE ROTOR SUPPORTED ON HYDRO-DYNAMIC BEARINGS AND CONDITIONS FOR BACKWARD WHIRL IN ROTORS - THEORY AND EXPERIMENTS

An extensive literature review has been presented in the previous chapter about the quantum of work carried out by various researchers to evaluate the dynamic characteristics of rotor-bearing systems. The important design parameters of any rotor-bearing system are (i) unbalance response and (ii) critical speeds. In the vicinity of the critical speeds of the rotor, the response is quite large and hence, the normal steady-state operating speeds of the rotor must be away from these speeds. When the rotors are mounted on hydrodynamic bearings, the evaluation of damped critical speeds and the unbalance response is more involved due to the asymmetry in the direct and cross-coupled stiffness and damping co-efficients in the horizontal and vertical directions. Moreover, these co-efficients are dependent on the operating speed of the rotor.

While designing a rotor-bearing system, for a specific operating range, it is customary to evaluate the dynamic responses at a location of heavy disk, impeller or mechanical coupling etc., in order to ensure that the unbalance response and critical speeds at these locations do not fall in the critical regions; whereas the responses at the bearing locations are not generally taken into consideration. In the event of the rotor response exceeding the bearing clearances, the rotor cannot operate satisfactorily. And hence, it is essential to consider the responses at the bearing locations also as one of the prime factors of design of rotor systems in order to achieve a more reliable operating

condition.

In this chapter, an analytical procedure is discussed to obtain dynamic responses of a simple rotor to specified residual unbalance. The rotor-bearing system is modelled as a Jeffcott rotor and the system equations are derived using energy method and are solved by direct method. The dynamic responses of the rotor are obtained at the disk and at the bearing locations as well, with different clearances and loads at the bearings. The whirl pattern of the rotor is obtained through orbit diagrams for different speeds of the rotor at the disk and the bearing locations. The responses and critical speeds of the rotor obtained through analysis are verified with experiments. Also, a simple analysis is used to derive the conditions for the occurrence of backward whirl in rotor systems.

2.1 Mathematical Model and Analysis

A typical single disk rotor supported on hydrodynamic bearings at its two extreme ends is shown in Fig. 2.1. The disk is located at the center of the shaft and the residual unbalance is specified at this location. The kinetic and potential energies for the given rotor system are set up and using Lagrange's method, equations of motion are derived. The details of energy expressions are given as shown.

The kinetic energy of the rotor shown in Fig. 2.1 is

$$\bar{T} = \frac{1}{2} m (\dot{z}_o^2 + \dot{y}_o^2) + \frac{1}{2} I_d(\dot{\theta}_z^2 + \dot{\theta}_y^2) + \frac{1}{2} I_p [\omega^2 + \omega(\dot{\theta}_z\theta_y - \dot{\theta}_y\theta_z)] \quad (2.1)$$

The potential energy is,

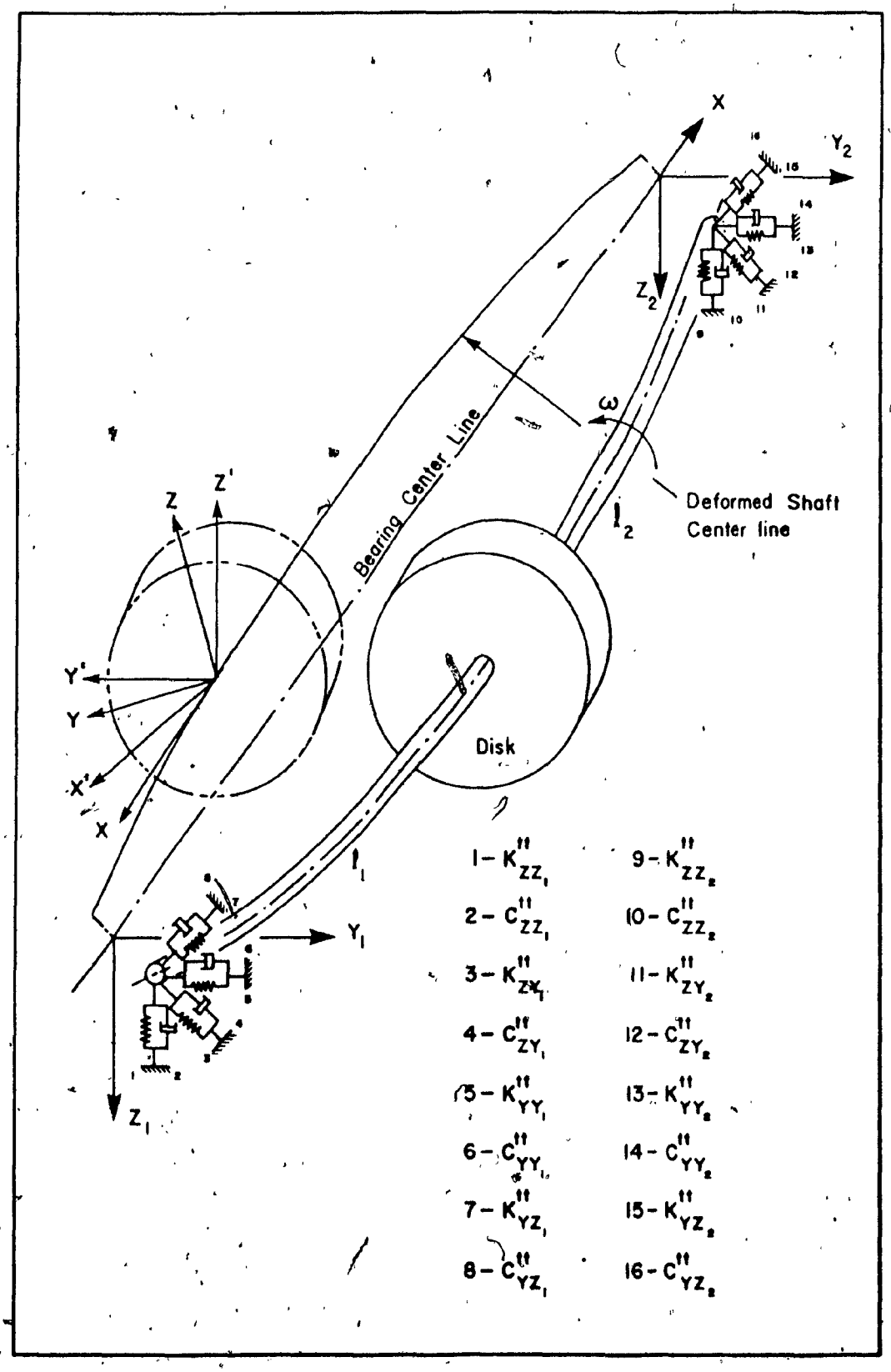

Figure 2.1 A Single Mass Rotor on Fluid-Film Bearings.

$$\bar{V} = \frac{\alpha}{2}\left[\left(z_o - \frac{\ell_1}{\ell} z_2 - \frac{\ell_2}{\ell} z_1\right)^2 + \left(y_o - \frac{\ell_1}{\ell} y_2 - \frac{\ell_2}{\ell} y_1\right)^2\right]$$

$$+ \gamma\left[\left(z_o - \frac{\ell_1}{\ell} z_2 - \frac{\ell_2}{\ell} z_1\right)\left(\theta_z - \frac{z_2 - z_1}{\ell}\right) + \left(y_o - \frac{\ell_1}{\ell} y_2 - \frac{\ell_2}{\ell} y_1\right) \cdot \left(\theta_y - \frac{y_2 - y_1}{\ell}\right)\right] + \frac{\beta}{2}\left[\left(\theta_z - \frac{z_2 - z_1}{\ell}\right)^2 + \left(\theta_y - \frac{y_2 - y_1}{\ell}\right)^2\right]$$

The virtual work expression for the forces due to constraints present in the system and are not derivable from a potential function can be written as,

$$\delta\bar{W} = \sum_{i=1}^{N} \bar{Q}_i \, \delta q_i \qquad (2.2)$$

$$\delta\bar{W} = \frac{1}{2}\left[k^{tt}_{zz_1} \cdot z_1^2 + k^{tt}_{zz_2} \cdot z_2^2 + k^{tt}_{yy_1} \cdot y_1^2 + k^{tt}_{yy_2} \cdot y_2^2\right] + \left(k^{tt}_{zy_1} \cdot y_1\right) z_1 + \left(k^{tt}_{zy_2} \cdot y_2\right) z_2 + \left(k^{tt}_{yz_1} \cdot z_1\right) y_1 + \left(k^{tt}_{yz_2} \cdot z_2\right) y_2 \qquad (2.2a)$$

Non-conservative forces present are dissipative type and the virtual work expression is given by,

$$\delta\bar{W} = \sum_{i=1}^{N} Q_i \tilde{\delta}_{qi} = -\sum_{i=1}^{N} \frac{\partial \bar{D}}{\partial \dot{q}_i} \delta q_i \qquad (2.3)$$

$$\bar{D} = \frac{c_\alpha}{2}\left[\left(\dot{z}_o - \frac{\ell_1}{\ell}\dot{z}_2 - \frac{\ell_2}{\ell}\dot{z}_1\right)^2 + \left(\dot{y}_o - \frac{\ell_1}{\ell}\dot{y}_2 - \frac{\ell_2}{\ell}\dot{y}_1\right)^2\right]$$

$$+ c_\gamma\left[\left(\dot{z}_o - \frac{\ell_1}{\ell}\dot{z}_2 - \frac{\ell_2}{\ell}\dot{z}_1\right)\left(\dot{\theta}_z - \frac{\dot{z}_2 - \dot{z}_1}{\ell}\right) + \left(\dot{y}_o - \frac{\ell_1}{\ell}\dot{y}_2 - \frac{\ell_2}{\ell}\dot{y}_1\right) \cdot \left(\dot{\theta}_y - \frac{\dot{y}_2 - \dot{y}_1}{\ell}\right)\right] + \frac{c_\beta}{2}\left[\left(\dot{\theta}_z - \frac{\dot{z}_2 - \dot{z}_1}{\ell}\right)^2 + \left(\dot{\theta}_y - \frac{\dot{y}_2 - \dot{y}_1}{\ell}\right)^2\right]$$

$$+ \frac{1}{2}\left[c^{tt}_{zz_1} \cdot \dot{z}_1^2 + c^{tt}_{zz_2} \cdot \dot{z}_2^2 + c^{tt}_{yy_1} \cdot \dot{y}_1^2 + c^{tt}_{yy_2} \cdot \dot{y}_2^2\right]$$

$$+ \left(c^{tt}_{zy_1} \cdot \dot{y}_1\right)\dot{z}_1 + \left(c^{tt}_{zy_2} \cdot \dot{y}_2\right)\dot{z}_2 + \left(c^{tt}_{yz_1} \cdot \dot{z}_1\right)\dot{y}_1 + \left(c^{tt}_{yz_2} \cdot \dot{z}_2\right)\dot{y}_2$$

(2.3a)

where

$$\alpha = \frac{3EI_o\ell}{\ell_1^2\ell_2^2}$$

$$\beta = \frac{3EI_o\ell}{(\ell_1^2 + \ell_2^2 - \ell_1\ell_2)}$$

$$\gamma = \frac{3EI_o\ell}{\ell_1\ell_2(\ell_1 - \ell_2)}$$

$$I_o = \frac{\pi}{64} \times (\text{diameter of the shaft})^4 .$$

Lagrange's equation of motion is given by,

$$\frac{d}{dt}\left(\frac{\partial \bar{L}}{\partial \dot{q}_i}\right) - \frac{\partial \bar{L}}{\partial q_i} = -\frac{\partial \bar{D}}{\partial \dot{q}_i} + Q_i \qquad (2.4)$$

where $\bar{L} = \bar{T} - \bar{V}$

and $[q]^T = [z_o, y_o, \theta_z, \theta_y, z_1, y_1, z_2, y_2]$

This results in four dynamical equations and four constraint equations and the details of these equations are as shown.

The dynamical equations are:

$$m\frac{d^2}{dt}(z_o + a\cos\omega t) + \alpha\left(z_o - \frac{\ell_1}{\ell}z_2 - \frac{\ell_2}{\ell}z_1\right) + \gamma\left(\theta_z - \frac{z_2 - z_1}{\ell}\right)$$

$$+ c_\alpha\left(\dot{z}_o - \frac{\ell_1}{\ell}\dot{z}_2 - \frac{\ell_2}{\ell}\dot{z}_1\right) + c_\gamma\left(\dot{\theta}_z - \frac{\dot{z}_2 - \dot{z}_1}{\ell}\right) = 0 \qquad (2.5)$$

$$m\frac{d^2}{dt^2}(y_o + a\sin\omega t) + \alpha(y_o - \frac{\ell_1}{\ell}y_2 - \frac{\ell_2}{\ell}y_1) + \gamma(\theta_y - \frac{y_2 - y_1}{\ell})$$

$$+ c_\alpha(\dot{y}_o - \frac{\ell_1}{\ell}\dot{y}_2 - \frac{\ell_2}{\ell}\dot{y}_1) + c_\gamma(\dot{\theta}_y - \frac{\dot{y}_2 - \dot{y}_1}{\ell}) = 0 \qquad (2.6)$$

$$I_d\ddot{\theta}_z + I_p\omega\dot{\theta}_y + \gamma(z_o - \frac{\ell_1}{\ell}z_2 - \frac{\ell_2}{\ell}z_1) + \beta(\theta_z - \frac{z_2 - z_1}{\ell})$$

$$+ c_\gamma(\dot{z}_o - \frac{\ell_1}{\ell}\dot{z}_2 - \frac{\ell_2}{\ell}\dot{z}_1) + c_\beta(\dot{\theta}_z - \frac{\dot{z}_2 - \dot{z}_1}{\ell}) = 0 \qquad (2.7)$$

$$I_d\ddot{\theta}_y - I_p\omega\dot{\theta}_z + \gamma(y_o - \frac{\ell_1}{\ell}y_2 - \frac{\ell_2}{\ell}y_1) + \beta(\theta_y - \frac{y_2 - y_1}{\ell})$$

$$+ c_\gamma(\dot{y}_o - \frac{\ell_1}{\ell}\dot{y}_2 - \frac{\ell_2}{\ell}\dot{y}_1) + c_\beta(\dot{\theta}_y - \frac{\dot{y}_2 - \dot{y}_1}{\ell}) = 0 \qquad (2.8)$$

The constraint equations are:

$$-\alpha\frac{\ell_2}{\ell}(z_o - \frac{\ell_1}{\ell}z_2 - \frac{\ell_2}{\ell}z_1) + \gamma\left[-\frac{\ell_2}{\ell}(\theta_z - \frac{z_2 - z_1}{\ell}) + \frac{1}{\ell}(z_o - \frac{\ell_1}{\ell}z_2 - \frac{\ell_2}{\ell}z_1)\right]$$

$$+ \frac{\beta}{\ell}(\theta_z - \frac{z_2 - z_1}{\ell}) + k^{tt}_{zz_1}\cdot z_1 + k^{tt}_{zy_1}\cdot y_1 - c_\alpha\frac{\ell_2}{\ell}(\dot{z}_o - \frac{\ell_1}{\ell}\dot{z}_2 - \frac{\ell_2}{\ell}\dot{z}_i)$$

$$+ c_\gamma\left[-\frac{\ell_2}{\ell}(\dot{\theta}_z - \frac{\dot{z}_2 - \dot{z}_1}{\ell}) + \frac{1}{\ell}(\dot{z}_o - \frac{\ell_1}{\ell}\dot{z}_2 - \frac{\ell_2}{\ell}\dot{z}_1)\right]$$

$$+ \frac{c_\beta}{\ell}(\dot{\theta}_z - \frac{\dot{z}_2 - \dot{z}_1}{\ell}) + c^{tt}_{zz_1}\cdot\dot{z}_1 + c^{tt}_{zy_1}\cdot\dot{y}_1 = 0 \qquad (2.9)$$

$$- \alpha \frac{\ell_1}{\ell} \left(z_0 - \frac{\ell_1}{\ell} z_2 - \frac{\ell_2}{\ell} z_1\right) + \gamma \left[- \frac{\ell_1}{\ell} \left(\theta_z - \frac{z_2 - z_1}{\ell}\right) - \frac{1}{\ell} \left(z_0 - \frac{\ell_1}{\ell} z_2 - \frac{\ell_2}{\ell} z_1\right)\right]$$

$$- \frac{\beta}{\ell} \left(\theta_z - \frac{z_2 - z_1}{\ell}\right) + k^{tt}_{zz_2} \cdot z_2 + k^{tt}_{zy_2} \cdot y_2 - \frac{c_\alpha \ell_1}{\ell} \left(\dot{z}_0 - \frac{\ell_1}{\ell} \dot{z}_2 - \frac{\ell_2}{\ell} \dot{z}_1\right)$$

$$+ c_\gamma \left[- \frac{\ell_1}{\ell} \left(\dot{\theta}_z - \frac{\dot{z}_2 - \dot{z}_1}{\ell}\right) - \frac{1}{\ell} \left(\dot{z}_0 - \frac{\ell_1}{\ell} \dot{z}_2 - \frac{\ell_2}{\ell} \dot{z}_1\right)\right]$$

$$- \frac{c_\beta}{\ell} \left(\dot{\theta}_z - \frac{\dot{z}_2 - \dot{z}_1}{\ell}\right) + c^{tt}_{zz_2} \cdot \dot{z}_2 + c^{tt}_{zy_2} \cdot \dot{y}_2 = 0 \qquad (2.10)$$

$$- \alpha \frac{\ell_2}{\ell} \left(y_0 - \frac{\ell_1}{\ell} y_2 - \frac{\ell_2}{\ell} y_1\right) + \gamma \left[- \frac{\ell_2}{\ell} \left(\theta_y - \frac{y_2 - y_1}{\ell}\right) + \frac{1}{\ell} \left(y_0 - \frac{\ell_1}{\ell} y_2 - \frac{\ell_2}{\ell} y_1\right)\right]$$

$$+ \frac{\beta}{\ell} \left(\theta_y - \frac{y_2 - y_1}{\ell}\right) + k^{tt}_{yy_1} \cdot y_1 + k^{tt}_{yz_1} \cdot z_1 - c_\alpha \frac{\ell_2}{\ell} \left(\dot{y}_0 - \frac{\ell_1}{\ell} \dot{y}_2 - \frac{\ell_2}{\ell} \dot{y}_1\right)$$

$$+ c_\gamma \left[- \frac{\ell_2}{\ell} \left(\dot{\theta}_y - \frac{\dot{y}_2 - \dot{y}_1}{\ell}\right) + \frac{1}{\ell} \left(\dot{y}_0 - \frac{\ell_1}{\ell} \dot{y}_2 - \frac{\ell_2}{\ell} \dot{y}_1\right)\right]$$

$$+ \frac{c_\beta}{\ell} \left(\dot{\theta}_y - \frac{\dot{y}_2 - \dot{y}_1}{\ell}\right) + c^{tt}_{yy_1} \cdot \dot{y}_1 + c^{tt}_{yz_1} \cdot \dot{z}_1 = 0 \qquad (2.11)$$

$$- \alpha \frac{\ell_1}{\ell} \left(y_0 - \frac{\ell_1}{\ell} y_2 - \frac{\ell_2}{\ell} y_1\right) + \gamma \left[- \frac{\ell_1}{\ell} \left(\theta_y - \frac{y_2 - y_1}{\ell}\right) - \frac{1}{\ell} \left(y_0 - \frac{\ell_1}{\ell} y_2 - \frac{\ell_2}{\ell} y_1\right)\right]$$

$$- \frac{\beta}{\ell} \left(\theta_y - \frac{y_2 - y_1}{\ell}\right) + k^{tt}_{yy_2} \cdot y_2 + k^{tt}_{yz_2} \cdot z_2 - c_\alpha \frac{\ell_1}{\ell} \left(\dot{y}_0 - \frac{\ell_1}{\ell} \dot{y}_2 - \frac{\ell_2}{\ell} \dot{y}_1\right)$$

$$+ c_\gamma \left[- \frac{\ell_1}{\ell} \left(\dot{\theta}_y - \frac{\dot{y}_2 - \dot{y}_1}{\ell}\right) - \frac{1}{\ell} \left(\dot{y}_0 - \frac{\ell_1}{\ell} \dot{y}_2 - \frac{\ell_2}{\ell} \dot{y}_1\right)\right]$$

$$- \frac{c_\beta}{\ell} \left(\dot{\theta}_y - \frac{\dot{y}_2 - \dot{y}_1}{\ell}\right) + c^{tt}_{yy_2} \cdot \dot{y}_2 + c^{tt}_{yz_2} \cdot \dot{z}_2 = 0 \qquad (2.12)$$

Then, these equations of motion of the rotor system can be written in matrix form as,

$$[m]\{\ddot{q}\} + [c]\{\dot{q}\} + [k]\{q\} = \{f\} \qquad (2.13)$$

where matrices [m], [c] and [k] are given below:

Mass matrix [m]

$$\begin{bmatrix} m_d & 0 & 0 & 0 \\ 0 & m_d & 0 & 0 \\ 0 & 0 & I_d & 0 \\ 0 & 0 & 0 & I_d \end{bmatrix} \qquad (2.14)$$

Stiffness matrix [k]

$$
\begin{bmatrix}
\alpha & 0 & \gamma & 0 & \left(\frac{-\alpha\ell_2+\gamma}{\ell}\right) & 0 & -\left(\frac{\alpha\ell_1+\gamma}{\ell}\right) & 0 \\
0 & \alpha & 0 & \gamma & 0 & \left(\frac{-\alpha\ell_2+\gamma}{\ell}\right) & 0 & -\left(\frac{\alpha\ell_1+\gamma}{\ell}\right) \\
\gamma & 0 & \beta & 0 & \left(\frac{-\gamma\ell_2+\beta}{\ell}\right) & 0 & -\left(\frac{\gamma\ell_1+\beta}{\ell}\right) & 0 \\
0 & \gamma & 0 & \beta & 0 & \left(\frac{-\gamma\ell_2+\beta}{\ell}\right) & 0 & -\left(\frac{\gamma\ell_1+\beta}{\ell}\right) \\
\left(\frac{-\alpha\ell_2+\gamma}{\ell}\right) & 0 & \left(-\frac{\gamma\ell_2+\beta}{\ell}\right) & 0 & (a_1+k^{tt}_{zz_1}) & k^{tt}_{zy_1} & a_2 & 0 \\
0 & \left(\frac{-\alpha\ell_2+\gamma}{\ell}\right) & 0 & \left(\frac{-\gamma\ell_2+\beta}{\ell}\right) & k^{tt}_{yz_1} & (a_1+k^{tt}_{yy_1}) & 0 & a_2 \\
-\left(\frac{\alpha\ell_1+\gamma}{\ell}\right) & 0 & -\left(\frac{\gamma\ell_1+\beta}{\ell}\right) & 0 & a_2 & 0 & (-a_3-k^{tt}_{zz_2}) & k^{tt}_{zy_2} \\
0 & -\left(\frac{\alpha\ell_1+\gamma}{\ell}\right) & 0 & -\left(\frac{\gamma\ell_1+\beta}{\ell}\right) & 0 & a_2 & k^{tt}_{yz_2} & (a_3+k^{tt}_{yy_2})
\end{bmatrix}
$$

where $a_1 = \dfrac{\alpha\ell_2^2 - 2\gamma\ell_2 + \beta}{\ell^2}$; $a_2 = \dfrac{\alpha\ell_1\ell_2 - \gamma(\ell_1-\ell_2) - \beta}{\ell^2}$; and $a_3 = \dfrac{\alpha\ell_1^2 + 2\gamma\ell_1 + \beta}{\ell^2}$

(2.15)

Damping matrix [c]

$$
\begin{bmatrix}
c_\alpha & 0 & c_\gamma & 0 & \left(\frac{-c_\gamma \ell_2 + c_\gamma}{\ell}\right) & 0 & -\left(\frac{c_\alpha \ell_1 + c_\gamma}{\ell}\right) & 0 \\
0 & c_\alpha & 0 & c_\gamma & 0 & \left(\frac{-c_\gamma \ell_2 + c_\gamma}{\ell}\right) & 0 & -\left(\frac{c_\alpha \ell_1 + c_\gamma}{\ell}\right) \\
c_\gamma & 0 & c_\beta & (I_p\omega) & \left(\frac{-c_\gamma \ell_2 + c_\beta}{\ell}\right) & 0 & -\left(\frac{c_\gamma \ell_1 + c_\beta}{\ell}\right) & 0 \\
0 & c_\gamma & (-I_p\omega) & c_\beta & 0 & \left(\frac{-c_\gamma \ell_2 + c_\beta}{\ell}\right) & 0 & -\left(\frac{c_\gamma \ell_1 + c_\beta}{\ell}\right) \\
\left(\frac{-c_\alpha \ell_2 + c_\gamma}{\ell}\right) & 0 & \left(\frac{-c_\gamma \ell_2 + c_\beta}{\ell}\right) & 0 & (b_1 + c^{tt}_{zz_1}) & c^{tt}_{zy_1} & b_2 & 0 \\
0 & \left(\frac{-c_\alpha \ell_2 + c_\gamma}{\ell}\right) & 0 & \left(-\frac{c_\gamma \ell_2 + c_\beta}{\ell}\right) & c^{tt}_{yz_1} & (b_1 + c^{tt}_{yy_1}) & 0 & b_2 \\
-\left(\frac{c_\alpha \ell_1 + c_\gamma}{\ell}\right) & 0 & -\left(\frac{c_\gamma \ell_1 + c_\beta}{\ell}\right) & 0 & b_2 & 0 & (b_3 + c^{tt}_{zz_2}) & c^{tt}_{zy_2} \\
0 & -\left(\frac{c_\gamma \ell_1 + c_\gamma}{\ell}\right) & 0 & -\left(\frac{c_\gamma \ell_1 + c_\beta}{\ell}\right) & 0 & b_2 & c^{tt}_{yz_2} & (b_3 + c^{tt}_{yy_2})
\end{bmatrix}
$$

where $b_1 = \dfrac{c_\alpha \ell_2^2 - 2c_\gamma \ell_2 + c_\beta}{\ell^2}$; $b_2 = \dfrac{c_\gamma \ell_1 \ell_2 - c_\gamma (\ell_1 - \ell_2) - c_\beta}{\ell^2}$; and $b_3 = \dfrac{c_\alpha \ell_1^2 + 2c_\gamma \ell_1 + c_\beta}{\ell^2}$.

(2.16)

Assuming a solution of the form,

$$q = q_o \quad e^{j\omega t} , \tag{2.17}$$

the undamped homogenous case of equation (2.13) becomes,

$$\det \left|[k] - \omega^2[m]\right| = 0 \tag{2.18}$$

This is an eigenvalue problem and the undamped eigenvalues and the corresponding eigenvectors are obtained from equation (2.18). When one of the eigenvalues coincide with the rotor speed, that eigenvalue becomes the critical speed of the rotor. However, since damping is significant in fluid film bearings, critical speeds obtained by this method will not be exact. Damped critical speeds can be found from the unbalance response plots by locating the speed corresponding to the peak response.

The vector of unbalance force f can be written as,

$$\{f\} = \{f_c\} + \{f_s\} \tag{2.19}$$

where $\{f_c\}^T = [f_o \cos\omega t, 0, 0, 0, 0, 0, 0, 0]$

$\{f_s\}^T = [0, f_o \sin\omega t, 0, 0, 0, 0, 0, 0]$

and $f_o = ma\omega^2$

where a is the eccentricity of the disk.

The steady state solution of equation (2.13) may be written as,

$$\{q\} = \{q_c\} + \{q_s\} \tag{2.20}$$

where $\{q_c\} = \{q\} \cos\omega t$

and $\{q_s\} = \{q\} \sin\omega t$

Substitution of equations (2.19) and (2.20) in equation (2.13) yields

$$\begin{Bmatrix} q_c \\ q_s \end{Bmatrix} = \begin{bmatrix} ([k] - \omega^2[m]) & -\omega[c] \\ +\omega[c] & ([k] - \omega^2[m]) \end{bmatrix}^{-1} \begin{Bmatrix} f_c \\ f_s \end{Bmatrix} \qquad (2.21)$$

The out of balance response is the vector sum of responses in Z and Y directions and is expressed non-dimensionally as,

$$r = (\{z\} + j\{y\})/a \qquad (2.22)$$

where

$$\{z\}^T = [z_o, \theta_z, z_1, z_2]$$

and $$\{y\}^T = [y_o, \theta_y, y_1, y_2]$$

The response at the disk location along Z and Y directions can be expressed as follows:

$$z_o = z_{oc} \frac{e^{j\omega t} + e^{-j\omega t}}{2} + z_{os} \frac{e^{j\omega t} - e^{-j\omega t}}{2j} \qquad (2.23)$$

$$y_o = y_{oc} \frac{e^{j\omega t} + e^{-j\omega t}}{2} + y_{os} \frac{e^{j\omega t} - e^{-j\omega t}}{2j} \qquad (2.24)$$

Therefore, whirl amplitude of the rotor at the disk location can be written as,

$$r_d = z_o + j\, y_o \tag{2.25}$$

$$= \frac{1}{2}(z_{oc} - j\, z_{os})\, e^{j\omega t} + \frac{1}{2}(z_{oc} + j\, z_{os})\, e^{-j\omega t}$$

$$+ j\left[\frac{1}{2}(y_{oc} - j\, y_{os})\, e^{j\omega t} + \frac{1}{2}(y_{oc} + j\, y_{os})\, e^{-j\omega t}\right] \tag{2.26}$$

$$r_d = r_d^+ \; e^{j\omega t} + r_d^- \; e^{-j\omega t} \tag{2.27}$$

where, $r_d^+ = \frac{1}{2}\;(z_{oc} - j\, z_{os}) + (y_{os} + j\, y_{oc})$ is the forward whirl amplitude and $r_d^- = \frac{1}{2}\;\; (z_{oc} + j\, z_{os}) + (-y_{os} + j\, y_{oc})$ is the backward whirl amplitude at the disk location. Similar expressions can be obtained for bearing locations also. These quantities together with the respective phase angles are useful in determining the whirl direction.

2.2 Dynamic Characteristics

The above analysis is used to obtain the damped critical speeds and the normalized unbalance response of a single disk rotor, the details of which are given in Table-2.1. The dynamic responses are obtained at the disk as well as at the two bearings. In hydrodynamic bearings, variations of bearing clearances and bearing loads alter the Sommerfeld number which in turn influences the bearing film stiffness and damping values.

TABLE 2.1: Details of Rotor

Disk Mass	:	11 kg
Type of bearings	:	Plain cylindrical
Bearing diameter	:	0.0254 m
Bearing L/D ratio	:	1
Viscosity of oil at 25.5°C	:	0.0241 N. sec/m^2
Total length of rotor	:	0.5105 m
Modulus of elasticity of the material of shaft	:	2.145×10^{11} N/m^2
Shaft diameter	:	0.022 m
Disk diameter	:	0.2032 m
Disk eccentricity	:	1.084×10^{-4} kg.m

2.2.1 Dissimilar Bearings by Variation of Clearances

The variation of unbalance response for a specified unbalance at the disk is shown in Fig. 2.2 when the disk is at the center of the shaft. The bearing clearance value c_1 at the left end is kept constant at 0.0000533m and the clearance value c_2 at the right end is varied as shown in Fig. 2.2. The rotor exhibits single peak in the response for different c_2 values except for one c_2 value of 0.000188m where the rotor exhibits a double peak in the response. Moreover, the peak amplitude of the response drops down considerably while the peaks themselves shift towards lower rotor speeds as the c_2 values are increased.

The unbalance responses of the central disk, when the bearing clearance value c_1 at the left end is kept at a constant value of 0.000188m and clearance value c_2 at the right end is varied, are as shown in Fig. 2.3 for a specified unbalance at the disk. For such configurations of the rotor, the response exhibits double peaks for different c_2 values. The peak amplitude values are smaller and the critical speeds are lower when compared with those values obtained for different rotor configurations discussed before.

In general, when the bearing clearances are increased, the Sommerfeld number lowers, thereby lowering the fluid film stiffness values; however, their damping counterparts are on the increase. This effect not only lowers the rotor critical speeds, but also the peak amplitude values of the rotor system. This trend is observed in both Figs. 2.2 and 2.3.

The above results are consolidated and the effect of various bearing clearance values on the unbalance response and critical speeds are shown in Figs. 2.4 and 2.5 respectively. It is seen that there is a

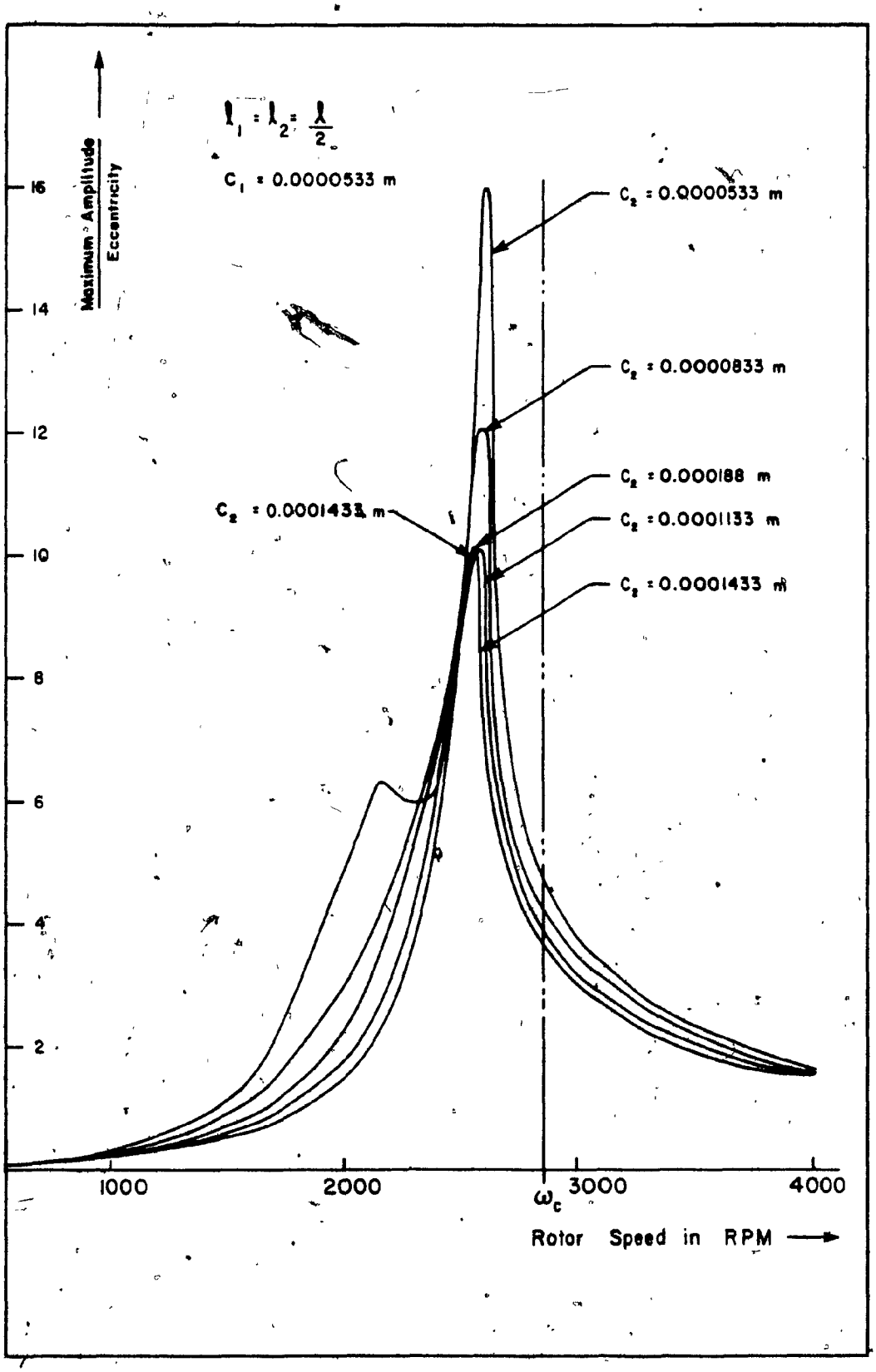

Figure 2.2 Normalized Unbalance Response of the Rotor .

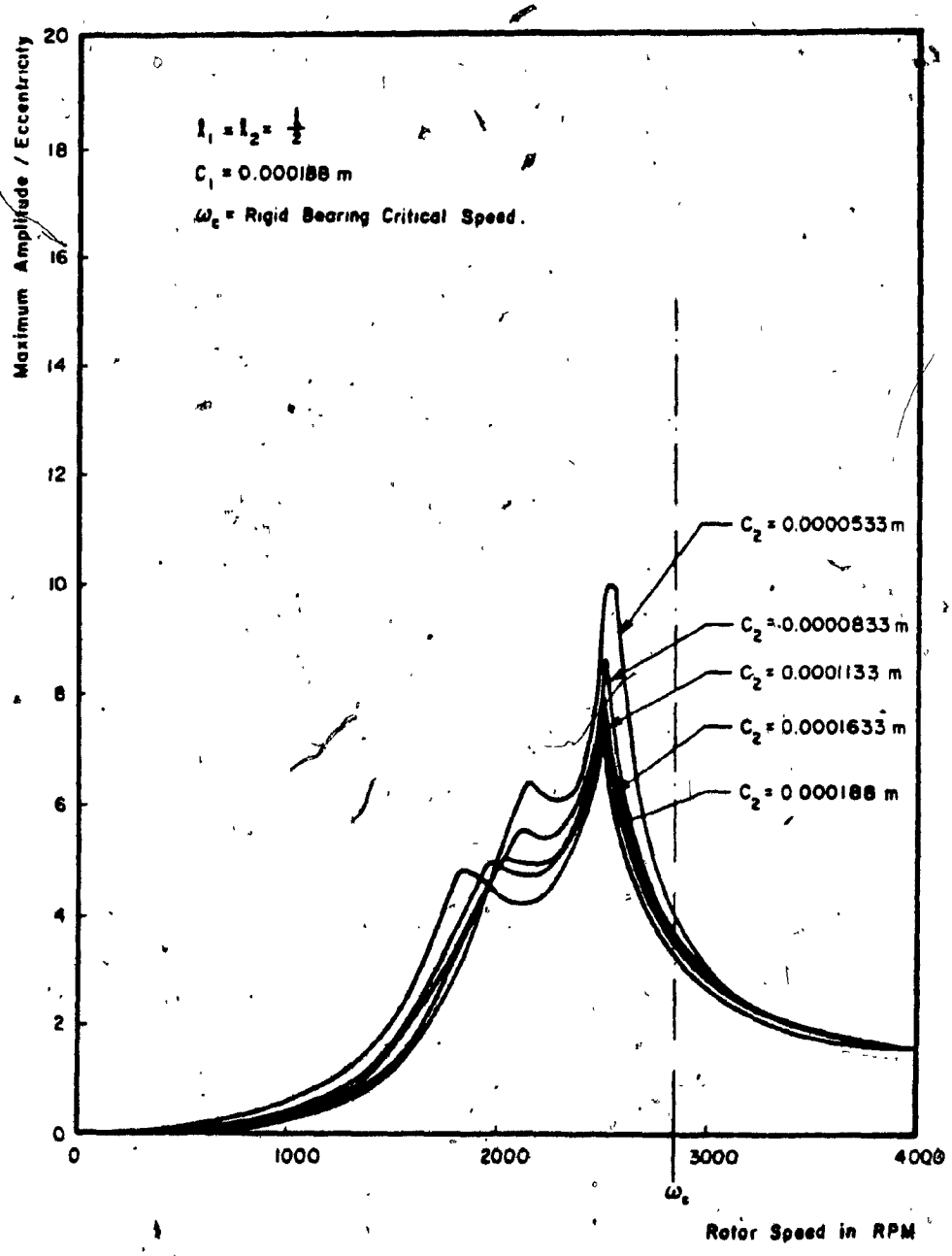

Figure 2.3 Normalized Unbalance Response of Rotor.

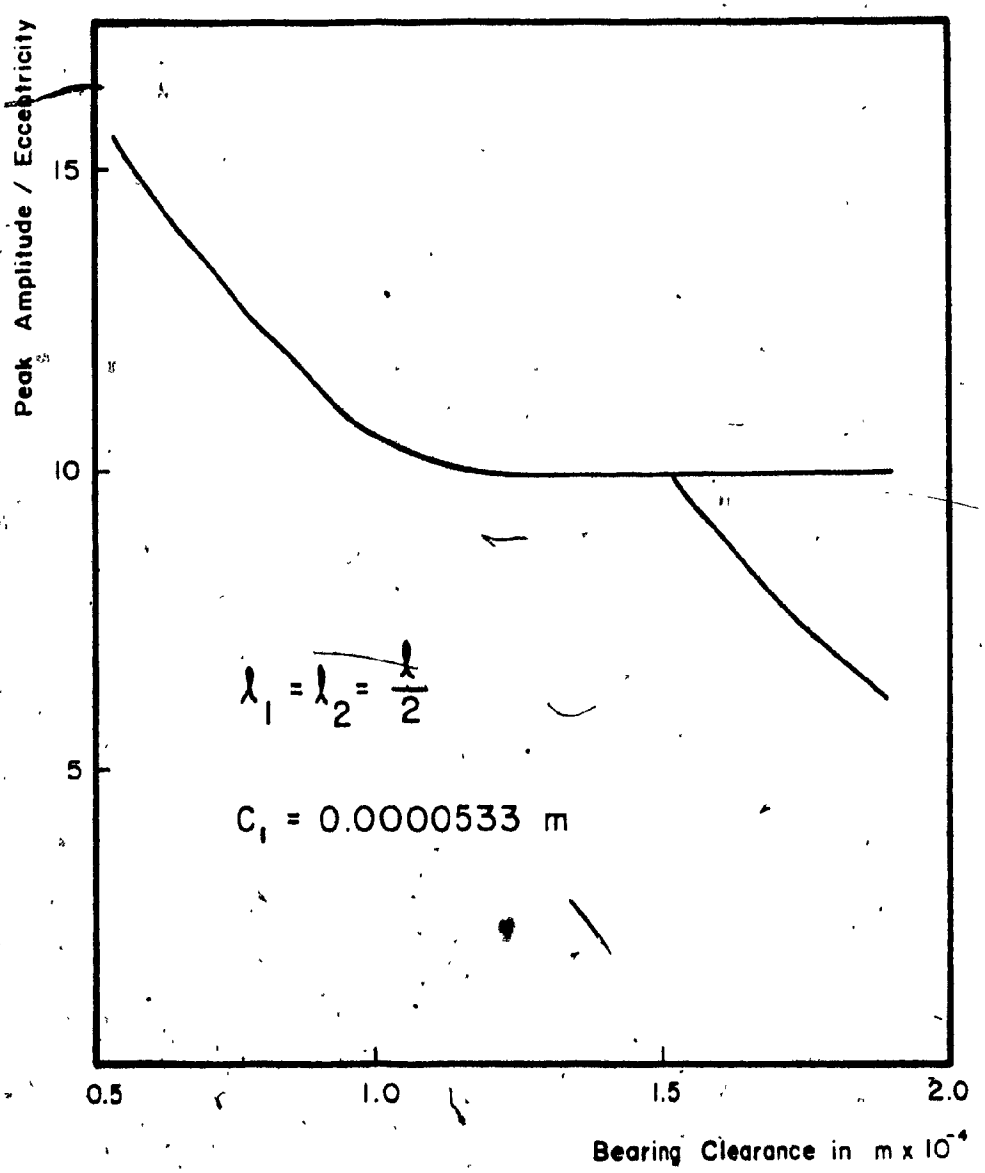

Figure 2.4 Variation of Peak Response of Rotor .

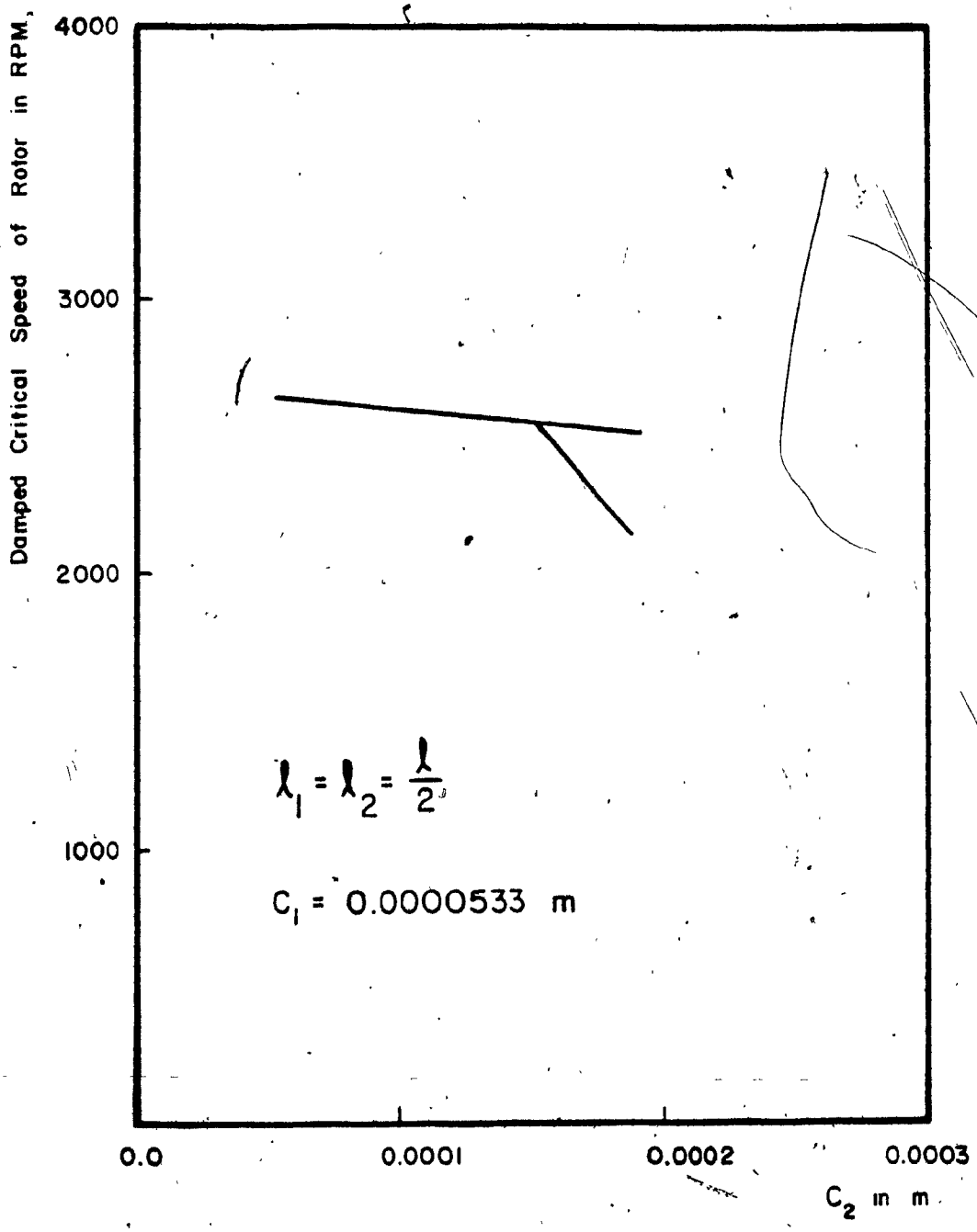

Figure 2.5 Variation of Critical Speeds of Rotor.

range of bearing clearances where the rotor has split criticals and double peak responses and out of this range, the split critical and double peak responses coalesced into one.

2.2.2 Dissimilar Bearings by Variation of Disk Positions

Dissimilarity in the bearings can be introduced by repositioning the disk along the rotor shaft. The noncentral disk exerts different loads on the two bearings and hence the Sommerfeld numbers for the two bearings will be different. The details of this rotor configurations are given in Table 2.2. The unbalance response of the rotor is shown in Fig. 2.6 when the bearing clearances at the two ends are kept at a constant value of 0.0000533m for different positions of the disk along the rotor shaft. As the disk is moved away from the center, the response decreases. There is a small peak in each of the response curves, however the response goes on increasing with speed beyond this peak.

So far, the unbalance responses and critical speeds of a single disk rotor system were studied for various combinations of bearing clearances and bearing loads. The peak responses were obtained at the disk locations. Based on the response plots, a designer can choose an operating speed range of the rotor arbitrarily, by avoiding the critical regions in the response. However, it is not certain that the bearings may operate satisfactorily at this chosen operating range. Hence, it is recommended that for a more viable and reliable design of rotor systems, the response information at the bearings should also be taken into consideration.

TABLE 2.2: Details of Rotor

Disk Mass	:	2.23 kg
Type of bearings	:	Plain cylindrical
Bearing diameter	:	0.0254 m
Bearing L/D ratio	:	1
Viscosity of oil at 25.5°C	:	0.0241 N. sec/m^2
Total length of rotor	:	0.5105 m
Modulus of elasticity of the material of shaft	:	2.145×10^{11} N/m^2
Shaft diameter	:	0.022 m
Disk diameter	:	0.0958 m
Disk eccentricity	:	1.084×10^{-4} kg.m

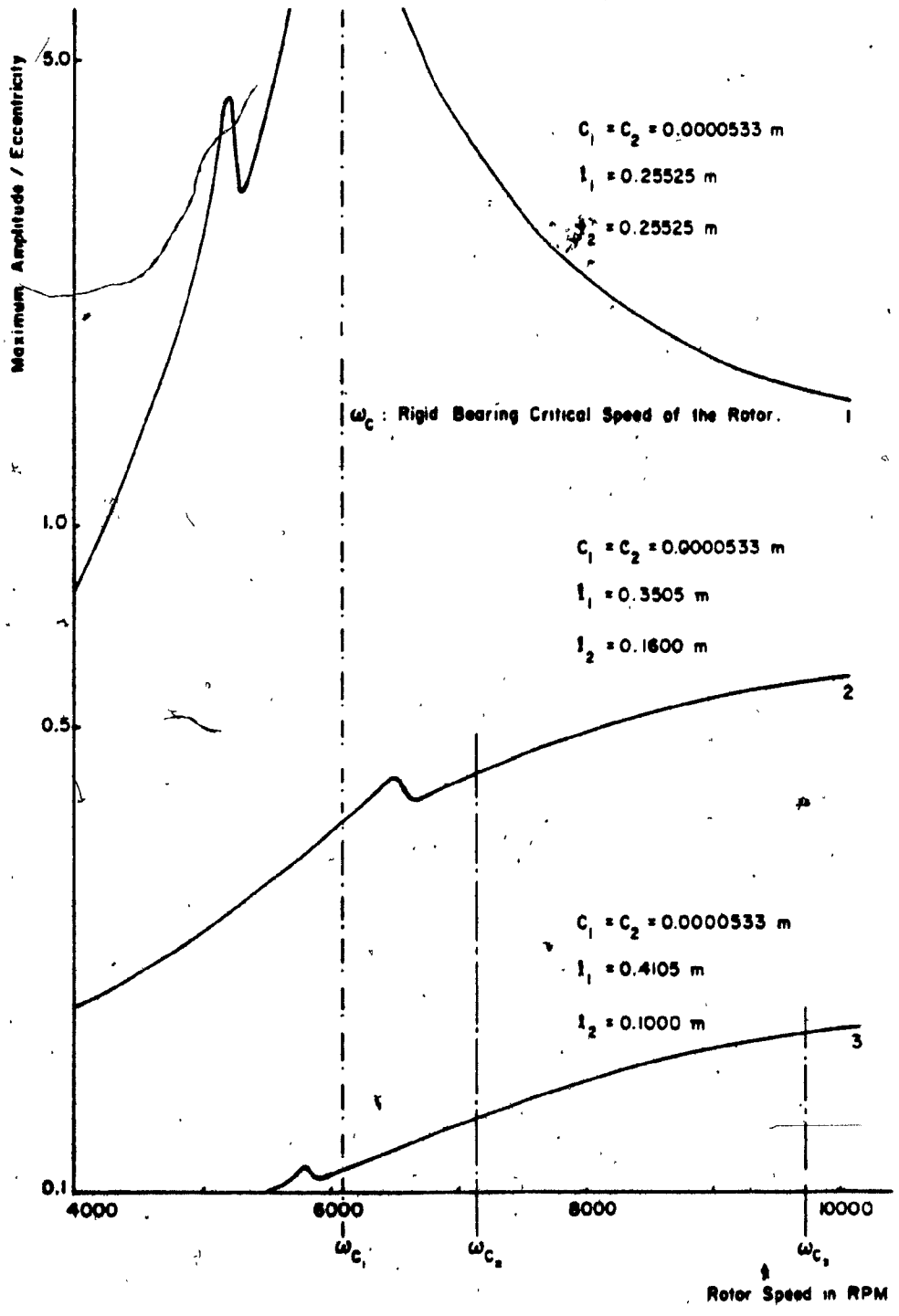

Figure 2.6 Unbalance Response of Rotor.

2.3 Orbital Diagrams

Orbital diagrams provide the amplitude and direction of whirl path at any particular location of a rotor-bearing system. Due to non-symmetric nature of fluid film properties of the bearings, the rotor whirl path is not circular, but it is elliptic for all stable conditions of the rotor. However, for unstable conditions of the rotor, the orbital diagram shows a deviation from this elliptic path and the behaviour of the orbit also changes. Hence, the orbital diagram provides more information regarding the dynamic behaviour of the system.

Orbital diagrams for the rotor system with central disk and equal bearing clearance values of 0.000188m at both ends are studied because this configuration of the rotor exhibits split criticals and hence the whirl patterns of the system at different rotor speeds are of interest. The rotor exhibits split criticals, one occurs at a rotor speed of 1865 RPM and the other occurs at a rotor speed of 2500 RPM. The orbital diagrams are obtained at the disk and at the bearing locations for three different rotor speeds viz, (i) 1700 RPM which lies below the first critical, (ii) 2100 RPM which lies between the two criticals and (iii) 2700 RPM which is above the second critical and they are shown in Figs. 2.7 through 2.9. Figure 2.7 shows that the rotor executes a forward whirl both at the disk and bearing locations with their relative phase angles. Figure 2.8 shows the orbital diagram for a rotor speed in between the two criticals. The rotor experiences forward whirl only. The rotor motion tends towards the backward whirl in between the criticals. The rotor motion at the bearing locations is similar to that of the disk, however, it has different amplitude and phase. The orbital

Motion is Counterclockwise, Corresponding to Forward Whirl.

Rotor Speed : 1700 rpm

Central Disk :

$C_1 = C_2 = 0.000188$ m

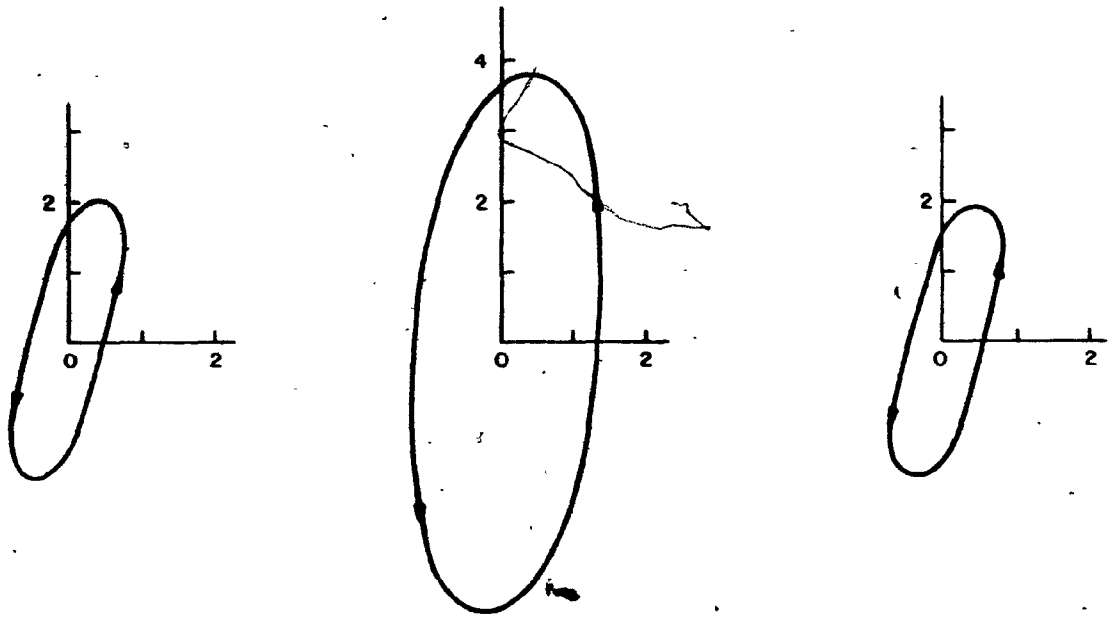

Bearing 1 Disk Bearing 2

Figure 2.7 Normalized Orbital Diagram at 1700 RPM.

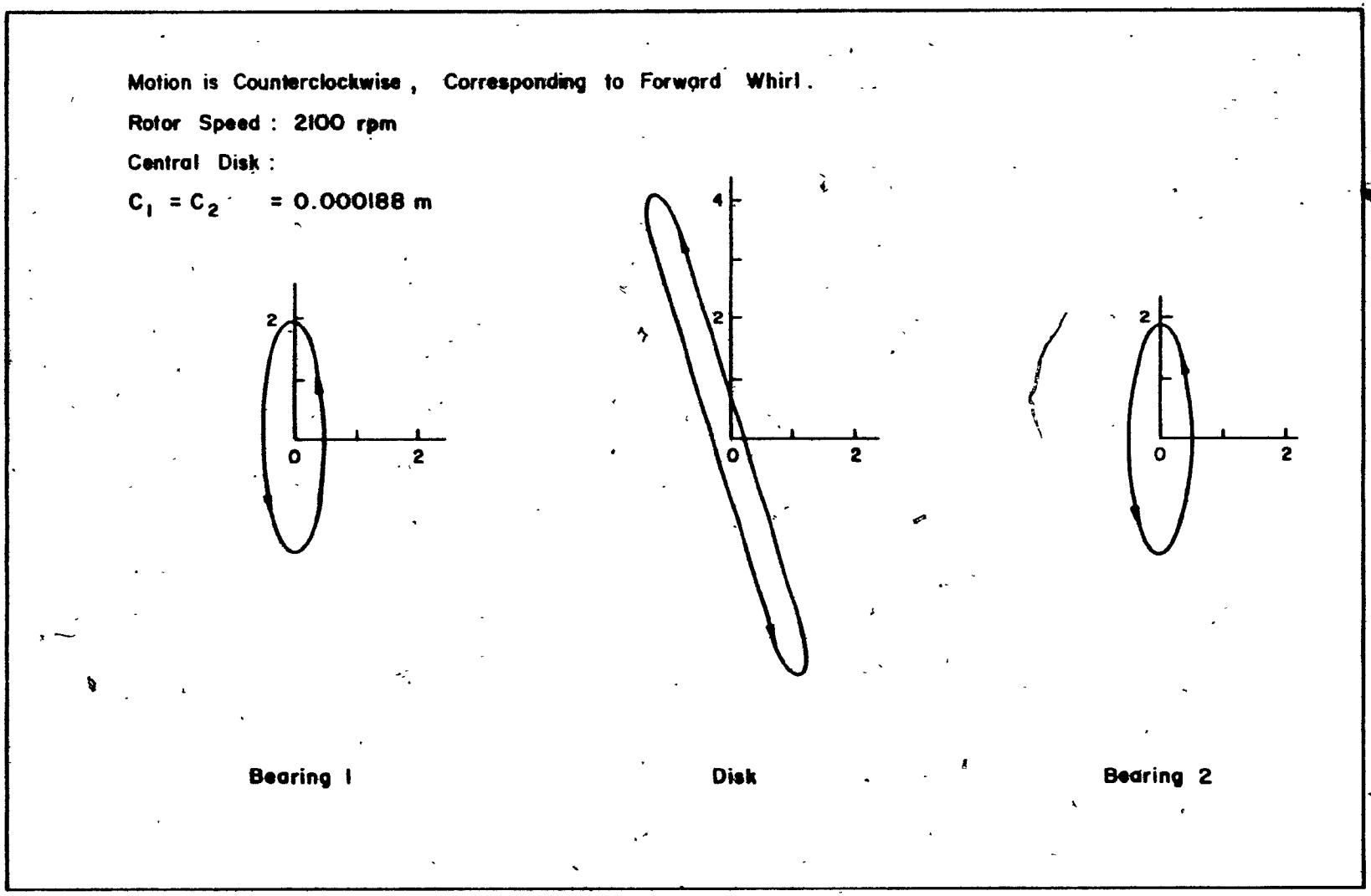

Figure 2.8 Normalized Orbital Diagram at 2100 RPM.

diagram, when the rotor is running above the second critical is shown in Fig. 2.9. This shows that the rotor is executing a forward whirl.

Orbital diagram for the rotor system with central disk and dissimilar bearing clearance values of c_1 = 0.0000533m and c_2 = 0.000188m is shown in Fig. 2.10 for a rotor speed of 2300 RPM, which lies in between the criticals. The rotor whirl is forward and whirl direction does not change in between the criticals. Here, the whirl is synchronous, however, the motion at the two bearing locations have different amplitudes and they are not in phase with each other and with the disk motion. This is due to different stiffness and damping values at the two bearings.

The orbital diagrams at the disk and bearing locations are shown in Fig. 2.11 when ℓ_1 = 0.3105m and ℓ_2 = 0.2m and equal bearing clearances of 0.0000533m for rotor speed of 4000 RPM. This shows that the rotor motion is dominated by forward whirl.

It is generally noted from these orbital diagrams that there are speeds at which the response at the bearing location is more than the bearing clearance. The present investigation considers only linear stiffness and damping co-efficients for the fluid film in the bearings. When the response at the bearing locations are of the order of the bearing clearance, a linear analysis is not enough to study the rotor behavior. However, on the basis of linear analysis, it seems that the rotor cannot operate satisfactorily under such conditions.

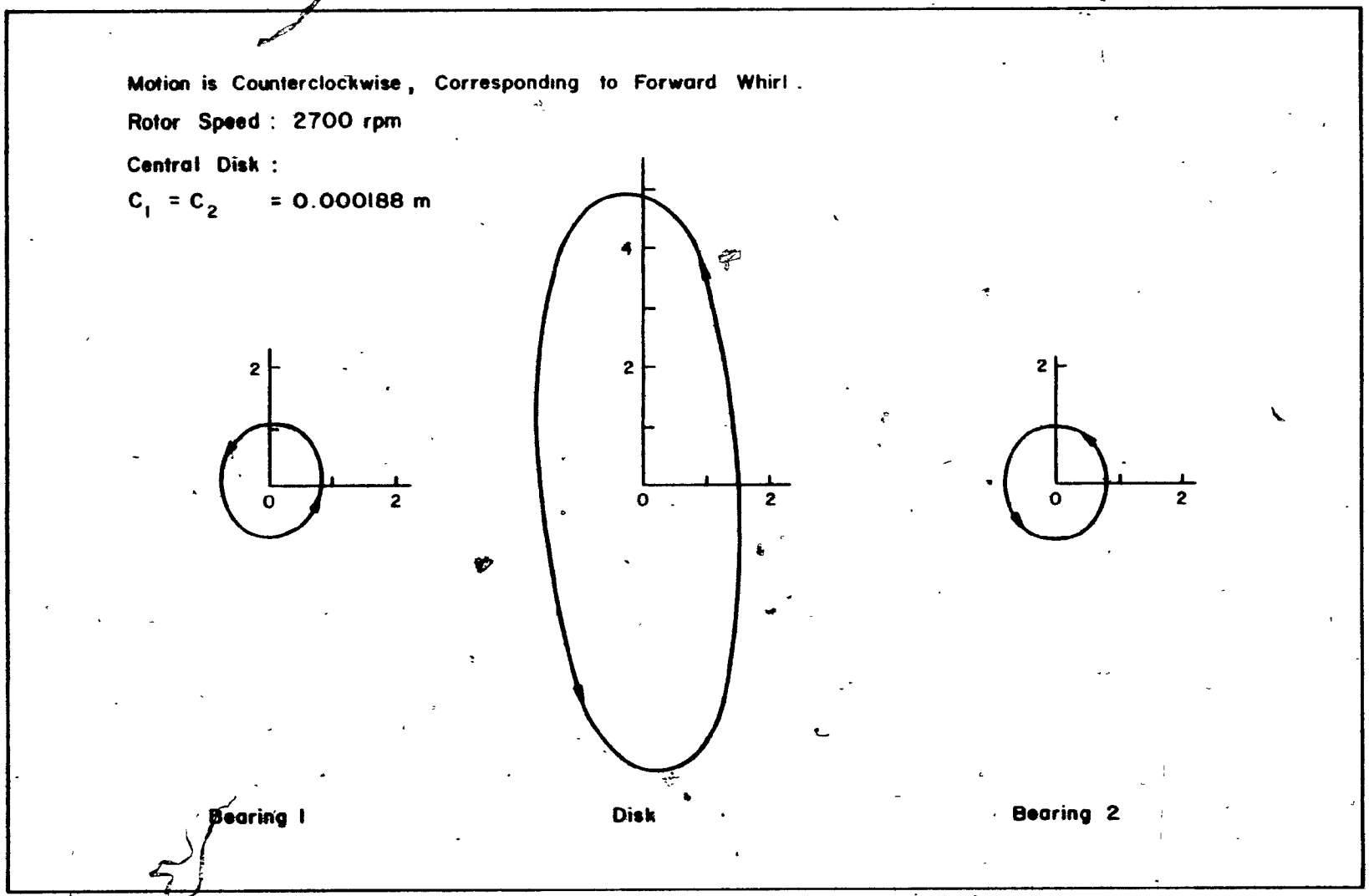

Figure 2.9 Normalized Orbital Diagram at 2700 RPM.

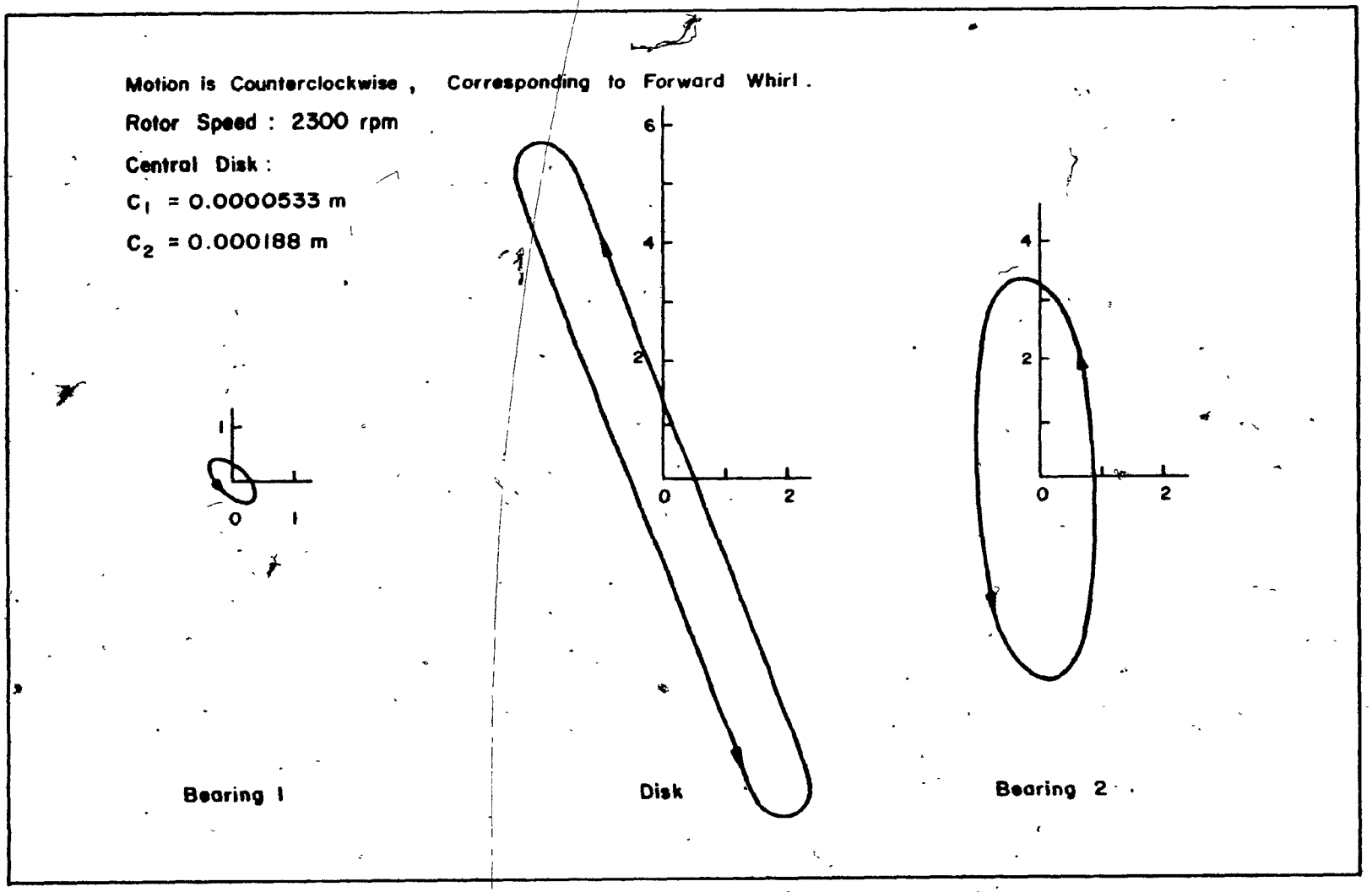

Figure 2.10 Normalized Orbital Diagram at 2300 RPM.

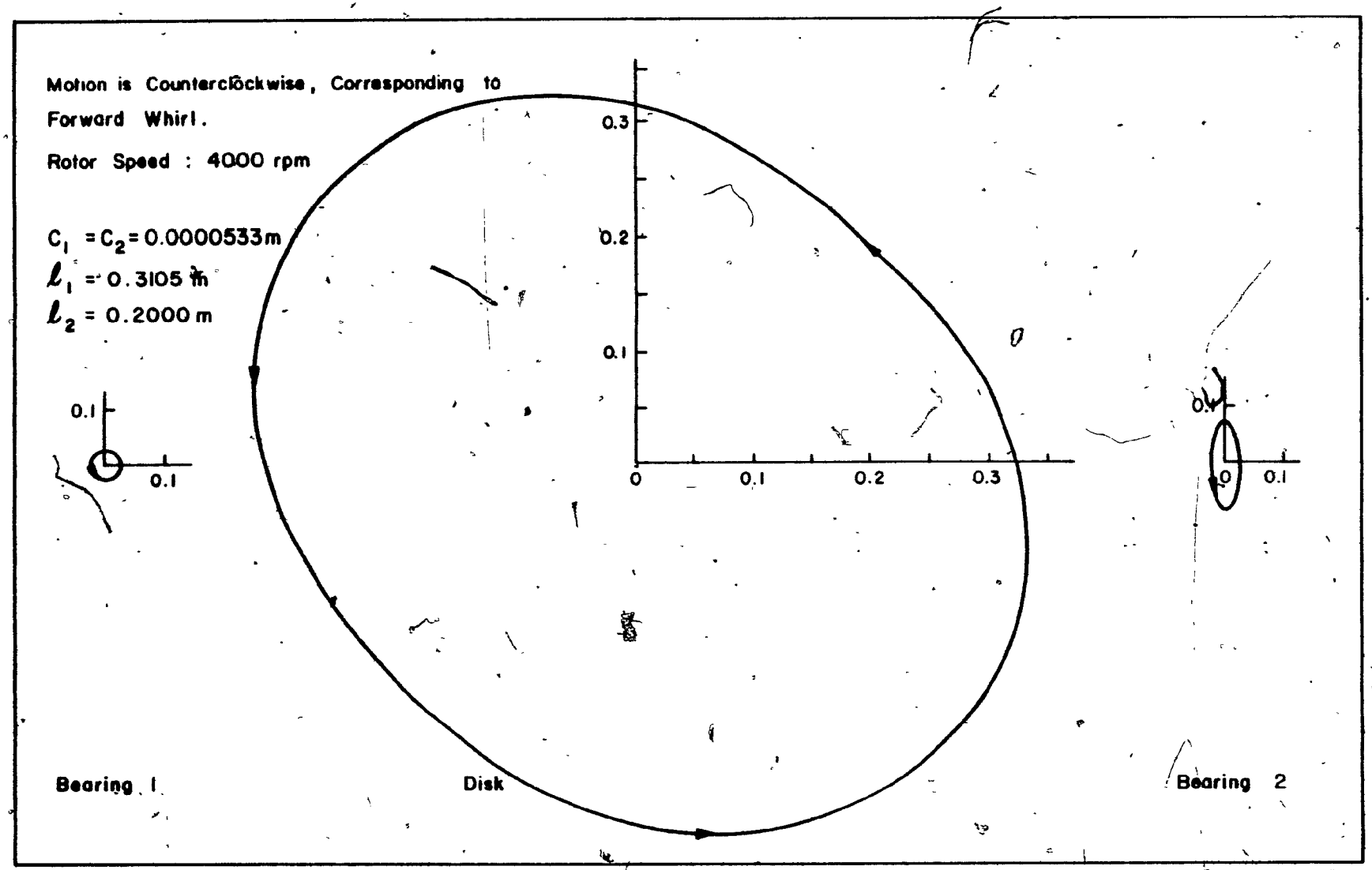

Figure 2.11 Normalized Orbital Diagram at 4000 RPM

2.4 Experimental Work

There are different analytical procedures available to predict the dynamic behavior of a rotor system; however, very few experimental works have been reported to support the theoretical analysis. Particularly so is the occurrence of backward whirl which is not reported in experimental work so far.

To verify the theoretical analysis described in section 2.1, an experimental facility was established. It consisted of a disk at the center of a shaft of circular cross-section, supported at its two ends on two plain cylindrical fluid film bearings. The oil for the bearings was gravity fed through polythene tubes. The rotor-bearing system is supported by heavy cast-iron pedestals at the two ends. The entire rotor system is mounted on a heavy steel frame which in turn is fastened to the floor. The details of the test rotor are the same as those given in Table 2.1 and the schematic diagram of the experimental facility is shown in Fig. 2.12.

The test rotor is driven by a variable speed motor and the rotor speed is measured using a photo-sensitive meter. Two displacement measuring shielded sensors which operate on the eddy current principle are used to measure the unbalance response of the rotor in both Z and Y directions at a point along the rotor shaft and closer to the disk. The sensors are mounted on two micrometer heads to enable precise adjustment of the gap between the sensors and the shaft surface.

The unbalance response or the whirl amplitude signals from the sensors, located along Z and Y directions, are amplified and fed to a FFT analyzer. The orbit diagrams are obtained on the screen of the

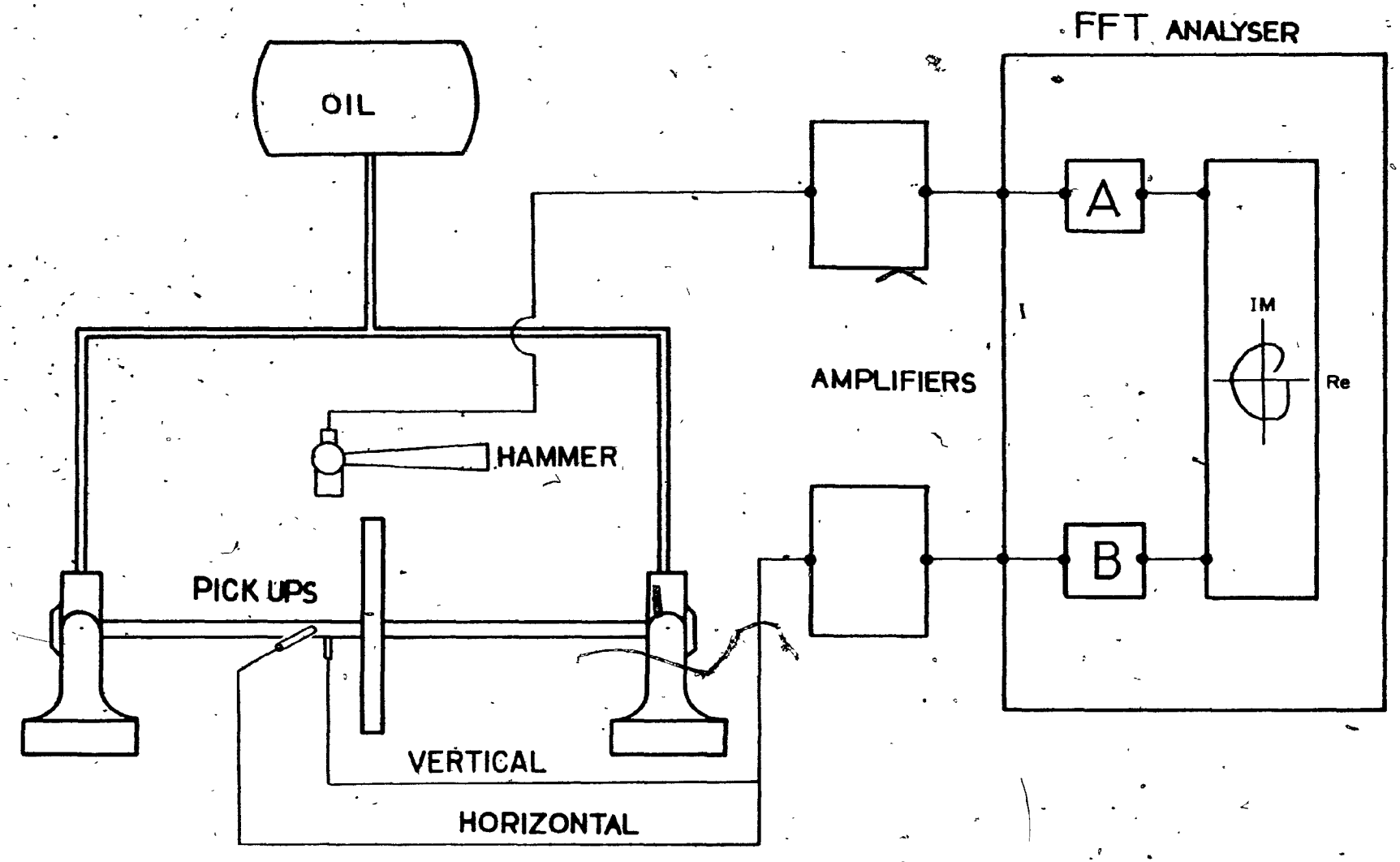

Figure 2.12 Schematic diagram of the experimental facility.

analyzer by combining the Z and Y signals. The orbital pattern at any steady-state speed of the rotor can be obtained by pushing the hold button on the FFT. The corresponding orbital diagram of the rotor is plotted by interfacing the Z and Y signals of the FFT analyzer to the corresponding plotter plane of the X-Y plotter. The unbalance response is measured from the orbit diagram plots.

2.4.1 Comparison of Experimental and Analytical Results

The unbalance response and critical speeds of a single disk rotor supported on hydrodynamic bearings are measured. Three different clearance values are used in the bearings. They are:

(i) 0.533×10^{-4}m

(ii) 0.6858×10^{-4}m

(iii) 1.88×10^{-4}m

The corresponding analytical results are compared. One set of bearing is made dissimilar by having different clearance values at the two bearings.

The variation of unbalance response of the rotor with the rotor speed in RPM is shown in Fig. 2.13. The clearances at both the bearings are kept at 0.533×10^{-4}m. Theoretical as well as experimental response plots exhibit single peak only. The experimental value of the response peak is 11.76 and the rotor critical speed corresponding to this peak occurs at 2550 RPM whereas, peak response value predicted by theoretical analysis is 16.0 at the corresponding critical speed of 2610 RPM.

The unbalance response of the rotor with the two end bearing clearance values kept at 0.6858×10^{-4}m is shown in Fig. 2.14. In this plot,

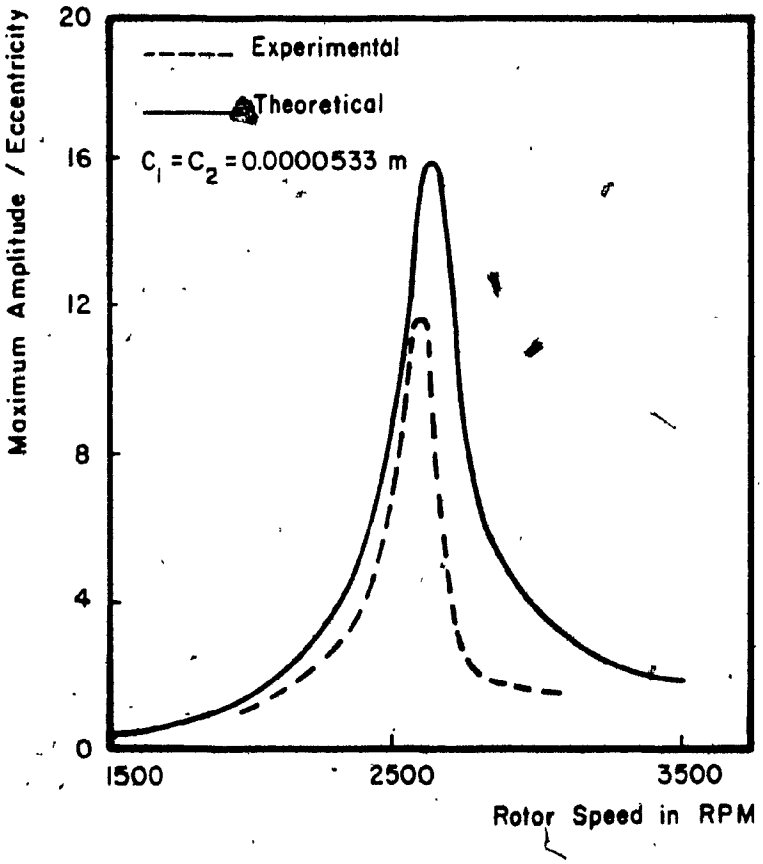

Figure 2.13 Unbalance Response of Rotor.

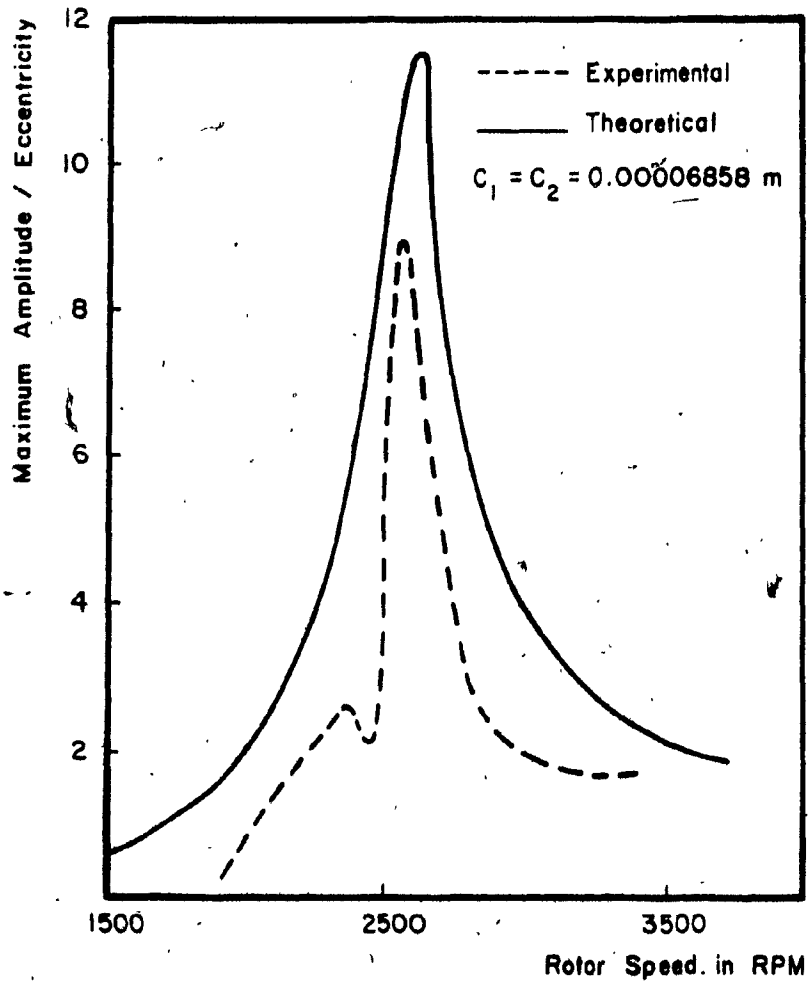

Figure 2.14 Unbalance Response of Rotor.

the theoretical response shows only a single peak. The experimentally measured response peak is 8.94 at a rotor critical speed of 2550 RPM and the theoretical prediction shows a peak response value of 11.5 at a rotor speed of 2600 RPM.

Figure 2.15 shows the response of the rotor for the bearing clearance of 1.88×10^{-4}m at both the ends. Theoretical analysis exhibits two distinct peaks whereas the experimentally measured response shows only a single peak. The second peak amplitude values are 8.1 and 5.53 for theoretical and experimental studies respectively. The critical speeds of the rotor corresponding to this peak response occurs at 2500 RPM for both theoretical and experimental cases.

The variation of critical speeds against the rotor speed is shown in Fig. 2.16 for the bearing clearances of 1.88×10^{-4}m at the left end and 0.533×10^{-4}m at the right end of the bearings. Both theory and experiment show two distinct peaks. The magnitude of first peak predicted by theory is 6.3 corresponding to the rotor speed of 2168 RPM whereas the same for the experimental case is 3.4 at 2250 RPM. The magnitudes at the second peak are 7.93 and 10.82 and correspond to the rotor speeds of 2500 RPM and 2550 RPM respectively, for the experimental and theoretical studies.

2.4.2 Analytical and Experimental Orbit Diagrams

Experimentally obtained orbit diagrams at the disk are shown in Figs. 2.17(a) and 2.18(a) along with the respective orbit diagrams obtained by theoretical analysis for two different bearing configurations of the rotor system. Figure 2.17(a) shows the orbit diagrms for the central disk and identical bearing clearance values of 0.00006858m at

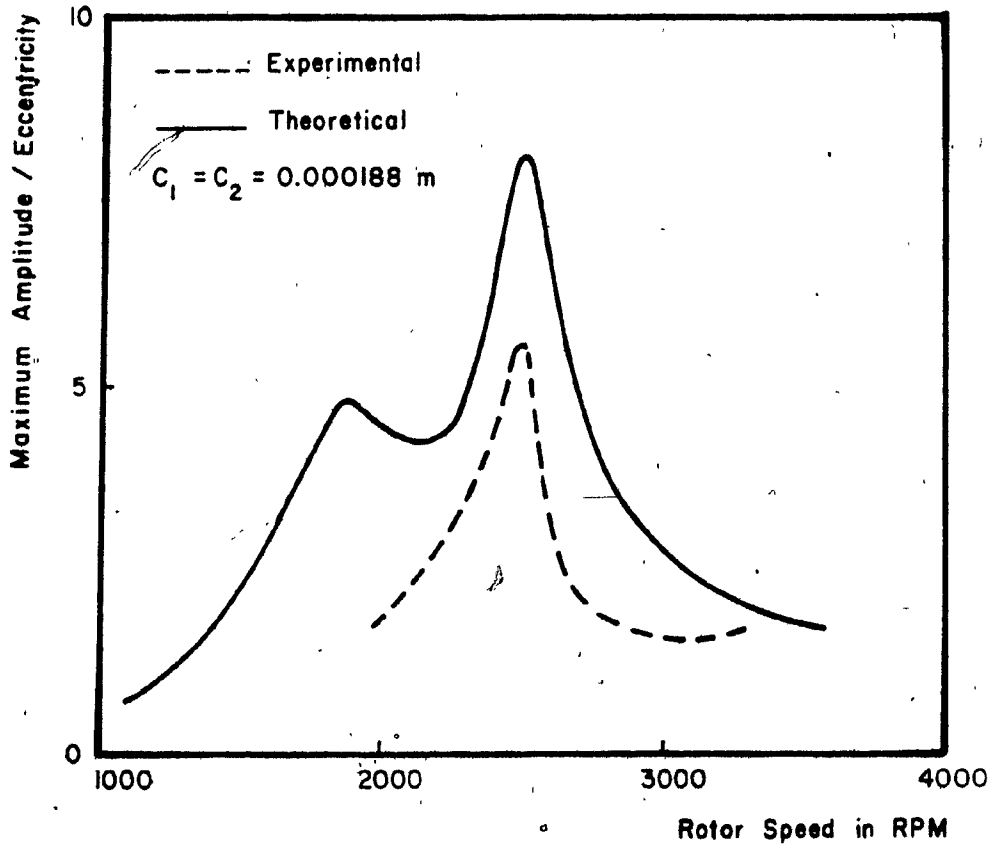

Figure 2.15 Unbalance Response of Rotor.

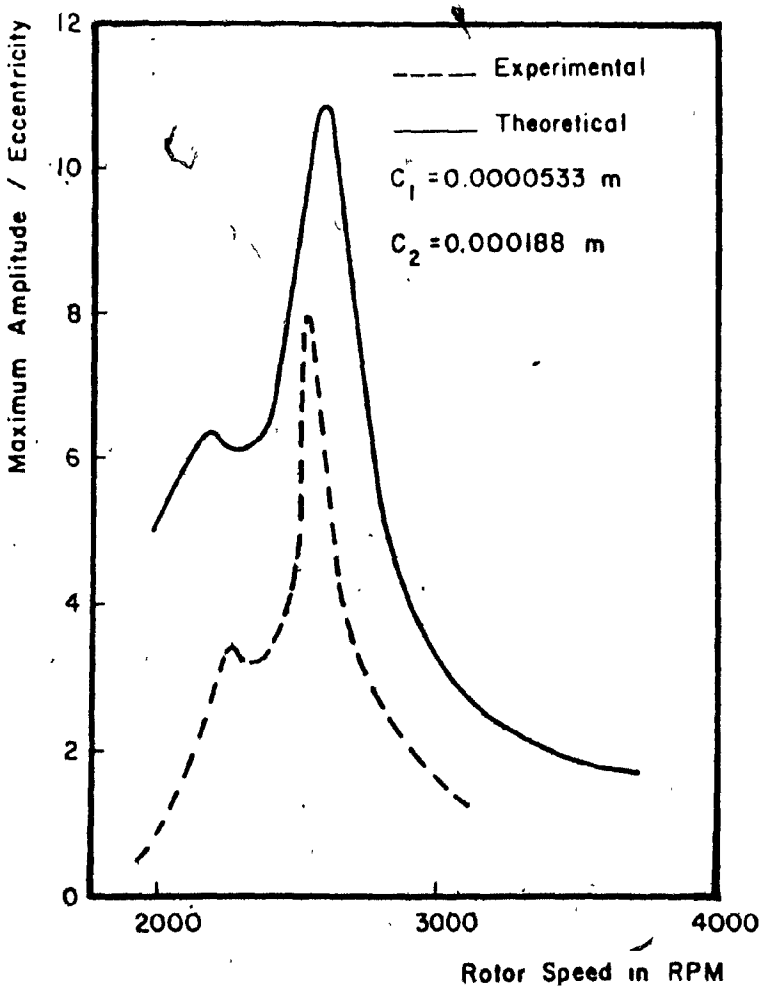

Figure 2.16 Unbalance Response of Rotor.

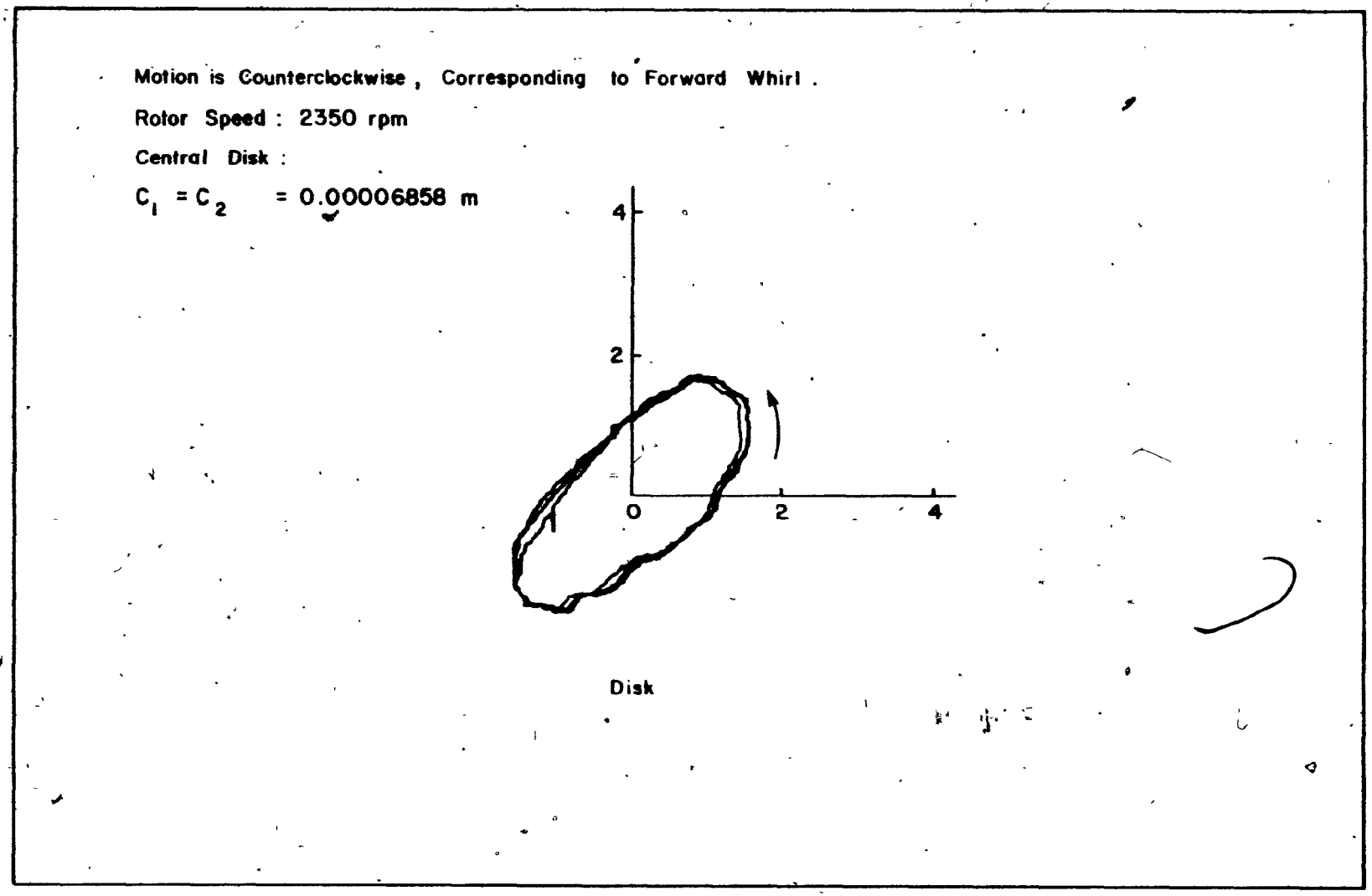

Figure 2.17(a) Experimental Orbital Diagram.

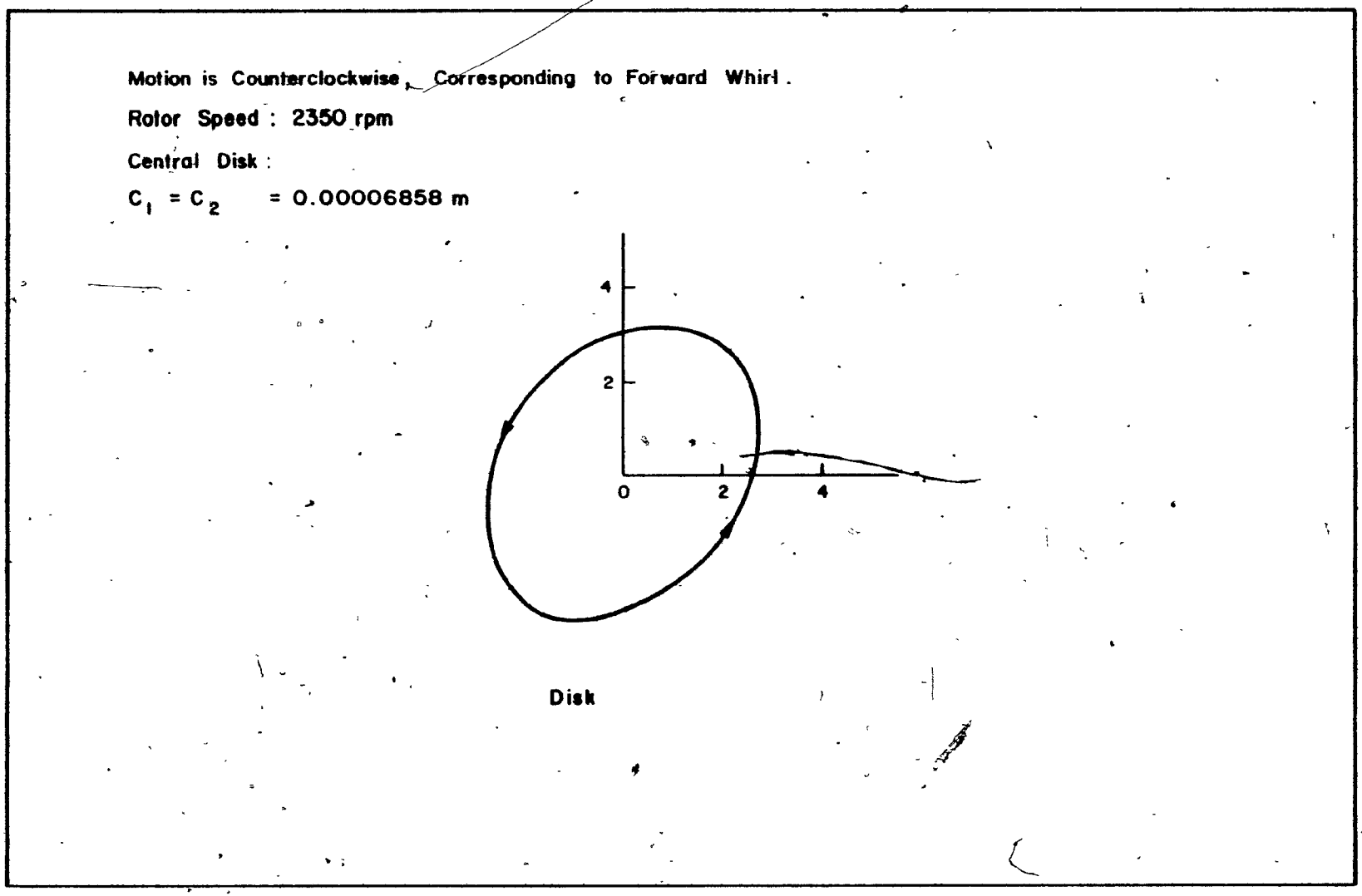

Figure 2.17(b) Theoretical Orbital Diagram at 2350 RPM.

both ends, for the rotor speed of 2350 RPM. Both theoretical and experimental diagrams show forward whirl only. Figure 2.18(a) shows the orbit diagrams for the central disk and dissimilar bearing clearance values of c_1 = 0.0000533m and c_2 = 0.000188m, at the rotor speed of 2475 RPM. The theoretical and experimental diagrams show that the forward whirl component is predominant and hence rotor has a forward whirl.

2.5 Conditions of Backward Whirl for the Given Rotor

In the previous sections, it was seen that single or double peak responses were exhibited by the rotor system depending upon the bearing configurations. It was also observed that for the configuration of the rotor, which exhibited double peaks in the response and hence split criticals in the synchronous whirl mode, had predominant backward whirl component in between the criticals. In this section, therefore, the conditions for split criticals and thus the occurrence of backward whirl in between them, are derived for the rotor system already described in Fig. 2.1, using a very simple analysis.

For the rotor-bearing system shown in Fig. 2.1, when $\ell_1 = \ell_2 = \ell/2$, $z_1 = z_2 = z_e$ and $y_1 = y_2 = y_e$, the equations of motion are as shown below:

$$m_d \frac{d^2}{dt^2} (z_o + a\cos\omega t) + c_\alpha(\dot{z}_o - \dot{z}_e) + \alpha(z_o - z_e) = 0 \qquad (2.28)$$

$$m_d \frac{d^2}{dt^2} (y_o + a\sin\omega t) + c_\alpha(\dot{y}_o - \dot{y}_e) + \alpha(y_o - y_e) = 0 \qquad (2.29)$$

and the constraint equations are,

$$c_\alpha(\dot{z}_o - \dot{z}_e) + \alpha(z_o - z_e) = 2\, k^{tt}_{zz} \cdot z_e + 2\, c^{tt}_{zz} \cdot \dot{z}_e + 2\, k^{tt}_{zy} \cdot y_e + 2\, c^{tt}_{zy} \cdot \dot{y}_e \qquad (2.30)$$

Motion is Counterclockwise, Corresponding to Forward Whirl.

Rotor Speed : 2475 rpm

Central Disk :

C_1 = 0.0000533 m

C_2 = 0.000188 m

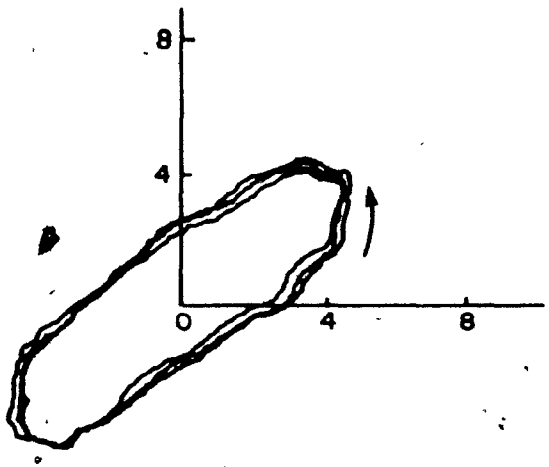

Disk

Figure 2.18(a) Experimental Orbital Diagram with Dissimilar Bearing.

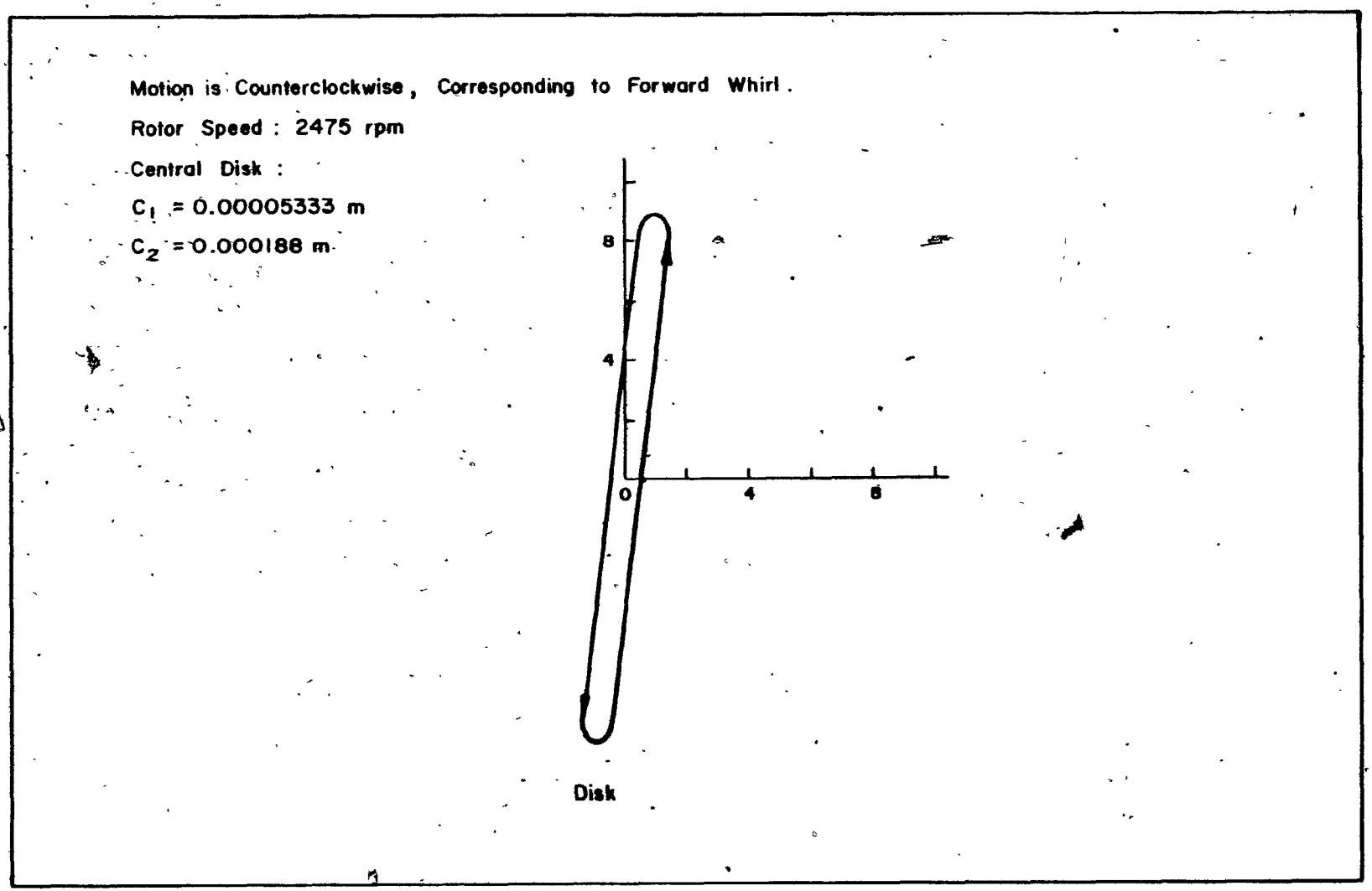

Figure 2.18(b) Normalized Orbital Diagram with Dissimilar Bearings at 2475 RPM.

$$c_\alpha(\dot{y}_o - \dot{y}_e) + \alpha(y_o - y_e) = 2\, k^{tt}_{yz}\cdot z_e + 2\, c^{tt}_{yz}\cdot \dot{z}_e + 2\, k^{tt}_{yy}\cdot y_e + 2\, c^{tt}_{yy}\cdot \dot{y}_e \qquad (2.31)$$

From equations (2.23) and (2.24), the total amplitude of the rotor at the disk location can be written as shown:

$$\left.\begin{aligned} z_o &= \bar{w}_o\ e^{j\omega t} + \bar{w}^*_o\ e^{-j\omega t} \\ \text{and}\quad y_o &= \bar{v}_o\ e^{j\omega t} + \bar{v}^*_o\ e^{-j\omega t} \end{aligned}\right\} \qquad (2.32)$$

where $\bar{w}_o = \frac{1}{2}(z_{oc} - j\, z_{os})$; $\bar{w}^*_o = \frac{1}{2}(z_{oc} + j\, z_{os})$

and $\bar{v}_o = \frac{1}{2}(y_{oc} - j\, y_{os})$; $\bar{v}^*_o = \frac{1}{2}(y_{oc} + j\, y_{os})$

similar relations can be written for the bearing locations also, as shown:

$$\left.\begin{aligned} z_e &= \bar{w}_e\ e^{j\omega t} + \bar{w}^*_e\ e^{-j\omega t} \\ y_e &= \bar{v}_e\ e^{j\omega t} + \bar{v}^*_e\ e^{-j\omega t} \end{aligned}\right\} \qquad (2.33)$$

Substituting equations (2.32) and (2.33) in equations (2.30) and (2.31), a relation between the motion at the bearing and disk locations can be obtained as,

$$\begin{bmatrix} (2\, k^*_{zz} + \alpha^*) & 2\, k^*_{zy} \\ 2\, k^*_{yz} & (2\, k^*_{yy} + \alpha^*) \end{bmatrix} \begin{Bmatrix} \bar{w}_1 \\ \bar{v}_1 \end{Bmatrix} = \alpha^* \begin{Bmatrix} \bar{w}_o \\ \bar{v}_o \end{Bmatrix} \qquad (2.34)$$

where $k^*_{zz} = k^{tt}_{zz} + j\omega\, c^{tt}_{zz}$

$$\left.\begin{aligned} k^*_{yy} &= k^{tt}_{yy} + j\omega\, c^{tt}_{yy} \\ k^*_{zy} &= k^{tt}_{zy} + j\omega\, c^{tt}_{zy} \\ k^*_{yz} &= k^{tt}_{yz} + j\omega\, c^{tt}_{yz} \\ \text{and}\quad \alpha^* &= \alpha + j\omega\, c_\alpha \end{aligned}\right\}$$

Equation (2.34) is solved to obtain $\bar{w}$ and $\bar{v}$ in terms of $\bar{w}_0$ and $\bar{v}_0$ and substituting these values in equations (2.28) and (2.29), it is possible to obtain the equations of motion in the following form,

$$(\bar{k}_1 - m_d\omega^2)\ \bar{w}_0 + \bar{k}_{12}\ \bar{v}_0 = \frac{m_d a\omega^2}{2} \qquad (2.35)$$

$$(k_2 - m_d\omega^2)\ \bar{v}_0 + k_{21}\ \bar{w}_0 = -j\,\frac{m_d a\omega^2}{2} \qquad (2.36)$$

Two more equations are obtained similar to equations (2.35) and (2.36) for the complex conjugates, where the right hand sides are changed to corresponding complex conjugates. In equations (2.35) and (2.36),

$$\bar{k}_1 = \alpha^* [2\, k^*_{zz} (2\, k^*_{yy} + \alpha^*) - 4\, k^*_{zy} \cdot k^*_{yz}] / \text{DET}$$

$$\bar{k}_2 = \alpha^* [2\, k^*_{yy} (2\, k^*_{zz} + \alpha^*) - 4\, k^*_{zy} \cdot k^*_{yz}] / \text{DET}$$

$$\bar{k}_{12} = 2\, k^*_{zy} \cdot (\alpha^*)^2 / \text{DET}$$

$$\bar{k}_{21} = 2\, k^*_{yz} \cdot (\alpha^*)^2 / \text{DET}$$

$$\text{and DET} = (2\, k^*_{zz} + \alpha^*)\ (2\, k^*_{yy} + \alpha^*) - 4\, k^*_{zy} \cdot k^*_{yz}\ .$$

The complex eigenvalues are obtained from the equation,

$$(\bar{k}_1 - m\omega^2)(k_2 - m_d\omega^2) - \bar{k}_{12} \cdot \bar{k}_{21} = 0 \qquad (2.37)$$

This gives two sets of complex conjugate eigenvalues, and their real parts correspond to rotational frequencies. An approximate idea about the critical speeds can be obtained by neglecting damping terms in equation (2.37). The roots of the resulting equation are given by

$$P^2_{1,2} = \left(\frac{k_1 + k_2}{2m_d}\right) \pm \left[\left(\frac{k_1 + k_2}{2m_d}\right)^2 - \left(\frac{k_1 \cdot k_2 - k_{12} \cdot k_{21}}{m_d^2}\right)\right]^{\frac{1}{2}} \qquad (2.38)$$

The critical speed of the rotor corresponds to the speed that matches approximately one of the roots of equation (2.38). When the quantity within the rectangular brackets in equation (2.38) is positive, the rotor will have two distinct critical speeds and when it is negative, the two critical speeds will be complex conjugates and hence the response will show only a single peak.

2.5.1 Backward Whirl in the Laboratory Rotor

The phenomenon of backward whirl has not been observed experimentally so far. According to the theoretical study presented earlier, a single disk rotor-bearing system with equal bearing clearance values of 0.000188m at both ends, exhibits double peak in the response. The orbit diagram shows that in between these two peaks the backward whirl component increases. The laboratory rotor designed using the conditions given in equation (2.38) exhibits backward whirl in between the criticals for a small range. Figures 2.19(a) and 2.19(b) show the orbit diagrams obtained for this rotor by theoretical and experimental methods

Rotor Motion Clockwise Corresponding to Backward Whirl.

Rotor Speed : 2500 rpm

$l_1 = l_2 = \frac{l}{2}$

$C_1 = C_2 = 0.000188$ m

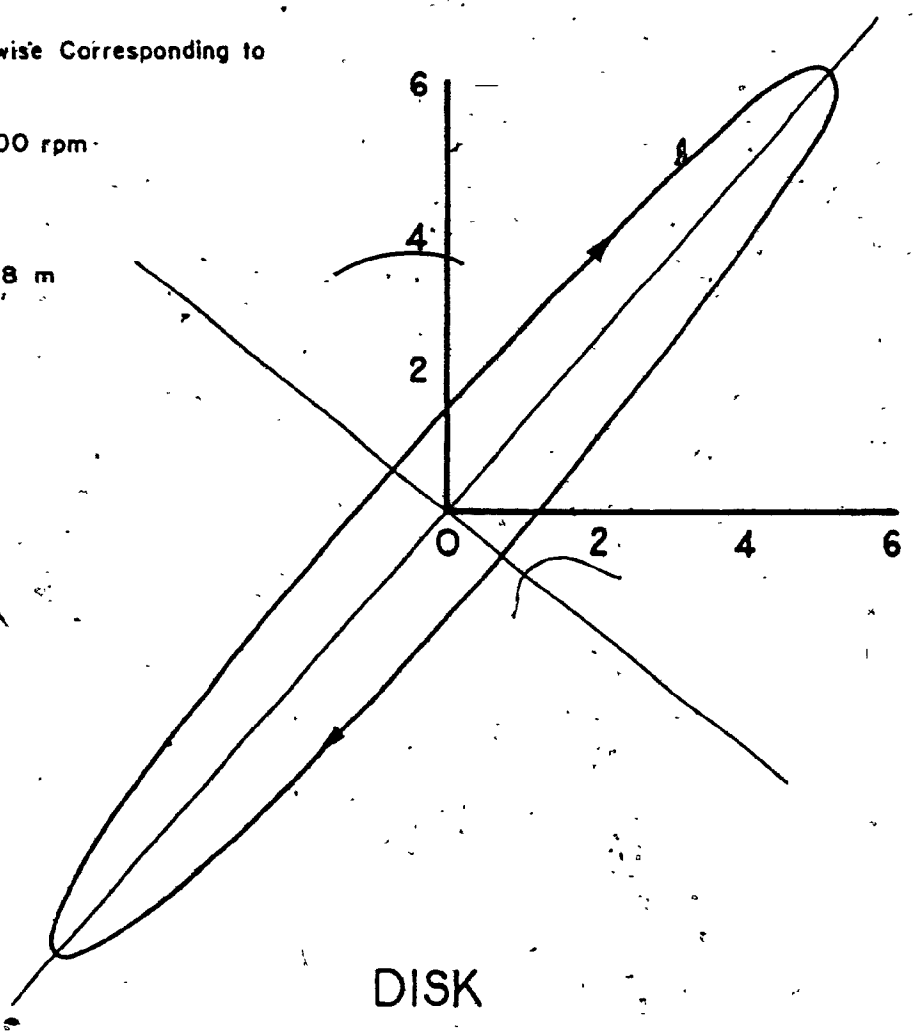

Figure 2.19(a) Theoretical Orbital Diagram of Rotor at 2500 RPM.

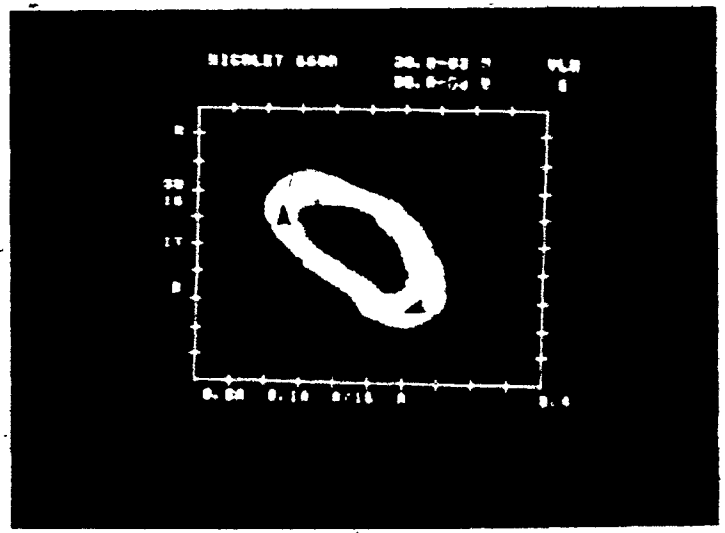

Rotor motion is clockwise corresponding to backward whirl.

Rotor Speed : 2500 rpm

$C_1 = C_2 = 0.000188$ m

$\ell_1 = \ell_2 = \frac{\ell}{2}$.

Figure 2.19(b) Experimental Orbital Diagram of Rotor.

respectively at a rotor speed of 2500 RPM. Both of them show that the rotor executes a backward whirl at this speed.

2.6 Conclusions

The unbalance response and critical speeds of a single disk rotor supported on hydrodynamic bearings are studied using the energy method for different combinations of bearing clearances. Based on the results presented, it is observed that the rotor exhibits synchronous whirl only in the operating speeds of concern. The dissimilarity in the bearings introduced in the analysis by having different bearing clearances and bearing loads at the two ends, influences the unbalance response and critical speeds significantly. A study of the response at the bearing locations is very important for a reliable design of any rotor system.

Some of the theoretical results are compared with those obtained by experiments and the comparison shows a very good qualitative agreement. Backward whirl was observed experimentally for a rotor configuration with equal bearing clearance values of 0.000188m at both bearings.

The analysis presented in this chapter predicts the design parameters, like the unbalance response and critical speeds of the rotor system whereas the very important system information such as stability is not available. Unlike the unbalance response and critical speeds which are affected by the physical parameters of the rotor system, the stability is not affected by these parameters because it is inherent in

the system. Since the analysis presented here does not provide the complete information of the system, a comprehensive study of the system behavior will be undertaken in the next chapter using modal analysis. The modal analysis of the rotor system provides the behavior of the system in its individual modes and the stability of the system as well.

CHAPTER 3

DYNAMIC BEHAVIOR OF SIMPLE ROTOR-BEARING SYSTEM BY MODAL ANALYSIS AND MODAL TESTING TECHNIQUES

In Chapter 2, a direct approach was used to evaluate the dynamic response of a single disk rotor supported on hydrodynamic bearings at its two ends. The direct method provided the unbalance response and critical speeds, however, stability information was absent. Modal analysis provides all the relevant information of the rotor system concerning its dynamic behavior including stability and this technique is used in this Chapter to analyze the simple rotor-bearing system.

Since the rotor supported on hydrodynamic bearings is a non-conservative and also a non-symmetrical system, modal analysis is much involved and therefore, a methodical review of the modal analysis procedures with increasing complexity will be introduced and discussed.

3.1 Undamped System

Here, a multi-degree of freedom system idealized by several masses connected by springs is considered. For N number of masses, it is necessary to have N coordinates to describe the system. This is a symmetric system and can be written in matrix form as,

$$[m]_{NXN} \{\ddot{q}\}_{NX1} + [k]_{NXN} \{q\}_{NX1} = \{f\}_{NX1} \qquad (3.1)$$

The homogenous form of eqn. (3.1) is written as,

$$[m] \{\ddot{q}\} + [k] \{q\} = \{0\} \qquad (3.2)$$

The solution for eqn. (3.2) is assumed in the form,

$$\{q\} = \{q_0\} \exp(j\bar{\omega}t) \qquad (3.3)$$

This solution satisfies the differential equation (3.2) if

$$[k - \bar{\omega}^2 m]\{q_o\} = \{0\} \tag{3.4}$$

Equation (3.4) is a system of N simultaneous equations and for a nontrivial solution we must have,

$$\det\ [k - \lambda m] = 0 \tag{3.5}$$

where $\lambda = \bar{\omega}^2$. This is a polynomial in λ of order N and there will be exactly N roots of λ, for which eqn. (3.5) is satisfied. The assumed solution in eqn. (3.3) is a harmonic solution and the roots for λ suggests that the system will perform harmonic motion at N number of frequencies. These are the natural frequencies of the system and substituting any one of these natural frequencies into eqn. (3.4), provides the system configuration at that natural frequency. System configurations corresponding to each of the natural frequencies are called normal modes.

The complete solution for the vibration of the multi-degree of freedom system can be expressed in terms of the motion in each mode of the system. A modal co-ordinate η_i, is associated with each mode of the system, and the relation between the physical co-ordinates q and the modal co-ordinates η is

$$\{q\} = [\Phi]\{\eta\} \tag{3.6}$$

where $[\Phi]$ is called the modal matrix which is a NXN matrix obtained by concatenating the N modal vectors.

Substitution of eqn. (3.6) in eqn. (3.1) yields,

$$[m][\Phi]\ddot{\eta} + [k][\Phi]\eta = \{f\} \tag{3.7}$$

Premultiplying eqn. (3.7) by $[\Phi]^T$ gives,

$$[\Phi]^T[m][\Phi]\ddot{\eta} + [\Phi]^T[k][\Phi]\eta = [\Phi]^T \{f\} \tag{3.8}$$

Employing the orthogonality relation for the normal modes, eqn. (3.8) becomes,

$$[\mu]\ddot{\eta} + [\kappa]\eta = \{\mathcal{F}(t)\} \tag{3.9}$$

$[\mu] = [\Phi]^T[m][\Phi]$ and $[\kappa] = [\Phi]^T[k][\Phi]$ are diagonal matrices and $\{\mathcal{F}\} = [\Phi]^T\{f\}$ and they provide N number of uncoupled equations of the form,

$$\mu_i \ddot{\eta}_i + \kappa_i \eta_i = \mathcal{F}_i \qquad i = 1,2,\ldots N \tag{3.10}$$

The eqn. (3.10) can be treated as N number of independent single degree of freedom systems. The complete response of the system (3.10) consists of a transient response and a steady-state response. Real systems possess damping which damps out transient response after a while, hence only the steady-state response of the system is considered here.

The steady-state solution of eqn. (3.10) can be obtained by assuming a solution of the form

$$\left.\begin{aligned} \mathcal{F}_i &= \mathcal{F}_{oi}\, e^{j\omega t} \\ \eta_i &= \eta_{oi}\, e^{j\omega t} \end{aligned}\right\} \tag{3.11}$$

Substitution of eqn. (3.11) in eqn. (3.10) yields,

$$-\omega^2 \mu_i \eta_{oi} e^{j\omega t} + \kappa_i \eta_{oi} e^{j\omega t} = \mathcal{F}_{oi} e^{j\omega t} \tag{3.12}$$

Equation (3.12) can be written as

$$\eta_i = \frac{\mathcal{F}_{oi}}{\omega^2 \mu_i + \kappa_i} \tag{3.13}$$

Substituting eqn. (3.13) in eqn. (3.6), the responses of the system are obtained.

3.2 Damped Systems

In general, the damping matrix of the system cannot be diagonalized by the operation $[\Phi]^T [c] [\Phi]$. If the damping is small, it is still possible to use the previous approach by neglecting the non-diagonal terms in the matrix $\Phi^T c \Phi$. However, if the damping is significant other methods should be used for damped systems.

3.2.1 Proportionally Damped Systems

If the damping matrix [c] can be expressed as a linear combination of mass and stiffness matrices as

$$[c] = \xi [m] + \delta[k] \tag{3.14}$$

where ξ and δ are proportionality constants.
it is possible to diagonalize the damping matrix since,

$$[\Phi]^T [c] [\Phi] = \xi[\hat{\mu}] + \delta[\hat{\kappa}] = [\hat{\mathcal{C}}] \tag{3.15}$$

It is seen from eqn. (3.11), that the modal matrix will be able to uncouple the equations completely and the system can be solved by normal mode analysis described in Section 3.1.

3.2.2 Non Proportionally Damped Systems

When the damping in the system is significant and in addition it is not proportional to either mass or stiffness matrices, a normal mode analysis based on the modes of the undamped system is tedious, [97].

However, it is possible to obtain the system eigenvalues and normal modes which will be complex in nature. This is accomplished by converting the N number of second order differential equations into 2N number of first order equations as follows:

$$[M]_{2NX2N} \{\dot{Q}\} + [K]_{2NX2N} \{Q\} = \{F\} \tag{3.16}$$

where $[M] = \begin{bmatrix} 0 & m \\ m & c \end{bmatrix}$, $[K] = \begin{bmatrix} -m & 0 \\ 0 & k \end{bmatrix}$

$$\{F\} = \left\{ \begin{matrix} 0 \\ \hline f \end{matrix} \right\}_{2NX1} \quad \text{and} \quad \{Q\} = \left\{ \begin{matrix} \dot{q} \\ \hline q \end{matrix} \right\}_{2NX1}$$

In the eqn.(3.16), the first N equations express the identity,

$$[m] \{\dot{q}\} - [m] \{\dot{q}\} = \{0\} \tag{3.17}$$

Transforming the physical co-ordinates $\{Q\}$ into modal co-ordinates $\{\eta\}$ gives,

$$\{Q\} = [\Phi] \{\eta\} \tag{3.18}$$

where $[\Phi]$ is the modal matrix. Substituting eqn.(3.18) in eqn. (3.16) and premultiplying throughout by $[\Phi]^T$, the eqn.(3.18) becomes,

$$[\Phi]^T[M][\Phi]\{\dot{\eta}\} + [\Phi]^T[K][\Phi]\{\eta\} = [\Phi]^T\{F\} \tag{3.19}$$

The complex eigen vectors $[\Phi]$ are orthogonal to each other and hence the 2N number of uncoupled system equations are as follows:

$$\mu_i \dot{\eta}_i + \kappa_i \eta_i = \mathcal{F}_i \qquad i = 1,2,\ldots 2N \tag{3.20}$$

Considering the steady-state response of the system,

$$\eta_i = \frac{\mathcal{F}_i}{\kappa_i + j\ \mu_i \omega} \qquad (3.21)$$

Substituting eqn. (3.21) into eqn. (3.18), the system response is obtained.

3.3 Non-Symmetrical Systems

In the last section, it was seen that N number of second order system equations are converted to 2N number of first order equations as shown from eqn. (3.16),

$$[M]\ \{\dot{Q}\} + [K]\ \{Q\} = \{F\} \qquad (3.22)$$

where the mass [M] and stiffness [K] matrices are symmetric about the diagonal and the complex normal mode analysis was used to uncouple the system equations. In the case of systems whose mass [M] and stiffness [K] matrices are not symmetric, it is not possible to uncouple the system equations using normal mode analysis. However, it is possible to uncouple such nonsymmetric system equations by considering the biorthogonality relation between the modes of the original system and those of the transposed system which are called the right and left eigenvectors, respectively. The left eigenvectors are obtained by solving the homogenous equation involving the transposed [M] and [K] matrices given by

$$[M]^T\ \{\dot{Q}\} + [K]^T\ \{Q\} = \{0\} \qquad (3.23)$$

The eigenvector matrix consisting of all the modes of the transposed system is obtained in the same manner as the right eigenvectors were obtained.

Hence, the system eqns. (3.22) are uncoupled as shown:

$$[\rho]^T[M][\Phi]\{\dot{\eta}\} + [\rho]^T[K][\Phi]\{\eta\} = [\rho]^T\{F\} \tag{3.24}$$

Equation (3.24) is 2N number of first order independent equations and can be written as

$$\mu_i \dot{\eta}_i + \kappa_i \eta_i = \sigma_i \tag{3.25}$$

The steady-state response of the system can be obtained from eqn. (3.25) converting the modal co-ordinates to physical co-ordinates as previously discussed in Section 3.2.

3.4 Dynamic Response of Rotor Systems Using Modal Analysis

A rotor supported on hydrodynamic bearings is a nonsymmetric system. This is because of asymmetry in the cross-coupled fluid film stiffness and damping co-efficients which in turn are dependent on rotor speeds. Moreover, when the rotor has several disks, the gyroscopic moments contribute to the nonsymmetry of the rotor system. Because of this general nonsymmetric nature of the problem, a conventional normal mode analysis is not possible and it is necessary to use the biorthogonality relations between the modes of the original system and those of the transposed system to decouple the system equations. The system response can be obtained as the sum of the responses of individual modes. Later, the system stability will be studied from the complex eigenvalues obtained in the present analysis.

In this section, a single disk rotor supported on hydrodynamic bearings at the two ends, which is already shown in Fig. 2.1 is studied for its dynamic behavior using modal analysis techniques. The kinetic

and potential energy expressions are developed as shown in eqns. (2.1), (2.2) and (2.3) of Chapter 2 and using the Lagragian approach, the system equations of motion are obtained. They are the same as shown in eqns. (2.5) through (2.12) of Chapter 2. The resulting four dynamical equations and four constraint equations are arranged in the following manner;

$$[m_1]\{\ddot{q}\} + [d_1]\{\dot{q}\} + [k_1]\{q\} + [d_2]\{\dot{q}_1\} + [k_2]\{q_1\} = \{f_1\} \qquad (3.26)$$

$$[d_3]\{\dot{q}\} + [k_3]\{q\} + [d_4]\{\dot{q}_1\} + [k_4]\{q_1\} = \{0\} \qquad (3.27)$$

where $\{q\}^T = [z_o, y_o, \theta_z, \theta_y]$ and $\{q_1\}^T = [z_1, y_1, z_2, y_2]$

and $[m_1]$, $[d_1]$, $[d_2]$, $[d_3]$, $[d_4]$, $[k_1]$, $[k_2]$, $[k_3]$ and $[k_1]$ are 4x4 matrices which are as shown below:

$$[m_1] = \begin{bmatrix} m_d & 0 & 0 & 0 \\ 0 & m_d & 0 & 0 \\ 0 & 0 & I_d & 0 \\ 0 & 0 & 0 & I_d \end{bmatrix}$$

$$d_1 = \begin{bmatrix} c_\alpha & 0 & c_\gamma & 0 \\ 0 & c_\alpha & 0 & c_\gamma \\ c_\gamma & 0 & c_\beta & I_p\omega \\ 0 & c_\gamma & -I_p\cdot\omega & c_\beta \end{bmatrix}$$

$$[d_2] = \begin{bmatrix} \left(\frac{-c_\alpha \ell_2 + c_\gamma}{\ell}\right) & 0 & -\left(\frac{c_\alpha \ell_1 + c_\gamma}{\ell}\right) & 0 \\ 0 & \left(\frac{-c_\alpha \ell_2 + c_\gamma}{\ell}\right) & 0 & -\left(\frac{c_\alpha \ell_1 + c_\gamma}{\ell}\right) \\ \left(\frac{-c_\gamma \ell_2 + c_\beta}{\ell}\right) & 0 & -\left(\frac{c_\gamma \ell_1 + c_\beta}{\ell}\right) & 0 \\ 0 & \left(\frac{-c_\gamma \ell_2 + c_\beta}{\ell}\right) & 0 & -\left(\frac{c_\gamma \ell_1 + c_\beta}{\ell}\right) \end{bmatrix}$$

$$[d_3] = \begin{bmatrix} \left(\frac{-c_\alpha \ell_2 + c_\gamma}{\ell}\right) & 0 & -\left(\frac{c_\gamma \ell_2 + c_\beta}{\ell}\right) & 0 \\ 0 & \left(\frac{-c_\alpha \ell_2 + c_\gamma}{\ell}\right) & 0 & -\left(\frac{c_\alpha \ell_1 + c_\beta}{\ell}\right) \\ -\left(\frac{c_\alpha \ell_1 + c_\gamma}{\ell}\right) & 0 & -\left(\frac{c_\gamma \ell_1 + c_\beta}{\ell}\right) & 0 \\ 0 & -\left(\frac{c_\alpha \ell_1 + c_\gamma}{\ell}\right) & 0 & -\left(\frac{c_\gamma \ell_1 + c_\beta}{\ell}\right) \end{bmatrix}$$

$$[d_4] = \begin{bmatrix} (b_1 + c^{tt}_{zz_1}) & c^{tt}_{zy_1} & b_2 & 0 \\ c^{tt}_{yz_1} & (b_1 + c^{tt}_{yy_1}) & 0 & b_2 \\ b_2 & 0 & (b_3 + c^{tt}_{zz_2}) & c^{tt}_{zy_2} \\ 0 & b_2 & c^{tt}_{yz_2} & (b_3 + c^{tt}_{yy_2}) \end{bmatrix}$$

where: $b_1 = \dfrac{c_\alpha \ell_2^2 - 2 c_\gamma \ell_2 + c_\beta}{\ell^2}$

$b_2 = \dfrac{c_\alpha \ell_1 \ell_2 - c_\gamma(\ell_1 - \ell_2) - c_\beta}{\ell^2}$

and $b_3 = \dfrac{c_\alpha \ell_1^2 + 2 c_\gamma \ell_1 + c_\beta}{\ell^2}$

$$[k_1] = \begin{bmatrix} \alpha & 0 & \gamma & 0 \\ 0 & \alpha & 0 & \gamma \\ \gamma & 0 & \beta & 0 \\ 0 & \gamma & 0 & \beta \end{bmatrix}$$

$$[k_2] = \begin{bmatrix} \left(\frac{-\alpha \ell_2+\gamma}{\ell}\right) & 0 & -\left(\frac{\alpha \ell_1+\gamma}{\ell}\right) & 0 \\ 0 & \left(\frac{-\alpha \ell_2+\gamma}{\ell}\right) & 0 & -\left(\frac{\alpha \ell_1+\gamma}{\ell}\right) \\ \left(\frac{-\gamma \ell_2+\beta}{\ell}\right) & 0 & -\left(\frac{\gamma \ell_1+c_\beta}{\ell}\right) & 0 \\ 0 & \left(\frac{-\gamma \ell_2+\beta}{\ell}\right) & 0 & -\left(\frac{\gamma \ell_1+\beta}{\ell}\right) \end{bmatrix}$$

$$[k_3] = \begin{bmatrix} \left(\frac{-\alpha\, l_2+\gamma}{l}\right) & 0 & \left(\frac{-\gamma\, l_2+\beta}{l}\right) & 0 \\ 0 & \left(\frac{-\alpha\, l_2+\gamma}{l}\right) & 0 & \left(\frac{-\gamma\, l_2+\beta}{l}\right) \\ -\left(\frac{\alpha\, l_1+\gamma}{l}\right) & 0 & -\left(\frac{\gamma\, l_1+\beta}{l}\right) & 0 \\ 0 & -\left(\frac{\alpha\, l_1+\gamma}{l}\right) & 0 & -\left(\frac{\gamma\, l_1+\beta}{l}\right) \end{bmatrix}$$

$$[k_4] = \begin{bmatrix} (a_1 + k^{tt}_{zz_1}) & k^{tt}_{zy_1} & a_2 & 0 \\ k^{tt}_{yz_1} & (a_1 + k^{tt}_{yy_1}) & 0 & a_2 \\ a_2 & 0 & (a_3 + k^{tt}_{zz_2}) & k_{zy_2} \\ 0 & a_2 & k^{tt}_{yz_2} & (a_3 + k^{tt}_{yy_2}) \end{bmatrix}$$

where $$a_1 = \frac{\alpha\, l_2^2 - 2\,\gamma\, l_2 + \beta}{l^2}$$

$$a_2 = \frac{\alpha\, l_1 l_2 - \gamma(l_1 - l_2) - \beta}{l^2}$$

$$a_3 = \frac{\alpha\, l_1^2 + 2\,\gamma\, l_1 + \beta}{l^2}$$

and $\{f_1\}^T = [m_d\, a\, \omega^2 \cos\omega t,\ m_d\, a\, \omega^2 \sin\omega t,\ 0,\ 0]$

Equations (3.26) and (3.27) can be written as twelve first order differential equations as follows:

$$[M]\{\dot{Q}\} + [K]\{Q\} = \{F\} \tag{3.28}$$

where

$$[M] = \begin{bmatrix} [0] & [m_1] & [0] \\ [m_1] & [d_1] & [d_2] \\ [0] & [d_3] & [d_4] \end{bmatrix}$$

$$[K] = \begin{bmatrix} -[m_1] & [0] & [0] \\ [0] & [k_1] & [k_2] \\ [0] & [k_3] & [k_4] \end{bmatrix}$$

$$\{F\} = \begin{Bmatrix} \{0\} \\ \{f_1\} \\ \{0\} \end{Bmatrix}$$

and $$\{Q(t)\} = \begin{Bmatrix} \{\dot{q}\} \\ \{q\} \\ \{q_1\} \end{Bmatrix}$$

The homogenous form of eqn. (3.28) is solved to obtain the eigenvalues and the right eigenvectors of the system. Subsequently, the left eigenvectors are obtained as explained in 3.3.

Making use of the right and left eigenvectors eqn. (3.28) is uncoupled to obtain

$$\mu_i \dot{\eta}_i(t) + \kappa_i \eta_i(t) = \{\sigma_i(t)\} \tag{3.29}$$

where

$$[\rho]^T [M] [\Phi] = [\hat{\mu}]$$

$$[\rho]^T [K] [\Phi] = [\hat{\kappa}]$$

and $\{\sigma\} = [\rho]^T \{F\}$

This results in twelve first order independent equations and can be solved by assuming steady-state solution of the form,

$$\begin{aligned} \eta_i(t) &= A_{\Phi i} \exp(j\omega t) + \bar{A}_{\Phi i} \exp(-j\omega t) \\ \sigma_i(t) &= E_{\Phi i} \exp(j\omega t) + \bar{E}_{\Phi i} \exp(-j\omega t) \end{aligned} \tag{3.30}$$

Substitution of eqn. (3.30) in eqn. (3.29) leads to

$$\begin{aligned} (\kappa_i + j\omega \mu_i) A_{\Phi i} \exp(j\omega t) + (\kappa_i - j\omega\mu_i) \bar{A}_{\Phi i} \exp(-j\omega t) \\ = E_{\Phi i} \exp(j\omega t) + \bar{E}_{\Phi i} \exp(-j\omega t) \end{aligned} \tag{3.31}$$

Equating the co-efficients of the forward and backward rotation terms, result in,

$$A_{\phi i} = \frac{E_{\phi i}}{(\kappa_i + j\omega\ \mu_i)}$$

$$\bar{A}_{\phi i} = \frac{\bar{E}_{\phi i}}{(\kappa_i - j\omega\ \mu_i)} \qquad (3.32)$$

The response of the rotor can be determined from eqns. (3.29), (3.30) and (3.31). The unbalance response of the rotor can be obtained non-dimensionally as

$$r = (z + jy)/a \qquad (3.33)$$

where z and y are the response components along the Z and Y directions respectively and a is the disk eccentricity.

Even though the analysis procedure discussed so far is confined to a single disk rotor system, the same treatment is equally applicable for a rotor with several disks and bearings. Such a large system can be modelled by the finite element method. If the order of matrices involved is quite large, it is possible to reduce the size of the matrices using a modal reduction procedure which will be discussed in Chapter 4.

3.5 Dynamic Responses

The above analysis is used to determine the dynamic responses of a single disk rotor supported on hydrodynamic bearings at its two ends whose details are given in Table 2.1. Dissimilar bearings are considered and the dissimilarity is achieved with different bearing clearances at the two ends.

The 12x12 overall system matrices provide twelve eigenvalues, out

of which four correspond to synchronous whirl and another four to conical whirl and these eight appear as complex conjugate pairs. The eigenvalues corresponding to conical whirl are quite high and hence are not discussed. Remaining four eigenvalues have their imaginary parts zero in general and negative real parts, implying that the corresponding motion is monotonically decreasing and not oscillatory. Sometimes, two of these eigenvalues appear as a complex conjugate pair, however, they never correspond to the rotor speed. All the twelve eigenvalues had their real parts negative, indicating that the rotor motion is stable, in the operating range under consideration. However, in certain configurations of the rotor due to different bearing clearances the real part of the eigenvalue becomes positive thereby the response increases monotonically making the system unstable for a certain range of rotor speed which lies much beyond this operating range. Since the unbalance response and critical speeds of rotors for different configurations of bearings are studied earlier, it is not repeated here and hence only the individual modal responses are studied for the following bearing clearances and their combinations.

(i) 0.0000533 m

(ii) 0.000188 m.

The individual modal responses of the rotor are shown in Fig. 3.1. for the clearance values of c_1 and c_2 being 0.000188 m at both ends. This system has two peaks in its response. At a particular critical speed, there are two modes with the corresponding eigenvalues being a complex conjugate pair. In showing the modal response, only one mode in the pair is considered here. The mode corresponding to the first of the

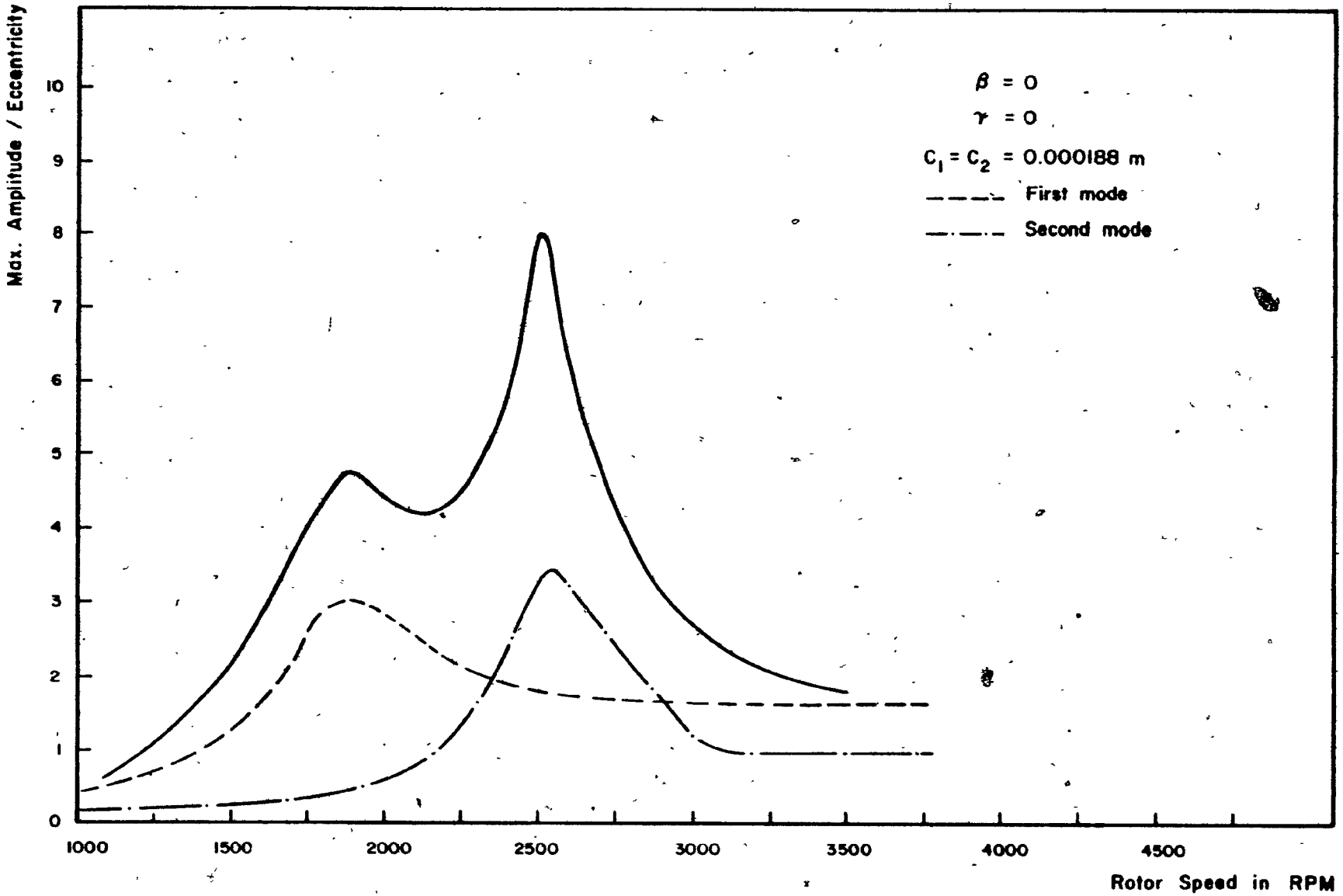

Figure 3.1 Unbalance Response of Rotor in the Individual Modes.

split criticals is predominant near the first peak. Similarly, the mode corresponding to the second of the split criticals is predominant near the second peak.

The orbital diagrams are shown in Figs. 3.2 through 3.5 for the central disk rotor with the bearing clearances c_1 and c_2 being at 0.000188 m. Figure 3.2 shows the orbital diagram at the disk and bearing locations for the rotor speed of 1700 RPM which lies below the first critical speed of 1865 RPM. It is seen that the rotor is executing a forward whirl. It was mentioned earlier that a complex conjugate pair of eigenvalues exist at a critical speed and modal response is shown corresponding to only one of these eigenvalues. However, at the rotor speed of 1700 RPM, the orbital diagram for the mode corresponding to the complex conjugate of the eigenvalue considered in Fig. 3.2 is shown in Fig. 3.3 for comparison. It is seen that this orbital diagram differs in magnitude and phase from that of Fig. 3.2. Figure 3.4 shows the orbital diagram for a rotor speed of 2100 RPM which lies in between the two criticals. The total and the modal responses at the disk and bearing locations are shown. Eventhough the modal response seems to be larger in the horizontal direction, the sum of the responses of all modes with due consideration for their phases will be equal to the total response.

The orbital diagram when the rotor is running at 2700 RPM which is above the second of the split criticals is shown in Fig. 3.5. This shows that the rotor is executing forward whirl. The orbital diagrams for the modes also follow a similar trend. The change from forward to backward whirl does not take place at the first of the split criticals unlike in the case of undamped rotor. The rotor motion tends towards

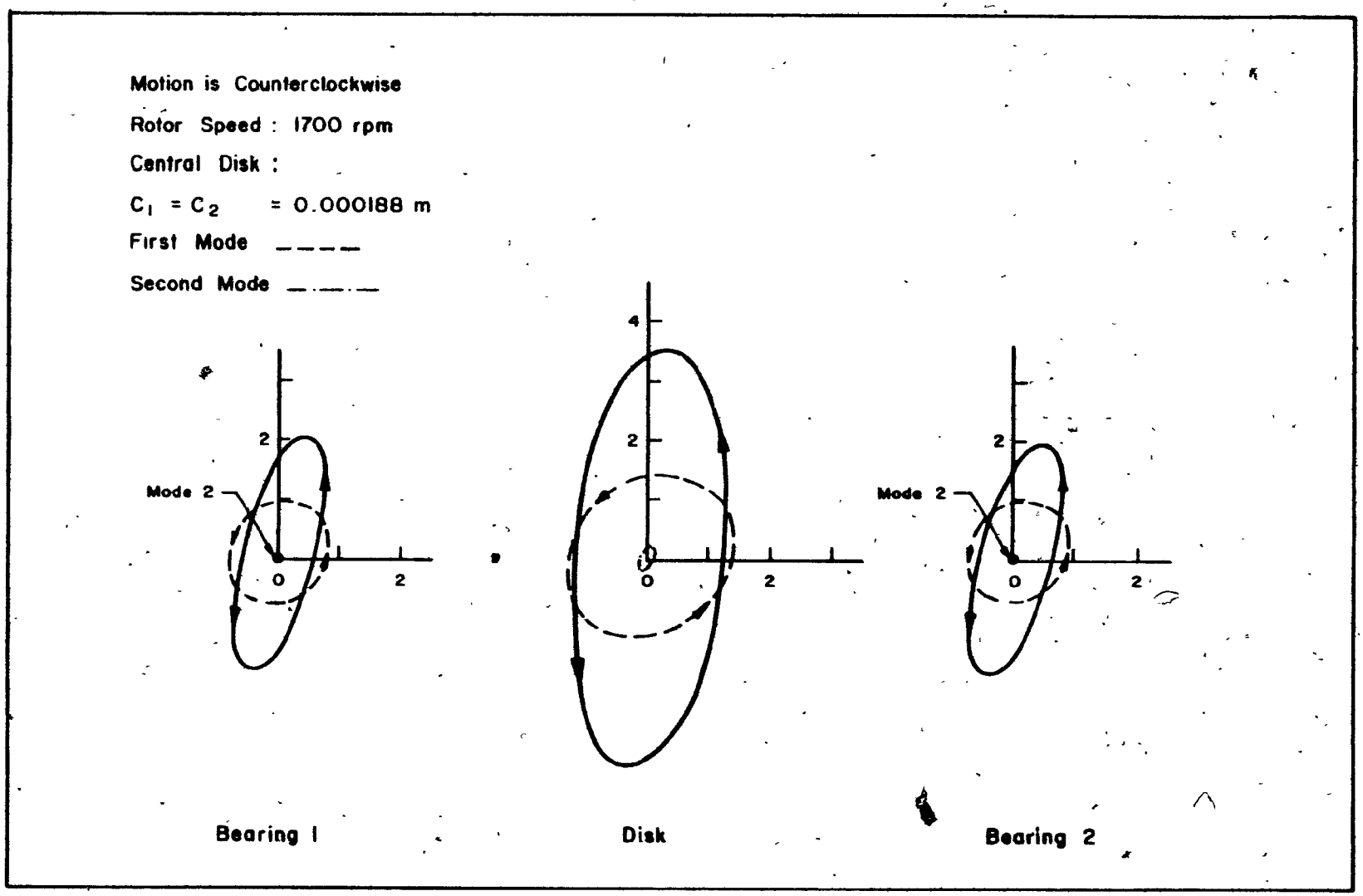

Figure 3.2 Normalized Orbital Diagram at 1700 RPM.

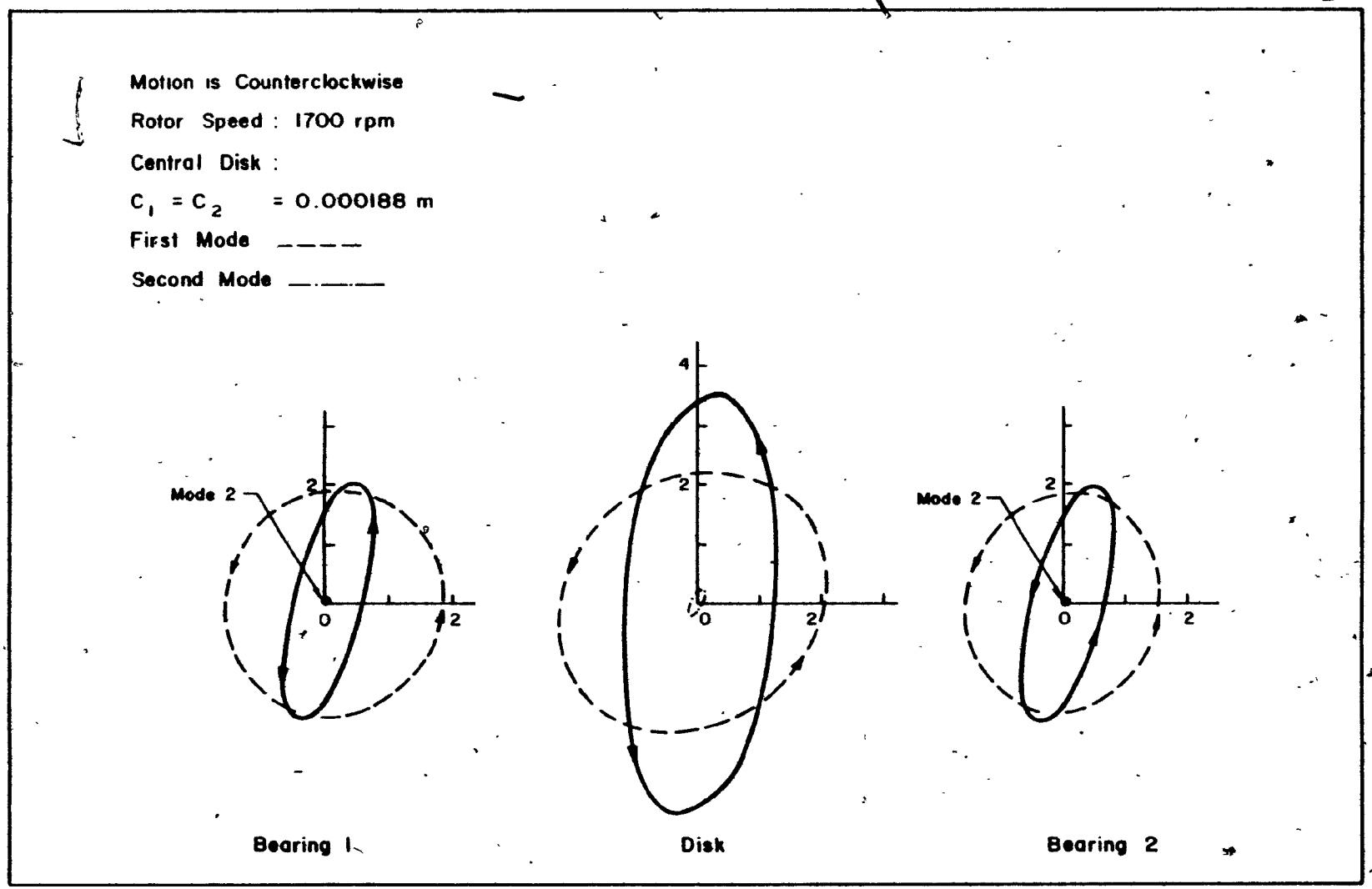

Figure 3.3 Normalized Orbital Diagram at 1700 RPM.
Modes Correspond to the Complex Conjugate of the Eigenvalue in Figure 3.2.

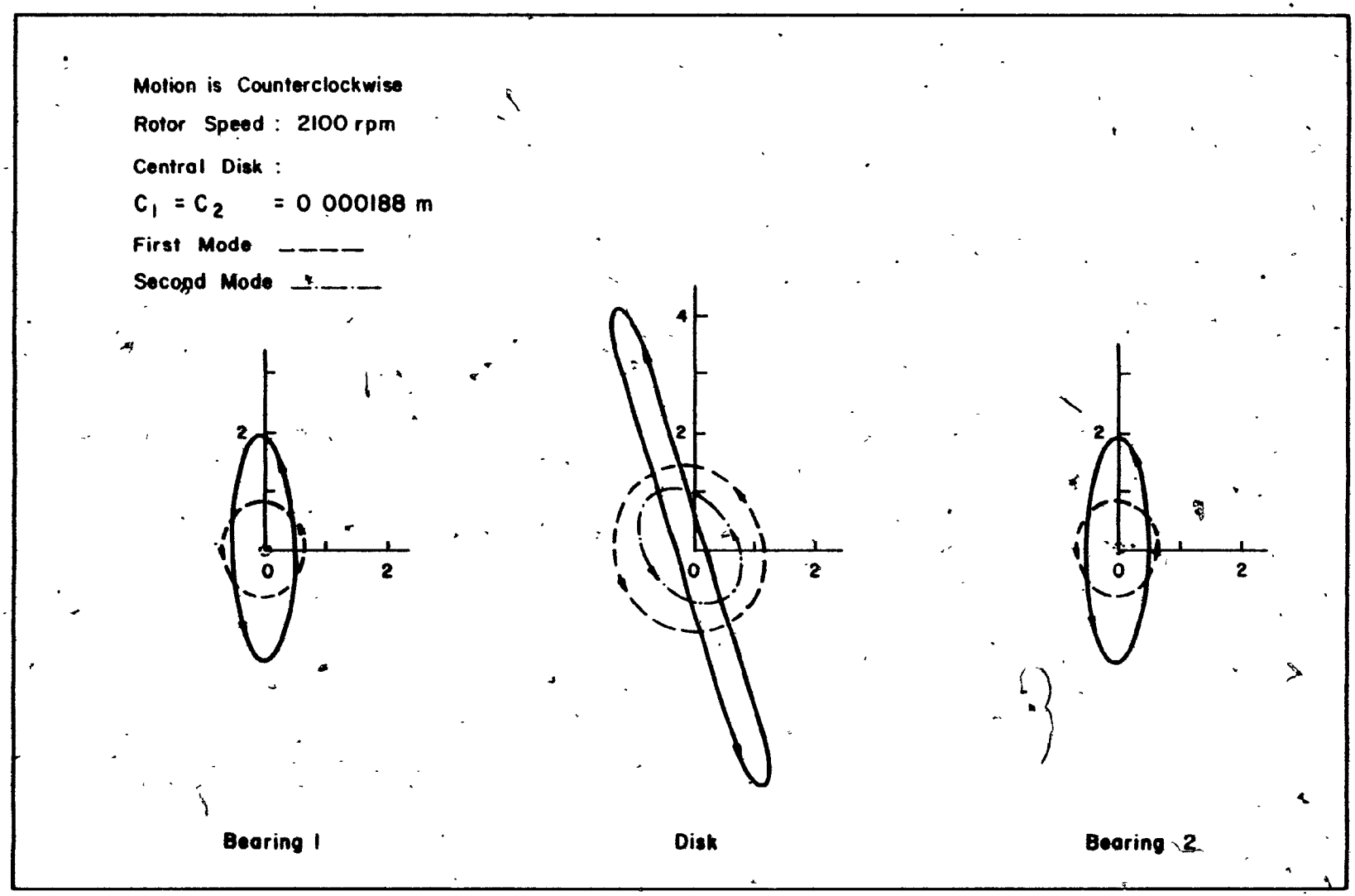

Figure 3.4 Normalized Orbital Diagram at 2100 RPM.

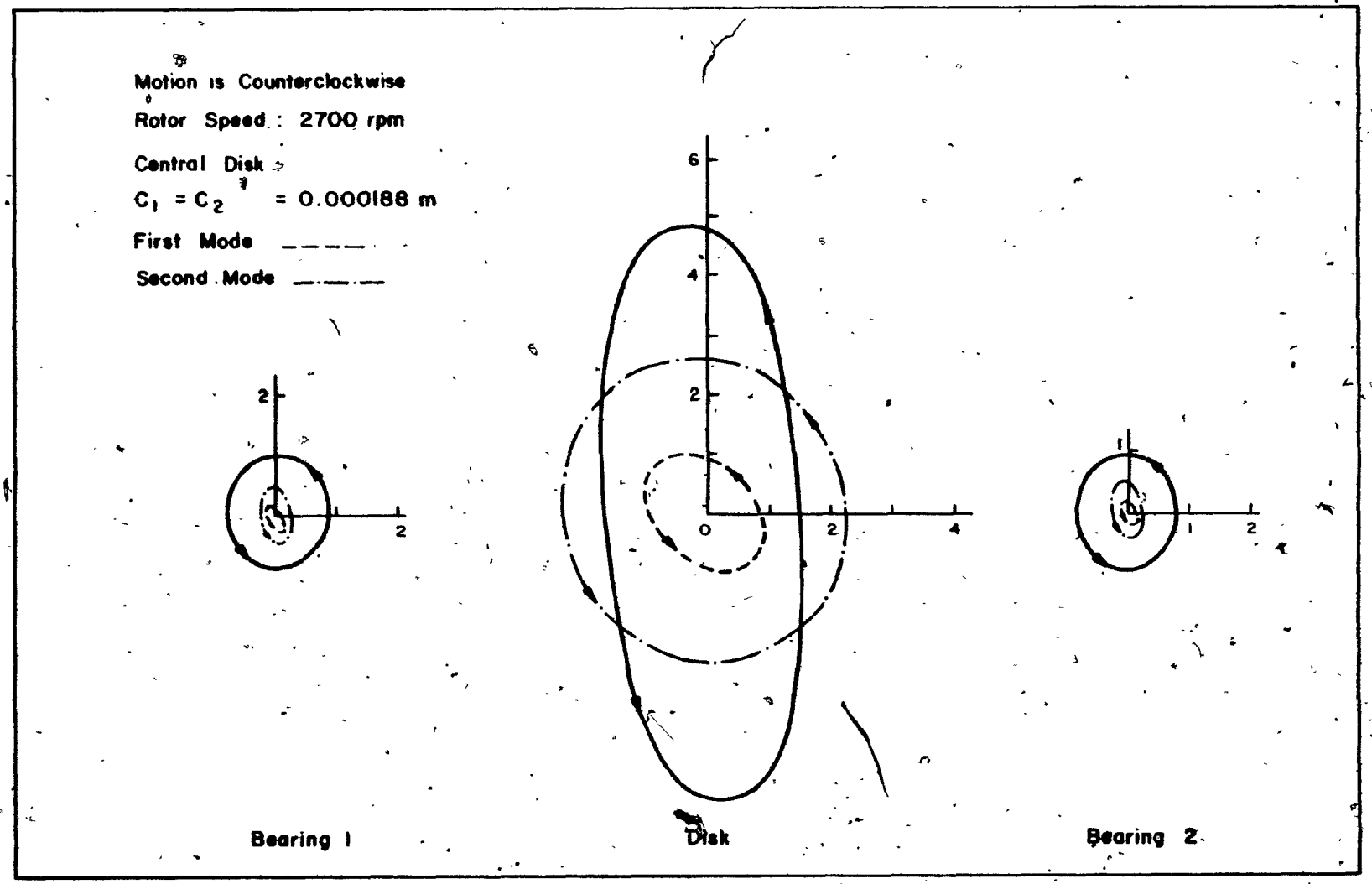

Figure 3.5 Normalized Orbital Diagram at 2700 RPM.

the backward whirl in between the criticals.

The shaft motion at the bearing locations is similar to that of the disk, however, it has different amplitudes.

Orbital diagrams for the case of central disk and dissimilar bearing clearances c_1 = 0.0000533 m and c_2 = 0.000188 m at the two ends, are shown in Figs. 3.6 through 3.8. Orbital diagrams for the rotor at the disk and bearing locations are shown along with those for the two modes corresponding to the split criticals. Figure 3.6 corresponds to a rotor speed of 1800 RPM which lies below the first of the split critical at 2168 RPM. Figure 3.7 shows the orbital diagram of this rotor at the speed of 2300 RPM which lies in between the criticals and Fig. 3.8 is the orbital diagram obtained at the rotor speed of 2700 RPM which is above the second of the split criticals at 2500 RPM. For this configuration of the rotor the whirl direction does not change in between the criticals because the second critical approaches before that could happen, the rotor continues to whirl in the forward direction.

3.6 Experimental Modal Analysis

Analytical investigations of dynamic behavior of structures in general do not match with experimental measurements. One of the reasons for this discrepancy is the approximations involved in the mathematical model of the structure among various other factors such as material properties and the analysis techniques. All these approximations make the analytical results vary considerably from the experimental results. Under this circumstance, one approach is to base the mathematical model on a simplified geometrical model of the structure, and use standard material properties in the analysis. An alternative approach is to

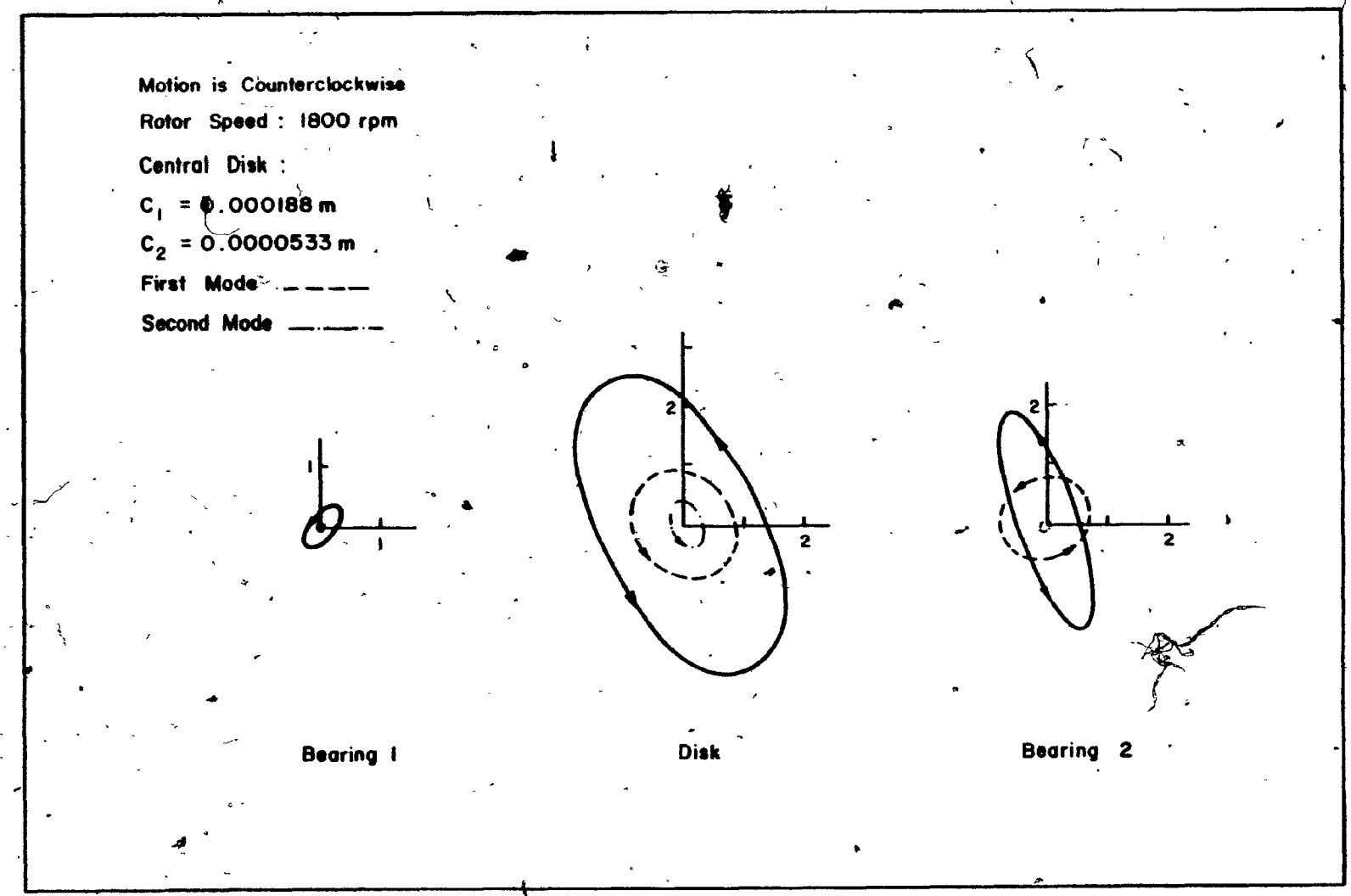

Figure 3.6 Normalized Orbital Diagram with Dissimilar Bearings at 1800 RPM.

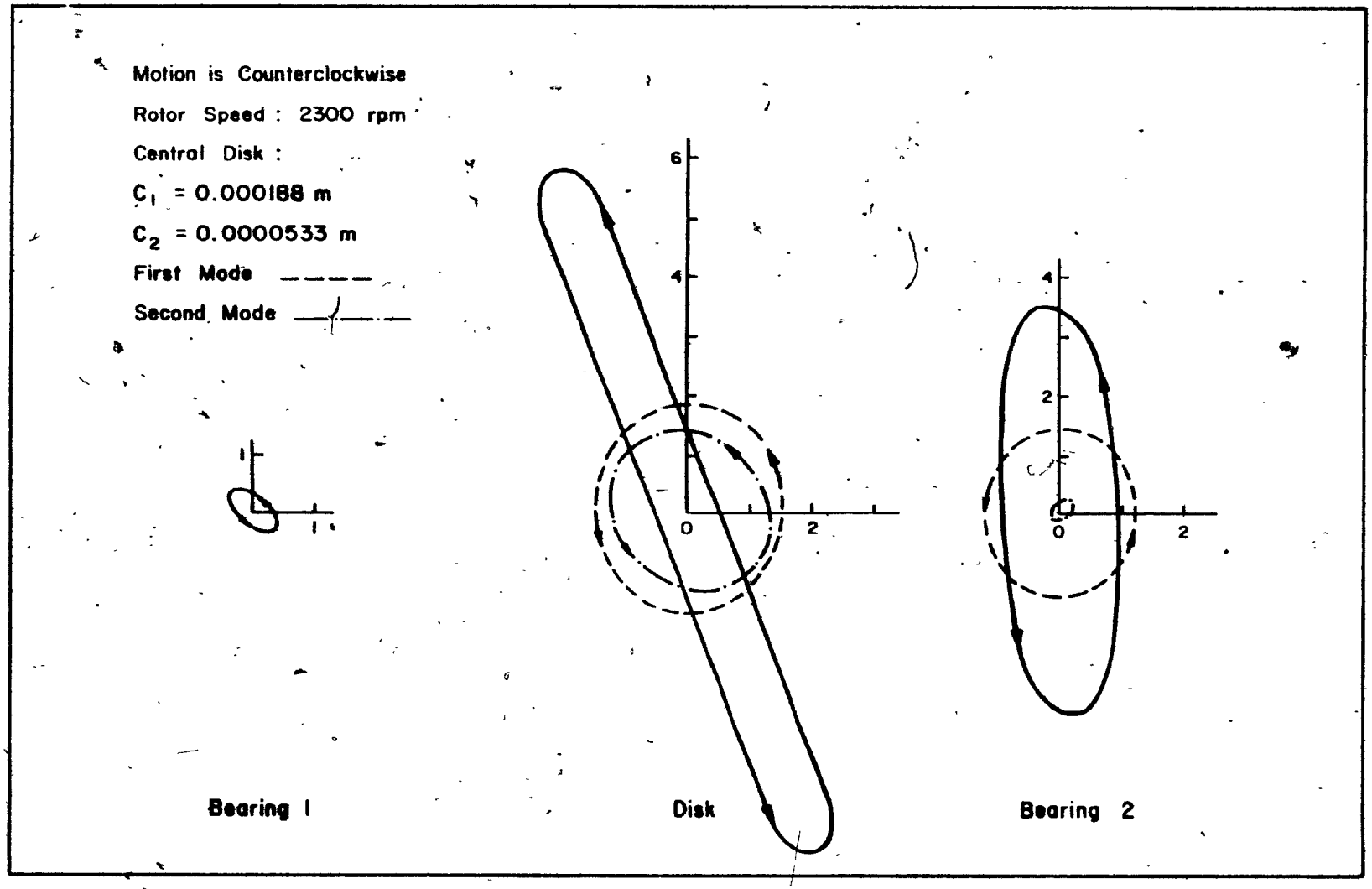

Figure 3.7 Normalized Orbital Diagram with Dissimilar Bearings at 2300 RPM.

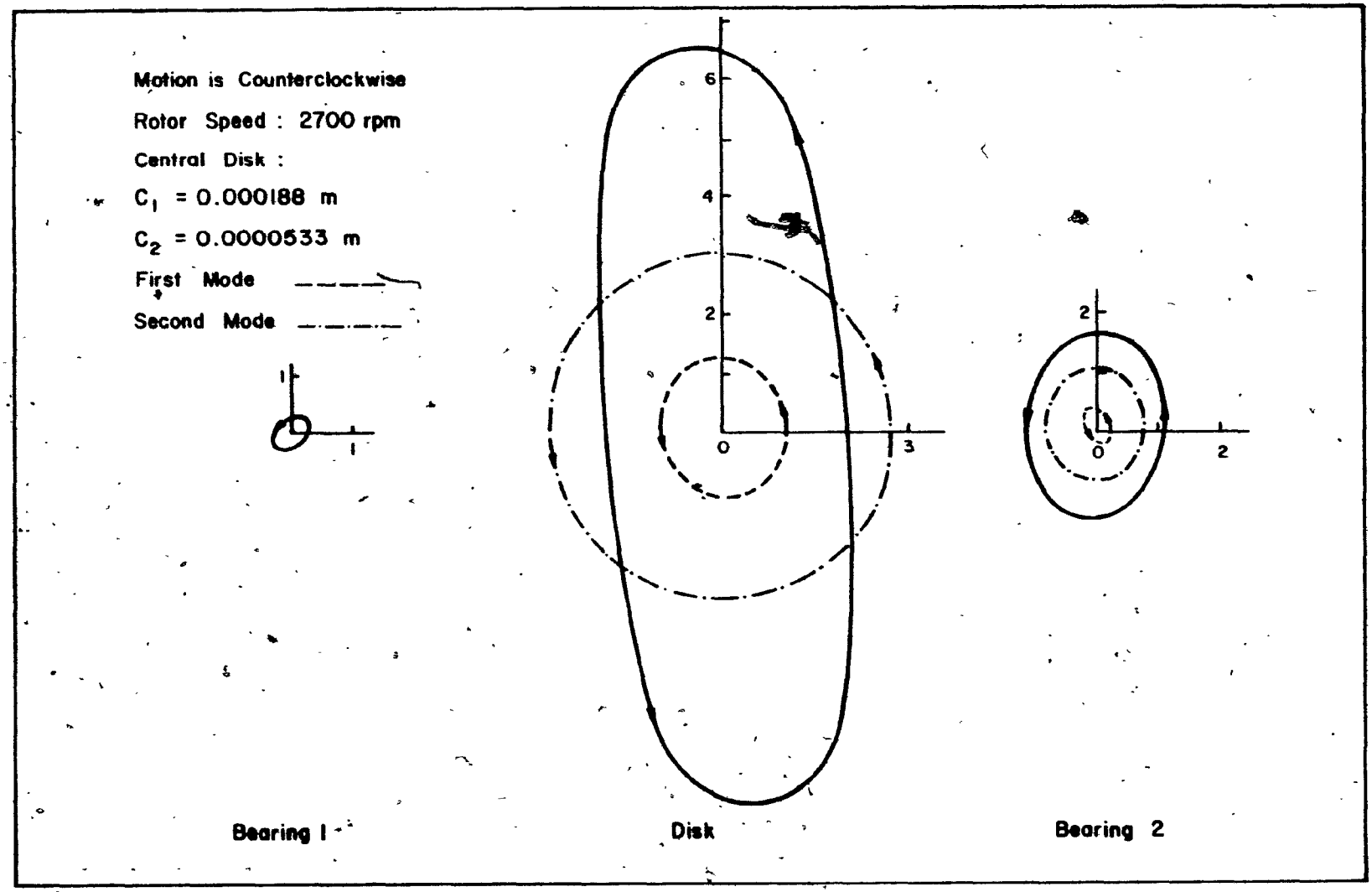

Figure 3.8 Normalized Orbital Diagram with Dissimilar Bearings at 2700 RPM.

measure some relevant gross parameters of the structure and using them in a different mathematical model. Recent developments in the measurement techniques enable the second method quite convenient where the mathematical model is the modal representation of the structure.

This experimental modal analysis techniques, usually termed as modal testing, is a process of testing the structure in order to obtain a mathematical model called modal model. There are three basic steps associated with the modal testing. They are: (i) measurement of transfer functions - Experimental stage (ii) curve-fitting of measured transfer functions and extraction of modal parameters like natural frequencies damping ratio, modal vectors, modal mass and modal stiffness of the system - Numerical Analysis stage (iii) establishment of modal model - Modelling stage. They will be discussed later.

3.7 Frequency Response Functions

Frequency response function at a particular frequency is the ratio of response and the force applied at that point. Depending upon the type of the response measured, it is called receptance, mobility or inertance of the system. The determination of frequency response functions is important because based on these functions, the modal parameters are later extracted using a curve fitting procedure. Hence, the analytical evaluation of frequency response functions for different types of systems are derived as shown.

3.7.1 Damped Symmetric Systems

The uncoupled equations of a symmetric system can be written as follows:

$$\mu_i \dot{\eta}_i + \kappa_i \eta_i = \sum_{i=1}^{2N} \{\phi_i\}^T F_i \qquad (3.34)$$

where modal mass μ and modal stiffness κ were already defined in Section 3.2.2.

In the case of harmonic excitation at a point r of the shaft,

$$\{F\}^T = \{0,0,.....f_r,0,0\}\ e^{j\omega t} \qquad (3.35)$$

where ω is the frequency of excitation.

For steady-state solution of the form

$$\eta = \bar{\eta}\ e^{j\omega t} \qquad (3.36)$$

the eqn. (3.34) becomes,

$$j\ \omega\ \mu_i\ \bar{\eta}_i + \kappa_i\ \bar{\eta}_i = \phi_{ri}\ f_r \qquad (3.37)$$

Now, the response at point s gives,

$$Q_s(t) = \begin{Bmatrix} \dot{q}_s \\ q_s \end{Bmatrix} = \sum_{i=1}^{2N} \frac{\phi_{ri}\ f_r}{\kappa_i + j\ \omega\ \mu_i} \begin{Bmatrix} \lambda_i\ \phi_i \\ \phi_i \end{Bmatrix} \qquad (3.38)$$

Knowing the relation,

$$\lambda_i = -\frac{\kappa_i}{\mu_i} \qquad (3.39)$$

q_s can be obtained by substituting eqn. (3.39) in eqn. (3.38),

$$q_s = \sum_{i=1}^{2N} \frac{\phi_{ri}\ \phi_{si}\ f_r}{\mu_i\ (j\omega - \lambda_i)} \qquad (3.40)$$

Hence, the frequency response function $H_{sr}(j\omega)$ can be written as,

$$H_{sr}(j\omega) = \frac{q_s}{f_r} = \sum_{i=1}^{2N} \frac{\Phi_{ri}\,\Phi_{si}}{\mu_i(j\omega-\lambda_i)} \tag{3.41}$$

Since the system equations are converted into 2N number of first order equations, eqn. (3.41) can be written as,

$$H_{sr}(j\omega) = \frac{q_s(j\omega)}{f_r(j\omega)} = \sum_{i=1}^{2N} \frac{1}{\mu_i\,\lambda_i'} \left[\frac{\Phi_{ri}\,\Phi_{si}}{2j(j\omega-P_i)} - \frac{\Phi^*_{ri}\,\Phi^*_{si}}{2j(j\omega-P_i^*)}\right] \tag{3.42}$$

where $P_i = -\zeta_i\omega + j\omega\,(1-\zeta_i^2)^{\frac{1}{2}}$

P_i^* and Φ_i^* are complex conjugates of P_i and Φ_i respectively and

$\lambda_i' = -\omega\,(1-\zeta_i^2)^{\frac{1}{2}}$

Equation (3.42) represents the frequency response function(FRF) for a

For a non-proportionally damped system, the transfer function equation becomes,

$$H_{sr}(j\omega) = \frac{q_s(j\omega)}{f_r(j\omega)} = \sum_{i=1}^{2N} \frac{\Phi_{ri}\,\Phi_{si}}{\mu_i(j\omega-P_i)} + \frac{\Phi^*_{ri}\,\Phi^*_{si}}{\mu_i^*(j\omega-P_i^*)} \tag{3.43}$$

where μ_i^* is the complex conjugate of μ_i.

3.7.2 Damped Nonsymmetric Systems

The decoupled system equations can be written as,

$$\mu_i \dot{\eta}_i + \kappa_i \eta_i = \sum_{i=1}^{2N} \{\rho_i\}^T F_i \qquad (3.44)$$

Proceeding in the same way as discussed in Section 3.7.1, the frequency response function $H_{sr}(j\omega)$ can be written as

$$H_{sr}(j\omega) = \frac{q_s(j\omega)}{f_r(j\omega)} = \sum_{i=1}^{2N} \frac{\phi_{ri}\, \rho_{si}}{\mu_i(j\omega - P_i)} + \frac{\phi^*_{ri}\, \rho^*_{si}}{\mu^*_i(j\omega - P^*_i)}$$

where μ^*_i and ρ^*_i are complex conjugates of μ_i and ρ_i . (3.45)

3.8 Modal Testing of Rotor System

Experimental determination of the modal parameters was mostly reported for non-rotating structures with symmetric properties. These techniques can be extended for rotating symmetric structures provided appropriate excitation or measurement techniques are adopted. However, the method is more involved when applied to a nonsymmetric structure such as a rotor system supported on fluid film bearings because the asymmetric fluid film properties along the vertical and the horizontal axes make the system a nonsymmetric one. Consequently, the left and the right eigenvectors of the system need to be evaluated in order to satisfy the biorthonality relationship between them to uncouple the system FRFs. measured along the rotor system by exciting at all the test points and measuring only at one fixed point provide the left eigenvectors. By measuring the responses at all the points while exciting only at one fixed point provides the right eigenvectors. These FRFs are curve-fitted with a suitable curve-fit method and then the modal model is developed. In the present work, the modal testing is performed on a single disk

rotor supported on hydrodynamic bearings, which was analyzed using modal analysis in Section 3.4.

3.8.1 Experimental Scheme

The experimental set up consists of a single disk rotor mounted centrally on an uniform steel shaft which in turn is supported on fluid film bearings at its two ends whose details were already given in Table 2.2. Figure 3.9 shows the experimental set up of the rotor-bearing system which is subjected to modal testing. Six test points are prescribed viz, two at the bearing locations, two at either side of the disk and the remaining two points along the length of the shaft. A schematic of the rotor with specified test points are shown in Fig. 3.10. The measurement at the disk location is avoided due to the signal impairment arising out of the high surface velocity of the disk which throws the hammer without absorbing impact energy. The measurements are made both along the vertical and horizontal directions, using sensors mounted on a sliding mount which facilitates measurement at any position along the rotor shaft. Test forces are applied systematically at the stipulated test points using an instrumented hammer. This response and force time signals are fed into a FFT analyzer in order to obtain the FRFs. This method provides a matrix of NXN frequency response functions as shown in Fig. 3.11 of which any one column provides all the right eigenvectors of the system whereas either a row or a column provides all the eigenvalues of the system.

It is important to note that the frequency content is influenced by the selection of the hammer mass and the flexibility of the tip of the impact cap. Since the frequency response functions are measured for the

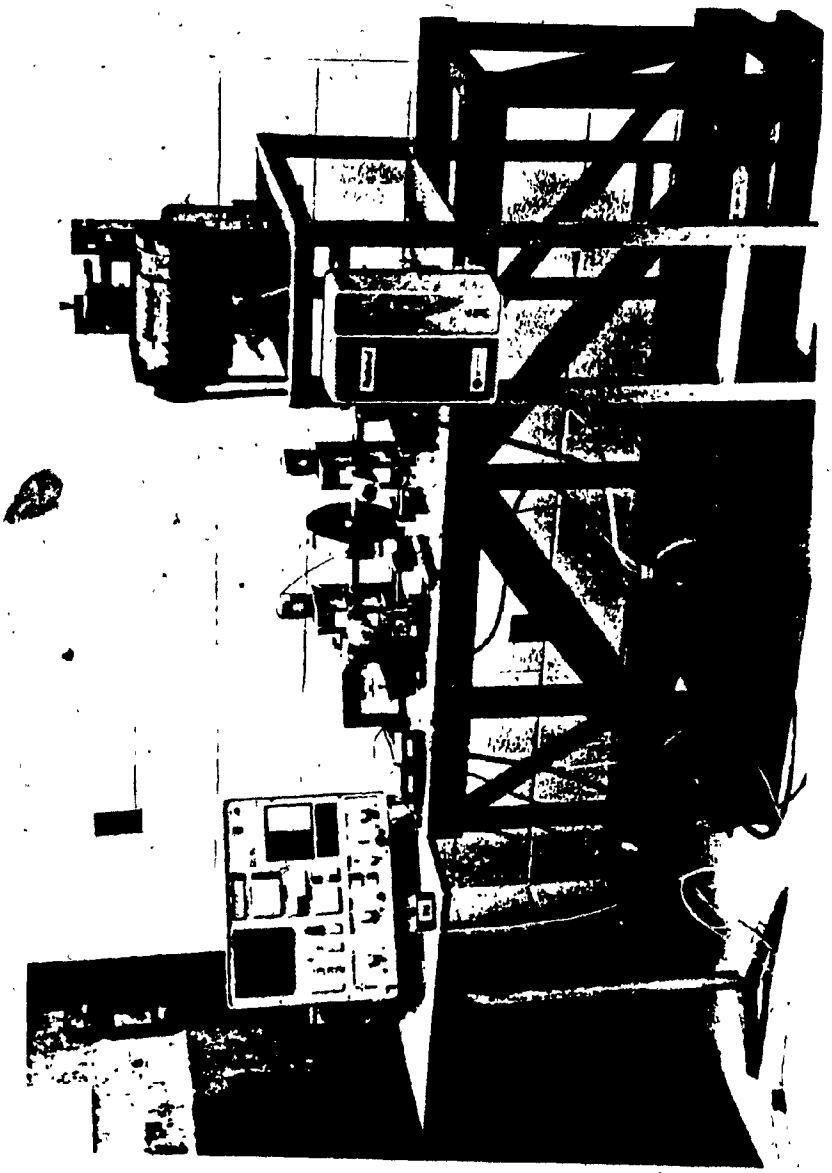

Figure 3.9 Experimental Set up of a Rotor-Bearing System

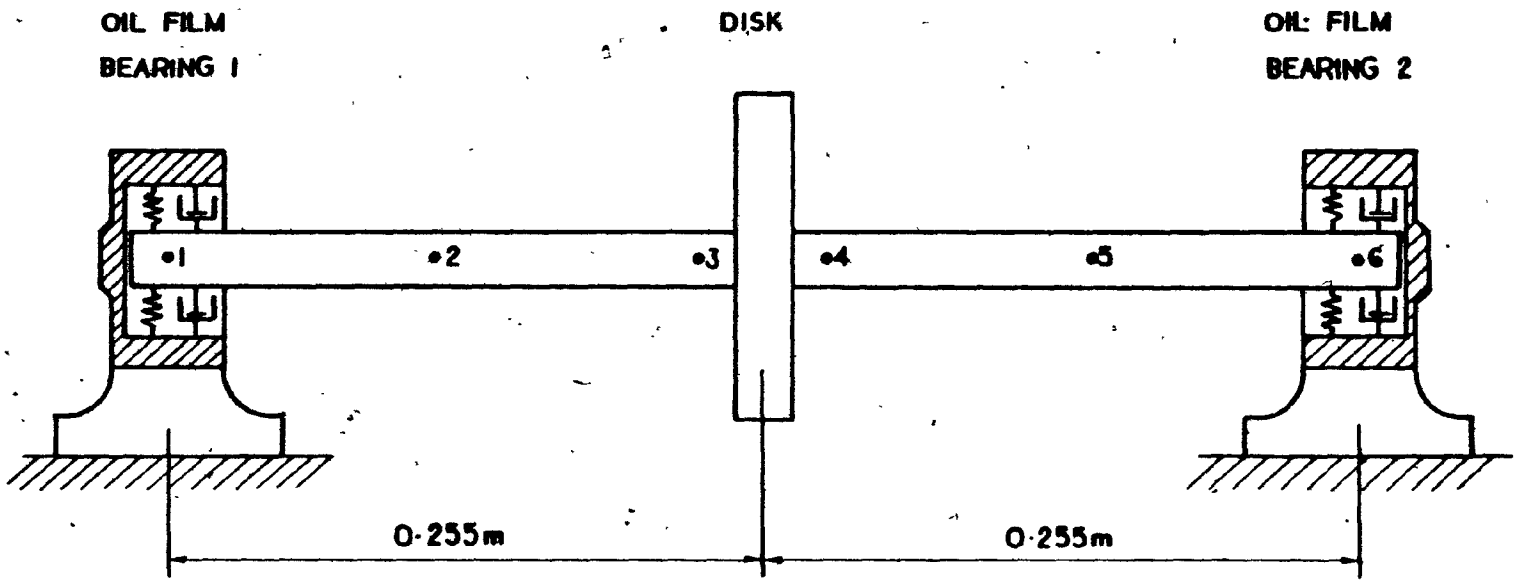

Figure 3.10 Test Points of the Rotor - Bearing System .

$$H_{sr}(\omega)^A = \begin{bmatrix} H_{11} & H_{12} & \cdots & H_{1r} & \cdots & H_{1N} \\ H_{21} & H_{22} & & H_{2r} & & H_{2N} \\ \vdots & & & & & \\ H_{s1} & H_{s2} & & H_{s3} & & H_{sN} \\ \vdots & \vdots & & \vdots & & \vdots \\ H_{N1} & H_{N2} & & H_{Nr} & & H_{NN} \end{bmatrix}$$

Fig. 3.11: Matrix of Frequency Response Function

rotating shaft system, the impact cap should be soft in order to avoid damage to the rotor shaft and to get a clear spectrum as well. The impact hammer excites all the possible frequencies of the system under consideration.

Different techniques are available to estimate modal parameters from frequency response data. However, depending upon the degree of modal coupling, a method most suited to the system is used. At any given frequency, the frequency response represents the sum of all the modes which have been excited as seen from eqn. (3.45). Because the rotor-bearing system has heavy modal coupling, a multi-degree of freedom curve fit based on eqn. (3.45) is used. This is an iterative method and hence the starting values can be obtained from the simple single degree of freedom curve fit methods. Accordingly, two such methods are discussed in the next section.

3.8.2 Numerical Methods:

In this section, some numerical methods to analyze the measured data will be discussed. Curve-fitting provides analytical expressions for the measured transfer functions. The purpose of this stage is to minimize the error between the experimental data and the analytical expressions at each data sample and the modal parameters are identified. Different algorithms are available depending upon the specific nature of the problem. The different approaches are:

(i) frequency domain or time domain methods,

(ii) single degree of freedom or multi-degree of freedom methods,

(iii) direct curve fitting procedures or least squares fit.

Most of the curve-fitting algorithms are based on the frequency domain analysis. There are methods which utilize the impulse response functions instead of frequency response functions. However, the time domain representation gives no real indication as to the number of natural frequencies, as can be seen readily in the frequency domain analysis. Moreover, FFT algorithms are very well developed and together with the recent measurement techniques, make the frequency domain methods easier and faster than the time domain measurements. For small perturbations, most of the structures behave linearly and therefore frequency domain analysis is found convenient and accurate.

Moreover, depending upon the complexity of the structure and the intensity of modal coupling, the curve fitting procedures are chosen. A single degree of freedom method is chosen when the modes of the structure are widely spaced and modal interactions are small. However, if the modal coupling is heavy, a multi-degree of freedom curve fit procedure is opted. With the following assumption, two single degree of freedom (SDOF)) curve-fit procedures are discussed.

1) The structure's modes of vibration are underdamped.

2) For each mode, the frequency and damping are assumed to be constant over the entire structure, or in other words there exists only one mode shape for each natural frequency.

3.8.3 The Peak-Pick SDOF Method

Figure 3.12 shows a typical FRF curve plotted against frequency for a system whose off resonance modes are very well separated and hence the contribution of other modes are almost negligible. The first piece of information that can be extracted from an amplitude response

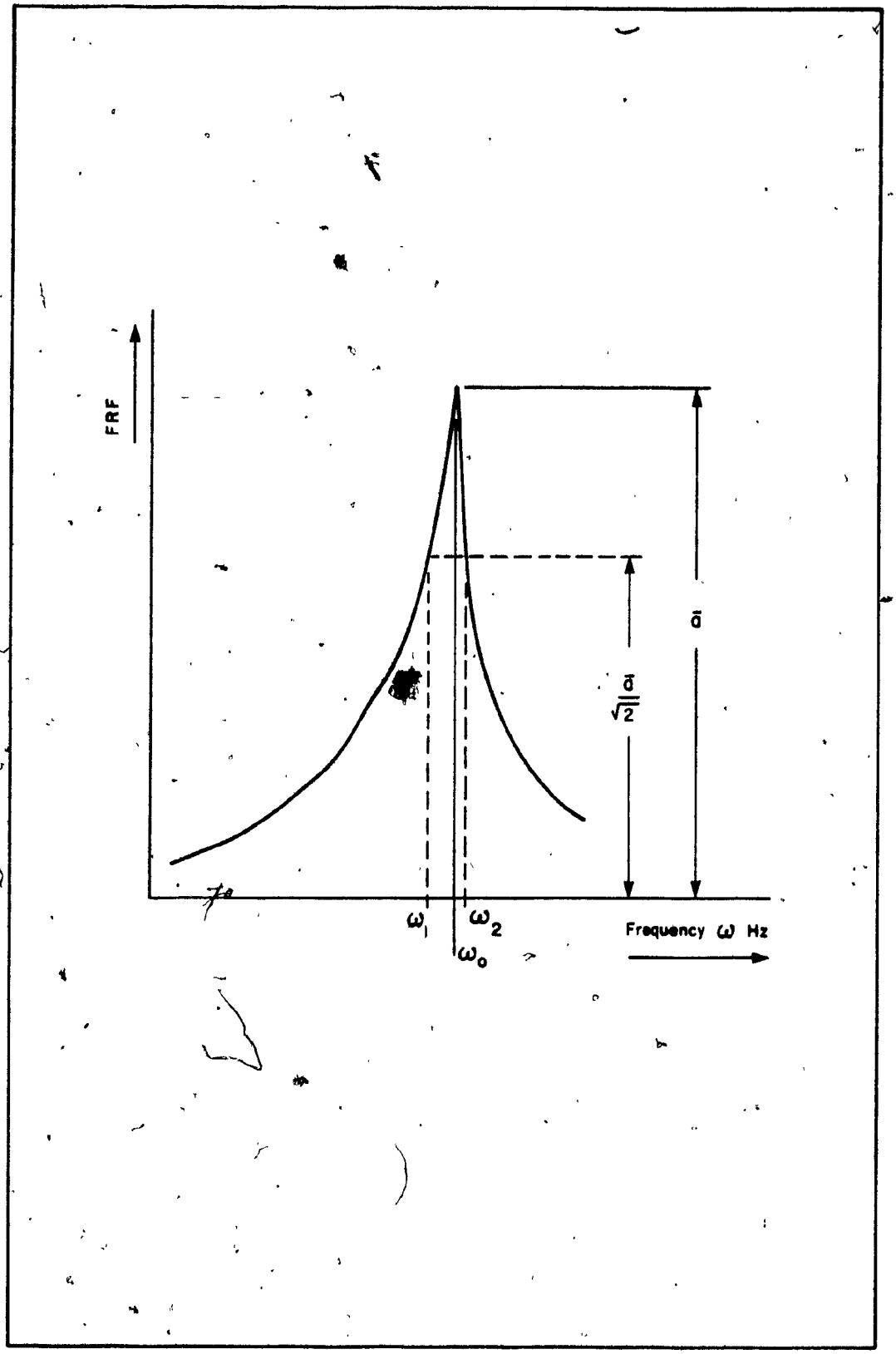

Figure 3.12 FRF Curve for a Second Order Simple Linear System.

curve is the natural frequencies of the system, which are usually identified as the frequencies whose peaks are attained - and thus the name peak-pick method. The second piece of information that can be extracted from the response curve is the amount of damping at that particular mode under consideration. Damping is determined from the sharpness of resonance and is given by

$$2\zeta = \frac{\omega_2 - \omega_1}{\omega_0} \tag{3.46}$$

where $\zeta = \frac{c}{c_c}$, c_c is the critical damping of the structure and ω_1 and ω_2 are the frequencies on either side of the natural frequency ω_0 where the peak amplitude is reduced by a factor of $\sqrt{2}$.

To determine the mode shape, the structure is excited at a natural frequency and the ratios of the amplitudes at various points on the structure are determined. There are certain disadvantages involved in this method. For example, the damping ratio ζ is evaluated from a single peak, but the mode shape is determined from the ratio of amplitudes at various points. Thus if an error is made in the estimation of a peak due to the contribution from other modes, the inaccuracies involved in evaluating the principal modes will be greater than those involved in the determination of damping.

3.8.4 Circle Fit SDOF Method

The circle fit method is based on the curve fitting of FRF data plotted in the complex Argand (Nyquist) plane. This method is by Kennedy and Pancu [82]. For weak modal coupling, the frequency response function $H_i(j\omega)$ can be written from eqn. (3.42) neglecting complex part,

$$H_i(j\omega) = \frac{1}{\mu_i \lambda_i'} \left[\frac{R_i}{2j(j\omega - p_i)} \right] \tag{3.47}$$

where $R_i = \Phi_{ri} \Phi_{si}$

Let $R_i = U^i + j V^i$ (3.48)

$$H_i(j\omega) = \frac{U^i + j V^i}{2j (j\omega - p_i)} \tag{3.49}$$

Now,

$$\frac{1}{2j (j\omega - p_i)} = \frac{1}{2j (j\omega + \zeta\omega - j\lambda_i')} \tag{3.50}$$

$$= \frac{(\lambda_i' - \omega) - j(\zeta_i \omega)}{2[(\lambda_i' - \omega)^2 + (\zeta_i \omega)^2]} \tag{3.51}$$

Letting $\zeta_i \omega = g_i$ (3.52)

equation (3.49) becomes, $\dfrac{U^i + jV^i e^{-j\theta_i}}{2 [(\lambda_i' - \omega)^2 + g_i^2]^{\frac{1}{2}}}$ (3.53)

where $\theta_i = \tan^{-1} \dfrac{g_i}{(\lambda_i' - \omega)}$

Real part aa $= \dfrac{\lambda_i' - \omega}{2[(\lambda_i' - \omega)^2 + g_i^2]}$ (3.54)

$$\text{Imaginary part } bb = -\frac{g_i}{2[(\lambda_i'-\omega)^2 + g_i^2]} \tag{3.55}$$

$$bb + \frac{1}{4g_i} = \frac{-g_i}{2[(\lambda_i'-\omega)^2 + g_i^2]} + \frac{1}{4g_i} \tag{3.56}$$

$$= \frac{(\lambda_i'-\omega)^2 - g_i^2}{4g_i[(\lambda_i'-\omega)^2 + g_i^2]} \tag{3.57}$$

$$aa^2 + \left(bb + \frac{1}{4g_i}\right)^2 = \frac{[(\lambda_i' - \omega)^2 + g_i^2]^2}{\{4g_i[(\lambda_i'-\omega)^2 + g_i^2]\}^2} \tag{3.58}$$

$$aa^2 + \left(bb + \frac{1}{4g_i}\right)^2 = \frac{1}{[4g_i]^2} \tag{3.59}$$

Equation (3.59) is the equation of a circle with the center displaced on the "bb" or imaginary axis downward a distance $1/4g_i$ and a radius of $1/4g_i$. The diagram shown in Fig. 3.13(a) represents a plot of

$$\frac{1}{2[(\lambda_i'-\omega)^2 + g_i^2]}.$$

Now, the complex value of $R_i e^{-j\theta_i}$ expands the diameter of the circle by counterclockwise angle θ_i away from the imaginary axis as shown in Fig. 3.13(b). The circle fit algorithm calculates the modal

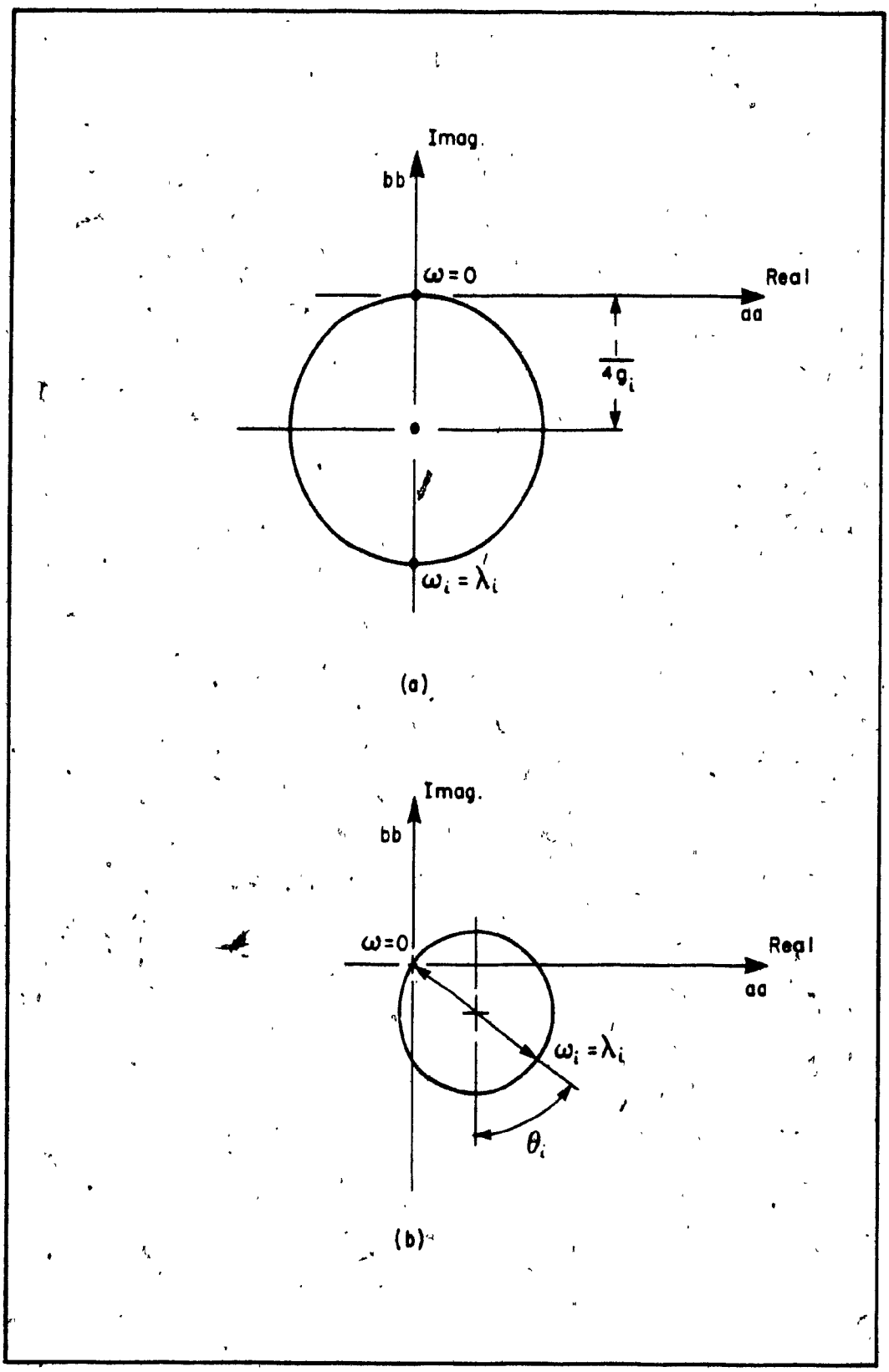

Figure 3.13 Circle fit method.

residues R_i by fitting the equation of a circle, using a least square error procedure, to a number of measured transfer function data points in the vicinity of a modes natural frequency. The magnitude of R_i is calculated from the diameter of the circle using

$$\|R_i\| = 4\, g_i \times \text{diameter} \tag{3.60}$$

If the measured response is in the vicinity of a resonance dominated by the contribution of single mode of the structure, then a SDOF curve fit method will be adequate to estimate the modal parameters of that mode. Otherwise, a more sophisticated algorithm based on a MDOF model is necessary.

The complex modal parameters are identified by fitting a best curve fit between the measured response plot and the generated plot from the analytical expression based on eqn. (3.45). The least square procedure is used and the criterion for minimization of the error is

$$H^A_{sr}(\omega, \lambda_i, \Phi_i) = H^M_{sr}(\omega) + E_p \tag{3.61}$$

where H^A_{sr} is the generated frequency response function and H^M_{sr} is the measured frequency response function at a particular frequency. E_p is the error between them, so

$$E_p = [H^A_{sr}(\omega, \lambda_i, \Phi_i) - H^M_{sr}(\omega)] \tag{3.62}$$

Summing up the error squared over "N" frequencies to obtain,

$$\sum_{p=1}^{N} E_p^{\,2} = \sum_{p=1}^{N} [H^A_{sr}(\omega, \lambda_i, \Phi_i) - H^M_{sr}(\omega)]^2 \tag{3.63}$$

Following along similar lines, the left eigenvectors p_i are also obtained from the rows of frequency response functions of the H-matrix.

Differentiating eqn. (3.63) with respect to each unknown in turn and setting the result to zero, gives a number of equations for the unknown modal parameters. The experimentally obtained frequency response functions are bode plotted and this plot provides the natural frequencies of the system corresponding to the peaks in the amplitude plot and the respective phase plot changing from 0° to 180°. Since the operating speed range from the rotor is only 4200 RPM, discussions are restricted to the first natural frequency and the first mode only. The bearing configurations arising out of different clearance values are used to compare rotor system natural frequencies with those obtained by analytical methods earlier. The experimental frequency response plots are obtained for the excitation at the test point number 5 and measurement at point number 2 of the rotor. The plots are shown in Figs. 3.14 through 3.21.

3.8.5 Configuration 1: Equal Bearing Clearances ($c_1 = c_2 = 0.0000533$m)

The frequency response plots obtained for the stationary rotor along Y and Z directions, respectively are shown in Figs. 3.14 and 3.15. From the plots, the rigid bearing natural frequencies when $\omega = 0$ along Y and Z directions are found to be 51.75 Hz and 47.75 Hz respectively. Figures 3.16 and 3.17 show the corresponding frequency response plots when the rotor speed is 33.3 Hz, where the rotor natural frequencies are found to be 39.75 Hz and 46 Hz respectively along Y and Z directions. When the rotor speed coincides with one of the natural frequencies, that speed corresponds to the critical speed of the rotor.

$C_1 = C_2 = 0.0000533$ m , $\lambda_1 = \lambda_2 = \frac{\lambda}{2}$

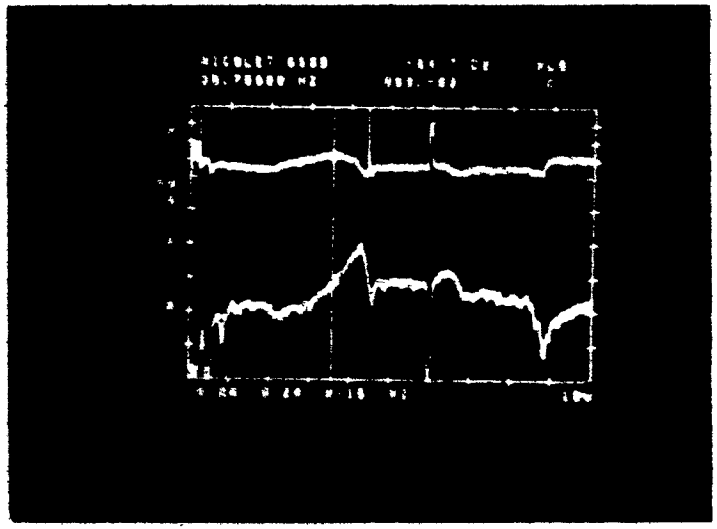

Figure 3.14 Measured Frequency Response Plot of the Rotor Along Y - Direction . $\omega = 0$

$C_1 = C_2 = 0.0000533$ m , $\lambda_1 = \lambda_2 = \frac{\lambda}{2}$

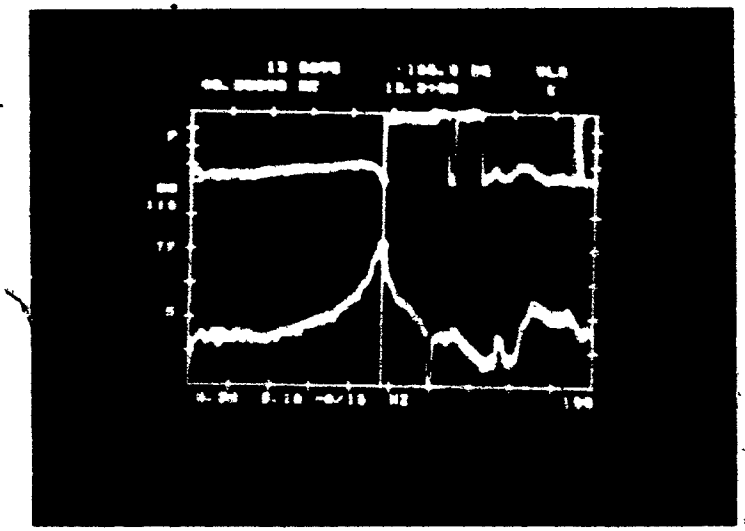

Figure 3.15 Measured Frequency Response Plot of the Rotor Along Z - Direction . $\omega = 0$

$C_1 = C_2 = 0.0000533$ m , $\ell_1 = \ell_2 = \frac{\ell}{2}$

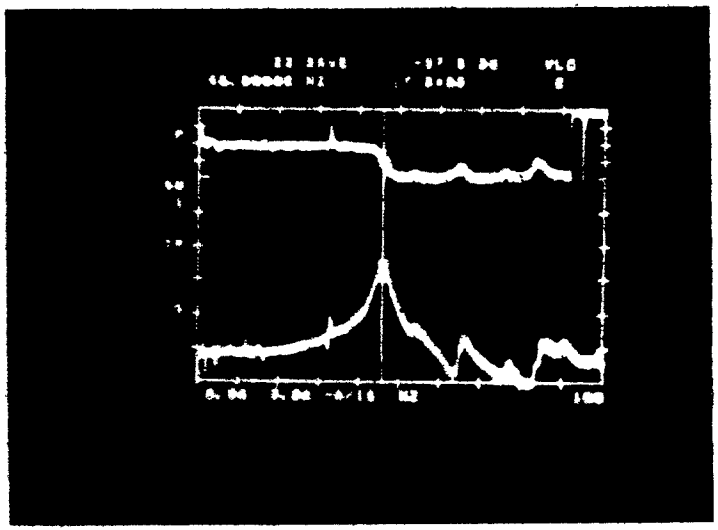

Figure 3.16 Measured Frequency Response Plot of the Rotor Along Y – Direction. ω= 33.3 Hz

$C_1 = C_2 = 0.0000533$ m , $\ell_1 = \ell_2 = \frac{\ell}{2}$

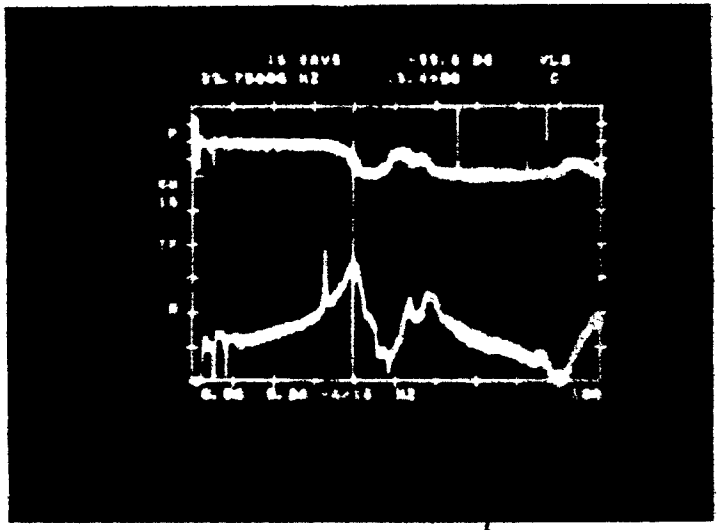

Figure 3.17 Measured Frequency. Response Plot of the Rotor Along Z - Direction. ω= 33.3 Hz

Figure 3.18 shows the plots of unbalance response at the disk location along Y and Z directions against the rotor speed. These are the analytical plots obtained, following the analysis discussed in Section 3.4. Since the measured and analytical frequency responses correspond to different locations and for different type of excitations, a direct comparison between them is not meaningful. However, the system natural frequencies from these two methods can be compared. It is observed that the amplitude peaks in the analytical frequency response plots occur at the frequency 43.5 Hz for both Y and Z directions. The analytical natural frequency along Y direction is larger than the measured frequency in Y direction.

3.8.6 Configuration 2: Dissimilar Bearing Clearances (c_1 = 0.0000533m, c_2 = 0.000188m

For this configuration, the measured frequency response plots, obtained at a rotor speed of 33.3 Hz show the natural frequencies to be 39 Hz and 44 Hz along Y and Z directions and they are shown respectively in Figs. 3.19 and 3.20.

The analytical amplitude response values against the running frequencies of the rotor is shown in Fig. 3.21. This shows two distinct peaks in the amplitude response plots. The first peak occurs around 35 Hz along Y-direction and the second one occurs at 43.5 Hz along Z-direction. it is observed that the analytical and measured natural frequencies agree well.

The frequency response plots of the rotor in all the above three bearing configurations show that the natural frequencies of the rigidly supported shaft is always larger than the shaft supported by flexible

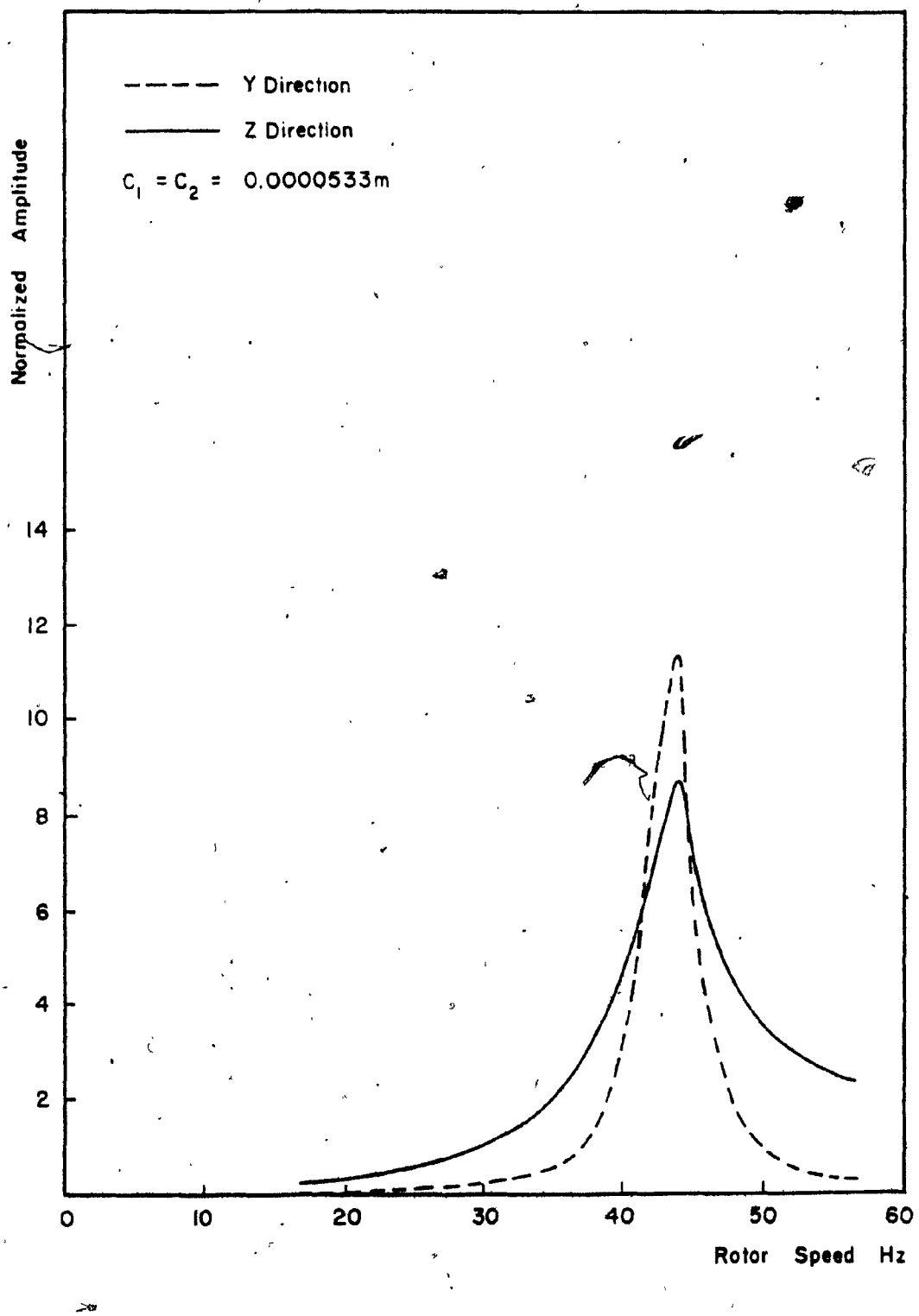

Figure 3.18 Unbalance Responce of Rotor .

C_1 = 0.0000533 m

C_2 = 0.000188 m

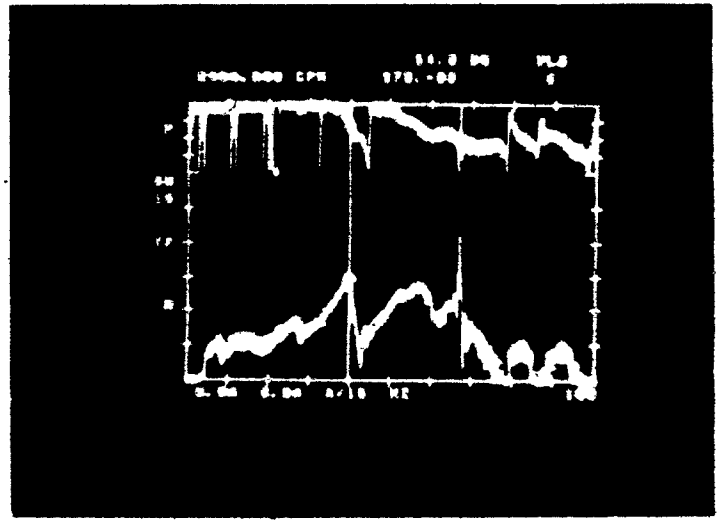

Figure 3.19 Measured Frequency Response of Rotor in Y - Direction.

C_1 = 0.0000533 m

C_2 = 0.000188 m

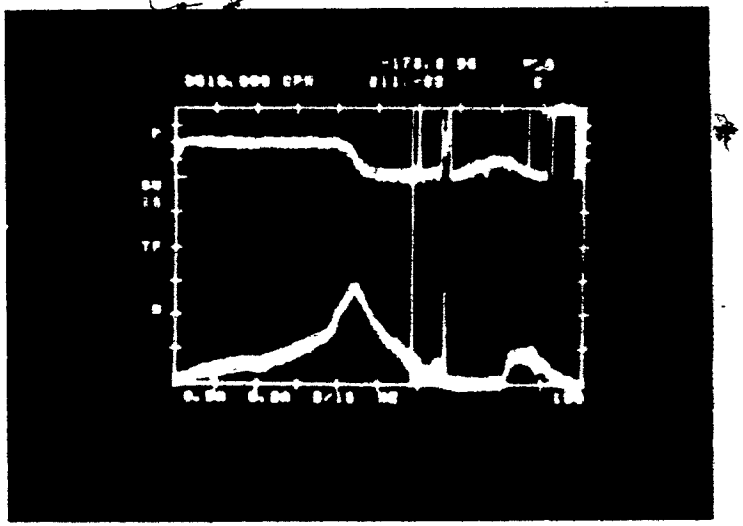

Figure 3.20 Measured Frequency Response of Rotor in Z - Direction.

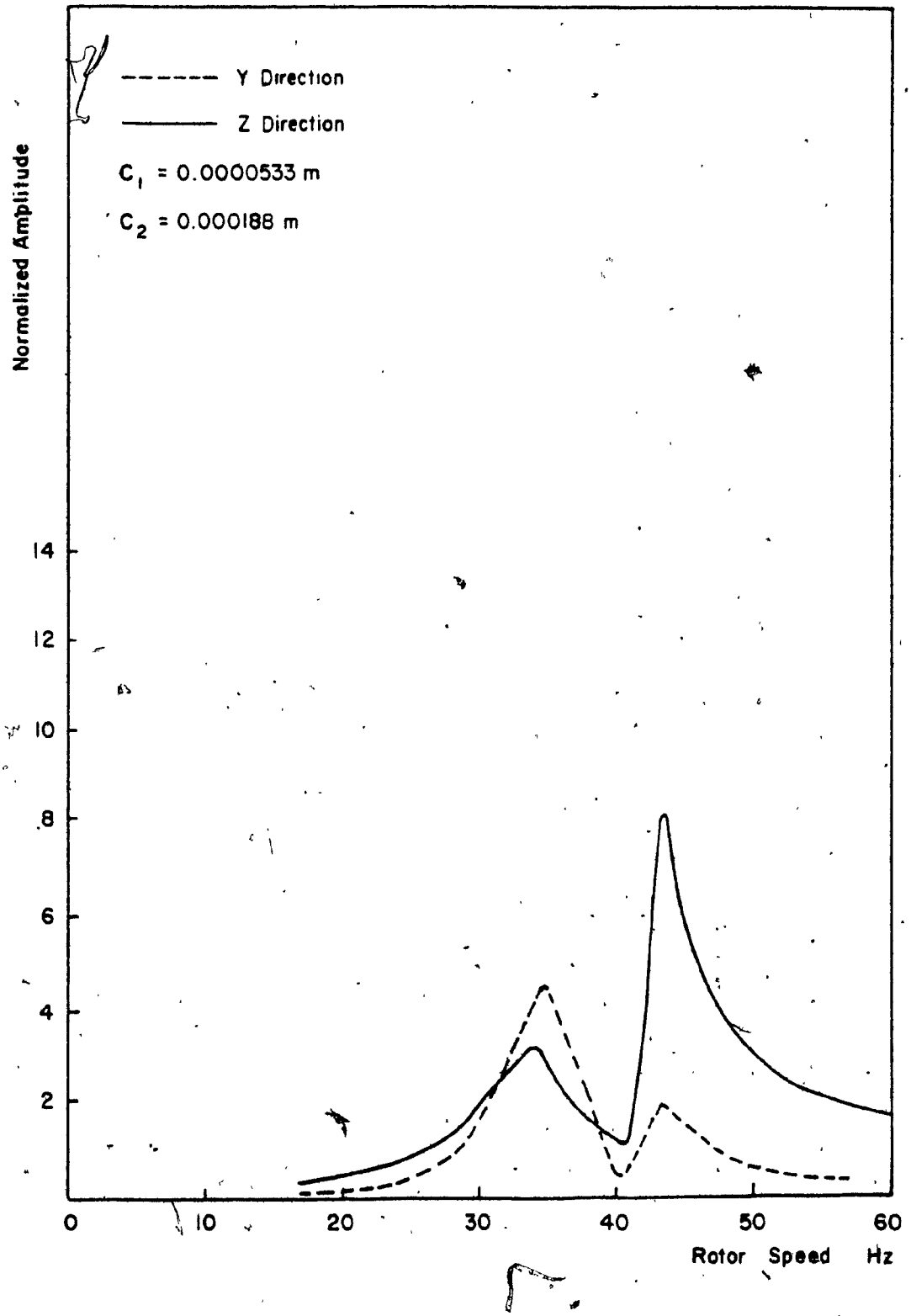

Figure 3.21 Unbalance Response of Rotor .

hydrodynamic film. Also, it is observed that under dynamic conditions of the rotor, the experimental frequency response has a small spike at the speed of the rotor.

3.8.7 Configuration 3: Equal Bearing Clearances ($c_1 = c_2 = 0.000188$m)

Complete modal information is obtained only for a rotor supported on fluid film bearings with identical clearance values of 0.000188 m at both ends. The comparison plot of the measured frequency response with the generated analytical expressions based on the multi-degree of freedom curve fit method is shown in Fig. 3.22. The complete mode shape plots corresponding to first mode for this configuration along Y and Z directions respectively are shown in Figs. 3.23 and 3.24 and they represent the left eigenvector of the system. Figures 3.25 and 3.26 show the above mentioned results in different planes. Similar mode shape plots of the right eigenvector of the system are shown in Figs. 3.27, 3.28, 3.29 and 3.30. These mode shapes are similar to the first mode of a simply supported beam. However, at the two ends, a small displacement of the shaft is seen. The modal parameters of this configuration of the rotor are given in Tables 3.1 through 3.4. It is observed from the experimental plots that the left and the right eigenvalues obtained for ZX and YX plane of the rotor differ approximately by 1 Hz. This is because of the approximation involved in the curve-fitting procedures over all the test points.

For this configuration, the analytical response plots show two distinct peaks and they are shown in Figs. 3.31. The first peak occurs approximately at 31Hz in Y-direction and the second one occurs at 42.66 Hz in Z-direction.

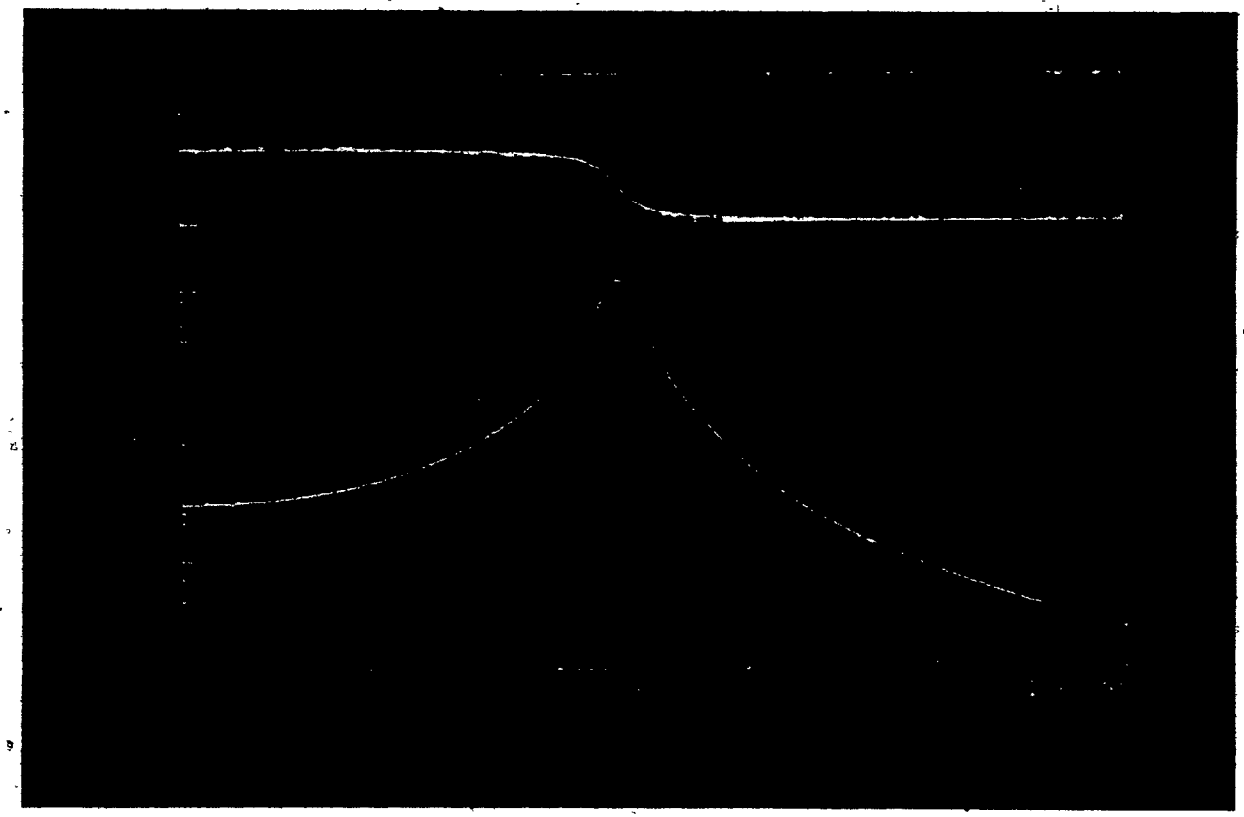

$C_1 = C_2 = 0.000188$ m , $l_1 = l_2 = \frac{l}{2}$

Figure 3.22 Comparison Plots of Generated and Measured Frequency Response Function .

$$C_1 = C_2 = 0.000188 \text{ m} \quad , \quad l_1 = l_2 = \frac{l}{2}$$

Figure 3.23 First Mode Shape of the Rotor Corresponding to the Y-X Plane.
(obtained from left eigen vectors)

$C_1 = C_2 = 0.000188$ m , $l_1 = l_2 = \frac{l}{2}$

Figure 3.24 First Mode Shape of the Rotor Corresponding to the Z-X Plane. (obtained from left eigen vector)

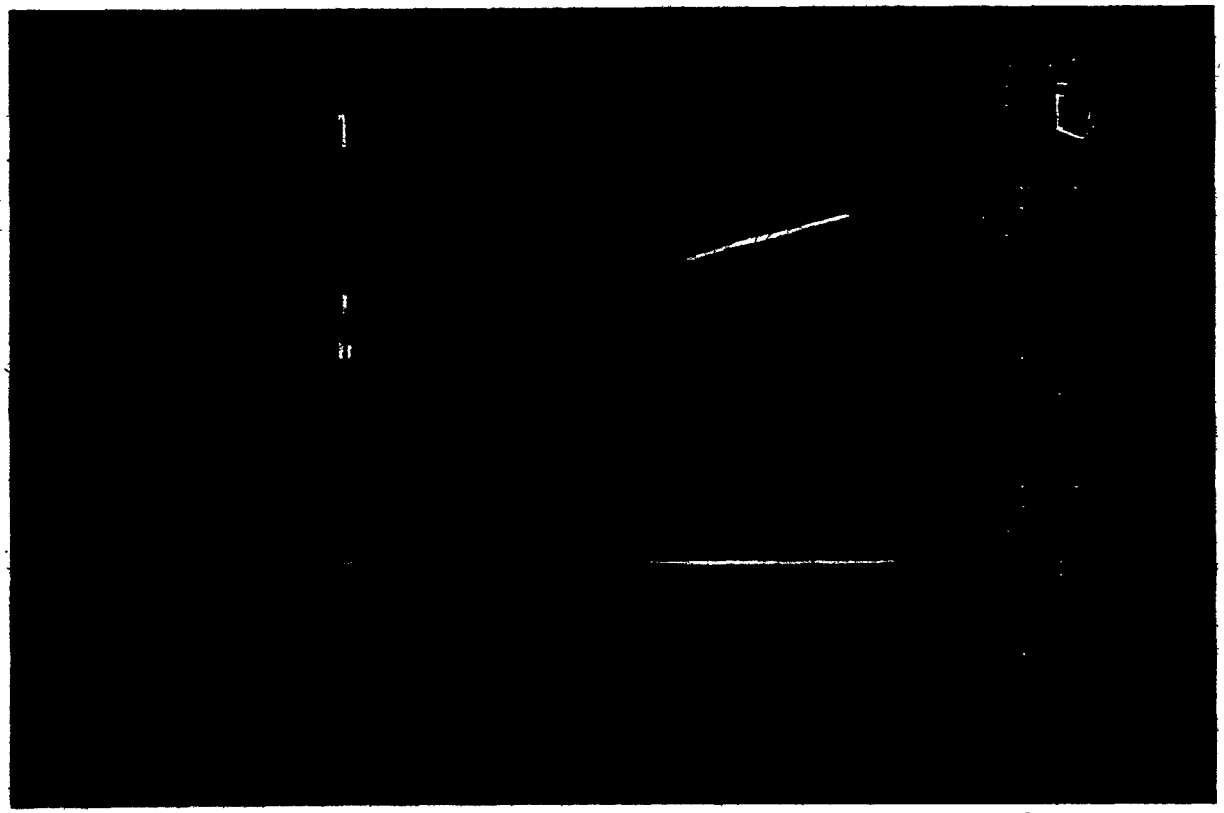

$C_1 = C_2 = 0.000188$ m , $l_1 = l_2 = \frac{l}{2}$

Figure 3.25 Mode Shapes Shown in Orthogonal Planes .
(Y – X Plane)

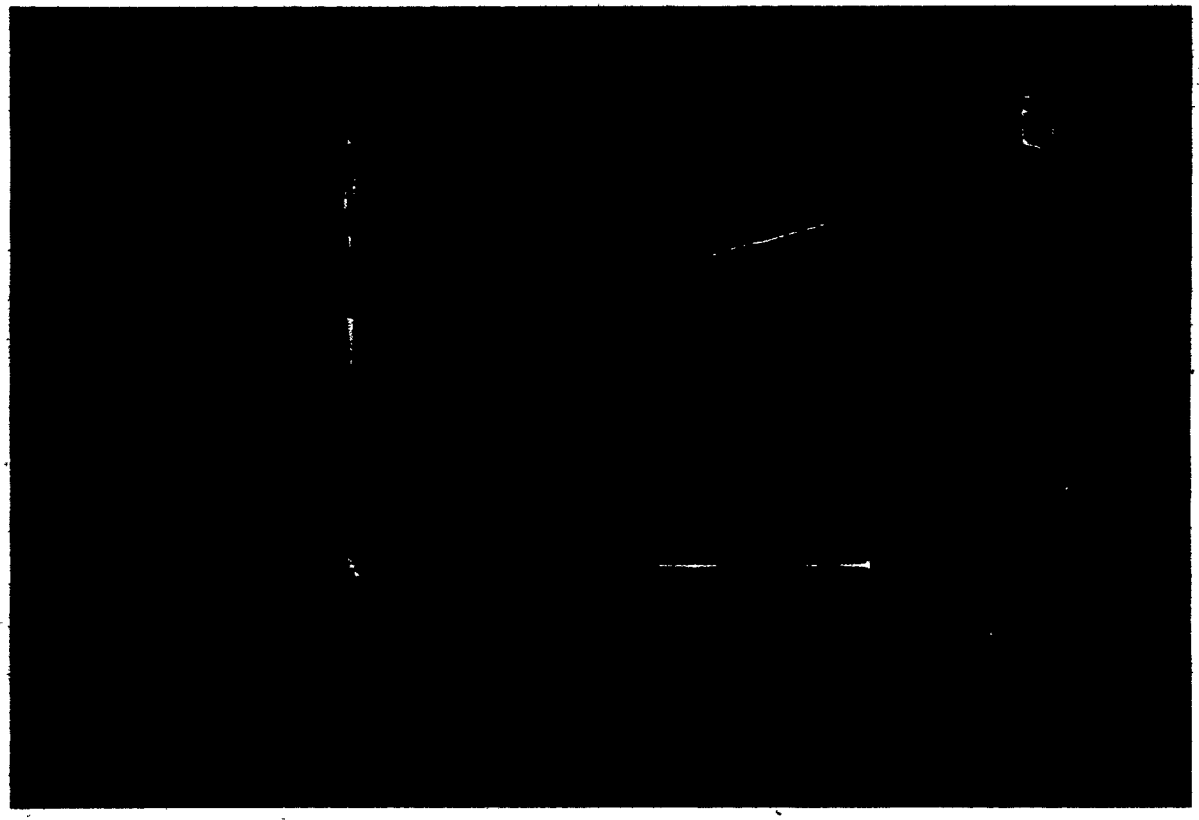

$C_1 = C_2 = 0.000188.\ m^{-1},\ l_1 = l_2 = \frac{l}{2}$

Figure 3.26 Mode Shapes Shown in Orthogonal Planes .
(Z - X Plane)

$C_1 = C_2 = 0.000188$ m, $l_1 = l_2 = \frac{l}{2}$

Figure 3.27 First Mode Shape of the Rotor Corresponding to the Y - X Plane (right eigen vector).

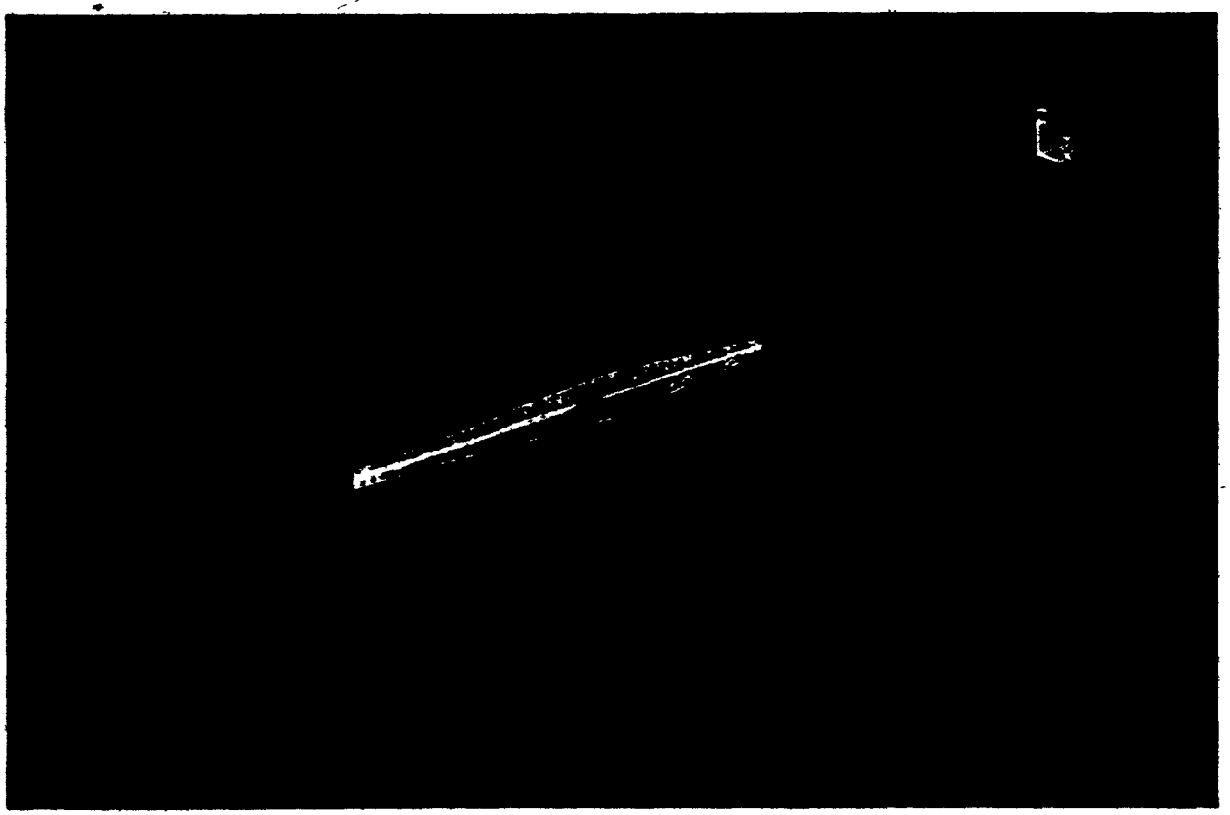

$$C_1 = C_2 = 0.000188 \text{ m}, \quad l_1 = l_2 = \frac{l}{2}$$

Figure 3.28 First Mode Shape of the Rotor Corresponding to the Z-X Plane (right eigen vector).

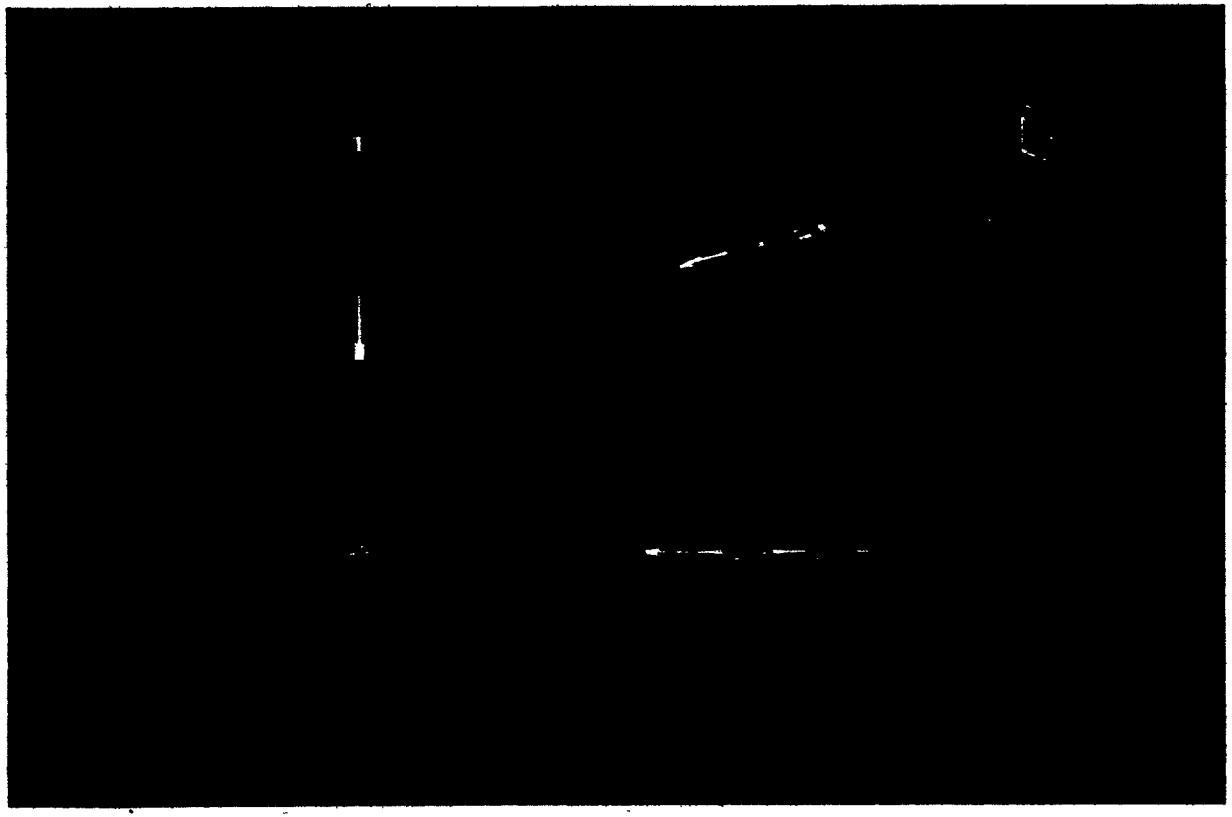

$C_1 = C_2 = 0.000188$ m , $l_1 = l_2 = \frac{l}{2}$

Figure 3.29 Mode Shapes Shown in Different Orthogonal Planes. (Y - X Plane)

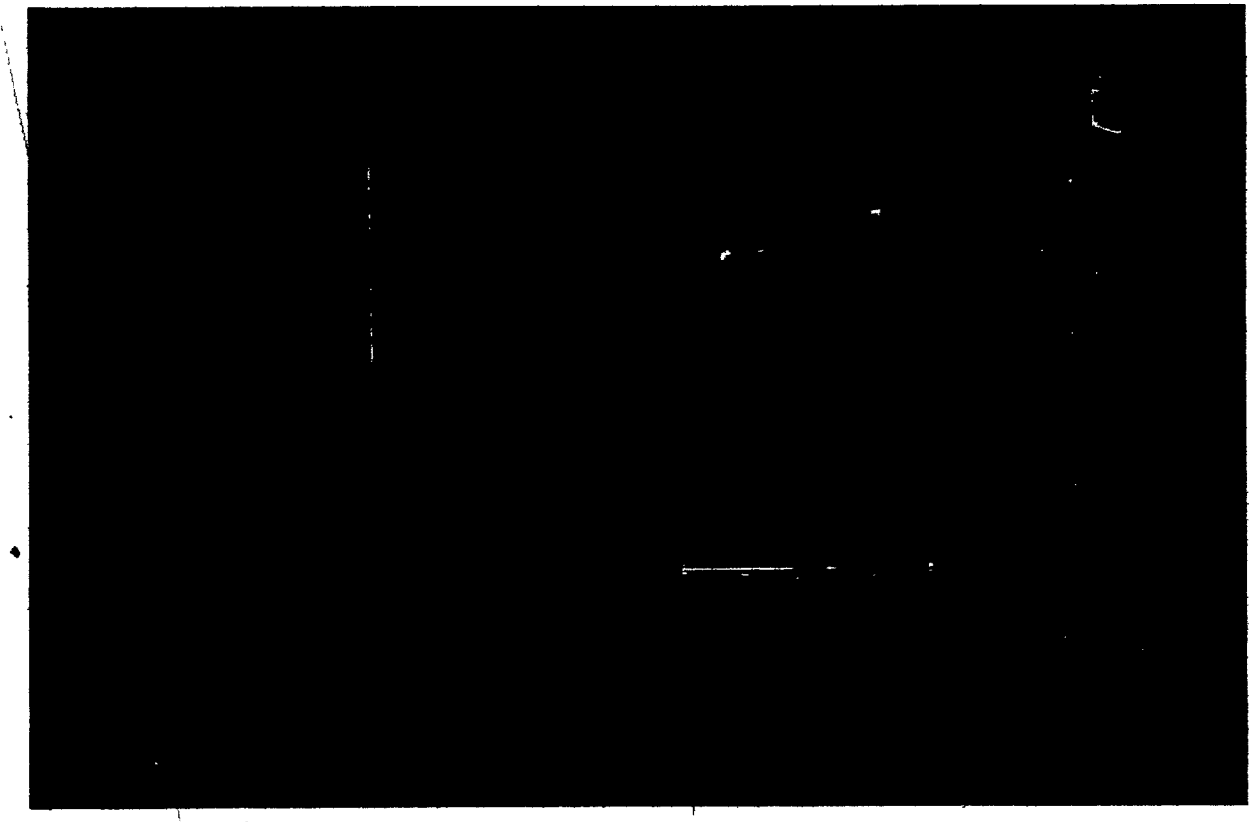

$C_1 = C_2 = 0.000188$ m , $\ell_1 = \ell_2 = \frac{\ell}{2}$

Figure 3.30 Mode Shapes Shown in Different Orthogonal Planes. (Z-X Plane)

TABLE 3.1: MODAL PARAMETERS OF THE ROTOR (ORIGINAL SYSTEM)

$c_1 = c_2 = 7.4\tau$

RPM = 2000

Right Eigenvectors

Mode 1	Res. Freq.	Vis. Damp.	Modal Mass	Modal Stiffness
	4.127E-01	4.078E-02	1.02E-05	0.69

Measurement Point	Driving Point	Real	Imaginary	Mag.	Phase
1	x 2	.423	-1.192E-02	0.423	-1.6
	y 2				
	z 2	.128	-0.161	.206	-51.7
2	x 2	.642	-1.342E-02	.642	-1.2
	y 2				
	z 2	.357	-.791E	.868	-65.7
3	x 2	.958	6.965E-02	.961	4.2
	y 2				
	z 2	.429	-.677	.802	-57.7
4	x 2	1.0	4.983E-08	1.00	0.0
	y 2				
	z 2	.411	-.0809	.908	-63.0
5	x 2	.888	4.74E-02	0.889	3.1
	y 2				
	z 2	.259	-0.717	.763	-70.2
6	x 2	.556	-1.698E-02	.556	-1.7
	y 2				
	z 2	.24	-0.458	0.517	-62.4

TABLE 3.2: MODAL PARAMETERS OF THE ROTOR (ORIGINAL SYSTEM)

$c_1 = c_2 = 7.4\tau$

RPM = 2000

Left Eigenvectors

Res. Freq.	Vis. Damp.	Modal Mass	Modal Stiffness
45.85	4.055E-02	2.145E-05	1.78

Driving Point	Measurement Point	Real	Imag.	Mag.	Phase
1	x 2	5.368E-02	-0.136	.146	-68.5
	y 2				
	z 2	0.532	1.312E-02	.532	-1.4
2	x 2	-0.409	-7.242E-02	.415	-170.0
	y 2				
	z 2	0.977	-4.958E-02	0.978	-2.9
3	x 2	-0.614	3.603E-02	0.615	176.6
	y 2				
	z 2	0.897	0.121	0.905	7.7
4	x 2	-.671	0.122	0.683	169.7
	y 2				
	z 2	1.0	1.019E-10	1.00	00
5	x 2	-.537	.276	0.604	152.8
	y 2				
	z 2	.726	.1597	.743	12.3
6	x 2	-.124	3.158E-02	.128	165.8
	y 2				
	z 2	.435	-0.121E00	.452	-15.5

TABLE 3.3: MODAL PARAMETERS OF THE ROTOR (TRANSPOSED SYSTEM)

$c_1 = c_2 = 7.4\tau$

RPM = 2000

Left Eigenvectors

Res. Freq.	Vis. Damp.	Modal Mass	Modal Stiffness
40.94 Hz	4.117E-02	1.28E-05	0.815

Driving Point	Measurement Point	Real	Imag.	Mag.	Phase
1	x 2	0.578	1.806E-02	0.578	1.8
	y 2				
	z 2	2.308E-02	-1.12E-03	2.31E-02	-2.8
2	x 2	0.641	0.138	0.656	12.1
	y 2				
	z 2	0.137	1.273E02	0.137	5.3
3	x 2	1.00	-1.304E-08	1.00	0.0
	y 2				
	z 2	0.157	4.737E-02	0.164	16.8
4	x 2	0.876	0.106	0.882	6.9
	y 2				
	z 2	0.157	1.594E-02	0.157	5.8
5	x 2	0.791	0.158	0.807	11.3
	y 2				
	z 2	.153	1.622E-02	0.153	6.1
6	x 2	0.389	9.9583E-02	0.401	14.4
	y 2				
	z 2	1.202E-02	4.294E-03	1.277E-02	19.7

TABLE 3.4: MODAL PARAMETERS OF THE ROTOR (TRANSPOSED SYSTEM)

$c_1 = c_2 = 7.4\tau$

RPM = 2000

Right Eigenvectors

Mode 1	Res. Freq.	Vis. Damp.	Modal Mass	Modal Stiffness
	44.81 Hz	0.03186	1.49E-05	672E-04

Measurement Point	Driving Point	Real	Imaginary	Mag.	Phase
1	x 2	2.033E-02	-6.665E-02	6.968E-02	-73.0
	y 2				
	z 2	0.374	-.133	0.397	-19.6
2	x 2	4.804E-02	-5.909E-2	7.616E-02	-50.9
	y 2				
	z 2	0.611	-7.403E-02	0.615	-6.9
3	x 2	.102	-7.818E-02	.128	-37.6
	y 2				
	z 2	.875	-.168	.891	-10.9
4	x 2	-6.955E-02	-4.344E-02	.2E-02	-148.0
	y 2				
	z 2	1.00	-6.519E-08	1.00	0.0
5	x 2	-1.124E-02	-7.593E-02	7.767E-02	-98.4
	y 2				
	z 2	0.726E00	-7.513E-02	0.730	-5.9
6	x 2	4.183E-03	-6.733E-03	7.925E-03	-58.2
	y 2				
	z 2	.355	1.756E-02	0.355	2.8

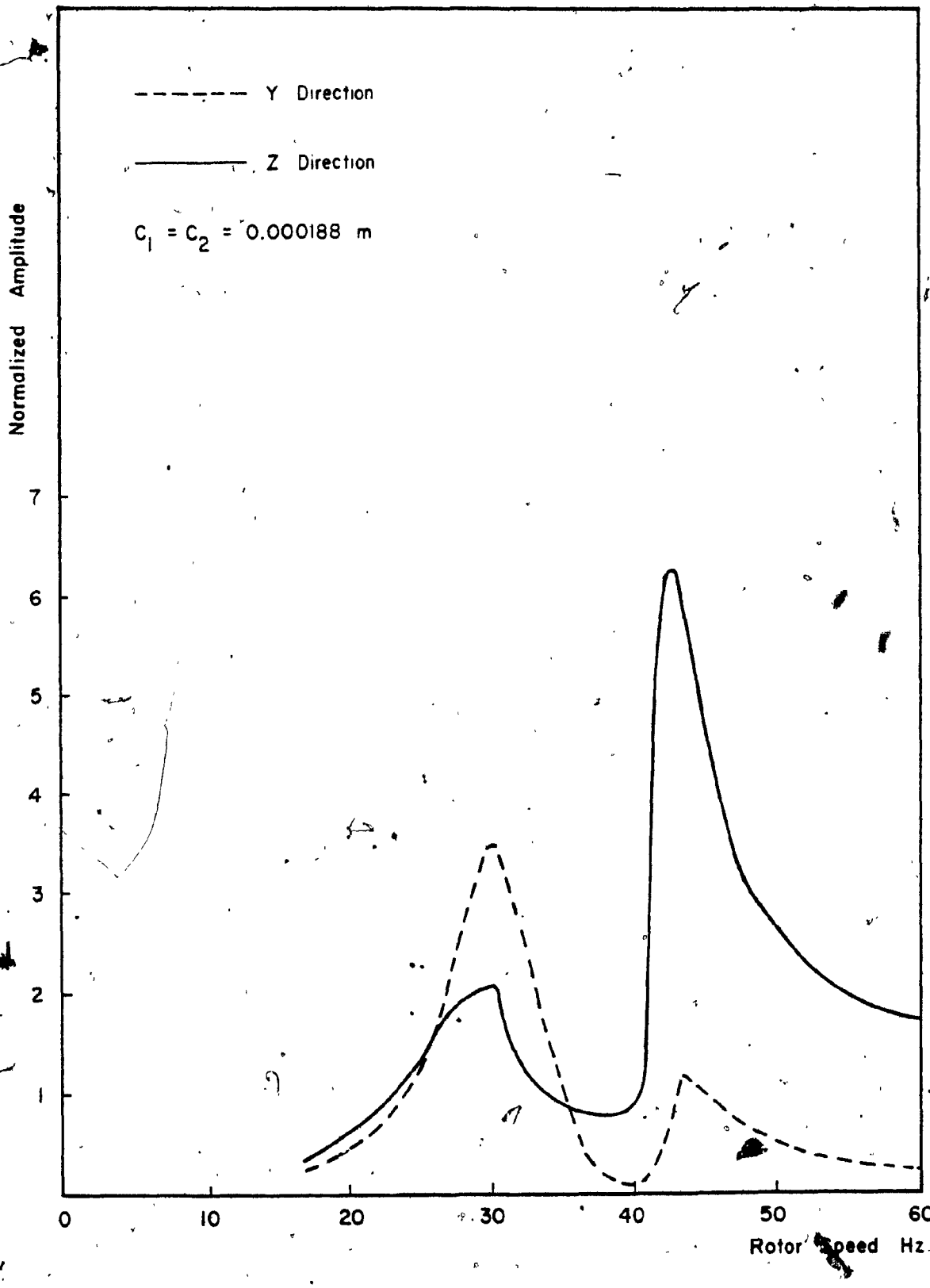

Figure 3.31 Analytical Unbalance Response of Rotor .

In general, the different stiffnesses of the support along Z and Y directions, make the rotor system natural frequencies also differ slightly along these directions.

3.9 System Stability

It was mentioned already that the direct approach did not provide the stability information of the system and hence a modal analysis procedure was resorted to get all the relevant system information. These modal analysis procedures are discussed in Section 3.4 for a simple rotor system and it is observed that the system eigenvalues consist of real and imaginary parts where the real part of the eigenvalue is the system damping and the imaginary part represents the whirl frequency of the rotor system. The value of the real part of the eigenvalue which represents the system damping remains negative for a stable system. If this value changes to a positive value, the system response increases monotonically thereby pushing the system to the unstable regions. Therefore, the "threshold speed" of instability of the rotor system corresponds to a speed at which the real part of the eigenvalues changes sign, i.e. negative value to a positive value. The imaginary part of the complex eigenvalue corresponding to this threshold speed of instability is the whirl speed of the rotor. In rotors supported on fluid film bearings, the whirl ratio which is the ratio between the whirl speed of the rotor to the spin speed of the rotor normally varies between 0.45 and 0.5.

Figure 3.32 shows the analytically obtained instability regions for a central disk rotor supported on oil film bearings whose clearances c_1 and c_2 are constant at 0.000188 m at both ends. The real part of the

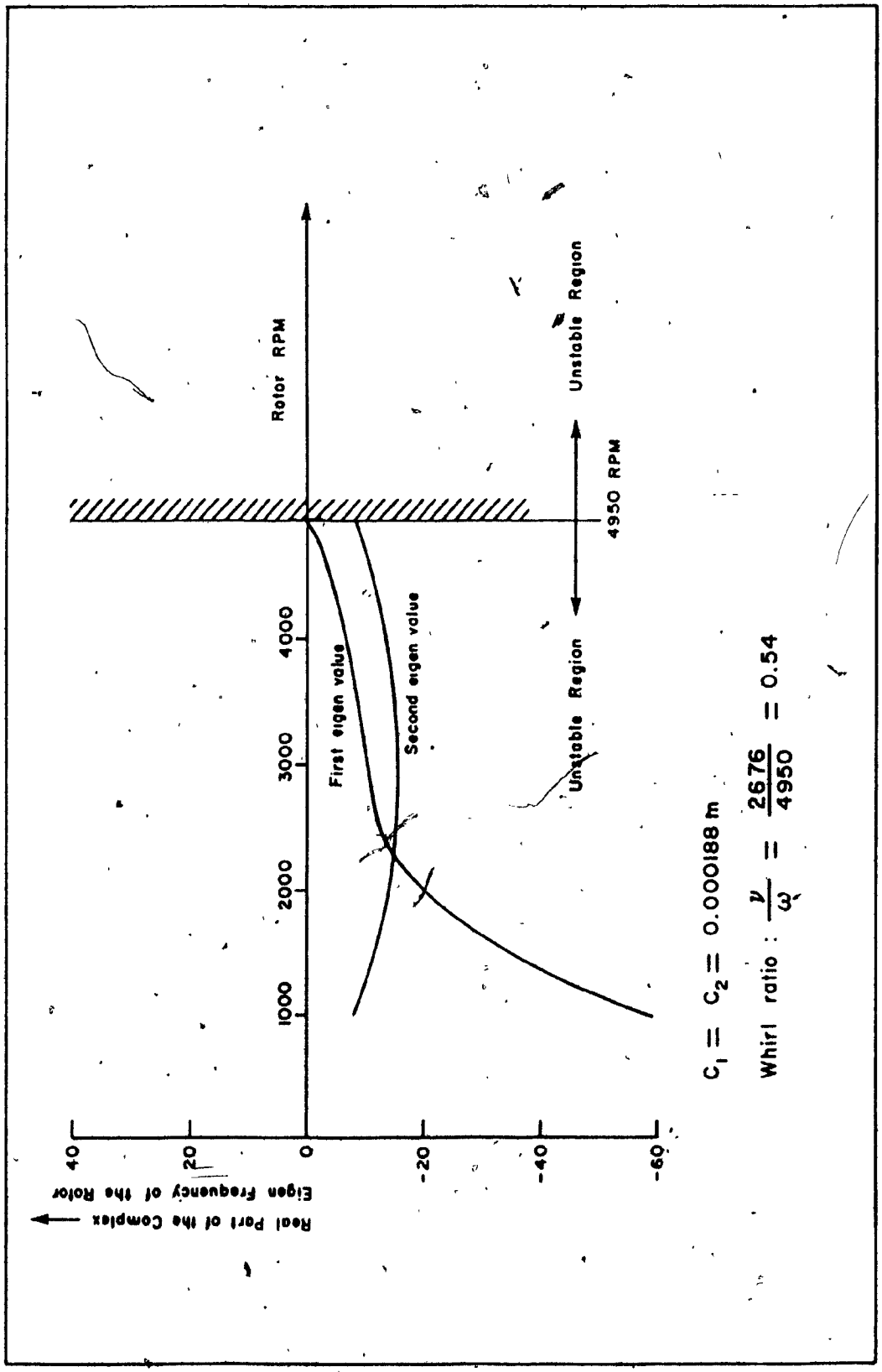

Figure 3.32 Stability of the Rotor System.

two eigenvalues are plotted against the rotor spin speed in RPM. This shows that the system enters the unstable region at the rotor speed of 4950 RPM and this corresponds to the real part of the first eigenvalue changing sign from negative value to the positive value. Hence, by analysis, the region of instability for this configuration of the rotor lies beyond the rotor spin speed of 4950 RPM. The threshold speed of instability is 4950 RPM and whirl ratio is about 0.5.

To compare this theoretically obtained threshold speed of instability of the rotor, the experimental value of the threshold speed of instability is obtained only for this configuration. The instability in the rotor system can be obtained from the shape and behavior of orbital diagram. For this configuration of the rotor, the experimentally obtained orbital diagram for a speed of 4100 RPM is shown in Fig. 3.33. The critical diagram looks like the shape of a heart which is different from the conventional shape of the ellipse and this corresponds to the position of journal rub in the bearings and appears similar to that obtained by Beatty [83]. Moreover, under steady-state conditions of the rotor, the shape itself is not stationary, but revolves at every instant around a central position. This clearly shows that the instability is just set into the system. Because the maximum operating speed of the rotor is limited to 4200 RPM, the complete details of the rotor behavior are not possible to obtain beyond the rotor speed of 4200 RPM.

The unstable regions for the rotor supported on dissimilar bearings at c_1 = 0.0000533m and c_2 = 0.000188m are shown in Fig. 3.34. The plot shows that the real part of the first eigenvalue does not change sign and hence the corresponding Y motion of the rotor does not develop in-

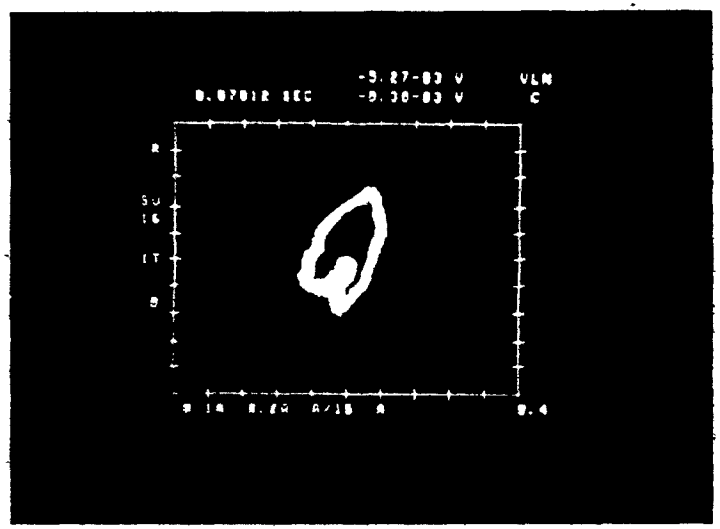

$C_1 = C_2 = 0.000188\,m$

$\ell_1 = \ell_2 = \frac{\ell}{2}$

Figure 3.33 Orbital Diagram at the Shaft Location obtained for a Rotor Speed of 4100 RPM.

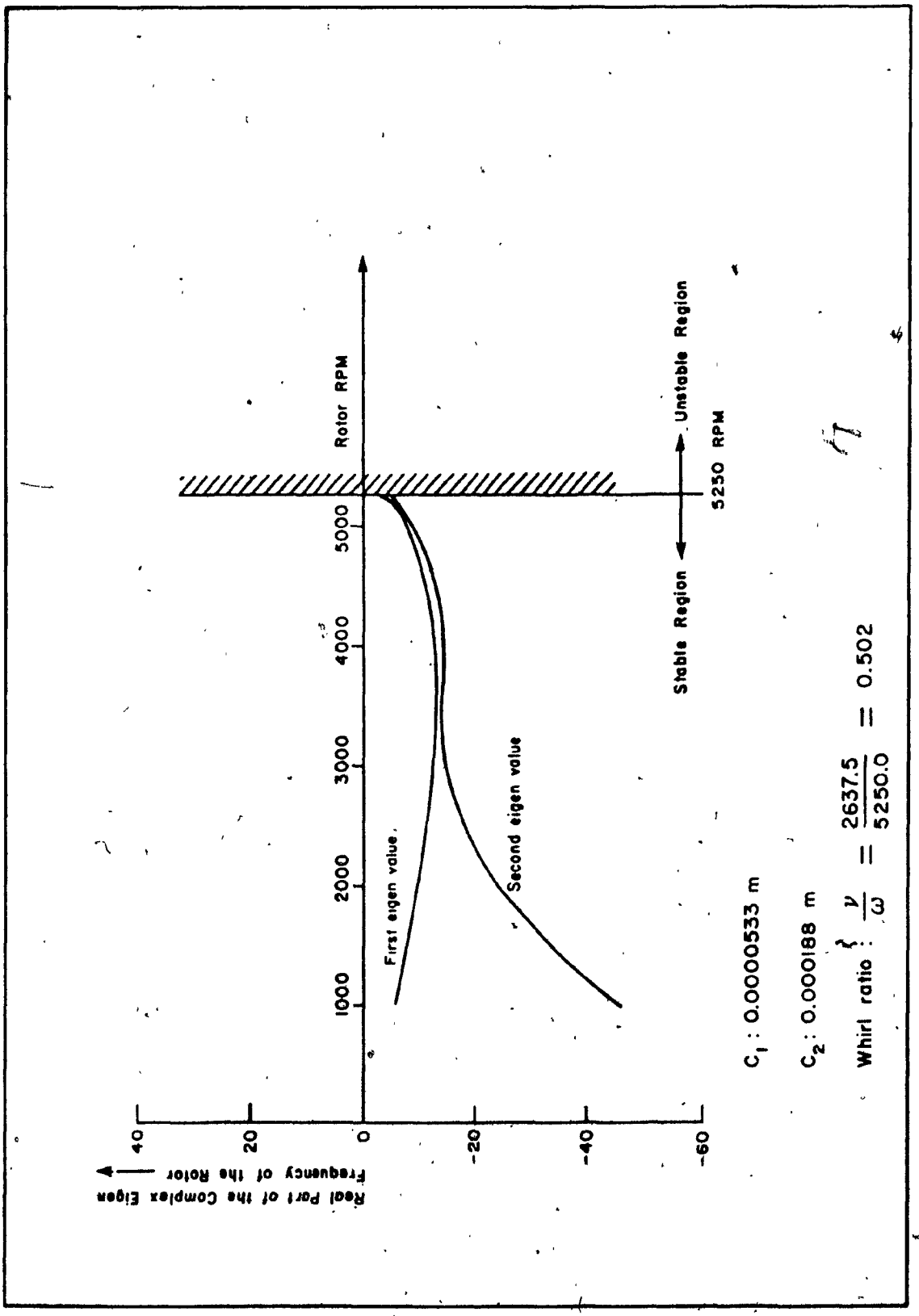

Figure 3.34 Stability of the Rotor System.

stability in the system. Whereas the real part of the second eigenvalue, which corresponds to Z motion of the rotor, changes from a negative value to a positive value at the rotor speed of 5250 RPM. Threshold speed of instability, therefore, is approximately 5250 RPM for this configuration of the rotor and the whirl ratio is again equal to 0.5.

3.10 Conclusions

Modal analysis procedure is used to evaluate the dynamic responses of a single disk rotor supported on hydrodynamic bearings at its two ends. This method provides system information such as stability and modal responses in addition to the unbalance response and critical speeds obtained using a direct approach discussed in Chapter 2. Total system responses and the individual modal responses are obtained both at the disk and bearing locations for different bearing configurations through orbital diagrams.

In general, the dynamic information obtained by experiments do not match exactly with theoretical results because of the approximations involved in several stages of the analysis. Such approximations are drastically reduced by resorting to a modal testing procedure which uses the experimentally measured gross parameters to curve fit with the analytical expressions in order to extract the modal parameters of the system. Using the modal testing procedures, the modal parameters of the single disk system are identified for a particular bearing configuration.

The simple rotor system is modelled using a discrete Jeffcott rotor assuming that the support conditions are rigid. Even though such a model is sufficient for a simple rotor system, larger systems which consist of varying shaft sections, several disks and bearings cannot be modelled very

accurately using the Jeffcott model. Such continuous systems can be modelled in a more elegant way by finite elements using consistent representation of system properties. But, the computational effort in handling the large size matrices is high; however, it is possible to reduce the size of the system matrices using a modal reduction procedure.
The finite element modelling and the subsequent reduction procedures, applicable to a rotor-bearing system, will be discussed in Chapter 4.

CHAPTER 4

FINITE ELEMENT MODEL OF THE ROTOR SYSTEM AND STUDY OF SYSTEM STABILITY

In the previous chapters, a lumped mass model was used for the rotor system in the form of a Jeffcott rotor and the resulting equations of motion were solved using modal analysis. For a simple rotor system, such a model will provide satisfactory results; however, it is not sufficient to represent large systems and therefore results obtained based on the model may not be reliable. Hence, a different method is required to model the large rotor system accurately. Finite element method has been used to model the rotor systems.

In this chapter, a simple rotor system is modelled by finite elements and the resulting equations are solved using modal analysis techniques. Because the system is simple, a few elements represent it very well. However, for large rotor systems with several disks and bearings, the system matrices are larger and the associated computational effort is exhorbitant. In order to reduce the time involved in computational effort and handle small size matrices, a modal co-ordinate reduction procedure is discussed. Further, a stability analysis for the simple rotor on fluid film bearings is carried out.

4.1 Analysis

The typical flexible rotor-bearing system consists of a rotor composed of symmetric rigid disk, symmetrical rotor segments with distributed mass and elasticity properties and the bearings at the two ends, as illustrated in Fig. 2.1. A typical cross-section of the rotor in a deformed state is defined relative to a fixed frame of reference

XYZ by the translations U(s,t) and V(s,t) along the Y and Z directions respectively with respect to the elastic centre line and the small angle rotations $\theta(s,t)$ and $\phi(s,t)$ about Y and Z respectively to orient the plane of cross-section with spin axis X. This is shown in Fig. 4.1.

The equations of motion for the rotor-bearing system obtained from Lagrange's equations are as follows:

$$\frac{d}{dt}\left(\frac{\partial \bar{L}}{\partial \dot{q}_i}\right) - \frac{\partial \bar{L}}{\partial q_i} + \frac{\partial \bar{D}}{\partial \dot{q}_i} - F_i = 0 \qquad (4.1)$$

where $\bar{L}$ is Lagrangian,

$\bar{L} = \bar{T} - \bar{V}$, and q_i, F_i are respectively the i-th generalized co-ordinates and forces. Now, relating the rotations (θ, ϕ) to the translations (U,V), the equations can be written as follows:

$$\theta = -\frac{\partial V}{\partial s} \; ; \quad \phi = \frac{\partial U}{\partial s} \quad \text{and} \quad \psi = \omega t \qquad (4.2)$$

The disc and the rotor element are fixed in the yz plane of the rotating frame xyz or the principal axes of the rotor systems. The successive rotational velocities about Y, Z and X axes can be related to the respective angular co-ordinates using Euler angles as,

$$\begin{Bmatrix} \omega_x \\ \omega_y \\ \omega_z \end{Bmatrix} = \begin{bmatrix} 1 & 0 & -\sin\theta \\ 0 & \cos\phi & \cos\theta \cdot \sin\phi \\ 0 & -\sin\phi & \cos\theta \cdot \sin\phi \end{bmatrix} \begin{Bmatrix} \dot{\psi} \\ \dot{\theta} \\ \dot{\phi} \end{Bmatrix} \qquad (4.3)$$

4.2 Rigid Disk Element

In this section, equations of motion for a rigid disk are developed using Lagrangian formulation. Accordingly, the kinetic energy of a

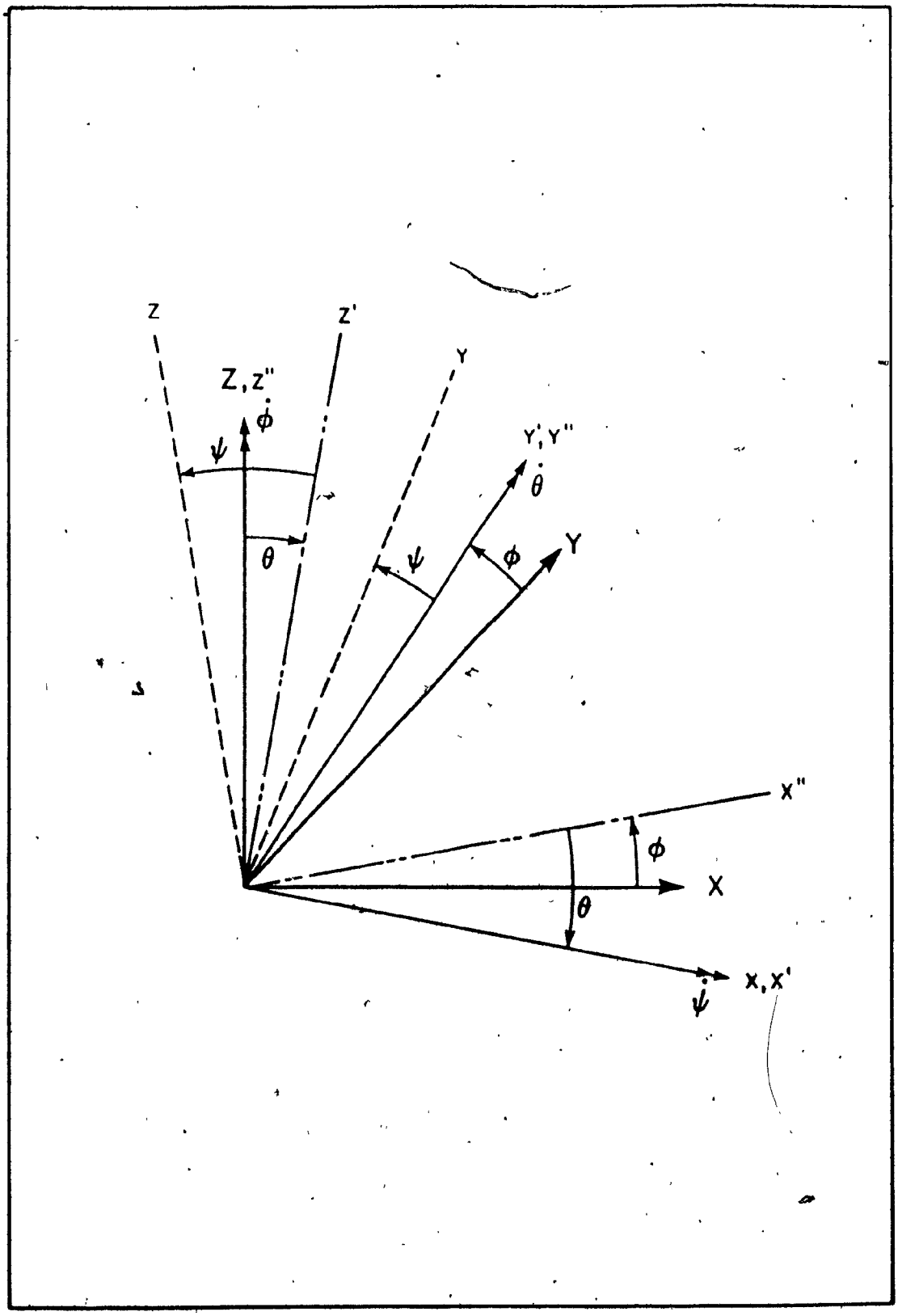

Figure 4.1 Schematic Diagram of Rotor Rotational Angles and Velocities.

typical rigid disk with mass centre coincident with the centre of the rotor shaft is derived as follows:

$$\bar{T}^d = \frac{m_d}{2}(\dot{U}^2+\dot{V}^2) + \frac{1}{2}(I_p\omega_x^2 + I_d\omega_y^2 + I_d\omega_z^2) \qquad (4.4)$$

with I_d = diametral mass moment of inertia

and $I_p \approx 2\, I_d$ for a thin disk.

Equation (4.4) can be written in the matrix form as shown:

$$\bar{T}^d = \frac{1}{2}\left[\begin{Bmatrix}\dot{U}\\ \dot{V}\end{Bmatrix}^T \begin{bmatrix} m_d & 0 \\ 0 & m_d\end{bmatrix}\begin{Bmatrix}\dot{U}\\ \dot{V}\end{Bmatrix} + \begin{Bmatrix}\omega_y\\ \omega_z\end{Bmatrix}^T \begin{bmatrix} I_d & 0 \\ 0 & I_d\end{bmatrix}\begin{Bmatrix}\omega_y\\ \omega_z\end{Bmatrix}\right]$$

$$+ \frac{1}{2} I_p \omega_x^2 \qquad (4.5)$$

where (4.3) ω_x^2 can be obtained from equation (4.3) as $\dot{\psi}^2 - 2\dot{\psi}\dot{\phi}\theta$ by neglecting the higher order angular velocity terms and their products. This is shown in equation (4.6).

$$\bar{T}^d = \frac{1}{2}\left[\begin{Bmatrix}\dot{U}\\ \dot{V}\end{Bmatrix}^T \begin{bmatrix} m_d & 0 \\ 0 & m_d\end{bmatrix}\begin{Bmatrix}\dot{U}\\ \dot{V}\end{Bmatrix} + \begin{Bmatrix}\dot{\theta}\\ \dot{\phi}\end{Bmatrix}^T \begin{bmatrix} I_d & 0 \\ 0 & I_d\end{bmatrix}\begin{Bmatrix}\dot{\theta}\\ \dot{\phi}\end{Bmatrix}\right]$$

$$+ \frac{1}{2} I_p \dot{\psi}^2 - \dot{\psi}\dot{\phi}\theta I_p \qquad (4.6)$$

With constant spin speed of the rotor $\omega = \dot{\phi}$, the equations of motion for the rigid disk can be formulated using Lagrangian and they are written as,

$$\left[[m_t^d] + [m_r^d]\right]\{\ddot{q}^d\} - \omega\,[g^d]\,\{\dot{q}^d\} = \{F^d\} \qquad (4.7)$$

$$[m_t^d] = \begin{bmatrix} m_d & 0 & 0 & 0 \\ 0 & m_d & 0 & 0 \\ 0 & 0 & 0 & 0 \\ 0 & 0 & 0 & 0 \end{bmatrix}$$

$$[m_r^d] = \begin{bmatrix} 0 & 0 & 0 & 0 \\ 0 & 0 & 0 & 0 \\ 0 & 0 & I_d & 0 \\ 0 & 0 & 0 & I_d \end{bmatrix}$$

and $$[g^d] \begin{bmatrix} 0 & 0 & 0 & 0 \\ 0 & 0 & 0 & 0 \\ 0 & 0 & 0 & -I_p \\ 0 & 0 & I_p & 0 \end{bmatrix}$$

4.3 Shaft Element

Typical rotor shaft element is illustrated in Fig. 4.2. The time dependent displacements (U,V,θ,ϕ) are also functions of position s along the axis of the element. The generalized co-ordinates

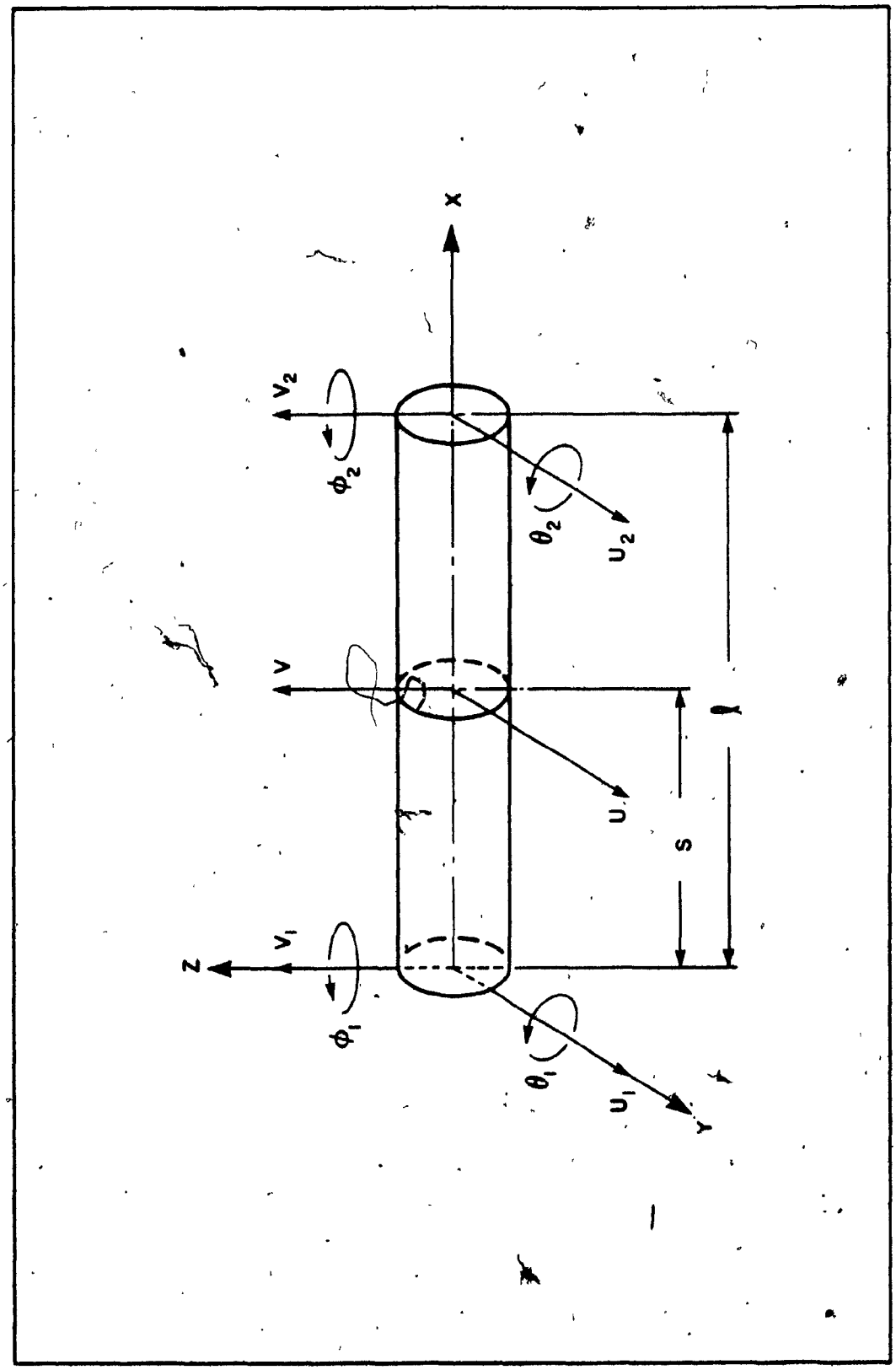

Figure 4.2 Beam Finite Element

$(q_1^e, q_2^e, \ldots, q_8^e)$ are the time dependent end point displacements (both translations and rotations) of the element of the symmetric rotor shaft.

The translation of the uniform shaft element is chosen to obey the relation,

$$\begin{Bmatrix} U(s,t) \\ V(s,t) \end{Bmatrix} = \left[N_1(s)\right] \left\{q^e(t)\right\} \tag{4.8}$$

$$\text{where } [N_1] = \begin{bmatrix} n_1 & 0 & 0 & n_3 & n_2 & 0 & 0 & n_4 \\ 0 & n_1 & -n_3 & 0 & 0 & n_2 & -n_4 & 0 \end{bmatrix}.$$

N_1 is a matrix of displacement shape functions only. The functions $n_1, \ldots, n_4$ represent the static displacement modes associated with a unit displacement of the one of the end point co-ordinates with all others constrained to zero. These functions can be written as shown below:

$$n_1 = 1 - 3\left(\frac{s}{\ell}\right)^2 + 2\left(\frac{s}{\ell}\right)^3 \qquad \text{(a)}$$

$$n_2 = 3\left(\frac{s}{\ell}\right)^2 - 2\left(\frac{s}{\ell}\right)^3 \qquad \text{(b)} \tag{4.9}$$

$$n_3 = s\left(1 - \frac{s}{\ell}\right)^2 \qquad \text{(c)}$$

$$n_4 = \frac{s^2}{\ell}\left(\frac{s}{\ell} - 1\right) \qquad \text{(d)}$$

From equation (4.2), the rotations can be expressed in the form,

$$\begin{Bmatrix} \theta \\ \phi \end{Bmatrix} = \left[N_2(s)\right] \left\{q^e(t)\right\} \tag{4.10}$$

$$\text{where } [N_2] = \begin{bmatrix} N_2(\theta) \\ N_2(\phi) \end{bmatrix} = \begin{bmatrix} 0 & -n_1' & n_3' & 0 & 0 & -n_2' & n_4' & 0 \\ n_1' & 0 & 0 & n_3' & n_2' & 0 & 0 & n_4' \end{bmatrix}$$

Hence N_1 and N_2 represent the translation and rotation shape functions respectively for the uniform shaft element.

For a point on the shaft located at a distance s from the fixed co-ordinate system, the elastic bending and kinetic energy expressions are as shown:

$$\text{Strain energy} = \frac{1}{2}\int_0^{\ell} \begin{Bmatrix} U'' \\ V'' \end{Bmatrix}^T \begin{bmatrix} EI_o & 0 \\ 0 & EI_o \end{bmatrix} \begin{Bmatrix} U'' \\ V'' \end{Bmatrix} ds \qquad (4.11)$$

$$\text{and Kinetic energy} = \frac{1}{2}\int_0^{\ell} \begin{Bmatrix} \dot{U} \\ \dot{V} \end{Bmatrix}^T \begin{bmatrix} \mu_1 & 0 \\ 0 & \mu_1 \end{bmatrix} \begin{Bmatrix} \dot{U} \\ \dot{V} \end{Bmatrix} ds +$$

$$+ \frac{1}{2}\int_0^{\ell} \begin{Bmatrix} \dot{\theta} \\ \dot{\phi} \end{Bmatrix}^T \begin{bmatrix} I_{ds} & 0 \\ 0 & I_{ds} \end{bmatrix} \begin{Bmatrix} \dot{\theta} \\ \dot{\phi} \end{Bmatrix} ds + \frac{1}{2} I_{ps} \dot{\psi}^2 ds$$

$$- I_{ps} \dot{\psi} \dot{\phi} \theta \, ds \qquad (4.12)$$

where EI_o is the bending rigidity of the shaft material.

The energy equation of the shaft element is obtained by integrating equations (4.11) and (4.12) over the length ℓ of the element to get,

$$\frac{1}{2}\{q^e\}^T[k_B^e]\{q^e\} + \frac{1}{2}\{\dot{q}^e\}^T[m_t^e] + [m_r^e]\{\dot{q}^e\}$$

$$+ \frac{1}{2} I_{ps}\dot{\phi}^2 - \dot{\phi}\{\dot{q}^e\}^T[g^e]\{q^e\} \qquad (4.13)$$

where $$[m_t^e] = \int_0^{\ell} m[N_1]^T[N_1]\,ds$$

$$[m_r^e] = \int_0^{\ell} I_{ds}[N_2]^T[N_2]\,ds$$

$$[g^e] = \int_0^{\ell} I_{ps}[N_2(\phi)]^T[N_2(\dot{\theta})]\,ds$$

$$[k_B^e] = \int_0^{\ell} EI_0[N_1"]^T[N_1"]\,ds$$

These individual matrices for the uniform cross section element are included in Appendix A and the axial load is maintained constant. The above mass and stiffness matrices are called consistant mass and stiffness matrices respectively.

Equation (4.13) has to be written with displacements expressed in the fixed frame XYZ in order to have a set of generalized co-ordinates as shown in Ref. [26].

4.4 Fluid Film Bearings

The rotor system is supported by fluid film bearings. The fluid film bearing forces can be equated to linearized film stiffness and damping co-efficients as shown.

$$[C]\{\dot{q}\} + [K]\{q\} = \{FB\} \qquad (4.14)$$

where $[C] = \begin{bmatrix} c_{zz}^{tt} & c_{zy}^{tt} \\ c_{yz}^{tt} & c_{yy}^{tt} \end{bmatrix}$ $[K] = \begin{bmatrix} k_{zz}^{tt} & k_{zy}^{tt} \\ k_{yz}^{tt} & k_{yy}^{tt} \end{bmatrix}$

$\{q\} = \begin{Bmatrix} U \\ V \end{Bmatrix}$ and F_B is the bearing film force.

The bearing properties are introduced at the appropriate bearing nodes.

4.5 Modal Co-ordinate Reduction

This reduction process is based on the "Multiple Component Mode Method" proposed by Masaaki Ookuma and A. Nagamatsu [33]. In this method, a structure is divided into few "first divided" components. Each first divided component is subdivided into some "second divided" ones. Repeating this process n times, the structure is divided into "n divided" components. The natural mode of (n-1)th divided component is analyzed using the natural modes of the n-th divided ones by the technique of ordinary component mode synthesis method. This is repeated for all other components and the vibration of a total structure is analyzed. However, the authors proposed this method for a general symmetric structure. Moreover, damping is not included in their approach.

The above method, when applied to a rotor-bearing system, simplifies the handling of large size matrices at the beginning of the process as compared to the method developed by Glasgow and Nelson [22]. Also, the size of the final system matrices are comparatively small.

Figure 4.3(a) shows the schematic diagram of a simple rotor-bearing system under consideration. This rotor has uniform circular

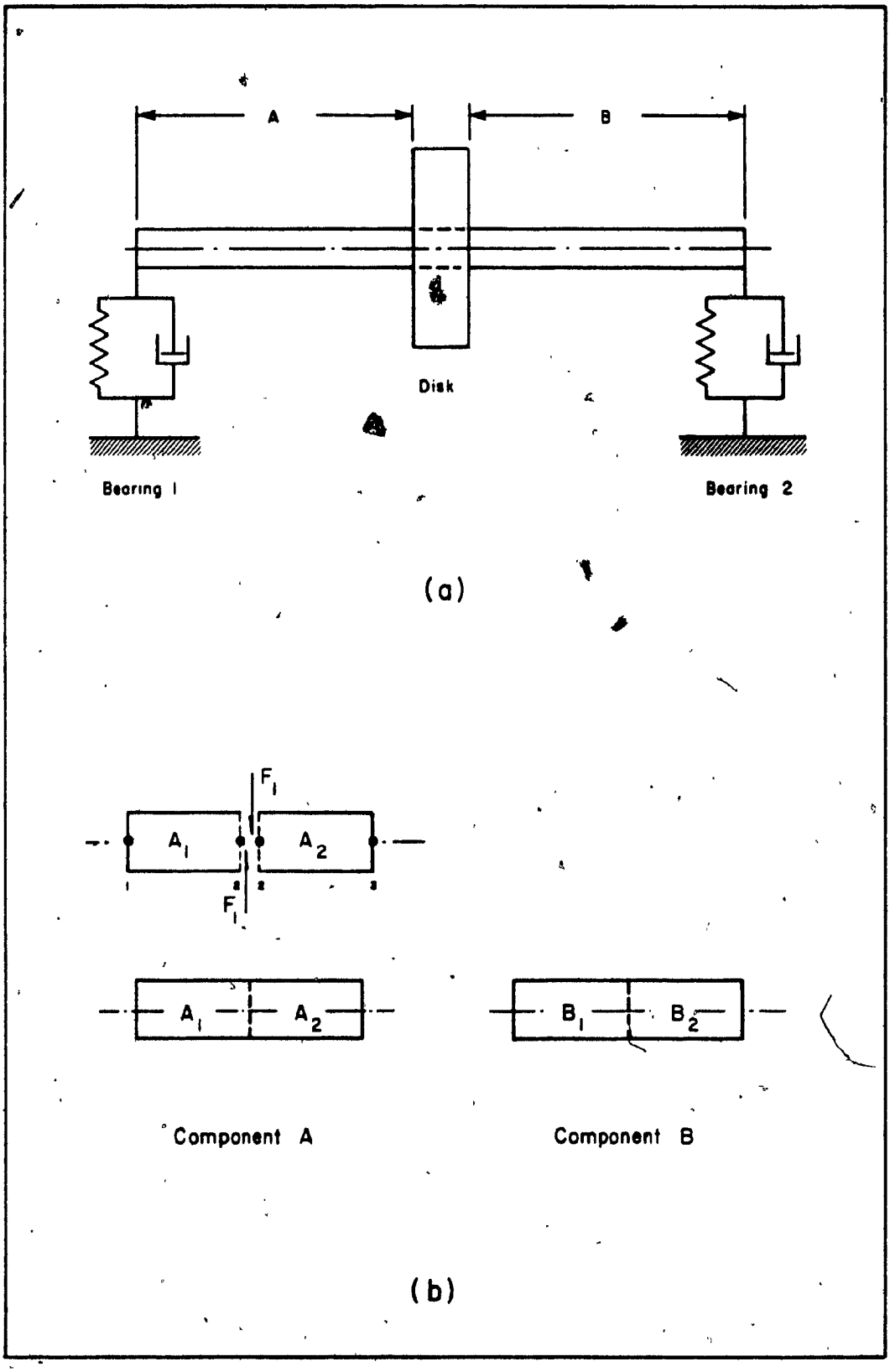

Figure 4.3 Component Discretization of a Single Rotor System.

shaft section with a rigid disk mounted at the centre. As explained before, this rotor system is discretized into two first divided components namely A and B. Then, these first divided components are again divided into two second divided components, namely A_1 and A_2 of component A and B_1 and B_2 of component B as shown in Fig. 4.3(b).

The component A is analyzed with the discretized segments A_1 and A_2 and this results in three nodal points with four degrees of freedom (two translations in XZ and XY planes and the corresponding rotations) at each node point. The interface node 2 is fixed and it is assumed that the modes at this interface point 2 is expressed as a linear combination of natural modes obtained by solving the equation for eigenvalue problem with the reduced mass and reduced stiffness matrices of component A_1 and component A_2.

For component A_1, the static displacement equation can be written as,

$$\begin{bmatrix} k_{11}^{A_1} & k_{12}^{A_1} \\ k_{21}^{A_1} & k_{22}^{A_1} \end{bmatrix} \begin{Bmatrix} q_1 \\ q_2 \end{Bmatrix} = \begin{Bmatrix} 0 \\ F_1 \end{Bmatrix} \tag{4.15}$$

$$q_1 = - [k_{11}^{A_1}]^{-1} [k_{12}^{A_1}] \{q_2\} = [T_1] \{q_2\} \tag{4.16}$$

The co-ordinates are reduced as shown,

$$\begin{Bmatrix} q_1 \\ q_2 \end{Bmatrix} = \begin{bmatrix} T_1 \\ I \end{bmatrix} \{q_2\} \tag{4.17}$$

where I is the identity square matrix.

Now, the mass and stiffness matrices of the component A_1 are reduced to the matrices of interface node 2 as shown below:

$$[m^{A_1}] = [T_1 \quad I] \begin{bmatrix} m_{11}^{A_1} & m_{12}^{A_1} \\ m_{21}^{A_1} & m_{22}^{A_1} \end{bmatrix} \begin{bmatrix} T_1 \\ I \end{bmatrix} \tag{4.18}$$

and

$$[k^{A_1}] = [T_1 \quad I] \begin{bmatrix} k_{11}^{A_1} & k_{12}^{A_1} \\ k_{21}^{A_1} & k_{22}^{A_1} \end{bmatrix} \begin{bmatrix} T_1 \\ I \end{bmatrix} \tag{4.19}$$

In the same way, the static displacement equation can be written for component A_2 as shown.

$$\begin{bmatrix} k_{22}^{A_2} & k_{23}^{A_2} \\ k_{32}^{A_2} & k_{33}^{A_2} \end{bmatrix} \begin{Bmatrix} q_2 \\ q_3 \end{Bmatrix} = \begin{Bmatrix} -F_1 \\ 0 \end{Bmatrix} \tag{4.20}$$

Again, reduced mass and stiffness matrices are written as,

$$[m^{A_2}] = [I \quad T_2] \begin{bmatrix} m_{22}^{A_2} & m_{23}^{A_2} \\ m_{32}^{A_2} & m_{33}^{A_2} \end{bmatrix} \begin{bmatrix} I \\ T_2 \end{bmatrix} \tag{4.21}$$

and

$$[k^{A_2}] = [I \quad T_2] \begin{bmatrix} k^{A_2}_{22} & k^{A_2}_{23} \\ k^{A_2}_{32} & k^{A_2}_{33} \end{bmatrix} \begin{bmatrix} I \\ T_2 \end{bmatrix} \tag{4.22}$$

where $T_2 = - [k_{33}]^{-1} [k_{32}]$.

Now, the natural modes $\{\Phi_2\}$ for the mid point 2 are obtained by solving the eigenvalue problem.

$$\left([k^{A_1} + k^{A_2}] - \omega_2^2 [m^{A_1} + m^{A_2}]\right) \{q_2\} = \{0\} \tag{4.23}$$

and hence $\{q_2\} = [\Phi_2] \{\eta_2\}$ (4.24)

The displacements of node points 1 and 3 are assumed to be expressed as a linear combination of constrained modes and the natural modes obtained by fixing node point 2.

Now, when the node 2 is fixed, the natural modes at point 1 can be obtained by solving,

$$\left[[k^{A_1}_{11}] - \omega_1^2 [m^{A_1}_{11}]\right] \{q_1\} = \{0\} \tag{4.25}$$

The modal matrix obtained by solving the eigenvalue problem of (4.25) is $[\Phi_1]$ and hence the displacement of point 1 is given by

$$\{q_1\} = [T_1] \{q_2\} + [\Phi_1] \{\eta_1\} \tag{4.26}$$

Substituting for $\{q_2\}$ from equation (4.24), equation (4.26) becomes,

$$\{q_1\} = [T_1]\,[\Phi_2]\,\{\eta_2\} + [\Phi_1]\,\{\eta_1\} \tag{4.27}$$

Similarly, the displacement at node point 3 can be expressed in the same way.

$$\{q_3\} = [T_2]\,[\Phi_2]\,\{\eta_2\} + [\Phi_3]\,\{\eta_3\} \tag{4.28}$$

The displacements at points 1, 2 and 3 can be written using equations (4.24), (4.26) and (4.28)

$$\begin{Bmatrix} \{q_1\} \\ \{q_2\} \\ \{q_3\} \end{Bmatrix} = \begin{bmatrix} \Phi_1 & T_1\Phi_2 & 0 \\ 0 & \Phi_2 & 0 \\ 0 & T_2\Phi_2 & \Phi_3 \end{bmatrix} \begin{Bmatrix} \eta_1 \\ \eta_2 \\ \eta_3 \end{Bmatrix} = [T_A] \begin{Bmatrix} \eta_1 \\ \eta_2 \\ \eta_3 \end{Bmatrix} \tag{4.29}$$

The equation of motion for component A is written as,

$$\left(\begin{bmatrix} k^{A_1}_{11} & k^{A_1}_{12} & 0 \\ k^{A_1}_{21} & (k^{A_1}_{22}+k^{A_2}_{22}) & k^{A_2}_{23} \\ 0 & k^{A_2}_{32} & k^{A_2}_{33} \end{bmatrix} - \omega^2 \begin{bmatrix} m^{A_1}_{11} & m^{A_1}_{12} & 0 \\ m^{A_1}_{21} & (m^{A_1}_{22}+m^{A_2}_{22}) & m^{A_2}_{23} \\ 0 & m^{A_2}_{32} & m^{A_2}_{33} \end{bmatrix} \right) \begin{Bmatrix} \{q_1\} \\ \{q_2\} \\ \{q_3\} \end{Bmatrix}$$

$$= \begin{Bmatrix} 0 \\ 0 \\ f_1 \end{Bmatrix} \tag{4.30}$$

Substituting equation (4.29) into equation (4.30) and premultiplying the resulting matrices by $[T_A]^T$, the homogenous form of equation can be written as,

$$\left([T_A]^T \begin{bmatrix} k^{A_1}_{11} & k^{A_1}_{12} & 0 \\ k^{A_1}_{21} & (k^{A_1}_{22}+k^{A_2}_{22}) & k^{A_2}_{23} \\ 0 & k^{A_2}_{32} & k^{A_2}_{33} \end{bmatrix} [T_A] - \omega^2 [T_A]^T \times \right.$$

$$\left. \times \begin{bmatrix} m^{A_1}_{11} & m^{A_1}_{12} & 0 \\ m^{A_1}_{21} & (m^{A_1}_{22} + m^{A_2}_{22}) & m^{A_2}_{23} \\ 0 & m^{A_2}_{32} & m^{A_2}_{33} \end{bmatrix} [T_A] \right) \begin{Bmatrix} \eta_1 \\ \eta_2 \\ \eta_3 \end{Bmatrix} = \{0\} \quad (4.31)$$

The natural modes $[\Phi_A]$ are obtained by solving the eigenvalue problem of equation (4.31). The component degrees of freedom can be reduced by truncating the number of modes due to higher frequencies of the system with little effect on the important lower modes of the system.

With truncation of modes in mind, the modes $[\Phi_A]$ can be written as one consisting of retained modes $[\Phi_{AR}]$ and truncated modes $[\Phi_{AT}]$ as shown:

$$[\Phi_A] = [\Phi_{AR} \quad \Phi_{AT}] \quad (4.32)$$

Hence, the displacement vector is written in terms of truncated modes of component A.

$$\begin{Bmatrix} \{q_1\} \\ \{q_2\} \\ \{q_3\} \end{Bmatrix} = [T_A]_{NXR}\ [\Phi_{AR}]_{RX1} \tag{4.33}$$

where N are the no. of nodes and R, the no. of retained nodes.

Similarly, the component B can be analyzed and the corresponding displacement vector is written as,

$$\begin{Bmatrix} \{q_3\} \\ \{q_4\} \\ \{q_5\} \end{Bmatrix} = [T_B]_{NXR}\ [\Phi_{BR}]_{RX1} \tag{4.34}$$

where

$$[T_B] = \begin{bmatrix} \Phi_3 & T_3\Phi_4 & 0 \\ 0 & \Phi_4 & 0 \\ 0 & T_4\Phi_4 & \Phi_5 \end{bmatrix}$$

$$T_3 = -\ [k_{33}{}^{B_1}]^{-1}\ \ [k_{34}{}^{B_1}]$$

and $T_4 = -\ [k_{55}{}^{B_2}]^{-1}\ \ [k_{54}{}^{B_2}]$.

Modes Φ_3, Φ_4 and Φ_5 are obtained in the same manner as those of Φ_1, Φ_2 and Φ_3.

Displacements for component A and component B are assembled to get the overall displacement of the structure.

$$\begin{Bmatrix} \{q_1\} \\ \{q_2\} \\ \{q_3\} \\ \{q_4\} \\ \{q_5\} \end{Bmatrix} = \left[\begin{array}{c} \overset{R}{\overbrace{}} \\ \left.\begin{array}{|c|} \hline \\ T_A \\ \\ \hline \end{array}\right\}N \\ \\ \left.\begin{array}{|c|} \hline \\ T_B \\ \\ \hline \end{array}\right\}R \\ \underbrace{}_{R} \end{array}\right]_{(2N-1)\times(2R-1)} \{\Phi_R\}_{(2R-1)\times 1} \tag{4.35}$$

The elements of the matrix in the hatched area, are divided by 2, because the displacement at the node point 3 is added twice while assembling the transformation matrices of component A and component B.

In general, equation (4.35) can be written as,

$$\{q\} = [\nabla]_{(2N-1)\times(2R-1)} \{\Phi_R\} \tag{4.36}$$

The total structural matrices are obtained by assembling the stiffness and mass matrices and force vectors of component A which are available in equation (4.30) and the corresponding matrices of component B. The resulting overall mass and stiffness matrices are $[M_{all}]$ and $[K_{all}]$ respectively. The structure's generalized coordinates are obtained as,

$$[\nabla]^T[M_{all}]\ [\nabla]\{\ddot{\eta}\} + [\nabla]^T[K_{all}][\nabla]\{\eta\} = [\nabla]^T\{F\} \tag{4.37}$$

where the size of $[M_{all}]$ and $[K_{all}]$ are (2N-1)x(2N-1).

The rigid disk properties are included at the appropriate nodal points of the mass matrix $[M_{all}]$. By solving the homogenous part of equation (4.37), the natural mode matrix of the system $[\Phi_{all}]$ is obtained and it is of the size (2R-1)x(2R-1).

Equation (4.37) can be transformed in the physical co-ordinate system by multiplying by $[\Phi_{all}]^{-1}$ as shown:

$$\left([\nabla]^T[M_{all}][\nabla]\right)[\Phi_{all}]^{-1}\{\ddot{q}\} + \left([\nabla]^T[K_{all}][\nabla]\right)[\Phi_{all}]^{-1}\{q\} = [\nabla]^T\{F\} \tag{4.38}$$

Now, the fluid film damping matrix is included and the equation of motion of the structure can be written as shown:

$$[M]\{q\} + [C]\{\dot{q}\} + [K]\{q\} = [\nabla]^T\{F\} \tag{4.39}$$

where

$$[M] = [\nabla]^T[M_{all}][\nabla][\Phi_{all}]^{-1}$$

$$[K] = [\nabla]^T[K_{all}][\nabla][\Phi_{all}]^{-1} + [K_{film}]$$

$[K_{film}]$ is fluid film stiffness matrix

and $[C]$ contains the damping properties of the system.

Equation (4.39) is a nonsymmetric second order equation of size (2R-1)x(2R-1). The solution of these equations using modal analysis method was already discussed in Chapter 3. The reduction depends upon the number of modes to be retained.

For the single disk rotor system supported on hydrodynamic bearings at the two ends, the overall system matrix is of size 20x20. Using, the reduction procedure, this has been reduced to the size of 12x12

which is sufficient since the first few modes of the system are of interest.

Three different configurations of the rotor system are considered for the response analysis using the finite element method with reduction procedure developed before.

4.5.1 Rotor with Equal Bearing Clearances ($c_1=c_2$ = 0.0000533m)

The rotor details are given as shown in Table 2.1 for a single disk rotor supported on hydrodynamic bearings at the two ends. Since, the rotor system is a simple one, the discrete model approximates the real system very closely. Consequently, the response obtained using this discrete model is close enough to the actual response of the system. Hence, it is reasonable to compare this response with the one obtained using the finite element model. Accordingly, Fig. 4.4 shows a comparative plot of normalized response of the rotor against the rotational speed. A good agreement is observed in the response and the critical speeds as well.

4.5.2 Rotor with Equal Bearing Clearances ($c_1=c_2$ = 0.000188)

The same rotor details as above are used with different bearing clearance values to determine the normalized response of the rotor system. Here, the response shows double peaks corresponding to the split first critical speeds of the rotor system. Again, a good correlation is seen between the responses obtained using two different system models. This is shown in Fig. 4.5.

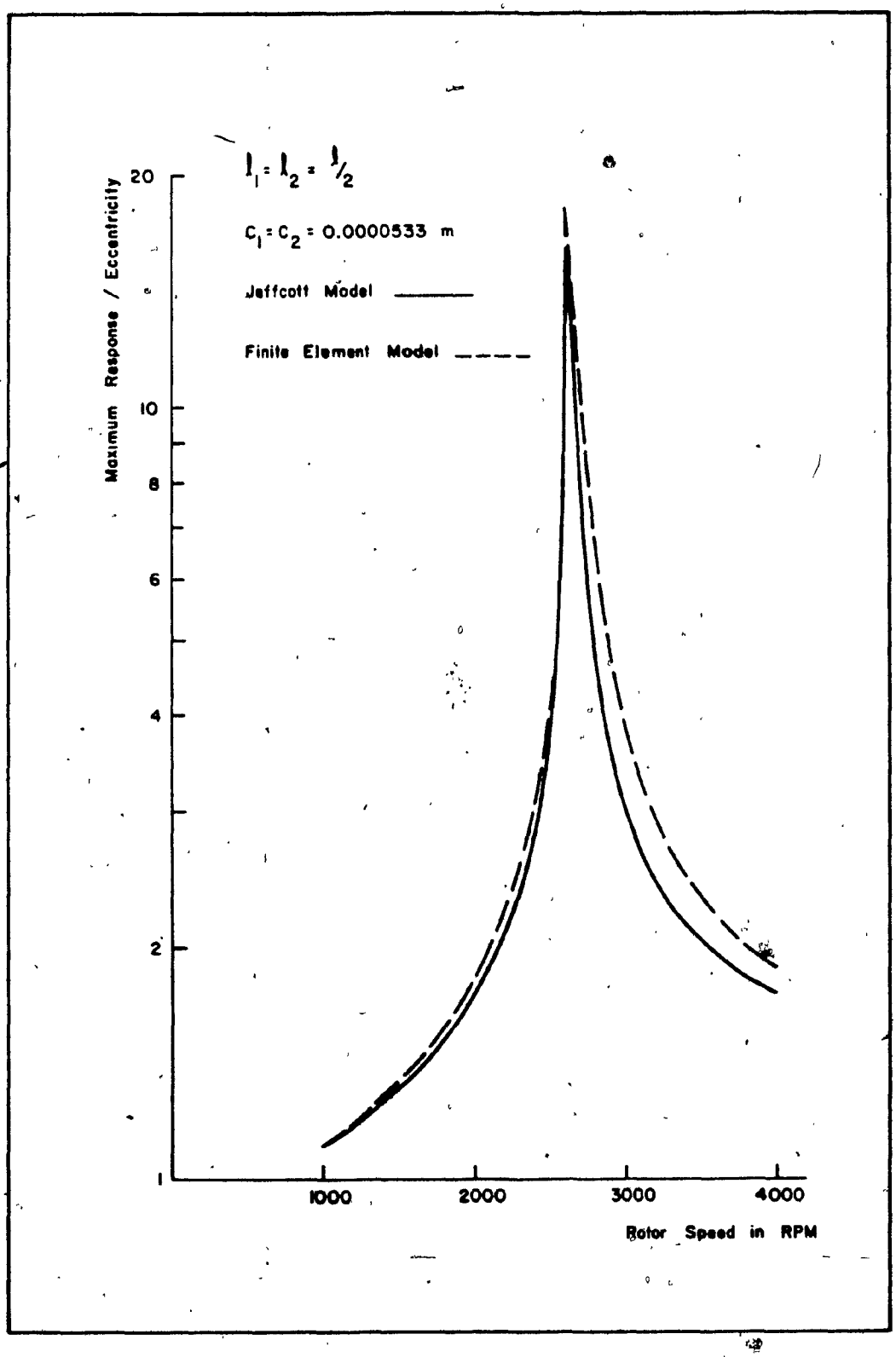

Figure 4.4 Unbalance Response Plots of a Single Disk Rotor.

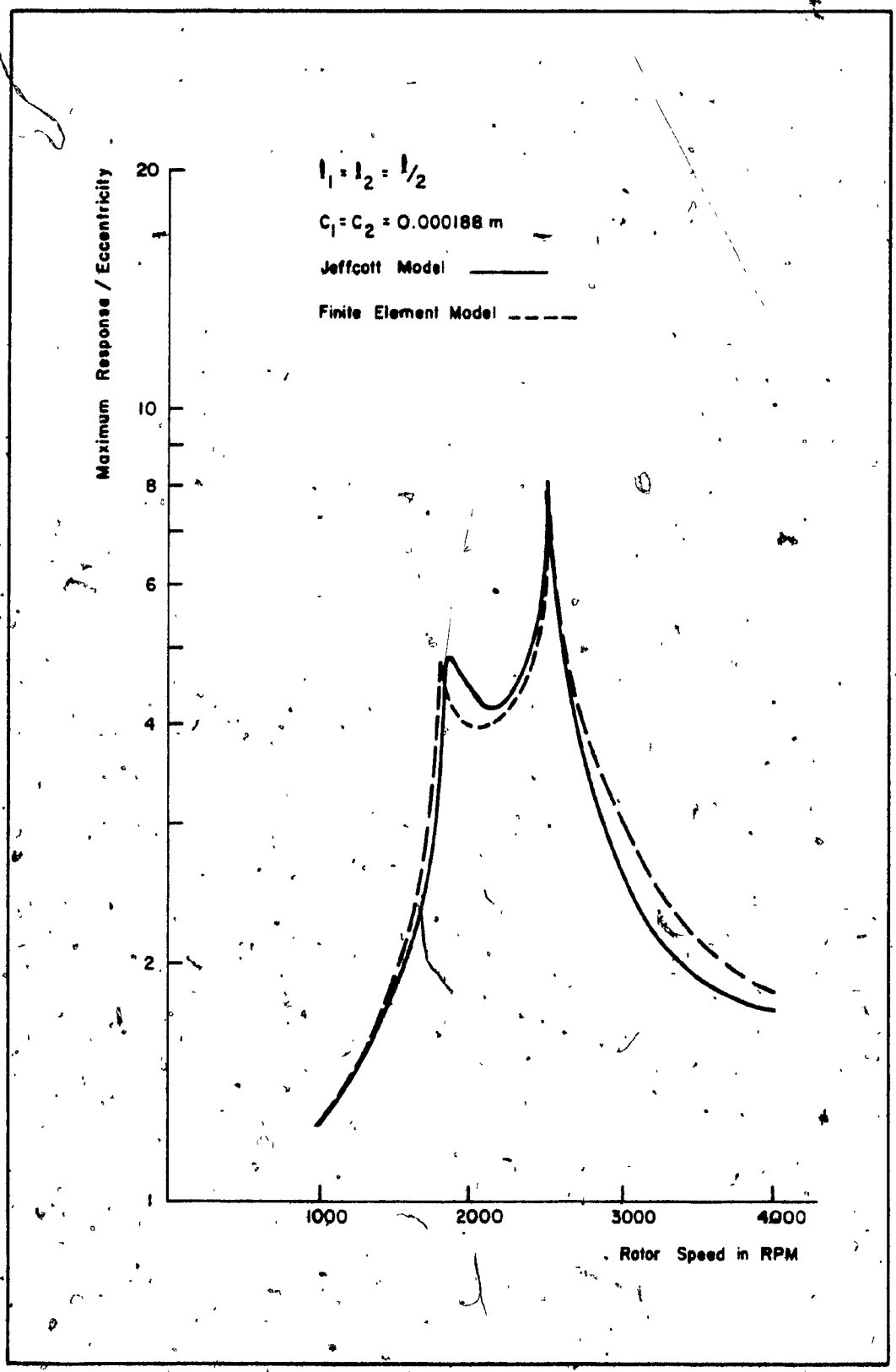

Figure 4.5 Unbalance Response Plots of a Single Disk Rotor.

Figure 4.6 shows the comparative response plots of the same rotor supported on dissimilar hydrodynamic bearings. Here, the bearing clearance values are different at each end, i.e. c_1 = 0.0000533m and c_2 = 0.000188m. Again double peak response corresponding to the split first criticals is obtained.

In general, it is found that the finite element model provides comparatively good results with those obtained using a Jeffcott model. However, using a finer mesh of the rotor system, it is possible to achieve responses which are closer to the results of the real system.

4.6 Stability Analysis

The instability of a rotor system supported on plain cylindrical bearings is a self-excited vibration attributed mainly to the different oil film properties in Z and Y directions and also the asymmetric cross-coupled film properties along the two directions. This instability in rotors is totally independent of any external forces. Rotor instability condition could occur in a given fluid film bearing design, when a threshold speed condition exists, beyond which the orbital path of the journal becomes unstable and the orbit grows in time.

A simple analysis developed by Rao [47] and Reiger [48] is discussed here and based on the analysis, the threshold speed of a simple rotor is determined. Since the translatory first critical speed is of interest, it is convenient to consider an equivalent rotor as shown in Fig. 4.7. The shaft carries two discs M each separated by a distance $\xi\ell$ symmetrically with the centre. For translatory whirl, ξ becomes 1, and the equations of motion of the rotor can be written along two directions as,

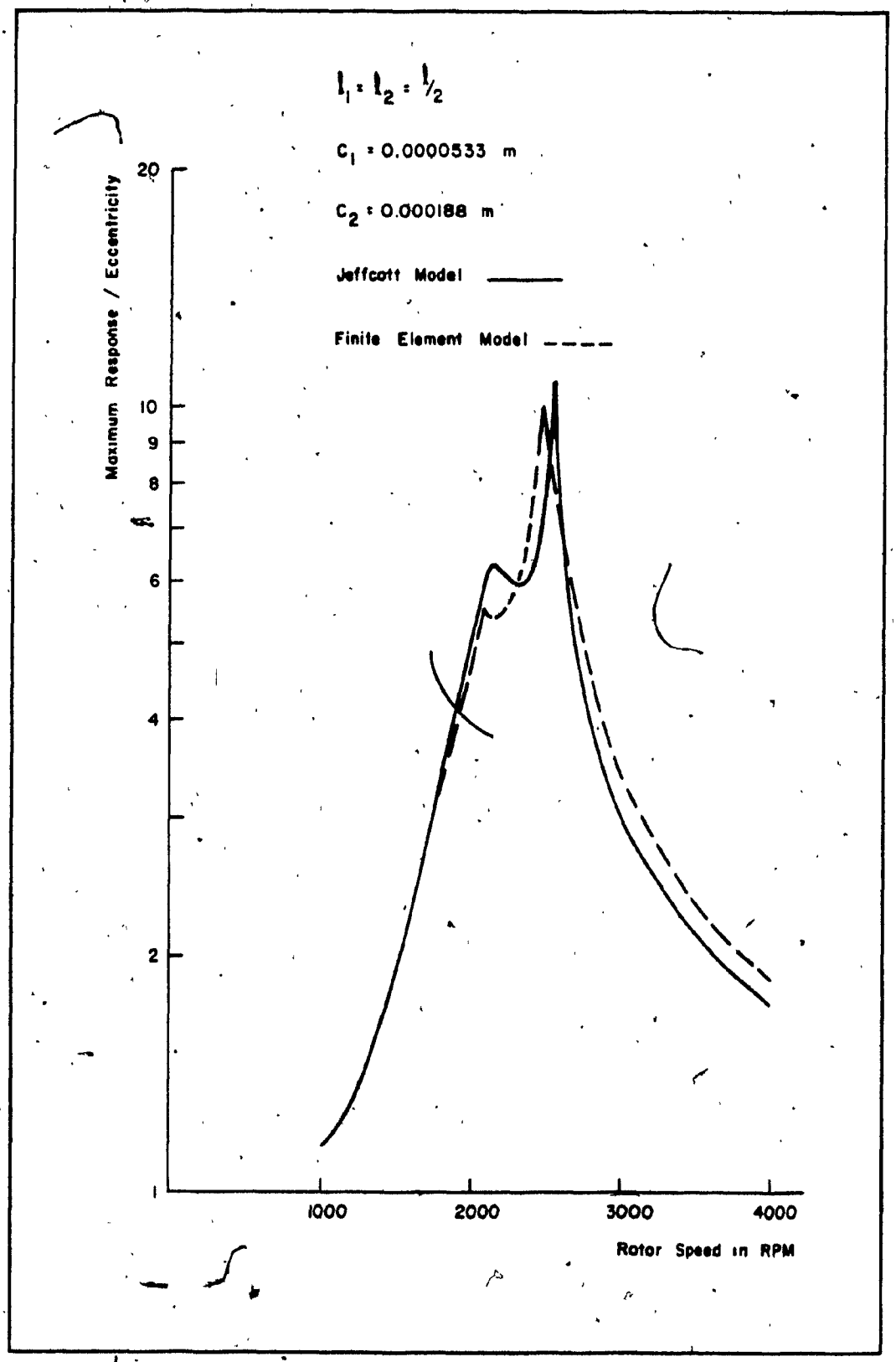

Figure 4.6 Unbalance Response Plots of a Single Disk Rotor.

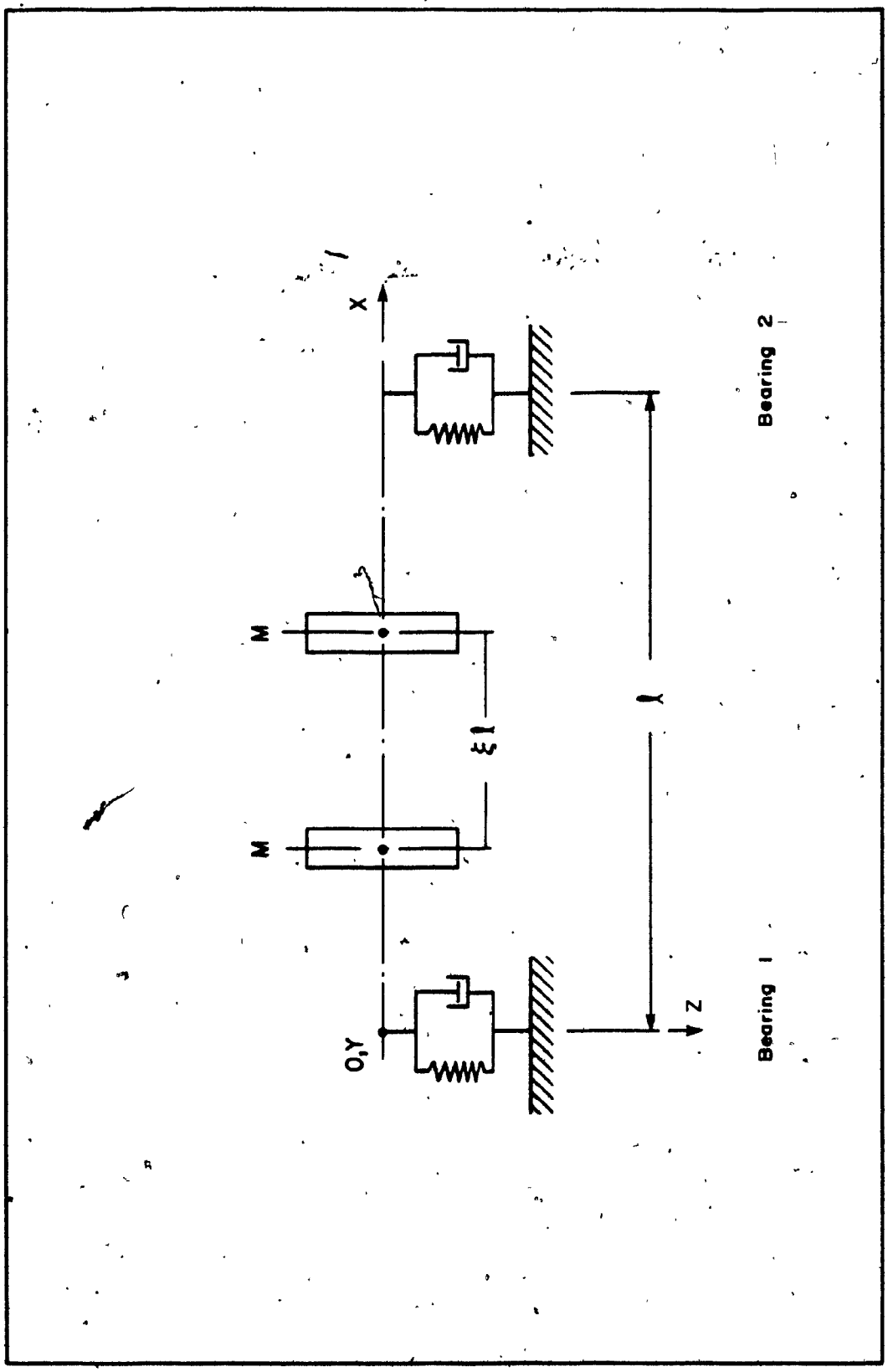

Figure 4.7 Flexible Rotor on Oil Film Bearings.

$$K(Z_1 - Z) = - M \ddot{Z}_1$$

$$K(Y_1 - Y) = - M \ddot{Y}_1 \qquad (4.40)$$

where K is the stiffness of the rotor.

For a whirl frequency ν

$$Z_1 = Z_1 e^{j\nu t} \qquad Z = Z e^{j\nu t}$$

$$Y_1 = Y_1 e^{j\nu t} \qquad Y = Y e^{j\nu t} \qquad (4.41)$$

Substitution of equation (4.43) in equation (4.42) leads,

$$Z_1 = \frac{Z}{1 - \frac{\nu^2}{2\omega_c^2}}$$

and

$$Y_1 = \frac{Y}{1 - \frac{\nu^2}{2\omega_c^2}} \qquad (4.42)$$

where $\omega_c^2 = \frac{K}{2M}$ and ω_c corresponds to the rigid bearing critical speed of the rotor.

Now, considering the force balance at bearings for translatory whirl gives,

$$K(Z_1-Z) = k_{zz}^{tt} \cdot Z + k_{zy}^{tt} \cdot Y + c_{zz}^{tt} \cdot \dot{Z} + c_{zy}^{tt} \cdot \dot{Y}$$

$$\text{and} \quad K(Y_1-Y) = k_{yy}^{tt} \cdot Y + k_{yz}^{tt} \cdot Z + c_{yy}^{tt} \cdot \dot{Y} + c_{yz}^{tt} \cdot \dot{Z} \qquad (4.43)$$

Substituting for Z_1 and Y_1 from equations (4.41) and (4.42) provides,

$$KZ\left(\frac{1}{1-\frac{\nu^2}{2\omega_c^2}}-1\right) = k_{zz}^{tt}\cdot Z + k_{zy}^{tt}\cdot Y + c_{zz}^{tt}\cdot \dot{Z} + c_{zy}^{tt}\cdot \dot{Y} \tag{4.44}$$

and

$$KY\left(\frac{1}{1-\frac{\nu^2}{2\omega_c^2}}-1\right) = k_{yy}^{tt}\cdot Y + k_{yz}^{tt}\cdot Z + c_{yy}^{tt}\cdot \dot{Y} + c_{yz}^{tt}\cdot \dot{Z}$$

Multiplying both sides of equations (4.44) by $\frac{c}{W}$, we get,

$$\frac{c}{W}KZ\left(\frac{\frac{1}{2}\frac{\nu^2}{\omega_c^2}}{1-\frac{1}{2}\frac{\nu^2}{\omega_c^2}}\right) = \bar{k}_{zz}Z + \bar{k}_{zy}Y + \frac{c}{W}\omega c_{zz}^{tt}\frac{j\nu}{\omega} + \frac{c}{W}\omega\, c_{zy}^{tt}\, j\,\frac{\nu}{\omega} \tag{4.45}$$

$$\frac{c}{W}KY\left(\frac{\frac{1}{2}\frac{\nu^2}{\omega_c^2}}{1-\frac{1}{2}\frac{\nu^2}{\omega_c^2}}\right) = \bar{k}_{yy}Y + \bar{k}_{yz}Z + \frac{c}{W}\omega\, c_{yy}^{tt}\frac{j\nu}{\omega} + \frac{c}{W}\omega\, c_{zy}^{tt}\, j\,\frac{\nu}{\omega}$$

where c = radial clearance of bearing

W = load on each bearing

$\bar{k}_{zz}^{tt}$, $\bar{k}_{zy}^{tt}$, $\bar{k}_{yz}^{tt}$ and $\bar{k}_{yy}^{tt}$ are nondimensional fluid film stiffness co-efficients

and ω speed of rotation.

Equations (4.45) can be rewritten as,

$$\chi Z = \bar{k}_{zz} \cdot Z + \bar{k}_{zy} \cdot Y + j\, \bar{c}_{zz} \Delta + j\, \bar{c}_{zy}\, \Delta$$

$$\chi Y = \bar{k}_{yy} \cdot Y + \bar{k}_{yz} \cdot Z + j\, \bar{c}_{yy} \Delta + j\, \bar{c}_{yz} \Delta \qquad (4.46)$$

where $\chi = \frac{c}{W} K \left(\frac{\frac{1}{2} \frac{\nu^2}{\omega_c^2}}{1 - \frac{1}{2} \frac{\nu^2}{\omega_c^2}} \right)$

$$\bar{c}_{zz} = \frac{c}{W} \omega\, c_{zz}^{tt}$$

$$\bar{c}_{yy} = \frac{c}{W} \omega\, c_{yy}^{tt}$$

$$\bar{c}_{yz} = \frac{c}{W} \omega\, c_{yz}^{tt}$$

$$\bar{c}_{zy} = \frac{c}{W} \omega\, c_{zy}^{tt}$$

and $\Delta = \frac{\nu}{\omega} = \frac{\text{frequency of whirl}}{\text{frequency of rotation}}$

Equations (4.46) can be written in the matrix form as,

$$\begin{bmatrix} (\bar{k}_{zz} - \chi + j\, \Delta\, \bar{c}_{zz}) & (\bar{k}_{zy} + j\, \Delta\, \bar{c}_{zy}) \\ (\bar{k}_{yz} + j\, \Delta\, \bar{c}_{yz}) & (\bar{k}_{yy} - \chi + j\, \Delta\, \bar{c}_{yy}) \end{bmatrix} \begin{Bmatrix} Z \\ Y \end{Bmatrix} = 0 \qquad (4.47)$$

The determinant of equation (4.47) above is required for the stability analysis. Hence equating the real and imaginary products of the characteristic equation to zero, provides the following conditions to determine instability threshold.

$$\frac{(\bar{k}_{zz} \cdot \bar{c}_{yy} + \bar{k}_{yy} \cdot \bar{c}_{zz}) - (\bar{c}_{zy} \cdot \bar{k}_{yz} + \bar{c}_{yz} \cdot \bar{k}_{zy})}{\bar{c}_{zz} + \bar{c}_{yy}} = \chi \qquad (4.48)$$

and

$$\frac{(\bar{k}_{zz} - \chi)(\bar{k}_{yy} - \chi) - \bar{k}_{zy} \cdot \bar{k}_{yz}}{\bar{c}_{zz} \cdot \bar{c}_{yy} - \bar{c}_{yz} \cdot \bar{c}_{zy}} = \vartheta^2 \qquad (4.49)$$

These expressions contain the whirl threshold rotational speed ω and the whirl frequency ν as unknowns and can be solved assuming a rotor speed ω. The corresponding bearing co-efficients are then obtained for the speed ω. Substituting these values in equation (4.48), the value of χ is obtained and then equation (4.49) can be used to solve for the whirl frequency ν. This method is continued until the calculated values for ω and ν agree with their assumed values. The guide line to achieve the convergence is given by,

$$0.45\ \omega < \nu < 0.5\ \omega$$

Based on the procedure discussed above, the threshold speed of instability for a single disk rotor supported on hydrodynamic bearings at the two ends with bearing clearance values of 0.000188m, is found to be at a rotor speed of 5000 RPM which agrees closely with the threshold instability speed of 4950 RPM determined earlier using modal analysis in Chapter 3.

4.7 Conclusions

Since a simple Jeffcott model of a rotor system is not sufficient to represent large rotors, a finite element method is used to model the rotor-bearing systems. In that, the shaft mass and stiffnesses are represented by means of the consistent formulation by Archer [84]. The model includes the effects of rotatory inertia, gyroscopic moments only. The effects of shear deformation, axial torque are not included. However, these effects can be included as shown by N. Özgüven and Z.L. Ozkan [85] for any general rotor system.

The overall system matrices are reduced using a modal reduction method based on the component mode synthesis procedure. The resulting reduced system equations are solved to obtain the critical speeds and unbalance response of the simple rotor system using modal analysis. The dynamic responses of the simple rotor system obtained using a discrete Jeffcott model, are compared with those obtained using the finite element model and a good qualitative agreement is seen. The threshold speed of instability of the rotor system for one configuration is obtained using the instability analysis developed by Rao [47] and Reiger [48].

In this Chapter, the fluid film bearing is modeled using linearized translational film properties only. However, when the shaft span is large, the inclined journal also produces rotational film properties. Hence, a comprehensive bearing model which includes both translational and rotational film properties, will be developed in the next Chapter.

CHAPTER 5

FLUID FILM PROPERTIES DUE TO MISALIGNED JOURNAL IN FINITE CYLINDRICAL BEARING

In previous chapters, different modelling and solution procedures were discussed to obtain the dynamic responses of a simple rotor-bearing system, assuming aligned shaft conditions in the bearings. Aligned journal conditions provide only force stiffness and damping co-efficients in the hydrodynamic bearings. When the rotor shaft is flexible or when the support span is large, journal tilt at the bearings is inevitable. Under such circumstances, it is highly essential to include the moment stiffness and damping co-efficients due to inclination of the journal at the bearings. This leads to an improved model of the rotor system by including the rotational springs and dampers together with the translational springs and dampers at the bearing supports. Consequently, in this chapter, Reynolds equation which governs the pressure in fluid flow is solved using a simple approach to evaluate the collinear and cross-coupled translational and rotational fluid film co-efficients for small perturbations around the mean position of the journal for a finite bearing model. Later, these co-efficients obtained through a finite bearing theory are compared with the corresponding co-efficients obtained using a short bearing approximation.

5.1 Analysis

In an oil film bearing, a convergent shape in the direction of motion draws the fluid adhering to the moving surface into the narrowing clearance space, and builds up a pressure sufficient to carry the load. Thus, the hydrodynamic pressure forces are generated in the fluid

film between the bearing and the journal surfaces. In the mathematical sense, the study of this hydrodynamic lubrication is the evaluation of the hydrodynamic pressure equation known as Reynolds equation. This Reynolds equation is derived from the Navier-Stokes equations as a particular form of the equation which relates velocity, film thickness, pressure and relative motion characteristics of the two surfaces. The basic assumptions involved in deriving such Reynolds equation are:

(i) The flow is laminar.

(ii) The effects of the curvature of the film are negligible; in other words, the radius of curvature of the moving surfaces is large as compared to the film thickness.

(iii) The variation of pressure across the film and also the rate of change of any one velocity component along the film are small and hence they are negligible.

(iv) The cross-section of the journal remains circular.

Based on these assumptions, the pressure equation for the incompressible fluid film can be written as,

$$\frac{1}{R^2}\frac{\partial}{\partial\bar{\beta}}\left(\frac{h^3}{12\Omega}\frac{\partial p}{\partial\bar{\beta}}\right)+\frac{\partial}{\partial x}\left(\frac{h^3}{12\Omega}\frac{\partial p}{\partial x}\right)=\frac{1}{2}\omega\frac{\partial h}{\partial\bar{\beta}}+\frac{\partial h}{\partial t}$$

where $\bar{\beta} = (\beta_1 + \beta_2)$, β_1 is the attitude angle of the journal, h is the film thickness at a point determined by $\bar{\beta}$ and x; $\bar{\beta}$ are measured from the vertical load line as shown in Fig. 5.1 and x is measured along the journal axis.

Since a rotor always has a certain amount of unbalance, the journal develops an additional forced vibration around the static point of

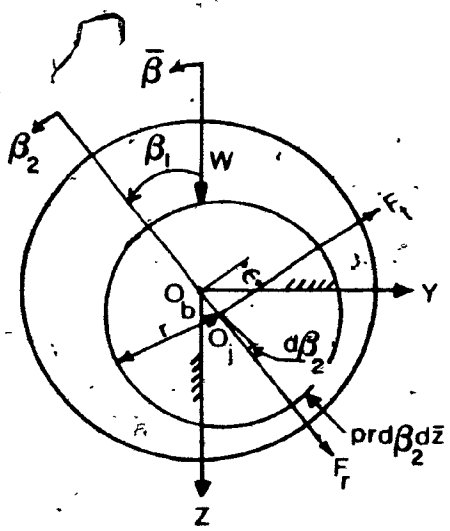

Figure 5.1 Cross section of the Journal.

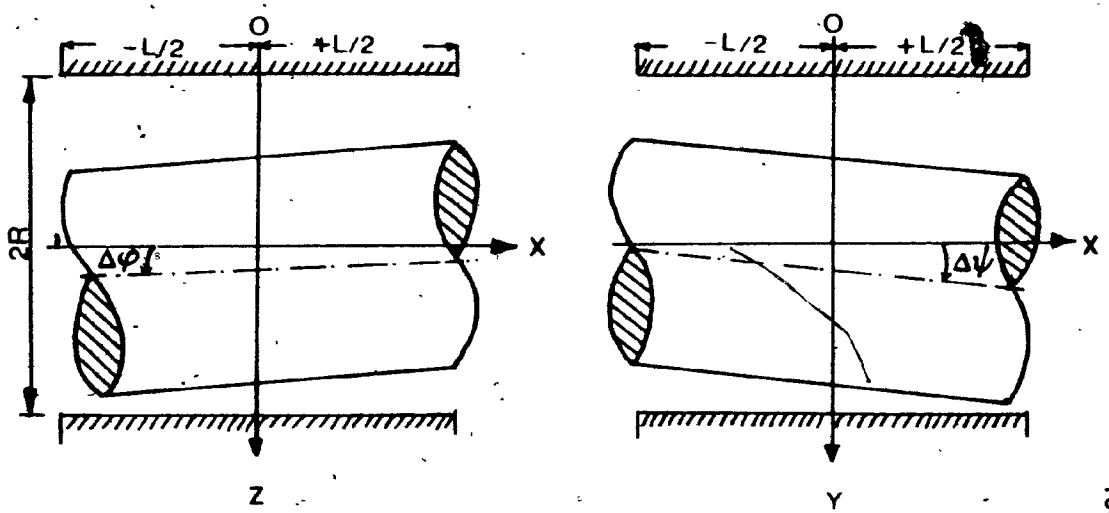

Figure 5.2 Inclined Journal in Bearing.

equilibrium due to the translational motion of the journal along Z and Y axes. In addition to this translational motion of the journal, the bending of the journal introduces a finite slope at the bearing location and the resulting inclination of the journal is shown in Fig. 5.2. Under this tilted configuration of the journal, if a load W acts vertically down at the midplane, there will be an axial couple of magnitude Wx at any point x along the bearing axis in the ZX plane. Also, there will be a twisting couple acting in the horizontal YX plane. Therefore, under dynamic conditions, the journal center motion can be described by the mutually perpendicular translations Δz and Δy, and the corresponding rotations $\Delta\Psi$ and $\Delta\varphi$ around the Z and Y axes respectively, such that the film thickness becomes,

$$h = h_0 + \Delta z \cos\bar{\beta} + \Delta y \sin\bar{\beta} + (x\cdot\Delta\varphi) \cos\bar{\beta} - (x\cdot\Delta\Psi) \sin\bar{\beta} \qquad (5.2)$$

where $h_0 = c + e\cos\beta_2$ and $\beta_2 = (\bar{\beta} - \beta_T)$

For small perturbations around the static equilibrium position of the journal, where a linear analysis is permissible, a first order expression of the pressure gives:

$$p = p_0 + p_z\cdot\Delta z + p_y\cdot\Delta y + p_{\dot{z}}\cdot\Delta\dot{z} + p_{\dot{y}}\cdot\Delta\dot{y} +$$

$$+ q_z\cdot\Delta\varphi \quad q_y\cdot\Delta\Psi + q_{\dot{z}}\cdot\Delta\dot{\varphi} + q_{\dot{y}}\cdot\Delta\dot{\Psi} \qquad (5.3)$$

where p_0 is the mean pressure under static equilibrium conditions and p_z, p_y, $p_{\dot{z}}$, $p_{\dot{y}}$, q_z, q_y, $q_{\dot{z}}$ and $q_{\dot{y}}$ are the perturbed pressures.

Substituting equations (5.2) and (5.3) in equation (5.1) and neglecting higher order terms in Δz, Δy, $\Delta\varphi$ and $\Delta\Psi$ and their products of displacements and velocities, nine equations are obtained. These nine

equations together with their non-dimensional conversions are shown in Appendix A. The final form of nine non-dimensional equations are as shown below:

$$\frac{\partial}{\partial\bar{\beta}}\left\{H_o^3\frac{\partial\bar{p}_o}{\partial\bar{\beta}}\right\}+\left(\frac{D}{L}\right)^2\frac{\partial}{\partial\bar{x}}\left\{H_o^3\frac{\partial\bar{p}_o}{\partial\bar{x}}\right\}=12\pi\frac{\partial H_o}{\partial\bar{\beta}} \tag{5.4}$$

$$\frac{\partial}{\partial\bar{\beta}}\left\{H_o^3\frac{\partial\bar{p}_z}{\partial\bar{\beta}}\right\}+\left(\frac{D}{L}\right)^2\frac{\partial}{\partial\bar{x}}\left\{H_o^3\frac{\partial\bar{p}_z}{\partial\bar{x}}\right\}=-12\pi\left(\sin\bar{\beta}+3\frac{\cos\bar{\beta}}{H_o}\frac{\partial H_o}{\partial\bar{\beta}}\right)$$

$$-3H_o^3\frac{\partial}{\partial\bar{\beta}}\left(\frac{\cos\bar{\beta}}{H_o}\right)\frac{\partial\bar{p}_o}{\partial\bar{\beta}} \tag{5.5}$$

$$\frac{\partial}{\partial\bar{\beta}}\left\{H_o^3\frac{\partial\bar{p}_y}{\partial\bar{\beta}}\right\}+\left(\frac{D}{L}\right)^2\frac{\partial}{\partial\bar{x}}\left\{H_o^3\frac{\partial\bar{p}_y}{\partial\bar{x}}\right\}=12\pi\left(\cos\bar{\beta}-\frac{3\sin\bar{\beta}}{H_o}\frac{\partial H_o}{\partial\bar{\beta}}\right)$$

$$-3H_o^3\frac{\partial}{\partial\bar{\beta}}\left(\frac{\sin\bar{\beta}}{H_o}\right)\frac{\partial\bar{p}_o}{\partial\bar{\beta}} \tag{5.6}$$

$$\frac{\partial}{\partial\bar{\beta}}\left\{H_o^3\frac{\partial\bar{p}_z^{\cdot}}{\partial\bar{\beta}}\right\}+\left(\frac{D}{L}\right)^2\frac{\partial}{\partial\bar{x}}\left\{H_o^3\frac{\partial\bar{p}_z^{\cdot}}{\partial\bar{x}}\right\}=12\cos\bar{\beta} \tag{5.7}$$

$$\frac{\partial}{\partial\bar{\beta}}\left\{H_o^3\frac{\partial\bar{p}_y^{\cdot}}{\partial\bar{\beta}}\right\}+\left(\frac{D}{L}\right)^2\frac{\partial}{\partial\bar{x}}\left\{H_o^3\frac{\partial\bar{p}_y^{\cdot}}{\partial\bar{x}}\right\}=12\sin\bar{\beta} \tag{5.8}$$

$$\frac{\partial}{\partial\bar{\beta}}\left\{H_o^3\frac{\partial\bar{q}_z}{\partial\bar{\beta}}\right\}+\left(\frac{D}{L}\right)^2\frac{\partial}{\partial\bar{x}}\left\{H_o^3\frac{\partial\bar{q}_z}{\partial\bar{x}}\right\}=-6\pi\bar{x}\left(\sin\bar{\beta}+3\frac{\cos\bar{\beta}}{H_o}\frac{\partial H_o}{\partial\bar{\beta}}\right)$$

$$-1.5\,H_o^3\left\{\left(\frac{D}{L}\right)^2\frac{\cos\bar{\beta}}{H_o}\frac{\partial\bar{p}_o}{\partial\bar{x}}+\bar{x}\frac{\partial}{\partial\bar{\beta}}\left(\frac{\cos\bar{\beta}}{H_o}\right)\frac{\partial\bar{p}_o}{\partial\bar{\beta}}\right\} \tag{5.9}$$

$$\frac{\partial}{\partial\bar{\beta}}\left\{H_o^3\ \frac{\partial\bar{q}_y}{\partial\bar{\beta}}\right\}+\left(\frac{D}{L}\right)^2\ \frac{\partial}{\partial\bar{x}}\left\{H_o^3\ \frac{\partial\bar{q}_y}{\partial\bar{x}}\right\}=6\pi\bar{x}\left(-\cos\bar{\beta}+\frac{3\sin\bar{\beta}}{H_o}\ \frac{\partial H_o}{\partial\bar{\beta}}\right)$$

$$-1.5\ H_o^3\left\{\left(\frac{D}{L}\right)^2\ \frac{\sin\bar{\beta}}{H_o}\ \frac{\partial\bar{p}_o}{\partial\bar{x}}+\bar{x}\ \frac{\partial}{\partial\bar{\beta}}\ \left(\frac{\sin\bar{\beta}}{H_o}\right)\frac{\partial\bar{p}_o}{\partial\bar{\beta}}\right\} \qquad (5.10)$$

$$\frac{\partial}{\partial\bar{\beta}}\left\{H_o^3\ \frac{\partial\bar{q}_z}{\partial\bar{\beta}}\right\}+\left(\frac{D}{L}\right)^2\ \frac{\partial}{\partial\bar{x}}\left\{H_o^3\ \frac{\partial\bar{q}_z}{\partial\bar{x}}\right\}=6\,\bar{x}\,\cos\bar{\beta} \qquad (5.11)$$

$$\frac{\partial}{\partial\bar{\beta}}\left\{H_o^3\ \frac{\partial\bar{q}_y}{\partial\bar{\beta}}\right\}+\left(\frac{D}{L}\right)^2\ \frac{\partial}{\partial\bar{x}}\left\{H_o^3\ \frac{\partial\bar{q}_y}{\partial\bar{x}}\right\}=-6\,\bar{x}\,\sin\bar{\beta} \qquad (5.12)$$

5.2 Finite Difference Method:

The nine differential equations shown above are evaluated numerically using a finite difference formulation. A grid mesh is developed as described by Pinkus [55] with finite number of intersection points r and s (r varies from 1 to 10 and s varies from 1 to 30 in the grid) varying along the dependant variable $\bar{x}$ and $\bar{\beta}$ directions respectively. With the grid network shown in Fig. 5.3, the nine Reynolds equations can be written in the finite difference form. Here, one differential equation corresponding to static mean pressure is shown in the finite difference form and the remaining eight equations can be formulated in a similar manner.

$$\frac{H_{o_{r,s+\frac{1}{2}}}\ \dfrac{\bar{p}_{o_{r,s+1}}-\bar{p}_{o_{r,s}}}{\Delta\bar{\beta}}-H_{o_{r,s-\frac{1}{2}}}\ \dfrac{\bar{p}_{o_{r,s}}-\bar{p}_{o_{r,s-1}}}{\Delta\bar{\beta}}}{\Delta\bar{\beta}}$$

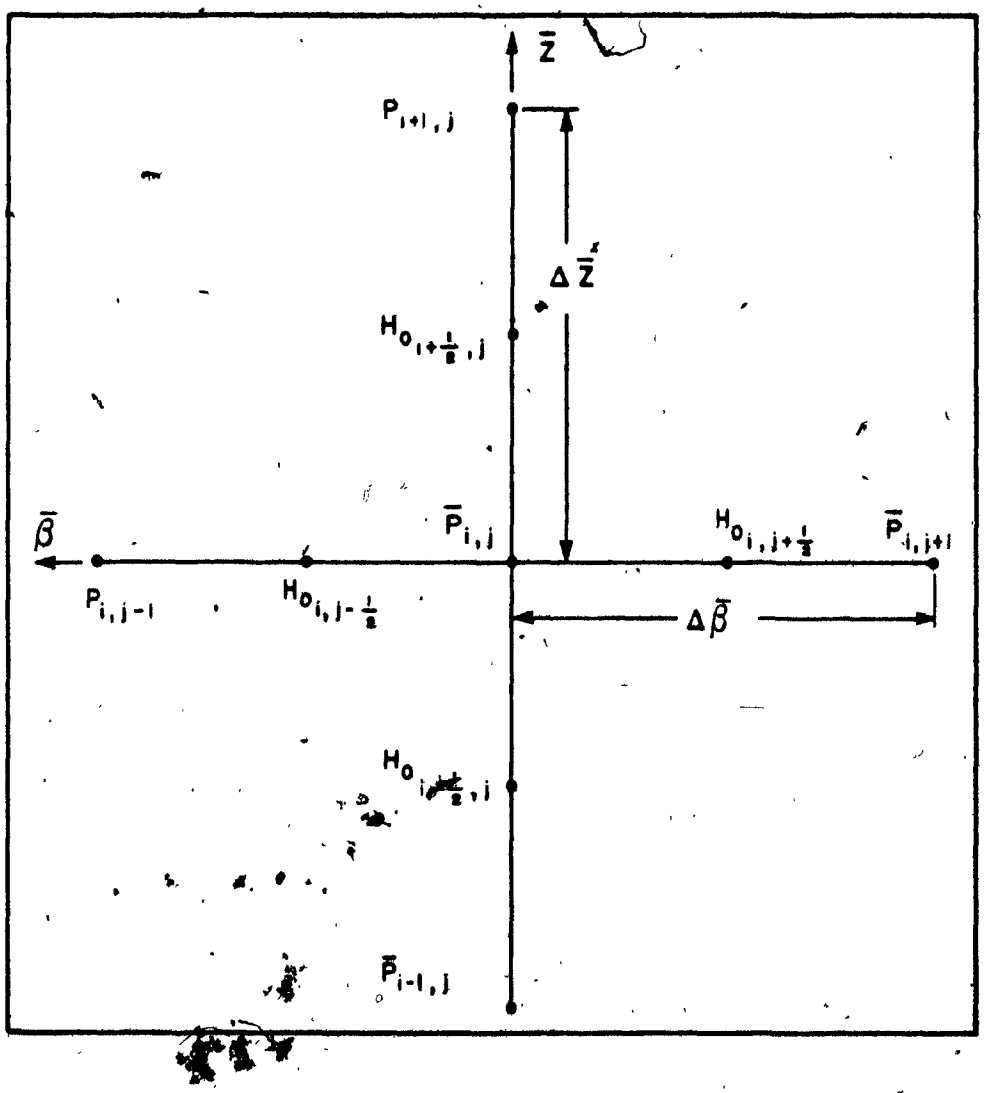

Figure 5.3 Finite Difference Grid Mesh.

$$+\left(\frac{D}{L}\right)^2 \frac{H_{o_{r+\frac{1}{2},s}}\left(\frac{p_{o_{r+1,s}} - p_{o_{r,s}}}{\Delta\bar{x}}\right) - H_{o_{r-\frac{1}{2},s}}\left(\frac{\bar{p}_{o_{r,s}} - \bar{p}_{o_{r-1,s}}}{\Delta\bar{x}}\right)}{\Delta\bar{x}}$$

$$= 12\pi \left\{ \frac{H_{o_{r,s+\frac{1}{2}}} - H_{o_{r,s-\frac{1}{2}}}}{\Delta\bar{\beta}} \right\} \qquad (5.13)$$

In solving these nine equations, it is observed that the left hand side of the equations remain the same and hence need not be repeated, whereas the right hand side equations need to be changed each time to determine the different pressures.

5.3 Boundary Conditions

The boundary conditions required to solve the resulting nine finite difference equations (5.4 through 5.12) are as follows.

$$\left.\begin{aligned} &\text{At } x = \pm \frac{L}{2}, \quad p = 0 \\ &\text{At } \theta = 0 \text{ and } 2\pi, \quad p = 0 \\ &\text{ie } \quad p_o = p_z = p_y = p_z^{\cdot} = p_y^{\cdot} = q_z = q_y = q_z^{\cdot} = q_y^{\cdot} = 0 \end{aligned}\right\} \qquad (5.14)$$

Using the above boundary conditions, the nine equations are solved by the "column method" [63]. Since this technique is found more economical in terms of savings in computer effort, this is preferred over other methods, such as relaxation methods. Moreover, the influences of the neighbouring columns are not multiplied out until all boundary conditions are satisfied.

5.4 Column Method

The general form of numerical approximation to the finite difference equation is represented in matrix form as follows:

$$[E_i'](p_i) + [G_i'](p_{i-1}) + [D_i'](p_{i+1}) = \{J_i\} \tag{5.15}$$

where i represents n number of columns in $\bar{\beta}$ direction, (n is 30 in the present work) $\{p_i\}$ is vector of i-th column of unknown pressures and $[E_i']$, $[G_i']$ and $[D_i']$ are m x m matrices of co-efficients (m is 10 in the present work). m is the number of rows of elements in $\bar{x}$ direction and $\{J_i\}$ is vector of i-th column of right hand side elements.

Since the above equations do not involve higher order terms in the present work, the matrices [G'] and [D'] are diagonal whereas [E'] is tridiagonal. Equation (5.15) is applicable to regular field points as well as points defining boundaries and recesses. The boundary points are specified by $p = p_{boundary}$, which can be considered a particular form of a row of equation (5.15). Then equation (5.15) can be solved by relations of the type

$$\{p_{i-1}\} = [A_i'](p_i) + \{B_i\} \tag{5.16}$$

Substituting equation (5.16) into equation (5.15) and solving for $\{p_i\}$ we obtain,

$$\{p_i\} = -\left[[E_i'] + [G_i'][A_i']\right]^{-1} [D_i'](p_{i+1}\}$$

$$+\left[[E_i'] + [G_i'][A_i']\right]^{-1} \{J_i\} - [G_i'](B_i\} \tag{5.17}$$

Comparing equation (5.16) and (5.17), the recurrence relations for matrix [A'] and vector {B} are obtained as follows:

$$[A'_{i+1}] = - [I_i] [D'_i] \tag{5.18}$$

$$\{B_{i+1}\} = [I_i]\{J_i\} - [G'_i]\{B_i\} \tag{5.19}$$

where $[I_i] = \left[[E'_i] + [G'_i][A'_i]\right]^{-1}$

If the boundary values of p are known on column n, equation (5.16) is used recursively for i = n, n-1, ..., 2. At the end of this process, all values of p have been determined.

Using the column method, the nine finite difference equations are evaluated numerically. Initially, the static pressure p_0 is calculated which is used in all subsequent equations to evaluate other pressure values. In doing so, any subambient pressure value is set equal to zero before proceeding to calculate the next pressure value.

5.5 Static Load-Displacements

When all the pressure values are obtained by solving each finite difference equation, they are integrated over the film domain to get the oil film forces and moments. For a given bearing, the dynamic force F of the oil film is a function of displacements (ε,β_1) and velocities $(\dot{\varepsilon},\dot{\beta}_1)$ and therefore $F = F(\varepsilon,\beta_1,\dot{\varepsilon},\dot{\beta}_1)$. Since the linear analysis is valid close to the static equilibrium of the journal, the nondimensional force $\bar{F}$ can be split up into static component $\bar{F}_0$ and dynamic component $\Delta\bar{F}_0$. Because the rotor shaft is flexible, the tilt of the journal at the bearings is inevitable. Therefore, in this work, fluid film properties arising out of moment due to rotations are considered together with the force film stiffness and damping co-efficients. The reaction forces and moments of the bearing are expressed in terms of journal deflections

Δz, Δy, $\Delta\varphi$, $\Delta\Psi$ and their velocities both along Z and Y directions and they consist of terms due to static and dynamic forces and moments as shown.

$$F_Z = F_{zo} + \left\{k_{zz}^{tt}\,\Delta z + k_{zy}^{tt}\,\Delta y + k_{zz}^{tr}\,\Delta\varphi + k_{zy}^{tr}\,\Delta\Psi + c_{zz}^{tt}\,\Delta\dot{z} + c_{zy}^{tt}\,\Delta\dot{y} + c_{zz}^{tr}\,\Delta\dot{\varphi} + c_{zy}^{tr}\,\Delta\dot{\Psi}\right\} \tag{5.20}$$

$$F_Y = F_{yo} + \left\{k_{yz}^{tt}\,\Delta z + k_{yy}^{tt}\,\Delta y + k_{yz}^{tr}\,\Delta\varphi + k_{yy}^{tr}\,\Delta\Psi + c_{yz}^{tt}\,\Delta\dot{z} + c_{yy}^{tt}\,\Delta\dot{y} + c_{yz}^{tr}\,\Delta\dot{\varphi} + c_{yy}^{tr}\,\Delta\dot{\Psi}\right\} \tag{5.21}$$

$$M_Z = M_{zo} + \left\{k_{zz}^{rr}\,\Delta\varphi + k_{zy}^{rr}\,\Delta\Psi + k_{zz}^{rt}\,\Delta z + k_{zy}^{rt}\,\Delta y + c_{zz}^{rr}\,\Delta\dot{\varphi} + c_{zy}^{rr}\,\Delta\dot{\Psi} + c_{zz}^{rt}\,\Delta\dot{z} + c_{zy}^{rt}\,\Delta\dot{y}\right\} \tag{5.22}$$

$$M_Y = M_{yo} + \left\{k_{yz}^{rr}\,\Delta\varphi + k_{yy}^{rr}\,\Delta\Psi + k_{yz}^{rt}\,\Delta z + k_{yy}^{rt}\,\Delta y + c_{yz}^{rr}\,\Delta\dot{\varphi} + c_{yy}^{rr}\,\Delta\dot{\Psi} + c_{yz}^{rt}\,\Delta\dot{z} + c_{yy}^{rt}\,\Delta\dot{y}\right\} \tag{5.23}$$

In the equations (5.20) through (5.23), the terms inside the double brackets are due to dynamic forces or moments. These forces and moments of the bearing can be evaluated as follows:

$$\left.\begin{aligned} F_Z &= -\int_0^{2\pi}\int_{-L/2}^{L/2} R\,p\,\sin\bar{\beta}\,d\bar{\beta}\,dx \\ F_Y &= -\int_0^{2\pi}\int_{-L/2}^{L/2} R\,p\,\cos\bar{\beta}\,d\bar{\beta}\,dx \end{aligned}\right\} \tag{5.24}$$

$$\left.\begin{aligned} M_Y &= -\int_0^{2\pi}\int_{-L/2}^{L/2} R\, p\, x \cos\bar{\beta}\, d\bar{\beta}\, dx \\ M_Z &= -\int_0^{2\pi}\int_{-L/2}^{L/2} R\, p\, x \sin\bar{\beta}\, d\bar{\beta}\, dx \end{aligned}\right\} \qquad (5.25)$$

Under static equilibrium condition of the journal, i.e. when $p = p_o$, the vertical reaction force F_{zo} becomes equal to W, the static load at the bearing whereas F_{yo} is zero. The corresponding attitude angle ϕ for this static position is determined.

When $p = p_o$

$$\left.\begin{aligned} F_{zo} = W &= -\int_0^{2\pi}\int_{-L/2}^{L/2} p_o \cos\bar{\beta}\, R\, d\bar{\beta}\, dx \\ \text{and} \qquad & \\ F_{yo} &= 0 \end{aligned}\right\} \qquad (5.26)$$

The nondimensional form of equation (5.26) is as follows:

$$\bar{F}_{zo} = \frac{F_{zo}}{\Omega N D L \left(\frac{R}{c}\right)^2} = -\frac{1}{4}\int_0^{2\pi}\int_{-L/2}^{L/2} \bar{p}_o \cos\bar{\beta}\, d\bar{\beta}\, d\bar{x} \qquad (5.27)$$

where $\bar{p}_o = \dfrac{p_o}{\Omega N \left(\frac{R}{c}\right)^2}$

Instead of the magnitude of the force F_{zo} or the vertical load W, a nondimensional parameter called Sommerfeld number S, is used and S is defined as,

$$S = \frac{\Omega N D L}{W}\left(\frac{R}{c}\right)^2 \qquad (5.28)$$

From this definition, it is apparent that F_{zo} or W is proportional to 1/S. When the static operating conditions change, the center point of the journal moves along the static curve of equilibrium. For the circular cylindrical bearing, this has an approximately semi-circular shape. The calculated β_1 values for different clearance ratios for the various static equilibrium of the circular-cylindrical bearing are plotted as shown in Fig. 5.4. This theoretical static equilibrium curve has been compared with the similar curves obtained by Someya [86] and Sassenfeld-Walther [87] and also compared with the measured bearing static equilibrium curve by Glienicke [38] and Kollmann and Glienicke [88]. They all show a very good agreement with the present work.

Now, it is clear that the bearing characteristics β_1 and ε are functions of W. Figure 5.5 shows one of the journal-bearing characteristics under steady operating conditions. Here, the quantity S which is proportional to W is plotted against ε. The relationship between ε and S, based on outlet oil film temperature obtained experimentally by Morton [89] is also shown in Fig. 5.5. Other useful contributions of fluid film dynamic properties are by Prabhu and Rao [90], Prabhu [91] and Hagg and Sankey [92]. The theoretical results show a very good correlation with the experiments. This gives a good starting point to proceed further and evaluate the fluid film co-efficients. Knowing the static position (β_1) of the journal in the bearing for different eccentricity values ε, the perturbed forces and moments are evaluated by simply replacing p in equations (5.24) and (5.25) with perturbed pressures p_z, p_y, etc. and the fluid film force and moment stiffness and damping values are determined. One set of translational and rotational stiffness co-efficients evaluated in nondimensional form are

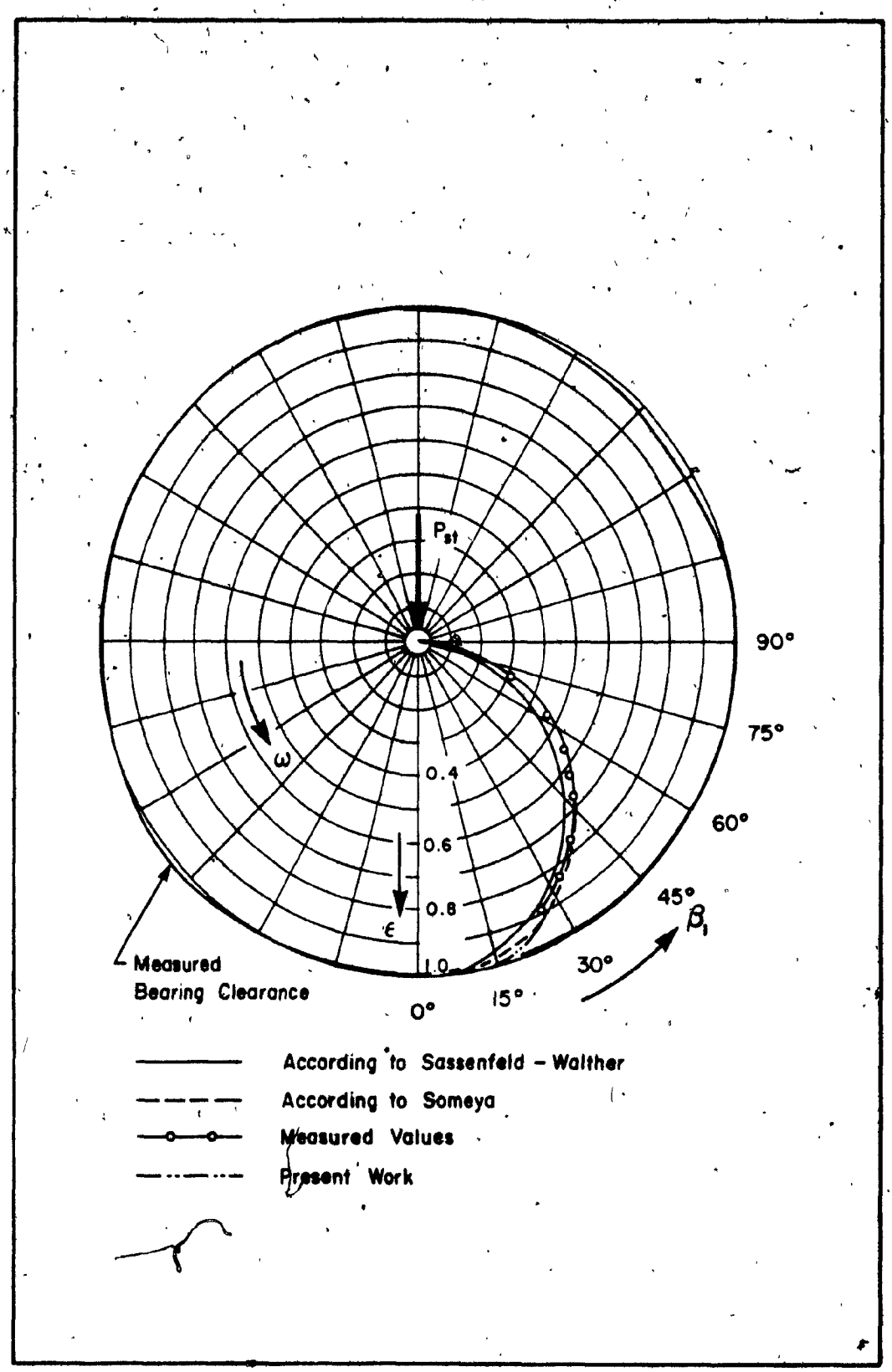

Figure 5.4 Measured Bearing Clearance and static Equilibrium Curves of the Circular – Cylindrical Bearing : Comparison with Theoretical values.

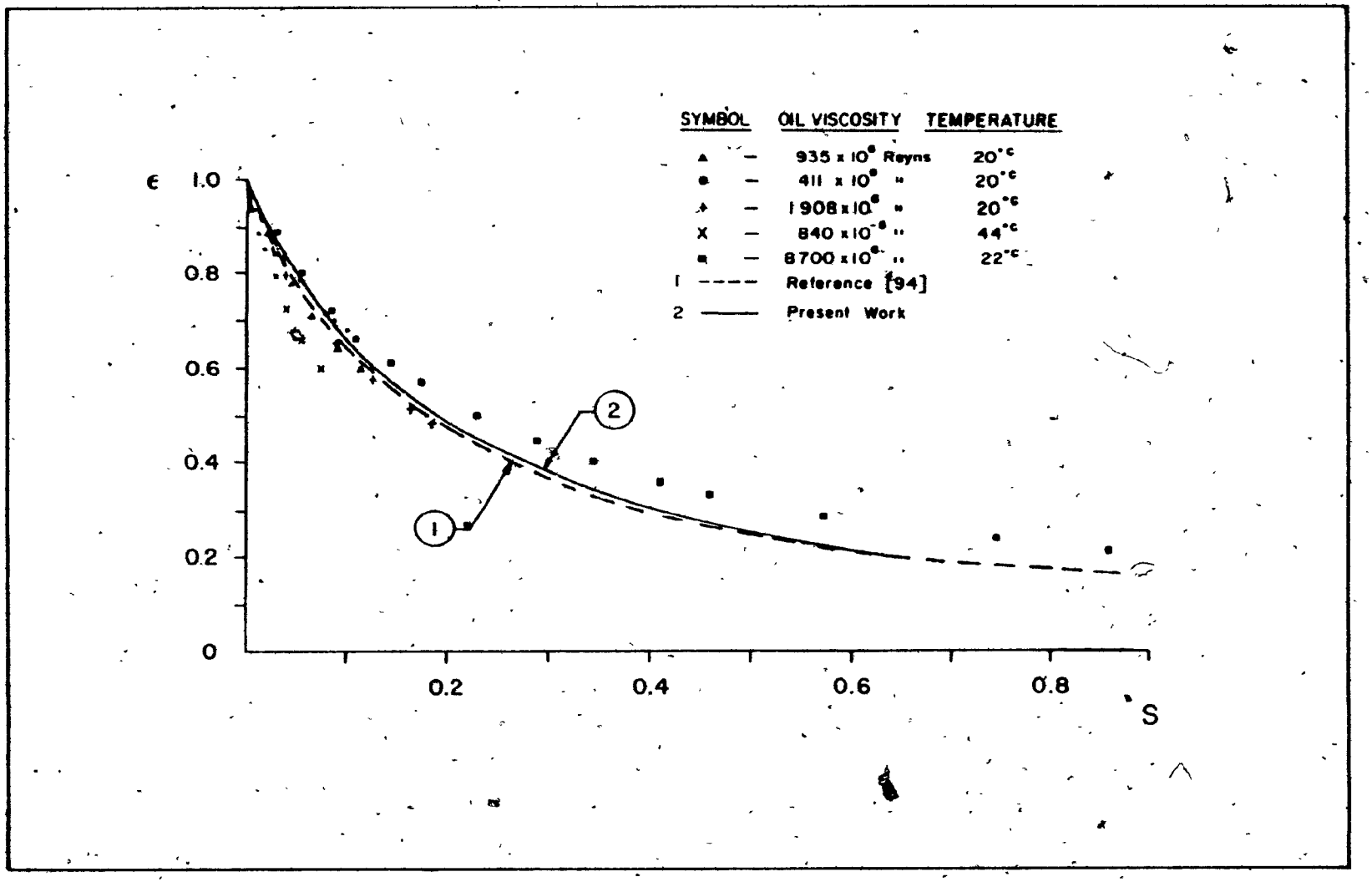

Figure 5.5 Relationship Between Sommerfeld Number and Eccentricity Ratio (for 4" Dia. Bearing).

as shown below:

$$\left.\begin{aligned} \bar{k}^{tt}_{zz} &= \frac{c \cdot k^{tt}_{zz}}{\Omega N D L \frac{R}{c}^2} = -\frac{1}{4} \int_0^{2\pi} \int_{-1}^{1} \bar{p}_z \cos\bar{\beta}\, d\bar{\beta}\, d\bar{x} \\ \bar{k}^{tt}_{yz} &= \frac{c \cdot k^{rr}_{yz}}{\Omega N D L \frac{R}{c}^2} = -\frac{1}{4} \int_0^{2\pi} \int_{-1}^{1} \bar{p}_y \sin\bar{\beta}\, d\bar{\beta}\, d\bar{x} \end{aligned}\right\} \quad (5.29)$$

$$\left.\begin{aligned} \bar{k}^{rr}_{zy} &= \frac{c \cdot k^{rr}_{zy}}{\Omega N D L \frac{R}{c}^2 L^2} = -\frac{1}{8} \int_0^{2\pi} \int_{-1}^{1} \bar{q}_z \bar{x} \cos\bar{\beta}\, d\bar{\beta}\, d\bar{x} \\ \bar{k}^{rr}_{zz} &= \frac{c \cdot k^{rr}_{zz}}{\Omega N D L \frac{R}{c}^2 L^2} = -\frac{1}{8} \int_0^{2\pi} \int_{-1}^{1} \bar{q}_y \bar{x} \sin\bar{\beta}\, d\bar{\beta}\, d\bar{x} \end{aligned}\right\} \quad (5.30)$$

where equations (5.29) and (5.30) represent the translational and rotational oil film co-efficients respectively. The remaining 28 co-efficients are also determined in a similar manner.

5.6 Fluid-Film Dynamic Co-efficients

The Reynolds equations derived earlier, for the finite cylindrical bearings are modelled as grid mesh points, with the dependent variables $\bar{\beta}$ and $\bar{x}$ represented by finite number of points, located at the intersections of the grid and they are solved by the column method to get the pressure field. This pressure field is integrated over the entire film domain and the fluid film reaction forces and moments of these forces are obtained.

The nondimensional form of translational fluid film stiffness, and damping co-efficients that were obtained from the fluid film reaction forces, for a finite cylindrical bearing are compared with the respective fluid film co-efficients, evaluated through the short bearing approximation

by Kikuchi [14], and through the finite bearing method by Lund [49,93]. Also these fluid film translational co-efficients are compared with the corresponding co-efficients obtained experimentally by Morton [89]. The rotational fluid film co-efficients obtained in the present work are compared with those evaluated through short bearing theory by Kikuchi [14] and with the rotational fluid film co-efficients obtained for finite bearings using Fedor's proportionality hypothesis by Mukherjee and Rao [59]. Also, these co-efficients are compared with those obtained by Capriz [60] using finite bearing theory.

The nondimensional, translational fluid film co-efficients are shown in Figs. 5.6 through 5.9 along with those of [14,49]. It is found that there is a good qualitative agreement between the collinear and cross-coupled translational fluid film co-efficients obtained in the present work and the corresponding film co-efficients obtained by [14,49]. It will be meaningful to compare these fluid film co-efficients with those obtained by experiments. Therefore, a comparison is made with the translational co-efficients obtained experimentally for a 4" diameter oil film bearing with different oil viscosities and temperatures by Morton [89]. Also, the translational film co-efficients are compared with those obtained by Smith [94]. The plots are shown in Figs. 5.10 and 5.11. An excellent correlation of the co-efficients are seen with those obtained by experiments and also with those obtained by Smith. In general, the stiffness and damping co-efficients obtained by Lund [49] are lower than the co-efficients obtained in the present work.

The rotational fluid film stiffness and damping co-efficients of

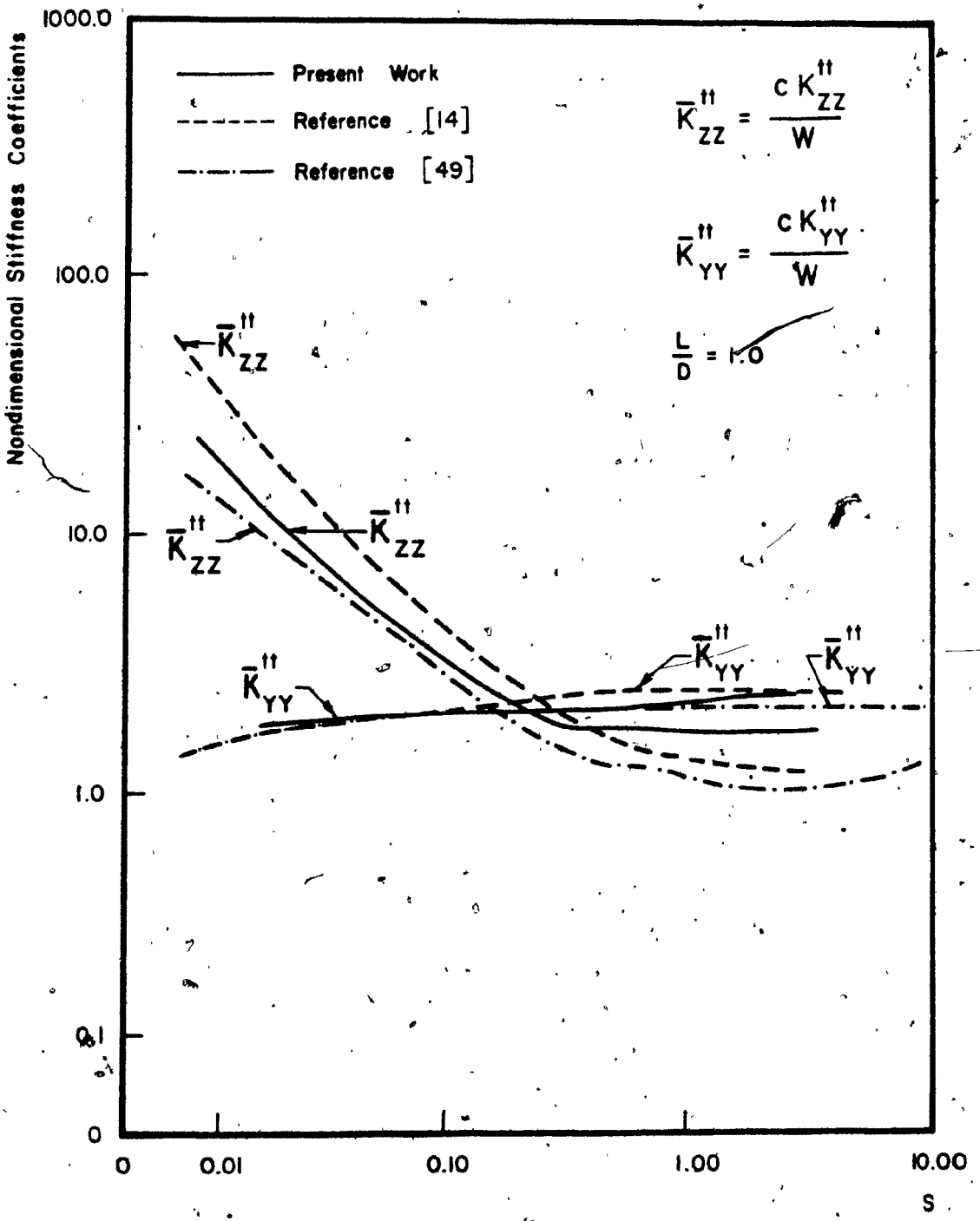

Figure 5.6 Translational Fluid Film Stiffness Coefficients (Collinear).

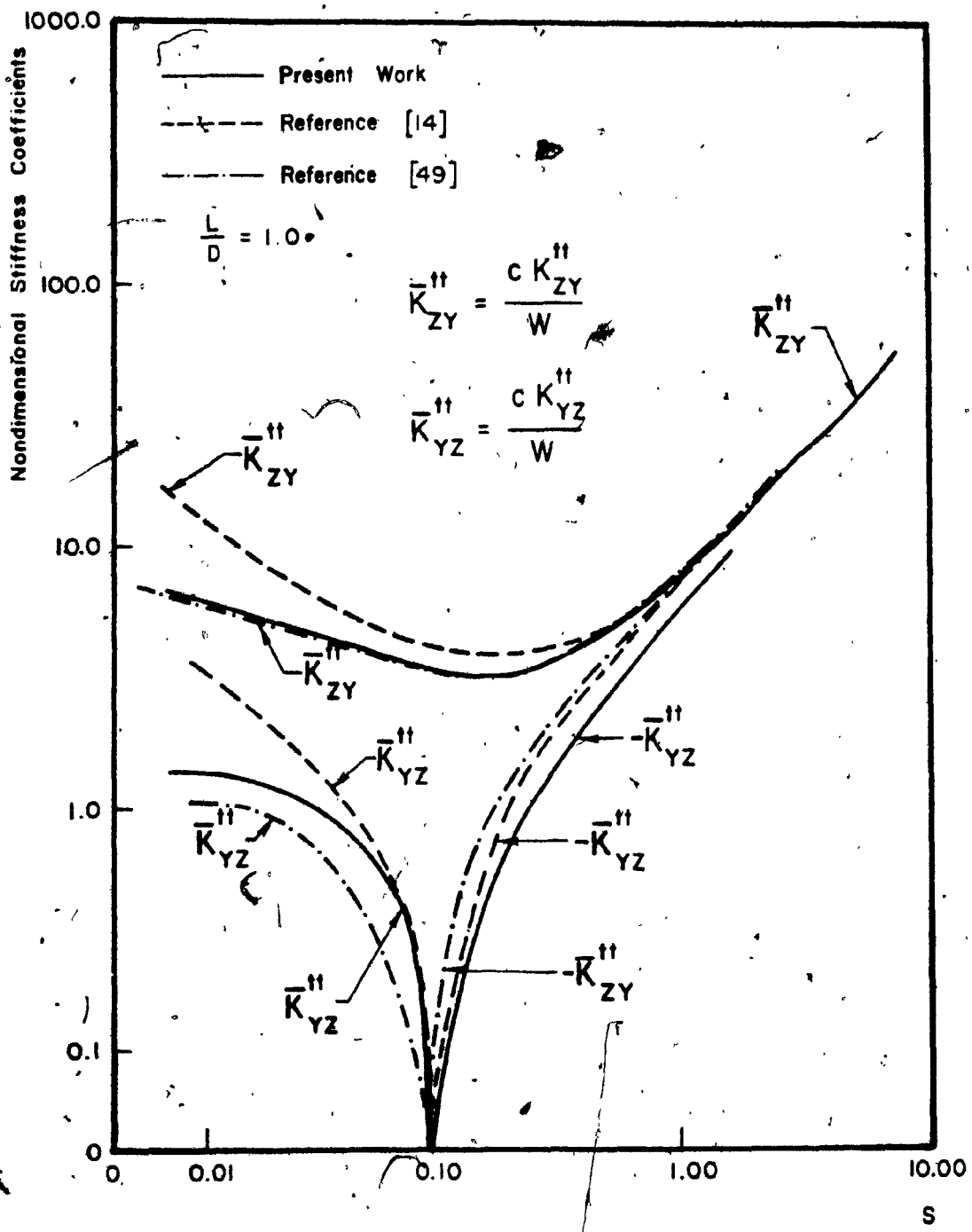

Figure 5.7 Translational Fluid Film Stiffness Coefficients (Cross-coupled).

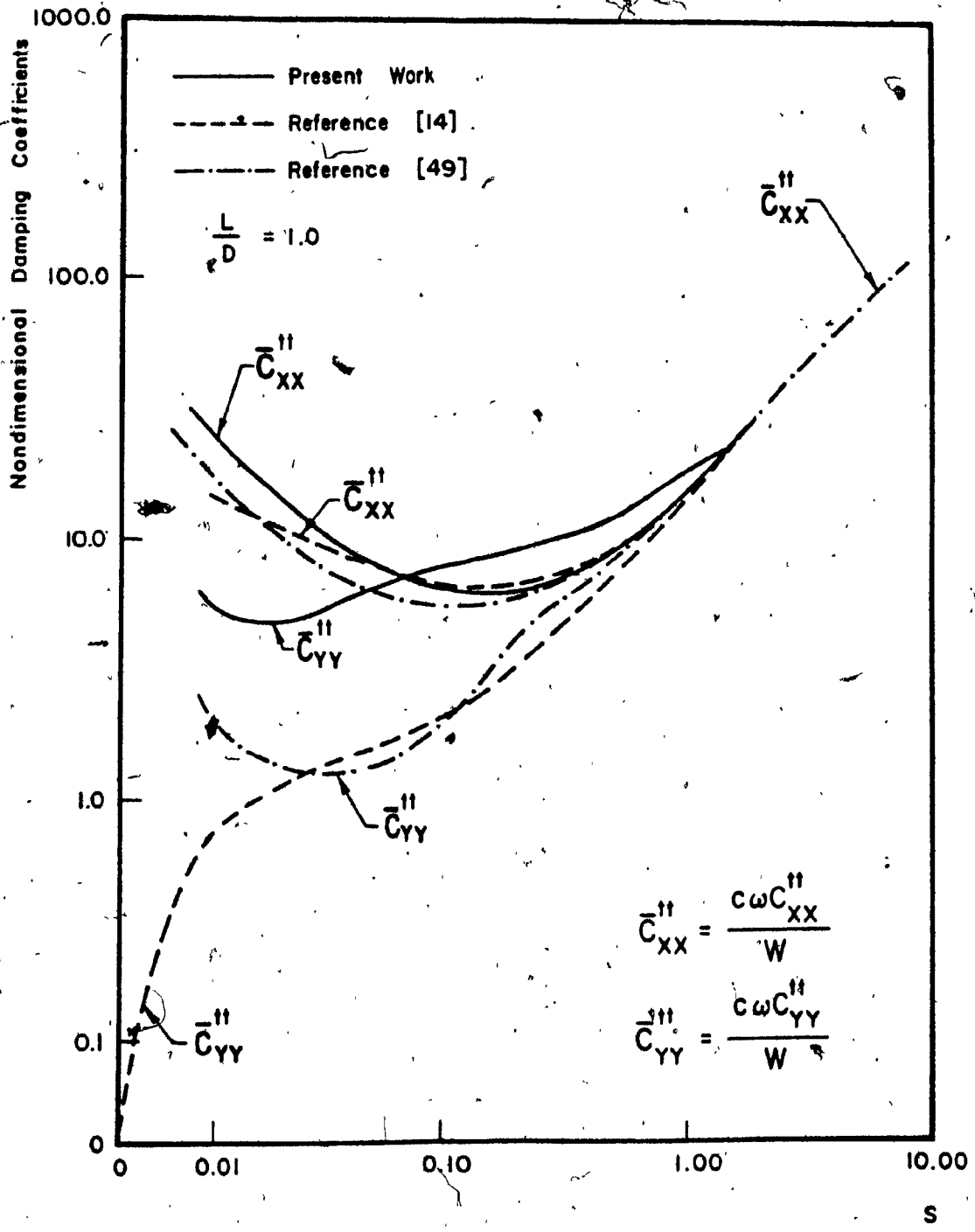

Figure 5.8 Translational Fluid Film Damping Coefficients (Collinear).

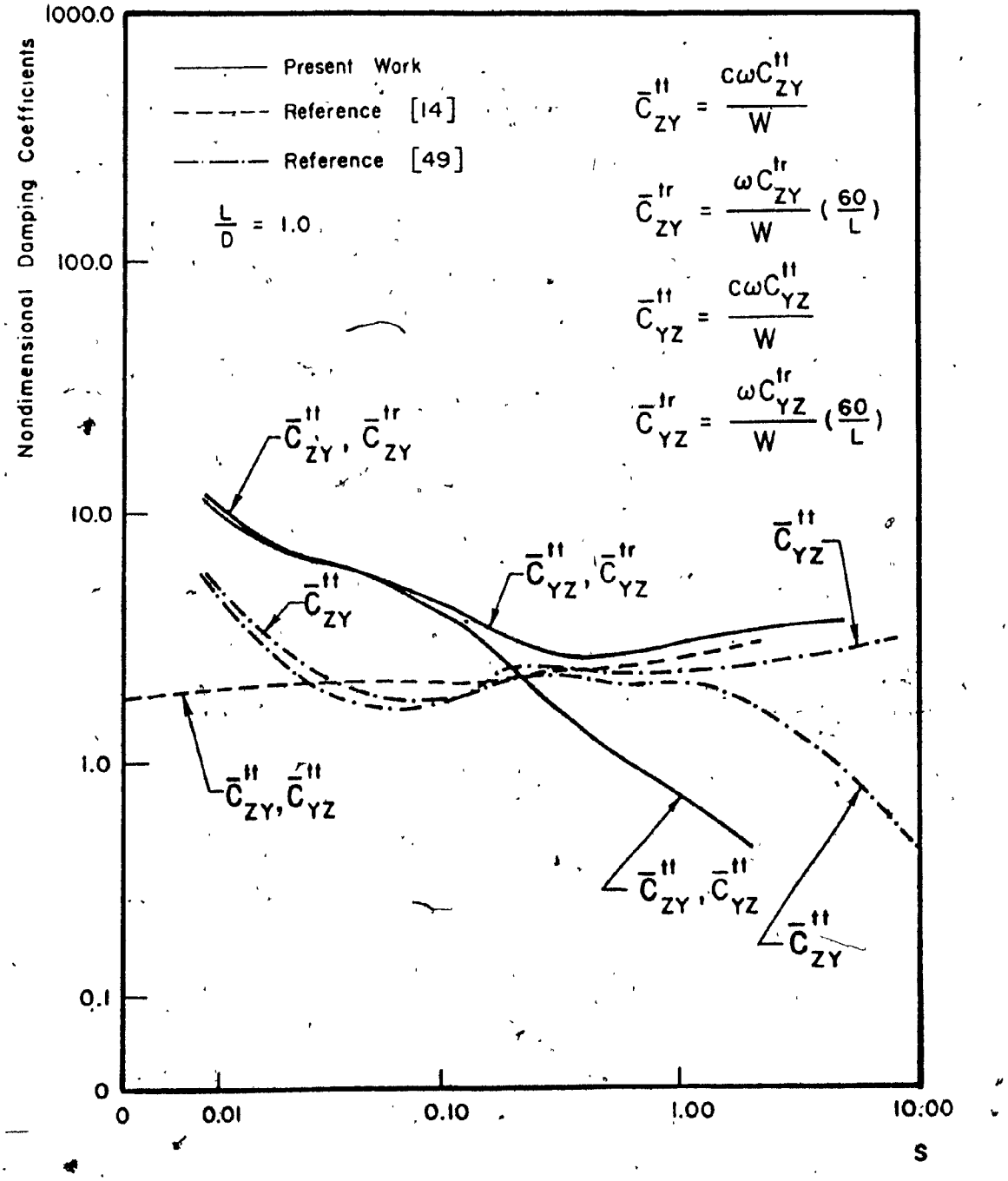

Figure 5.9 Translational Fluid Film Damping Coefficients (Cross - Coupled).

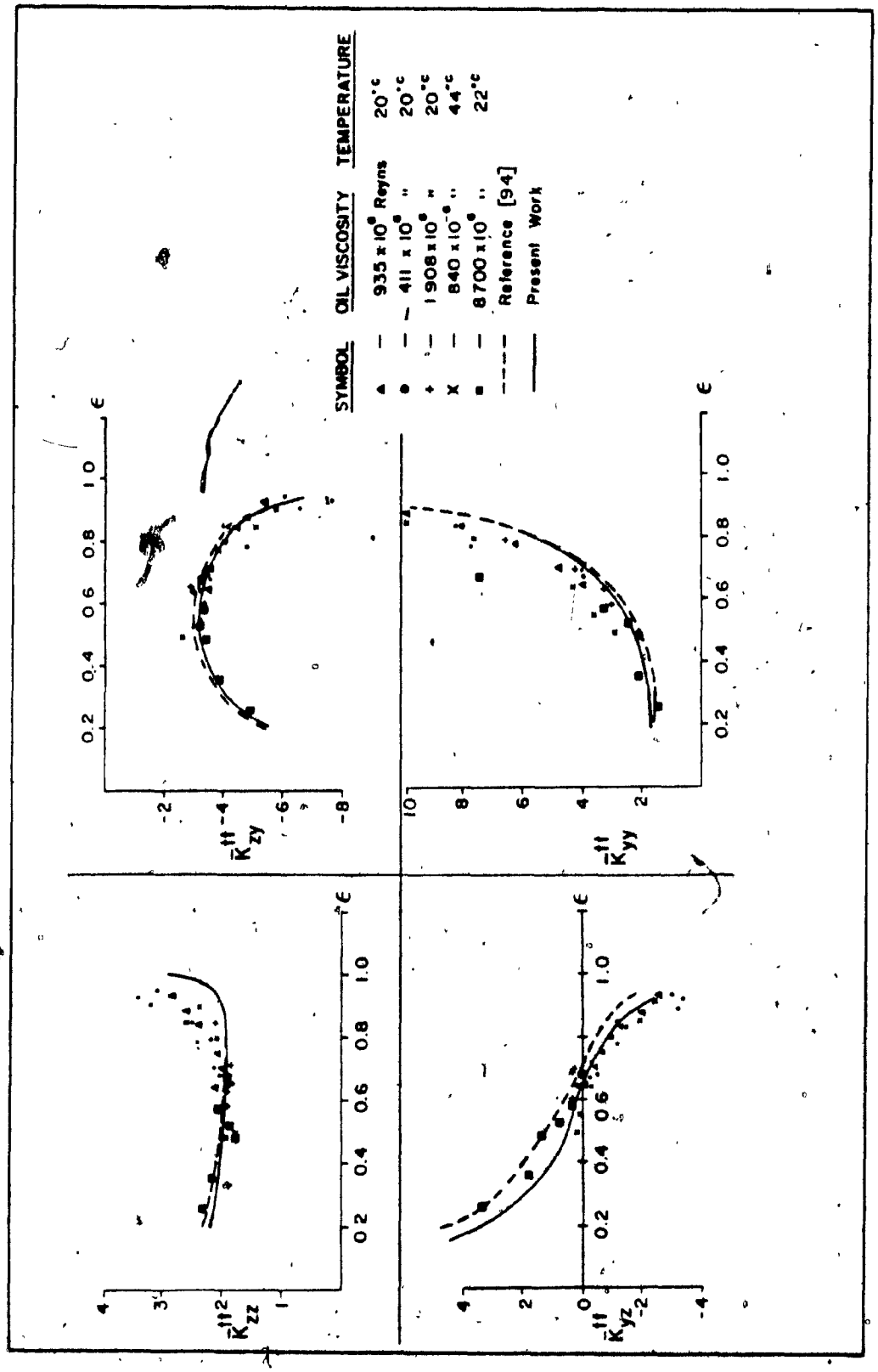

Figure 5.10 Nondimensional Stiffness Coefficients

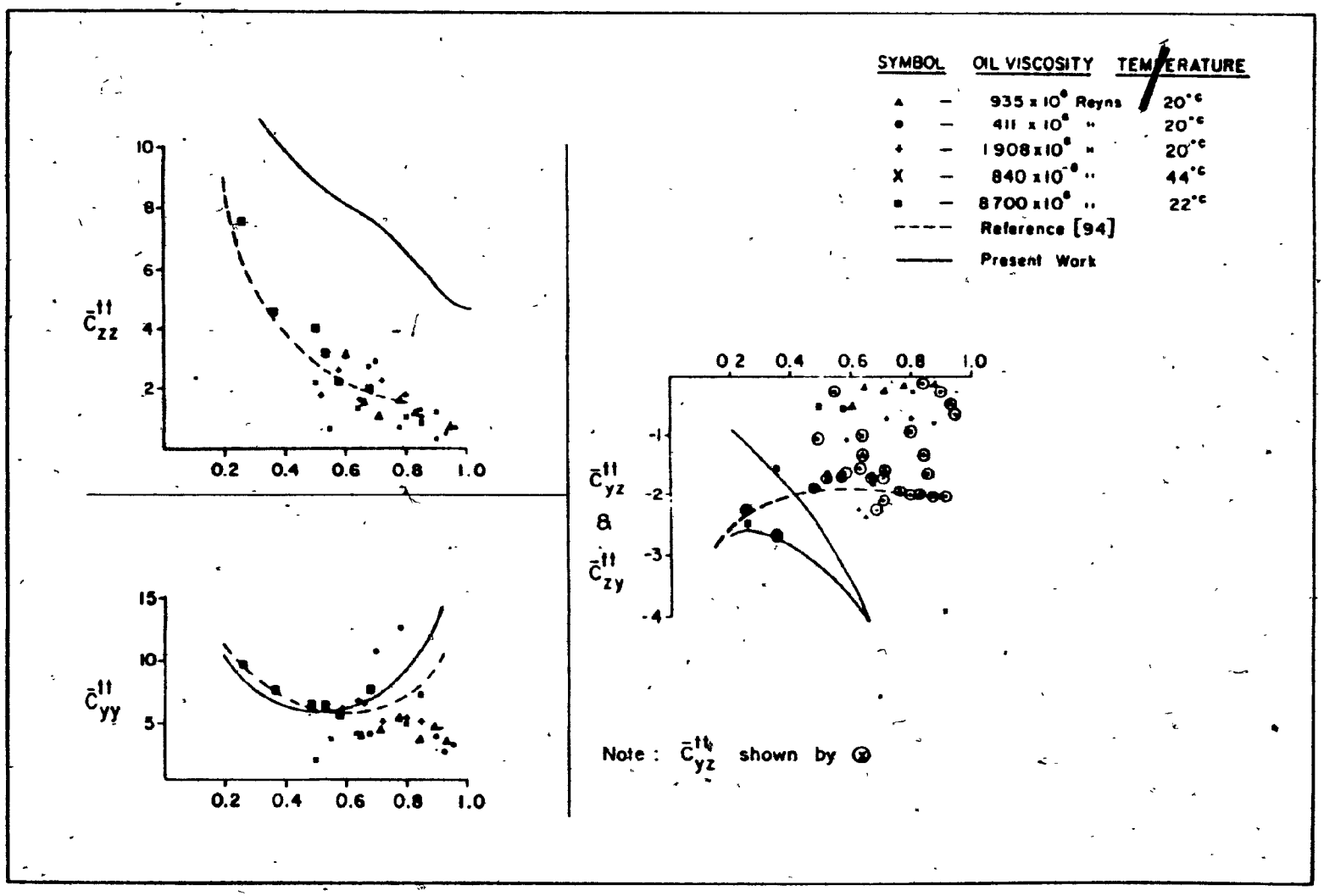

Figure 5.11 . Nondimensional Damping Coefficients .

the present study are compared with those of Kikuchi [14] and are shown in Figs. 5.12 through 5.15. For a range of Sommerfeld numbers, the rotational film co-efficients obtained by the two procedures show a good qualitative agreement. The only significant difference is in the rotational cross-coupled damping co-efficients c_{zy}^{rr} and c_{yz}^{rr}. These rotational film co-efficients obtained for a misaligned journal in a finite bearing is compared with those obtained by Mukherjee and Rao [59] and those obtained by Capriz [60]. They are shown in Figs. 5.16 through 5.19. A comparison of the rotational co-efficients obtained in the present investigation shows a good agreement with those obtained by Capriz. The rotational film co-efficients obtained by Mukherjee and Rao [59] show considerable discrepancy with the present work and also with the results obtained by Capriz [60] for higher eccentricities.

The coupled film co-efficients due to translational and rotational film reaction forces and moments are also obtained. The coupled force film co-efficients arising out of rotation of the journal and the coupled moment film co-efficients due to the displacement of the journal are obtained for finite bearings and are shown in Figs. 5.20 and 5.21. The corresponding coupled damping co-efficients are shown along with the pure translational film co-efficients in Figs. 5.8 and 5.9 and with pure rotational film co-efficients in Figs. 5.14 and 5.15.

5.7 Dynamic Response of Rotor

The translational and rotational fluid film co-efficients evaluated for the finite cylindrical bearings are used in the analysis of two rotor systems to determine the critical speeds and peak amplitude response. The first one is a simple rotor system which consists of a

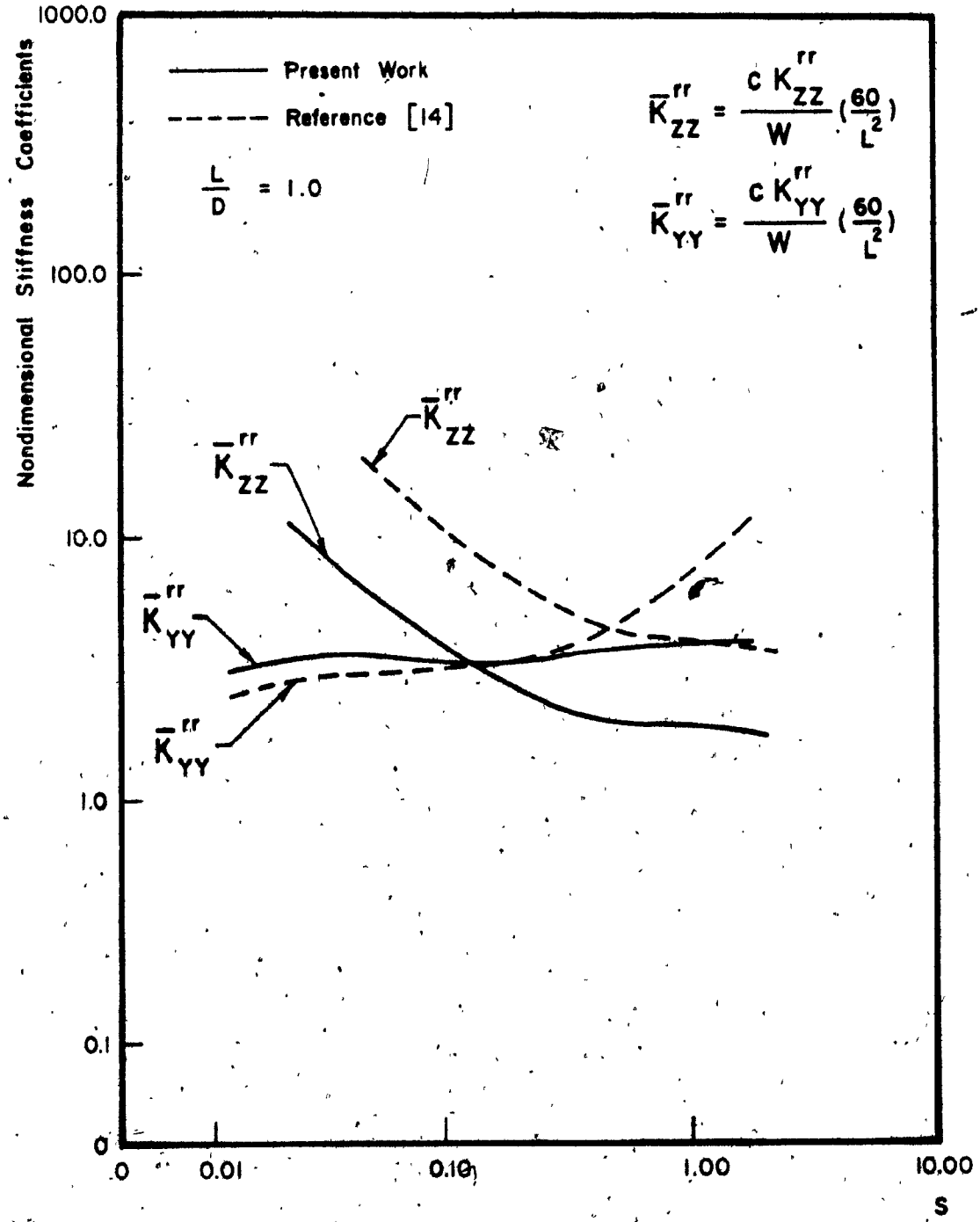

Figure 5:12 Rotational Fluid Film Stiffness Coefficients (Collinear).

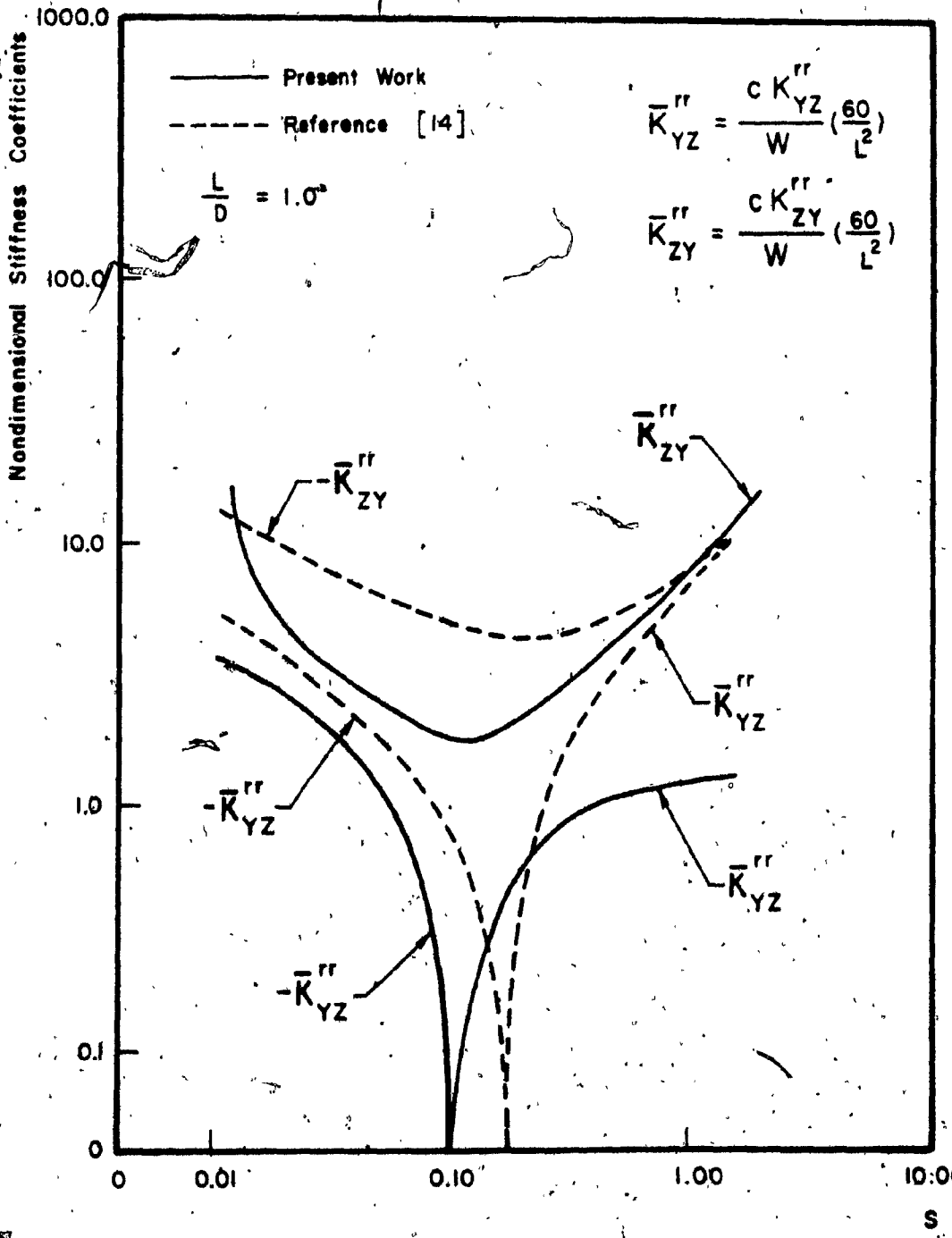

Figure 5.13 Rotational Fluid Film Stiffness Coefficients (Cross-Coupled).

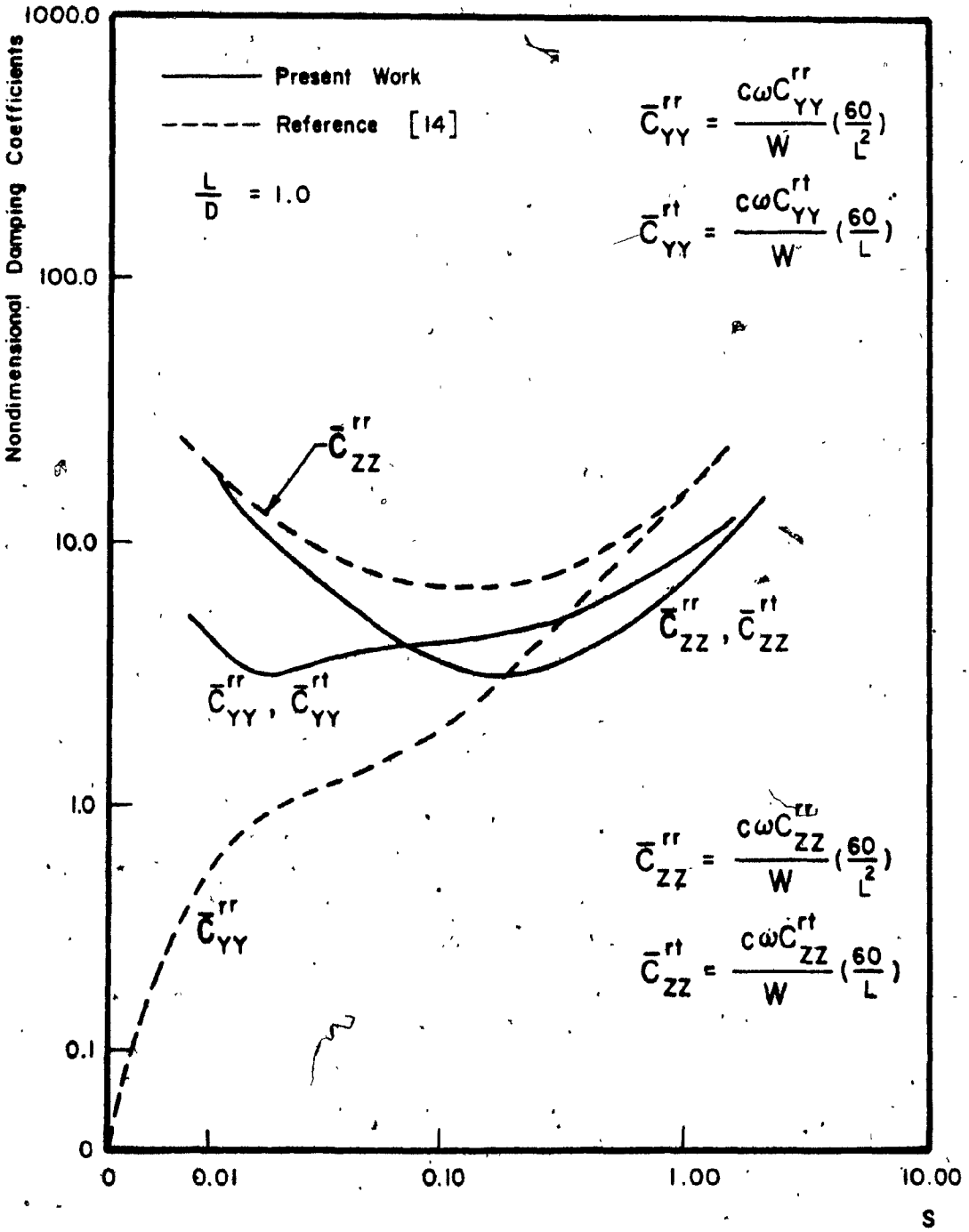

Figure 5.14 Rotational Fluid Film Damping Coefficients (Collinear).

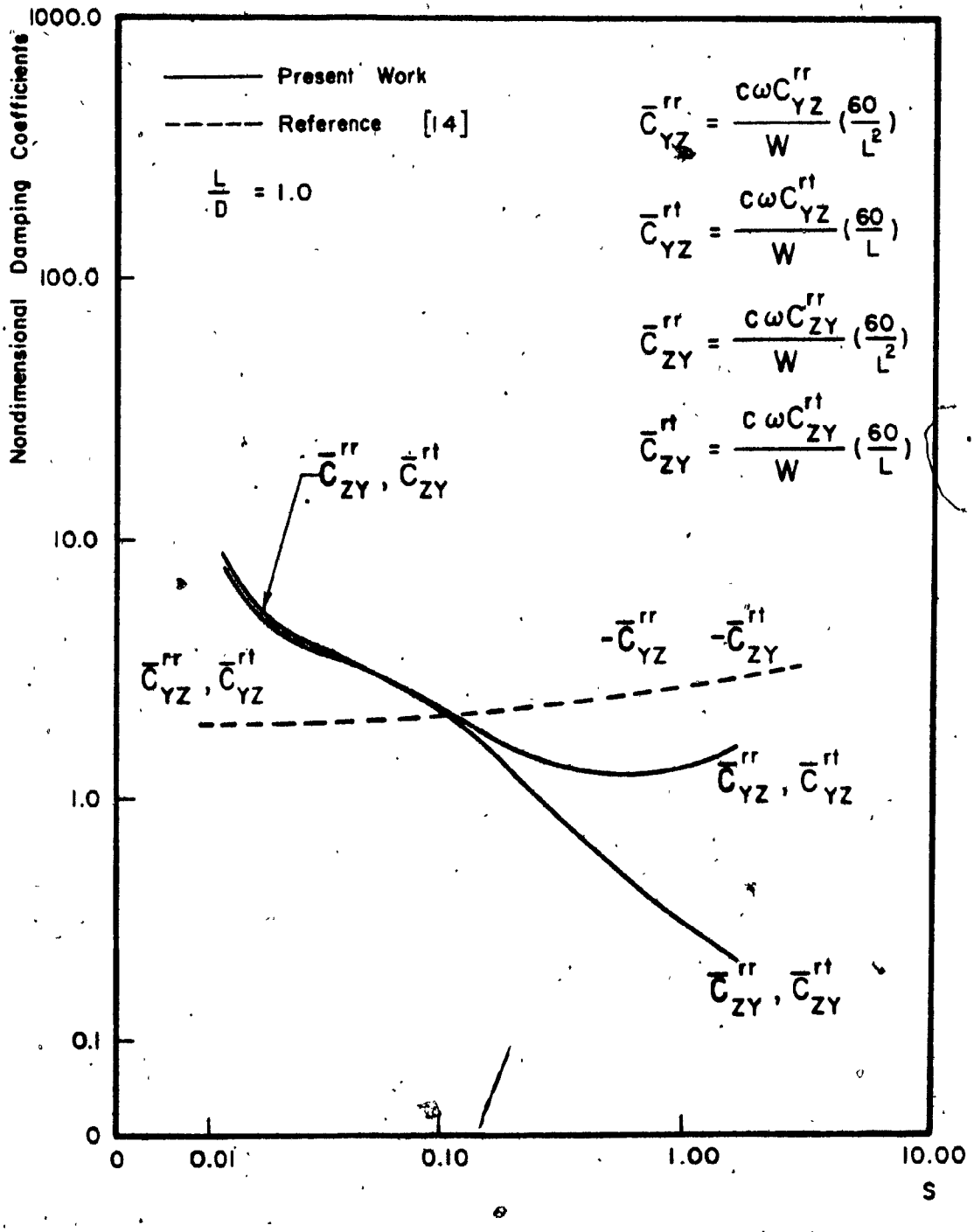

Figure 5.15 Rotational Fluid Film Damping Coefficients (Cross - Coupled).

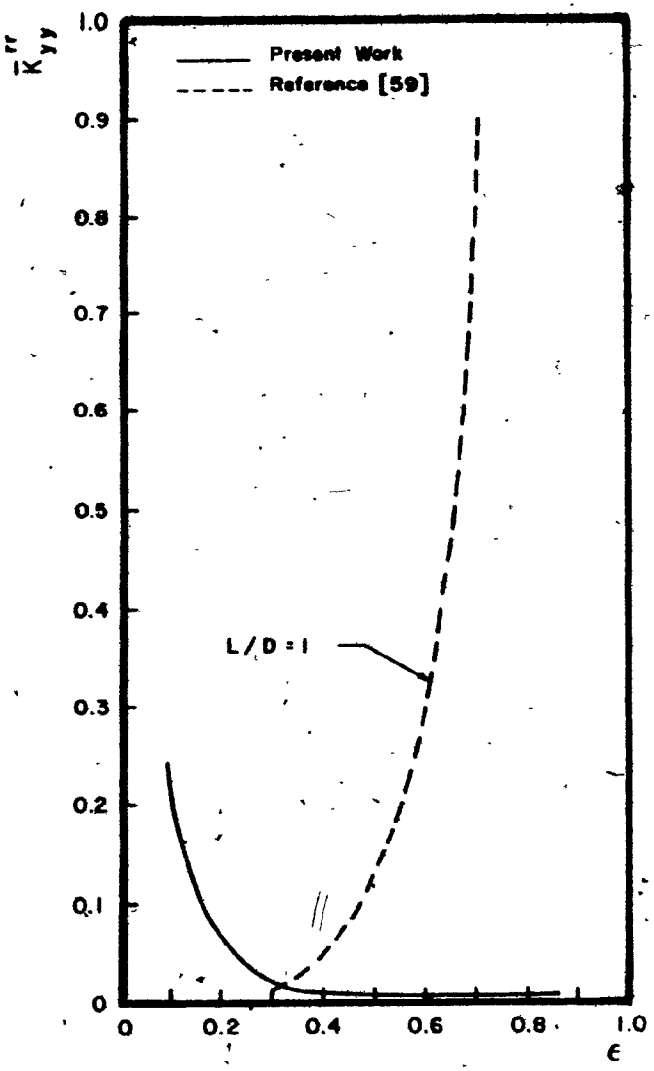

Figure 5.16 Non-Dimensional Rotational stiffness vs Eccentricity Ratio.

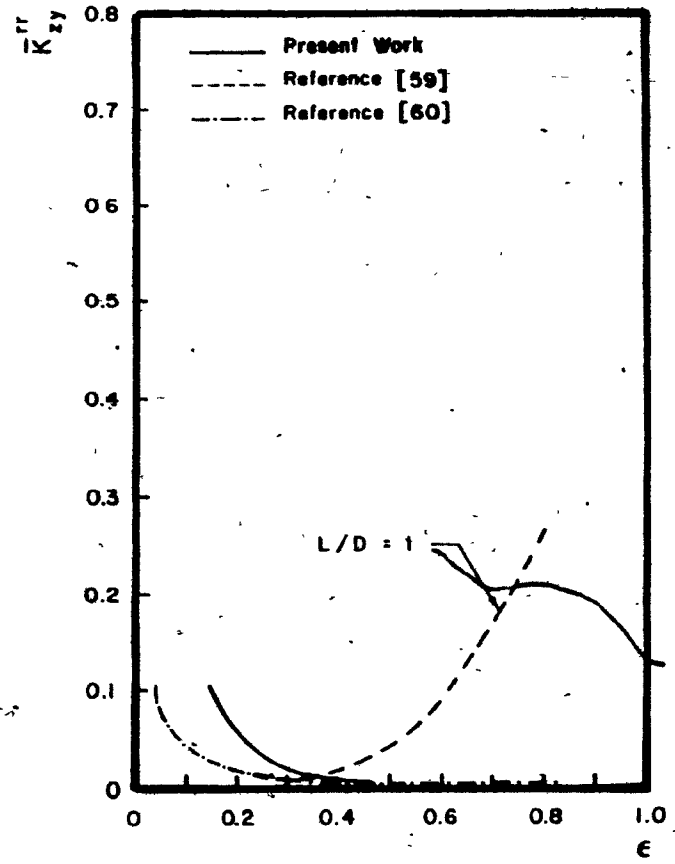

Figure 5.17 Non-Dimensional Rotational stiffness vs Eccentricity Ratio.

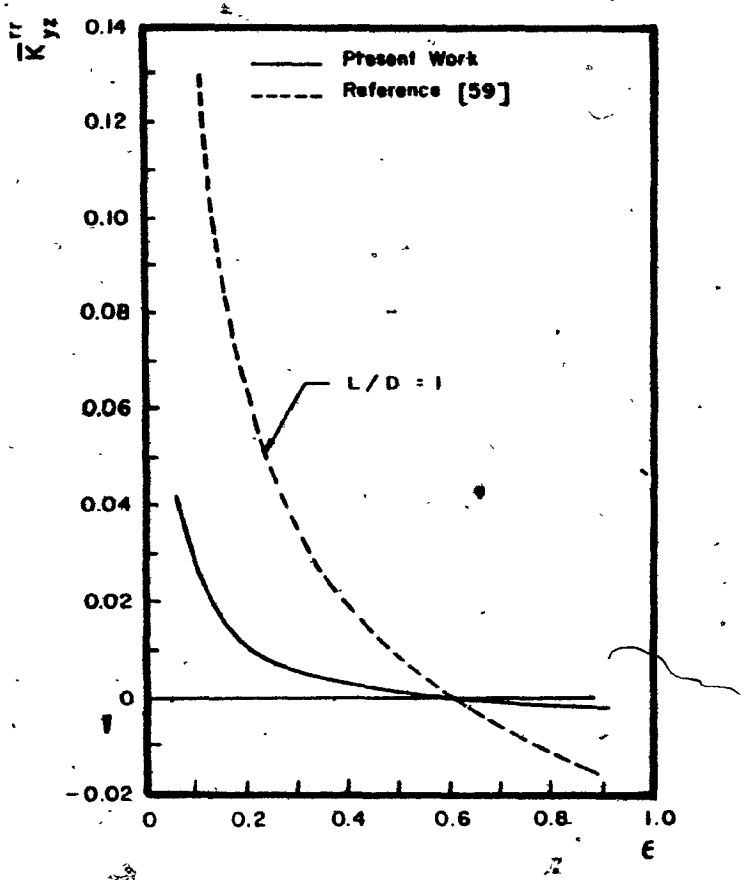

Figure 5.18 Non - Dimensional Rotational stiffness vs Eccentricity Ratio .

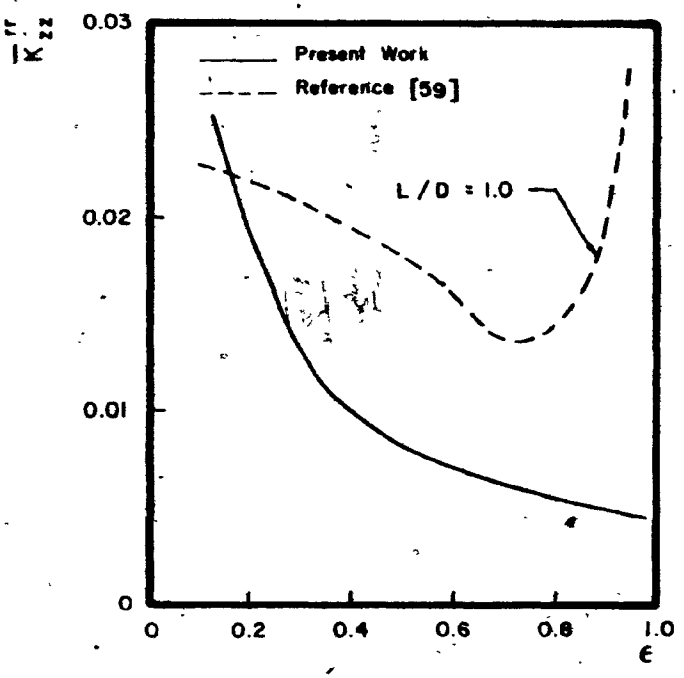

Figure 5.19 Non - Dimensional Rotational stiffness vs Eccentricity Ratio .

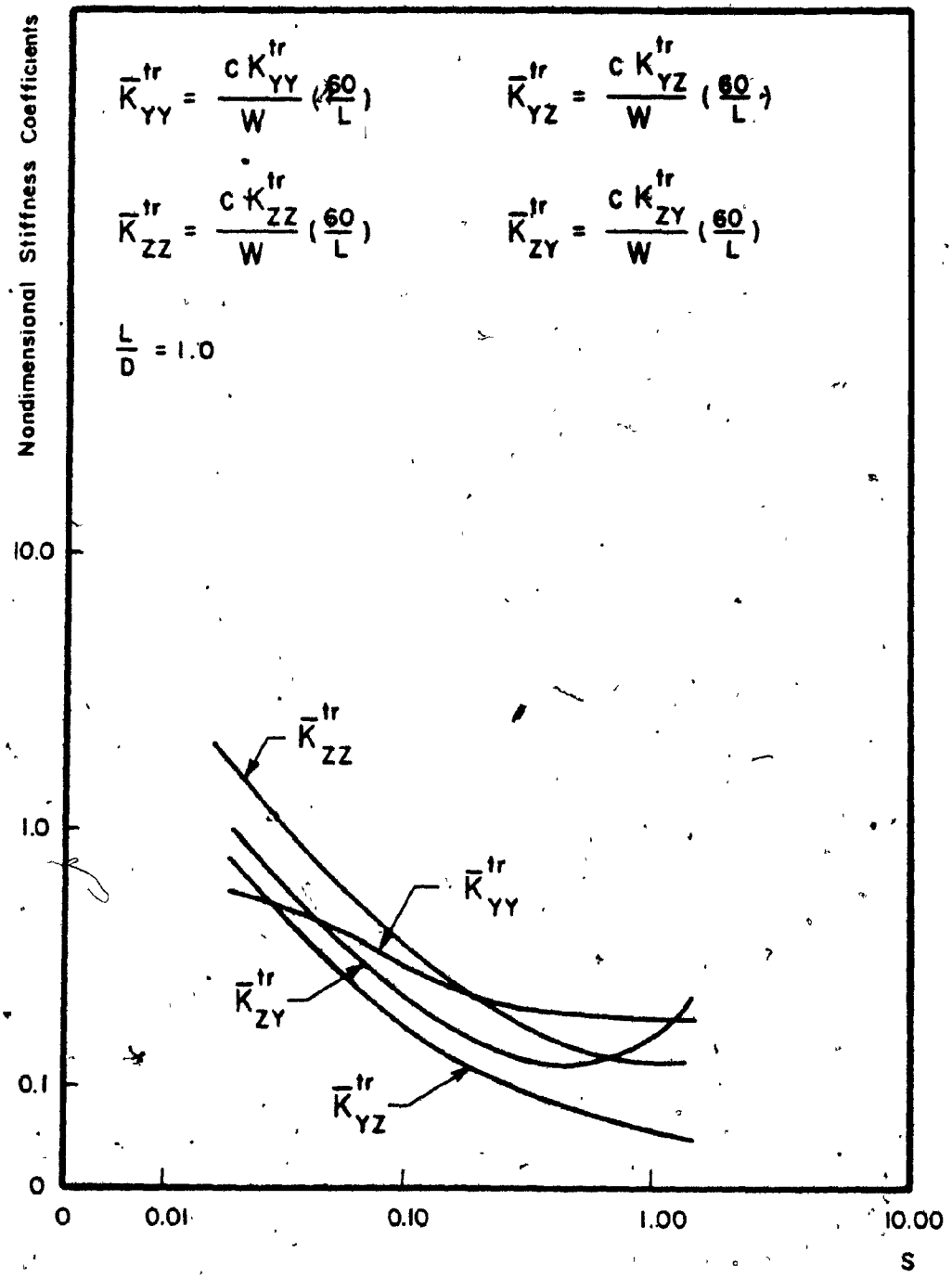

Figure 5.20 Coupled Stiffness (F/θ) Coefficients .

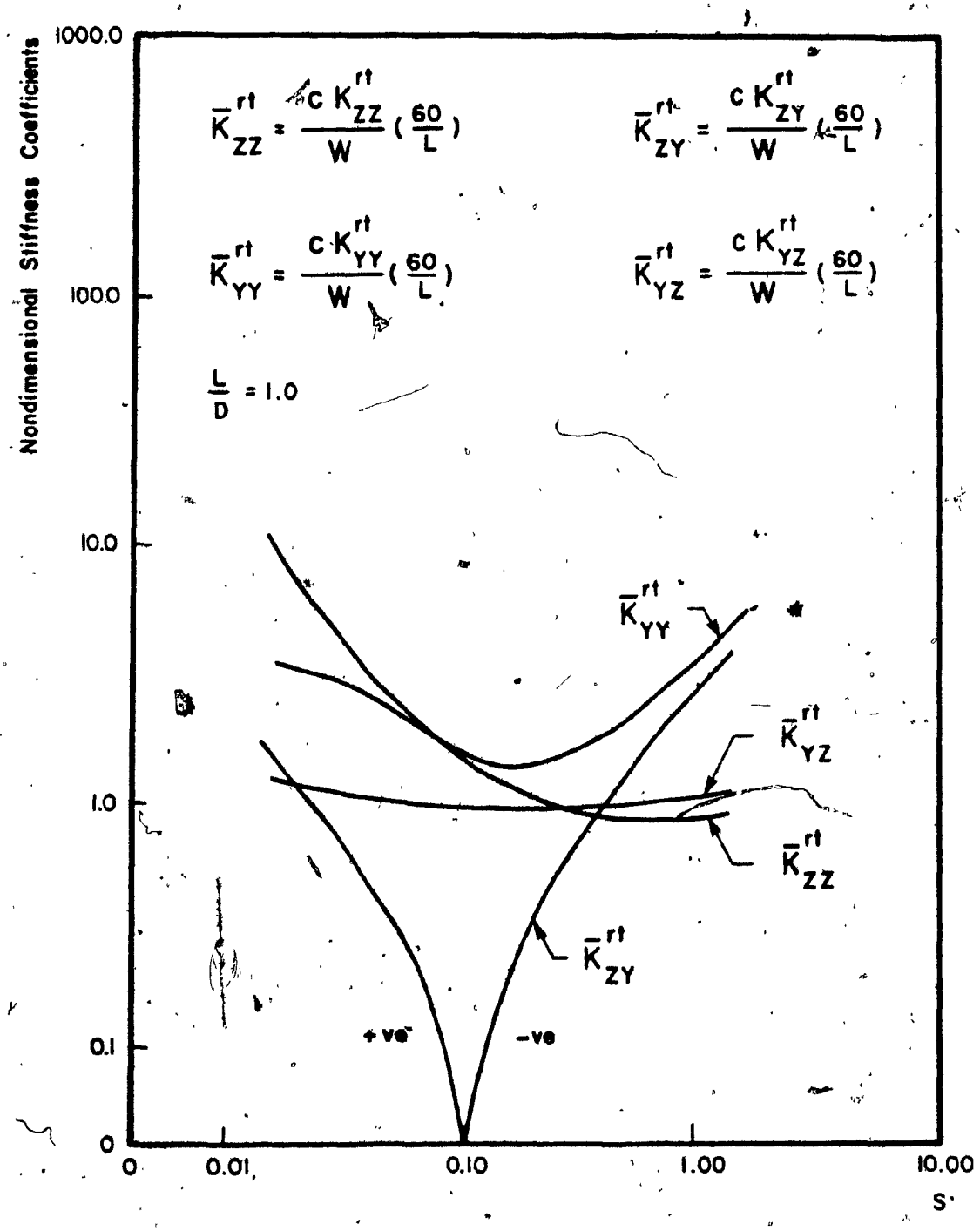

Figure 5.21 Coupled Stiffness (M/X) Coefficients.

single disk mounted at the center of the shaft, which in turn, is supported on hydrodynamic bearings at its two ends.

This simple rotor system is modelled using the finite element method. The entire system is discretized into bearing, shaft and disk elements. The overall assembled matrices are solved for the frequencies and responses by modal analysis. The stiffness and damping matrices for the bearing element are shown in Appendix B. The details of this simple rotor system were already shown in Table 2.1. Some case studies are made based on the different bearing clearances at the two bearing locations. Table 5.1 gives different configurations of the rotor system which are discussed subsequently. The present results are compared with those obtained by Kikuchi [14] and Lund [49]. For convenience, the analysis of the rotor system using the fluid film co-efficients obtained by present work, by Kikuchi [14] and by Lund [49] are referred to as Analysis I, Analysis II and Analysis III respectively.

5.7.1 Case I: Equal Bearing Clearances ($c_1 = c_2 = 0.0000533$m)

The frequencies and the normalized response amplitudes of the rotor are studied and the comparative plot of all the three analyses are shown in Fig. 5.22. It is observed that only a single peak exists in all the three analyses. The rotor critical speeds at the peak amplitudes are 2535, 2530 and 2610 rpm, for analyses I, II and III respectively. And, the respective normalized peak amplitudes are 22.58, 16.89 and 18.6.

TABLE 5.1: Rotor Configurations

Case No.	Disk Wt. N	ℓ_1 m	ℓ_2 m	c_1 m	c_2 m
1	116	0.25525	0.25525	0.0000533	0.0000533
2	116	0.25525	0.25525	0.000188	0.000188
3	116	0.25525	0.25525	0.0000533	0.000188

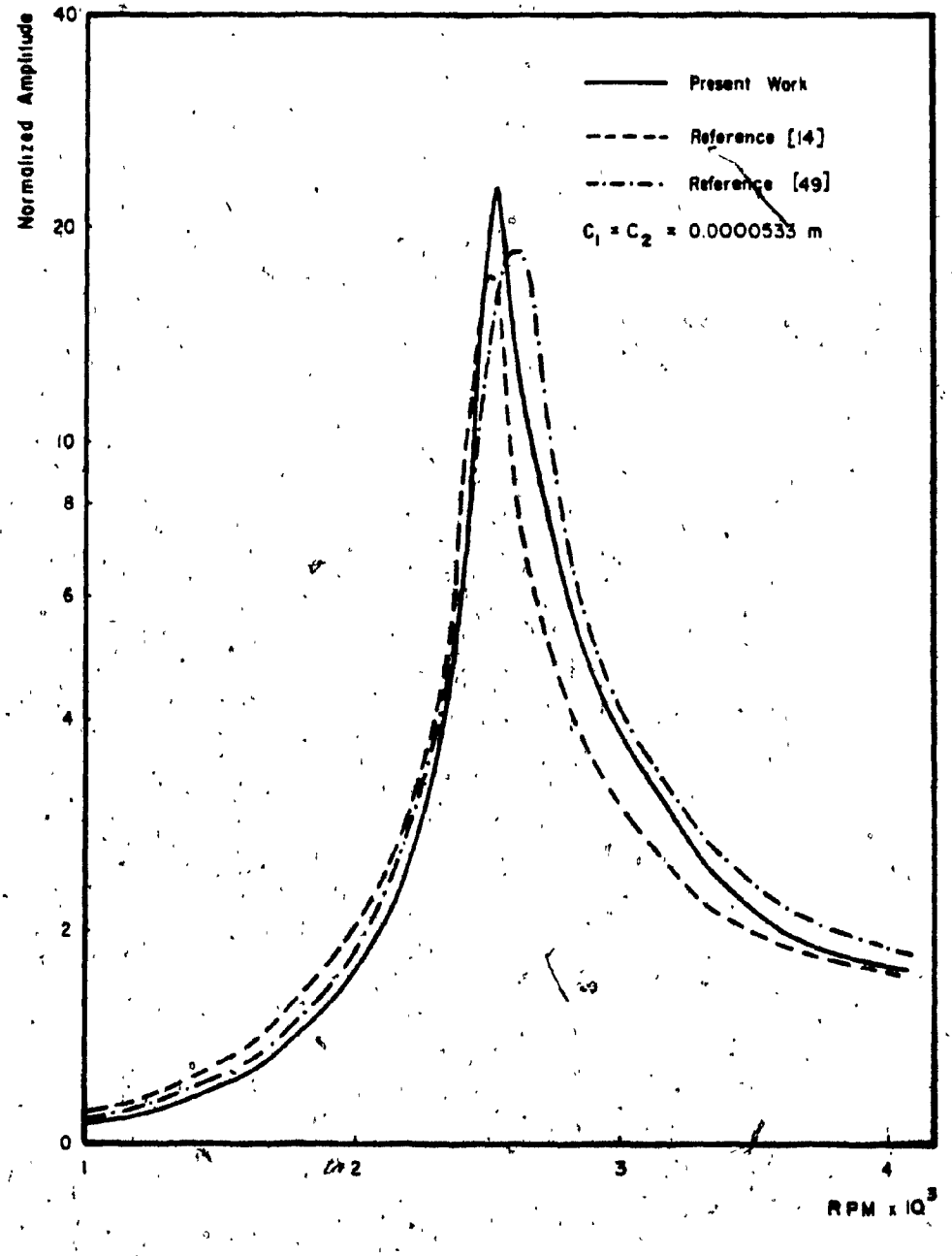

Figure 5.22 Unbalance Response of the Rotor.

Except in the critical frequency region, the difference in amplitude levels between the three analyses is small

5.7.2 Case II: Equal Bearing Clearances ($c_1 = c_2 = 0.000188m$)

The dynamic characteristics of this configuration of rotor system are studied and the comparative graph for all the three analyses is shown in Fig. 5.23. It is observed that the response plots obtained by Analysis I show a single peak at the rotor speed of 2481 rpm whereas those obtained by Analysis II and Analysis III show two distinct peaks. However, the predicted damped eigenvalues in Analysis I show two distinct peaks, one at 2216 rpm, and the other at 2482.6 rpm and these double peaks correspond to first split criticals due to bearing asymmetry. But, the first peak in Analysis I is hidden because the amount of damping at this rotor speed is comparatively large. The first peak for Analysis, II and III correspond to rotor speeds of 1700 rpm and 1850 rpm respectively and the corresponding second peak occurs at the rotor speeds of 2443 rpm and 2500 rpm.

5.7.3 Case III: Unequal Bearing Clearances ($c_1 = 0.0000533m, c_2 = 0.000188m$)

For this configuration of the rotor, the variation of critical speeds against the speed of the rotor is shown in Fig. 5.24. Again a single peak response is seen for Analysis I at a rotor speed of 2510 rpm and the peak response for Analysis II and Analysis III show two distinct peaks. However, the first and second predicted damped eigenvalues in Analysis I occur at the rotor speeds of 2409 rpm and 2509 rpm respectively and they are the first split criticals due to bearing asymmetry. But, the first peak is not seen in the frequency response plots due to the high amount of damping at this rotor speed. The first peak for Analysis II

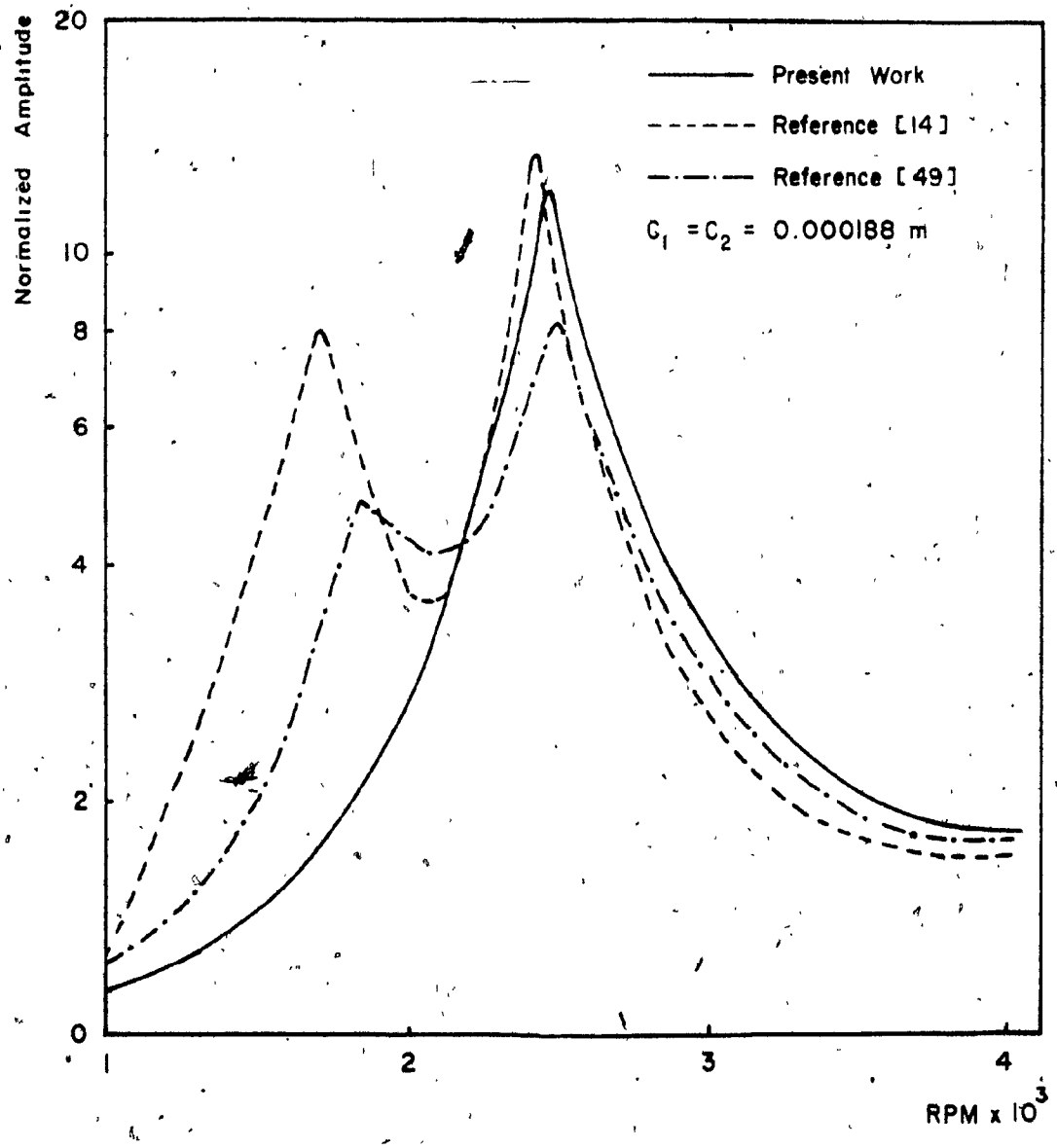

Figure 5.23 Unbalance Response of the Rotor .

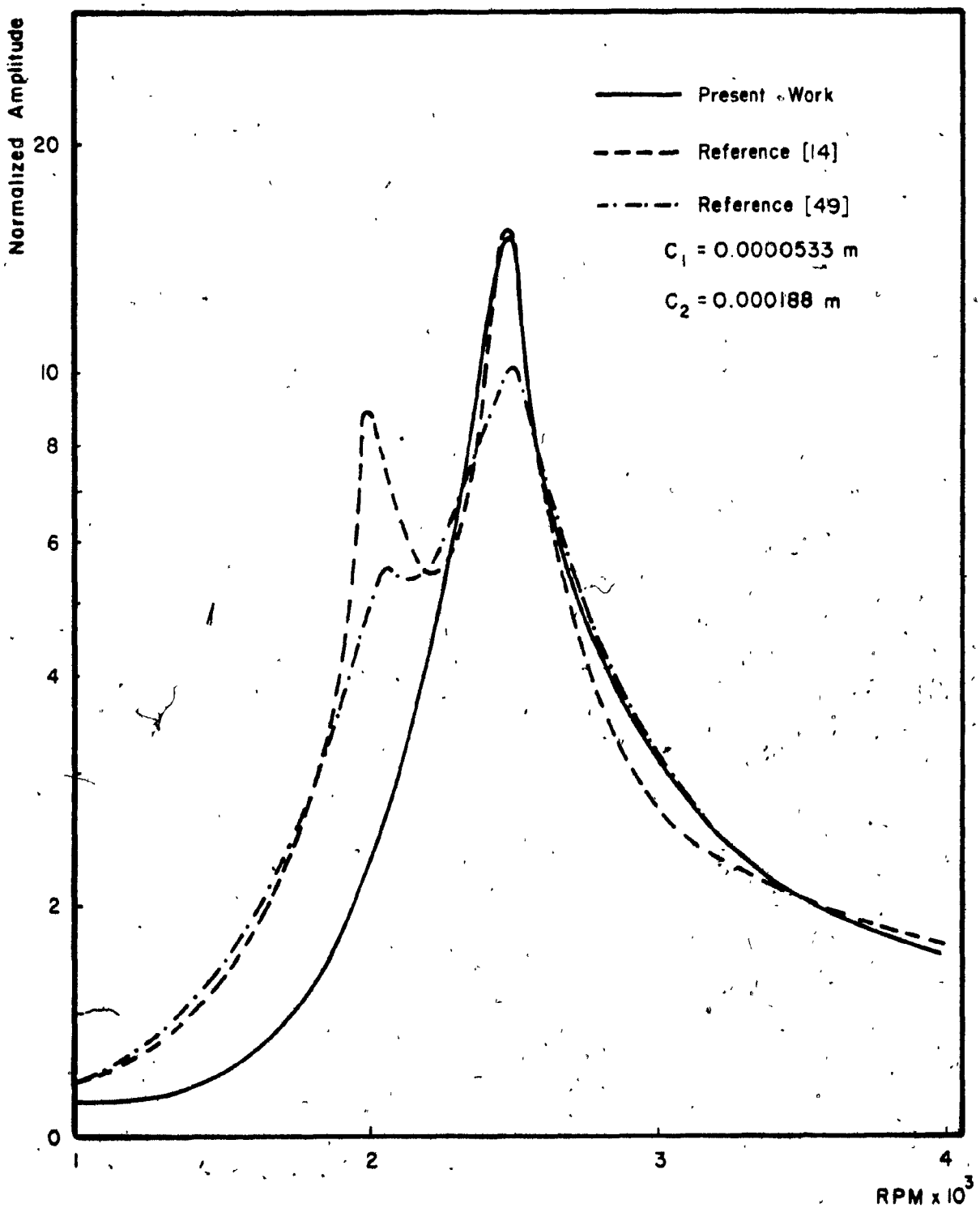

Figure 5.24 Unbalance Response of the Rotor.

and Analysis III correspond to rotor speeds of 1975 rpm and 2080 rpm and the corresponding second peak occurs at rotor speeds of 2485 rpm and 2490 rpm respectively.

Secondly, the rotor model-I used by Kikuchi [14] is analyzed using the fluid film co-efficients evaluated in the present analysis. The variation of response amplitudes against the rotational speeds of the shaft observed by Kikuchi [14] in his three rotor system (Model-I) is compared with the corresponding parameters obtained using finite bearing results. This comparative plot is shown in Fig. 5.25. It is observed that the rotor critical speed falls at 69.7 cycles/sec in Analysis I and that for Analysis II is 70.7 cycles/sec.

Also, the peak response amplitudes for Analysis I and Analysis II are about 360.8 and 485.0 respectively. It is important to note that the critical speed and the response amplitude determined in Analysis I are closer to the experimental results for this rotor model.

5.8 Conclusions

The translational and rotational stiffness and damping co-efficients of the fluid film are obtained for finite cylindrical bearings. The translational fluid film co-efficients are compared with those obtained by experiments.

The rotational film co-efficients are also compared with those obtained by short bearing approximation. They show a very good qualitative agreement. The critical speeds obtained for a single disk and three disk rotor systems using a finite bearing model differ by 2-8% when a short bearing model is considered. Also, the results obtained using the finite bearing approximation compares very well with the experimental

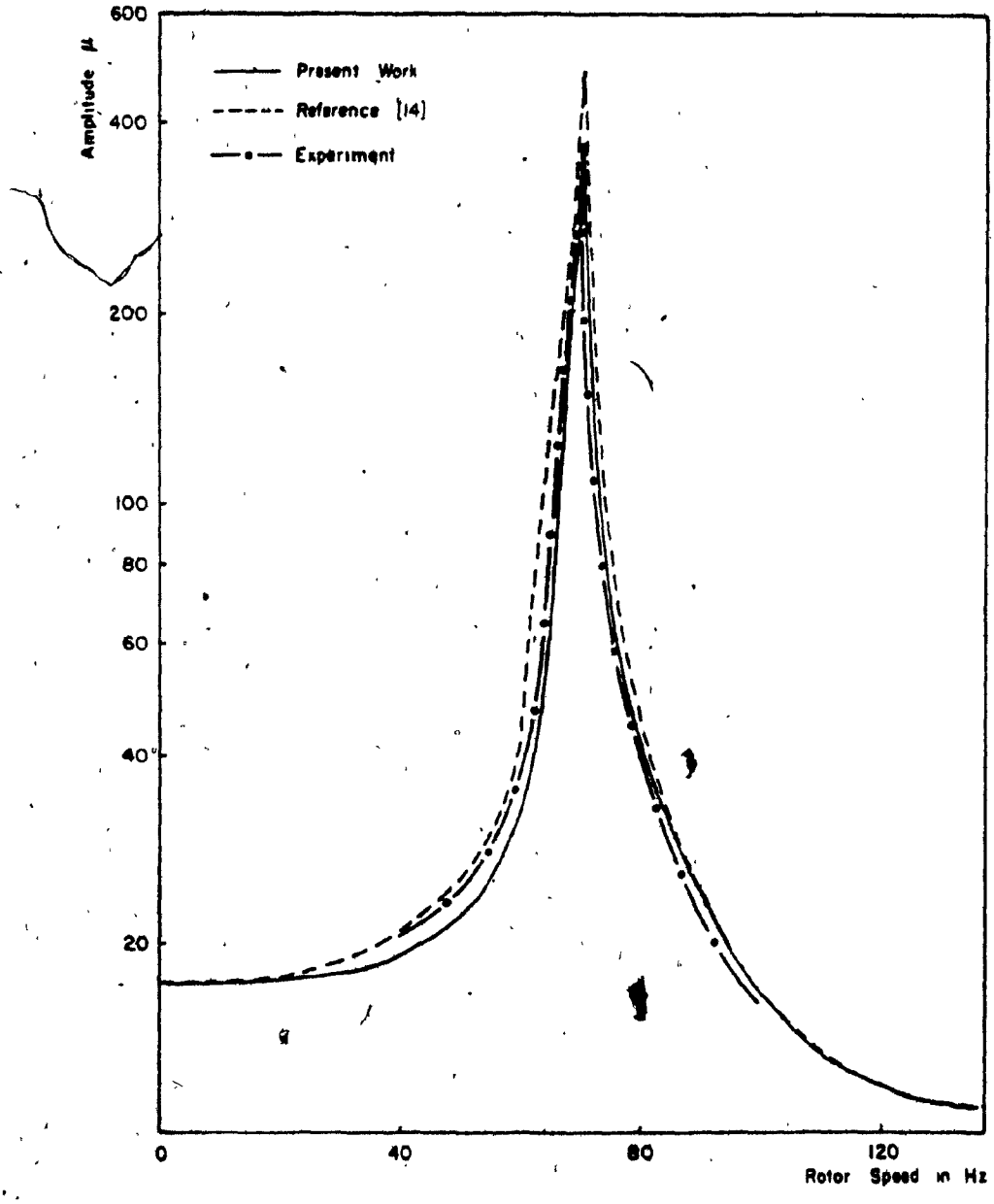

Figure 5.25 Unbalance Response of the Rotor Model - I of [14]

results of the three disk rotor system.

The coupling effect on the fluid film forces and moments due to the translational and rotational motion of the journal is also obtained. On the whole, a total of 32 fluid film stiffness and damping co-efficients are obtained for a bearing model. However, it is noted in general that the effects of rotational fluid film co-efficients have very little influence on the response of simple rotor systems.

In this chapter, a very comprehensive model of the bearing is considered and the corresponding fluid film dynamic co-efficients are obtained by solving appropriate Reynold's equation for the resulting fluid film. A total of 32 fluid film stiffness and damping co-efficients are considered. However, the support model is still not complete since the support structure, on which the bearings are mounted, is not modelled in this analysis and will be considered in Chapter 6. Moreover, the support structures are sometimes subjected to excitations due to various reasons. These excitations are not in general deterministic in nature. Under these circumstances, it is important to consider the random nature of the excitations through the support structure. The support structure model and the resulting influence of excitations through these supports will be dealt with in the next Chapter.

CHAPTER 6

THE STUDY OF THE RESPONSE OF ROTOR SYSTEMS SUBJECTED TO RANDOM SUPPORT EXCITATIONS

In the previous chapter, the fluid film bearings of the rotor system were modelled using rotational springs and dampers along with the lateral springs and dampers. The support structure of the bearings was assumed to have infinite stiffness along the two perpendicular directions. However, in practice, the rotor-bearing system is supported by means of resilient pedestals which have finite stiffness and damping properties along the two perpendicular directions. This requires that the support model be improved over the model used for the supports in the previous chapter. In this chapter, the support structure of rotors is modelled in addition to the fluid film bearing.

Of most practical concern in rotor dynamic analysis is the response to mass unbalance. When the excitation is due to mass unbalance, it is a single frequency excitation and the response is large in the vicinity of critical speeds. However, other forms of excitations are of interest, especially when the excitations are from outside sources, as it may occur in machinery on board various vehicles or for stationary machinery, in case of ground excitations. These support excitations can be of a single frequency type or random, involving several frequencies. For the machine installed onboard vehicles or the machinery installed in the regions of low or moderate seismological activity, the support excitations are random in nature. When the excitations are random with considerable power distributed at several frequencies, the system will also respond at these frequencies. Moreover, if one of the system

natural frequencies of the rotor coincides with the excitation frequencies, the resulting response may be quite significant and of concern. When the response of the structure is determined using modal analysis techniques, that becomes an uncoupled model and the response calculations can be carried out by the following three methods:

a) time-history response

b) response spectrum method

c) random vibration techniques.

Each one of these methods will be discussed briefly, before a method is chosen to solve the problem at hand.

6.1 Time History Response

The most straightforward way of specifying a support input to an analysis is to take an actual time history and apply it as an acceleration to the support points of the model. The dynamic response is then calculated directly as a time history of the structural displacements. For simplicity, discussions are advanced only for symmetric systems. However, the analysis can be extended for non-symmetric systems such as rotors on fluid film bearings, without much difficulty.

The equation of motion can then be transformed using a transformation matrix $\{q\} = [\Phi]\{\eta\}$ and premultiplying by $[\Phi]^T$ leads to

$$[\check{\mu}]\{\ddot{\eta}\} + [\check{c}]\{\dot{\eta}\} + [\check{\kappa}]\{\eta\} = [\Phi]^T\{f\} \qquad (6.1)$$

This is a set of uncoupled single degree of freedom equations, each of which can be solved separately by considering how each one responds to an impulse. Hence, the impulse response of the system at any time t can be written as,

$$\{q\} = \int_0^t w(t-\tau)\, f(\tau)\, d\tau \qquad (6.2)$$

where w is the impulse response matrix. It relates the dynamic response of the structure to the time history of the force input. The equation can be integrated by assuming that the force is constant over the interval or better still assuming that it varies linearly over the interval. Not all the modes need be included in the response. The force input will contain the frequency components of interest and hence the response of the other or high frequency modes will be constant and can be included as a single fictitious high frequency mode which is chosen to give, together with the active modes, the correct static stiffness. This means that $[\Phi]$ is a rectangular matrix containing only the mode shapes corresponding to the lower or at the range of frequencies of interest. Fewer modes are required to give a good respresentation of the displacement response.

The obvious objection to this method is that it can be used for one particular ground motion only. In order to have a safe evaluation of the response for a series of ground motions, a number of such time history evaluations are necessary. As more histories are analyzed so confidence is increased. Moreover, the bulk of computer effort is taken up in this method since a lot of time histories are to be evaluated.

6.2 Response Spectrum Method

Another technique used for the support motion of the structures is the response spectrum method. This is a valid technique for the calculation of response of simple and symmetric structures.

In this method one fundamental assumption made is that all of the support motions in any one direction are the same. Consequently, the ground motion $\ddot{q}_0$ can be subtracted from the structural motion $\ddot{q}$ by giving the structure an equal and opposite rigid body movement. The ground is then effectively still into structure accelerating,

$$\ddot{q}_r = \ddot{q} - b\,\ddot{q}_0 \tag{6.3}$$

where b is the rigid movement. Using the equation (6.3) in the general equation of motion of a structure we have,

$$m\,\ddot{q}_r + c\,\dot{q}_r + k\,q_r = -m\,b\,\ddot{q}_0 \tag{6.4}$$

Using the co-ordinate transformation,

$$q_r = \Phi\,\eta \tag{6.5}$$

and assuming that the mass matrix on the left side of equation (6.4) is normalized such that $\Phi^T m \Phi = I$, equation (6.4) can be written as,

$$\ddot{\eta} + \dot{\eta} + \kappa\,\eta = -\Phi^T m\,b\,\ddot{q}_0 = -\bar{P}\,\ddot{q}_0 \tag{6.6}$$

where P is called the participation factor. Again, equation (6.6) is a set of single degree of freedom equations and can be solved separately. The response for any mode can then be found by choosing the frequency on the response spectrum curve corresponding to the modal resonant frequency. The value of the response spectrum is then multiplied by the modal participation factor which gives the maximum response for the mode.

Just as with the time history method, it is not necessary to include all the modes in the analysis. However, the participation factor gives an indication of the relative importance of each mode, but unless

all the participation factors are evaluated, it is not possible to say that sufficient modes were used in the analysis in order to get a reliable spectrum. Also, this method lacks a great deal of mathematical rigour and this method is not suitable to a non-symmetric system such as rotors supported in fluid film bearings.

6.3 Spectral Density Methods

In order to be mathematically more rigorous, the fact that the support excitations are random can be recognized and formalized in a random analysis. Here a series of samples of the signal or representative signals are taken and averaged. The frequency content of each signal is found using a Fourier analysis. The amplitude of any one frequency will vary with each signal but an average is found by squaring and adding each component and finally dividing by the number of samples. Provided all of the signals are representative then this process will converge to a constant value as the number of samples is increased. This will give the spectral density of the signal at the frequency considered. If there are two simultaneous signals e.g., movement at two different points of the structure, then these signals, since they are both emanating from the same basic support excitations, will be related in some complex way. This relationship can be expressed as a cross spectral density and is found by multiplying the average amplitude of the signals. When expressed in terms of Fourier series, the frequency content can be complex numbers. The squaring and adding for the direct spectral densities will make these real, but cross spectral densities will generally be complex. This can be interpreted by recognizing that the two signals making the cross spectral density will be out of phase with each other. The complex number then represents

not only amplitude but also phase information. If there are a series of forces F, then these will combine to form a spectral density matrix $S_F(\omega)$ which can be defined at each frequency ω. In spectral density methods, the inputs are defined in terms of a spectral density matrix.

For any symmetric non-conservative system, the dynamic flexibility matrix $H(\omega)$ can be written as,

$$H(\omega) = \Phi\, D^{-1}\, \Phi^T \tag{6.7}$$

where $D = [(k_i - \omega^2 m_i) + j\,\omega\, c_i]^{-1}$

Then, the response spectral density matrix can be formulated as,

$$[S_R] = [H(\omega)]\,[S_F]\,[H^*(\omega)]. \tag{6.8}$$

where $H^*(\omega)$ is complex conjugate of $H(\omega)$.

The spectral density method has the distinct advantage that it is mathematically complete and well defined. It contains no ambiguities and retains full information about amplitude and relative phases of any set of inputs.

Since the support excitations in the present analysis are considered to be random and the spectral density method is by far the best approach, the response behavior of the rotor-bearing system subjected to random base excitations are studied using this method. To achieve the objective, certain assumptions are made regarding the characteristics of support motions in general. To simplify the analysis, the support excitation is assumed as a zero mean stationary, Gaussian and possessing a white noise type of power spectral density over a large frequency range [95]. Two different rotor systems are considered to study the system

response due to random base excitations.

6.4 Analysis

The rotor with its support model is shown in Fig. 6.1. This rotor can be discretized into beam, rigid disk and support elements. The properties of beam and disk elements are formulated by consistent parameter representation shown by Archer [84] which was discussed in chapter 4. Hence, only the equations of motion for the support element are given here. This support element consists of bearing and pedestal. Accordingly, the equations of motion of pedestal are as shown:

$$m_p\ddot{z}_p + c_{p_z}(\dot{z}_p-\dot{z}_b) + k_{p_z}(z_p-z_b) + c_{zz}^{tt}(\dot{z}_p-\dot{z}_1) + c_{zz}^{tr}(\dot{\theta}_p-\dot{\theta}_1)$$
$$+ k_{zz}^{tt}(z_p-z_1) + k_{zz}^{tr}(\theta_p-\theta_1) + c_{zy}^{tt}(\dot{y}_p-\dot{y}_1) + c_{zy}^{tr}(\dot{\phi}_p-\dot{\phi}_1)$$
$$+ k_{zy}^{tt}(y_p-y_1) + k_{zy}^{tr}(\phi_p-\phi_1) = 0 \qquad (6.9)$$

$$m_p\ddot{y}_p + c_{p_y}(\dot{y}_p-\dot{y}_b) + k_{p_y}(y_p-y_b) + c_{yy}^{tt}(\dot{y}_p-\dot{y}_1) + c_{yy}^{tr}(\dot{\phi}_p-\dot{\phi}_1)$$
$$+ k_{yy}^{tt}(y_p-y_1) + k_{yy}^{tr}(\phi_p-\phi_1) + c_{yz}^{tt}(\dot{z}_p-\dot{z}_1) + c_{yz}^{tr}(\dot{\theta}_p-\dot{\theta}_1)$$
$$+ k_{yz}^{tt}(z_p-z_1) + k_{yz}^{tr}(\theta_p-\theta_1) = 0 \qquad (6.10)$$

$$I_{p_{yy}}\ddot{\theta}_p + c_{p_\theta}(\dot{\theta}_p-\dot{\theta}_b) + k_{p_\theta}(\theta_p-\theta_b) + c_{zz}^{rr}(\dot{\theta}_p-\dot{\theta}_1) + c_{zz}^{rt}(\dot{z}_p-\dot{z}_1)$$
$$+ k_{zz}^{rr}(\theta_p-\theta_1) + k_{zz}^{rt}(z_p-z_1) + c_{zy}^{rr}(\dot{\phi}_p-\dot{\phi}_1) + c_{zy}^{rt}(\dot{y}_p-\dot{y}_1)$$
$$+ k_{zy}^{rr}(\phi_p-\phi_1) + k_{zy}^{rt}(y_p-y_1) = 0 \qquad (6.11)$$

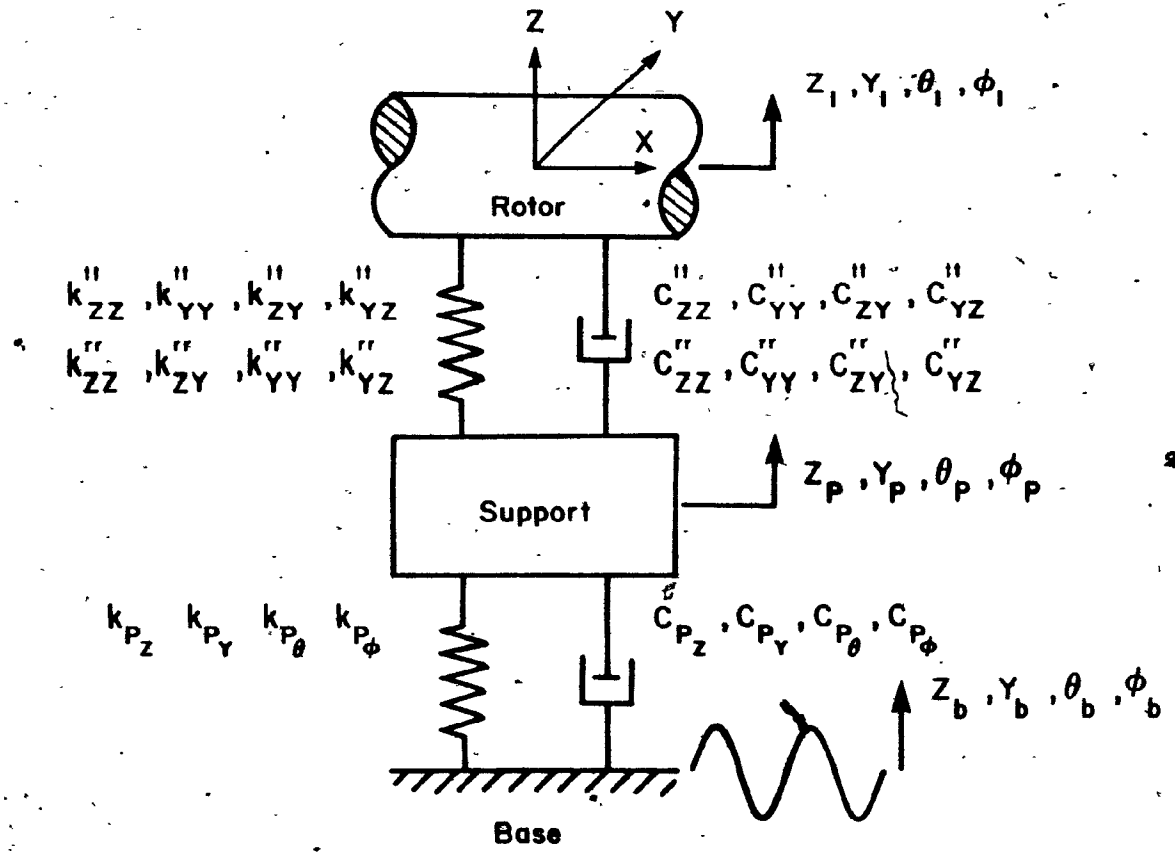

Figure 6.1 Support Model .

$$I_{p_{zz}}\ddot{\phi}_p + c_{p_\phi}(\dot{\phi}_p-\dot{\phi}_b) + k_{p_\phi}(\phi_p-\phi_b) + c^{rr}_{yy}(\dot{\phi}_p-\dot{\phi}_1) + c^{rt}_{yy}(\dot{y}_p-\dot{y}_1)$$

$$+ k^{rr}_{yy}(\phi_p-\phi_1) + k^{rt}_{yy}(y_p-y_1) + c^{rr}_{yz}(\dot{\theta}_p-\dot{\theta}_1) + c^{rt}_{yz}(\dot{z}_p-\dot{z}_1)$$

$$+ k^{rr}_{yz}(\theta_p-\theta_1) + k^{rt}_{yz}(z_p-z_1) = 0 \qquad (6.12)$$

Equations of motion of bearing:

$$c^{tt}_{zz}(\dot{z}_1-\dot{z}_p) + c^{tr}_{zz}(\dot{\theta}_1-\dot{\theta}_p) + k^{tt}_{zz}(z_1-z_p) + k^{tr}_{zz}(\theta_1-\theta_p)$$

$$+ c^{tt}_{zy}(\dot{y}_1-\dot{y}_p) + c^{tr}_{zy}(\dot{\phi}_1-\dot{\phi}_p) + k^{tt}_{zy}(y_1-y_p) + k^{tr}_{zy}(\phi_1-\phi_p) = F_{BZ} \qquad (6.13)$$

$$c^{tt}_{yy}(\dot{y}_1-\dot{y}_p) + c^{tr}_{yy}(\dot{\phi}_1-\dot{\phi}_p) + k^{tt}_{yy}(y_1-y_p) + k^{tr}_{yy}(\phi_1-\phi_p)$$

$$+ c^{tt}_{yz}(\dot{z}_1-\dot{z}_p) + c^{tr}_{yz}(\dot{\theta}_1-\dot{\theta}_p) + k^{tt}_{yz}(z_1-z_p) + k^{tr}_{yz}(\theta_1-\theta_p) = F_{BY} \qquad (6.14)$$

$$c^{rr}_{zz}(\dot{\theta}_1-\dot{\theta}_p) + c^{rt}_{zz}(\dot{z}_1-\dot{z}_p) + k^{rr}_{zz}(\theta_1-\theta_p) + k^{rt}_{zz}(z_1-z_p)$$

$$+ c^{rr}_{zy}(\dot{\phi}_1-\dot{\phi}_p) + c^{rt}_{zy}(\dot{y}_1-\dot{y}_p) + k^{rr}_{zy}(\phi_1-\phi_p) + k^{rt}_{zy}(y_1-y_p) = M_{BZ} \qquad (6.15)$$

$$c^{rr}_{yy}(\dot{\phi}_1-\dot{\phi}_p) + c^{rt}_{yy}(\dot{y}_1-\dot{y}_p) + k^{rr}_{yy}(\phi_1-\phi_p) + k^{rt}_{yy}(y_1-y_p)$$

$$+ c^{rr}_{yz}(\dot{\theta}_1-\dot{\theta}_p) + c^{rt}_{yz}(\dot{z}_1-\dot{z}_p) + k^{rr}_{yz}(\theta_1-\theta_p) + k^{rt}_{yz}(z_1-z_p) = M_{BY} \qquad (6.16)$$

Equations (6.9) to (6.16) can be rearranged and put in the matrix form by replacing the generalized displacements as shown:

$$
\left.
\begin{aligned}
(z_p - z_b) &= w_o \\
(z_1 - z_b) &= w_1 \\
(y_p - y_b) &= v_o \\
(y_1 - y_b) &= v_1 \\
(\theta_p - \theta_b) &= \bar{\theta}_o \\
(\theta_1 - \theta_b) &= \bar{\theta} \\
(\phi_p - \phi_b) &= \bar{\phi}_o \\
\text{and} \quad (\phi_1 - \phi_b) &= \bar{\phi}_1
\end{aligned}
\right\} \qquad (6.17)
$$

The present analysis does not consider the effect of coupling motions in the pedestal along Z and Y directions and hence, it is not included in the stiffness and damping matrices of the support structure.

The details of stiffness and damping matrices of the support structure are given in Appendix B.

The generalized displacement vector $\{q_i\}$ can be represented as

$$[w_i, v_i, \bar{\theta}_i, \bar{\phi}_i]^T. \qquad (6.18)$$

Now, the general form of equations of motion for N degrees of freedom of any rotor-bearing-pedestal systems can be written as,

$$[m]_{NXN} \{\ddot{q}\} + [c]_{NXN} \{\dot{q} - \dot{q}_b\} + [k]_{NXN} \{q - q_b\} = 0 \qquad (6.19)$$

Defining $\{q_r\} = \{q - q_b\}$, the equation (6.19) becomes,

$$[m]_{NXN} \{\ddot{q}_r\} + [c]_{NXN} \{\dot{q}_r\} + [k]_{NXN} \{q_r\} = -[m] \{\ddot{q}_b\} \quad (6.20)$$

where $\{q_b\} = \{q_{b_1}, 0, 0, \ldots, 0, q_{b_2}\}$

and q_{b_1} and q_{b_2} are support displacements at the left and right bearing-pedestal supports respectively.

Recasting the equation (6.20) in the first order form to get,

$$[M]_{2NX2N} \{\dot{Q}\} + [K]_{2NX2N} \{Q\} = \{F\} \quad (6.21)$$

where $$[M] = \begin{bmatrix} o & m \\ -m & c \end{bmatrix}, \quad [K] = \begin{bmatrix} -m & o \\ o & k \end{bmatrix}$$

$$\{Q\} = \begin{Bmatrix} \dot{q}_r \\ q_r \end{Bmatrix} \quad \text{and} \quad \{F\} = \begin{Bmatrix} o \\ -[m]\{\ddot{q}_b\} \end{Bmatrix}$$

Solving the homogenous form of equation (6.21), the eigenvalues and the right eigenvectors $[\Phi]$ are obtained. Because the rotor-bearing system is non-symmetric due to the presence of asymmetric cross-coupled fluid film stiffness and damping co-efficients, the right eigenvectors $[\Phi]$ are not orthogonal to each other and hence the left eigenvectors are necessary in order to decouple the system equations. The left eigenvectors $[\rho]$ are obtained by solving the homogenous form of the transposed system. The biorthogonality relation between the left and right eigenvectors is to decouple the overall mass [M] and stiffness [K] matrices of the system.

Using the transformation of the system,

$$\{Q(t)\} = [\Phi] \{n(t)\} \quad (6.22)$$

in equation (6.21) and premultiplying the resulting equation by $[\rho]^T$ the system equations are decoupled as shown:

$$[\hat{\mu}_i] \{\dot{\eta}_i\} + [\hat{\kappa}_i] \{\eta_i\} = [\rho]^T \{F_i\} \qquad i = 1,\ldots,2N \tag{6.23}$$

where $[\hat{\mu}] = [\rho]^T [M] [\Phi]$

and $[\hat{\kappa}] = [\rho]^T [K] [\Phi]$

Assuming steady-state solution of the form,

$$\{\eta(t)\} = \{\bar{\eta}(t)\} \; e^{j\omega t} \quad \text{and} \quad \{F\} = \{\bar{F}\} \; e^{j\omega t} \tag{6.24}$$

the equation (6.23) can be written as,

$$\{\eta_i(t)\} = \frac{\{\rho_i\}^T \{F_i\}}{(j\omega\mu_i + \kappa_i)} \qquad i = 1,\ldots,2N \tag{6.25}$$

The response in all modes is summed to obtain the total response as,

$$\{Q(t)\} = [\Phi] \{\eta(t)\} = [\Phi] [\mathscr{H}_i(j\omega)] [\rho]^T \{F_i\} \qquad i = 1,\ldots,2N \tag{6.26}$$

The frequency response of the rotor system is obtained as,

$$[H(j\omega)] = [\Phi] [\mathscr{H}(j\omega)] [\rho]^T \tag{6.27}$$

For multi-degree of freedom systems excited with a power spectral density S_F the resulting power spectral density of the amplitude S_R is given by,

$$S_R(\omega) = |H(j\omega)|^2 \; S_F(\omega) \tag{6.28}$$

Equation (6.28) can be written in the matrix form as shown,

$$[S_R(\omega)] = [\Phi] [\mathscr{H}(j\omega)] [\rho]^T [S_F(\omega)] [\Phi] [\mathscr{H}(-j\omega)] [\rho]^T \tag{6.29}$$

where $[\mathscr{H}(-j\omega)_{\sim}]$ is the complex conjugate of $[\mathscr{H}(j\omega)_{\sim}]$.

For white noise excitation, S_F is independent of frequency ω and simply it is S_0. The excitations coming through different supports are assumed to be statistically independent so that their cross correlations are zero and hence the matrix of excitation power spectral densities $[S_F]$ is a diagonal matrix with non-zero terms corresponding to the support location.

6.5 System Response

The rotor response due to random support excitations imparted to the system through different sources is studied. For example, the rotor system installed on board ships is subjected to random excitations by the wave motion; on the other hand, the machine installed on foundations is liable to random base motions of different order. However, in both the cases the response of the support point is highly controlled by the filtering effects of the structure itself. In view of this, it is quite reasonable to assume that the motions imparted to the pedestal of a rotor-bearing system to be a zero mean stationary Gaussian random process.

Based on this assumption, the power spectral densities of relative amplitudes of the two different rotor systems are obtained using the response evaluation technique discussed above. Rotor 1 has a single disk at the center of the shaft and is supported by fluid film bearings which in turn are mounted on identical pedestals at the two ends. The schematic diagram of this rotor system is shown in Fig. 2.1. The rotor details are given in Table 6.1. It is assumed that the base excitations at the two supports are of the same order along both vertical and horizontal

TABLE 6.1: Details of Rotor 1

Disk Mass	:	11 kg
Type of bearings	:	Plain cylindrical
Bearing diameter	:	0.0254 m
Bearing L/D ratio	:	1
Viscosity of oil at 25.5°C	:	0.0241 N. sec/m^2
Total length of rotor	:	0.5105 m
Modulus of elasticity of the material of shaft	:	2.145×10^{11} N/m^2
Shaft diameter	:	0.022 m
Disk diameter	:	0.2032 m
Pedestal mass	:	2.0412 kg
Transverse mass M.I. of pedestal	:	0.002191 kg.m^2
Polar mass M.I. of pedestal	:	0.00098 kg.m^2
Pedestal stiffnesses	:	0.8383×10^8 N/m

directions. The power spectral density of the resulting amplitudes at both the disk and the bearing locations of the rotor for the spin speed of 1000 rpm and in the frequency range of 0 to 500 rad/s is shown in Figs. 6.2 through 6.5.

For Rotor 1, equal bearing clearance values of 0.000188m are considered at both the ends with all other details of the rotor same as given in Table 6.1. The power spectral density plots of the relative amplitudes along Z and Y axes of the rotor system due to identical base excitations at the two supports in Z-direction are shown in Fig. 6.2. It is seen from the plots that there are two peaks in the response corresponding to the two eigenvalues of the system at 160.57 rad/sec and 263.04 rad/sec. It is observed from the plots that the amplitude power spectral densities are more predominant in the Z-direction for both disk and bearing locations than they appear in the Y-direction. However, the first peak corresponding to the eigenvalue of 160.57 rad/sec is very well pronounced in the amplitude response corresponding to the Y-direction. two eigenvalues become the two split critical speeds of the rotor system when they match with the corresponding rotational speeds of the rotor.

The power spectral densities of relative amplitude due to base excitations of equal value at both the supports in Y-direction are plotted as shown in Fig. 6.3. Here, again the amplitude spectrum shows two distinct peaks at the same frequencies as before. It is seen that the peak amplitude response in the Z-direction is larger at the second frequency of 263.04 rad/sec than that due to Y-direction.

The power spectral densities of relative amplitdue in both Z and Y directions are shown in Fig. 6.4 due to base excitations of equal

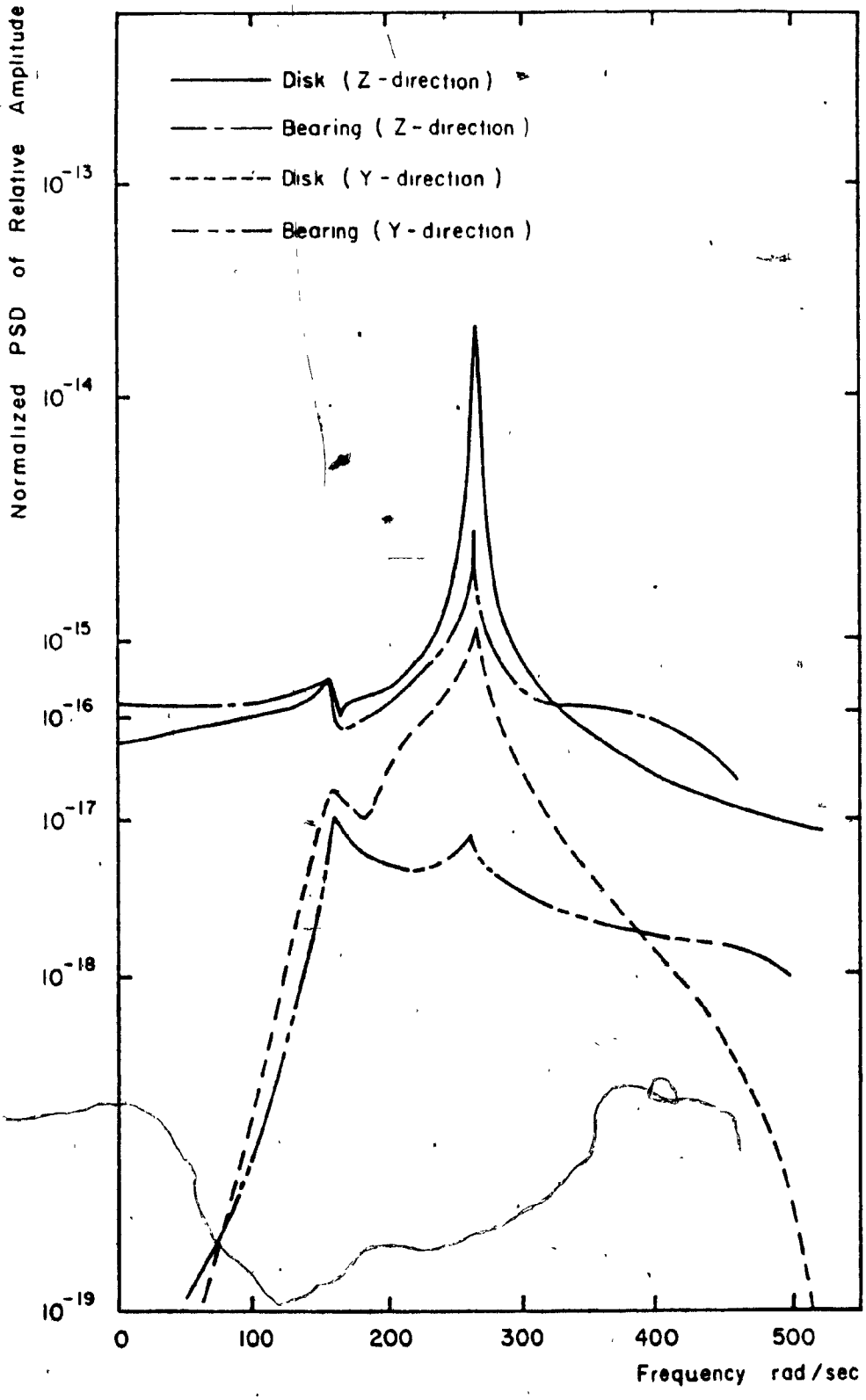

Figure 6.2 Amplitude Spectral Density Distribution Due to Support Excitations (Z - direction) at the Bearings of Rotor I .

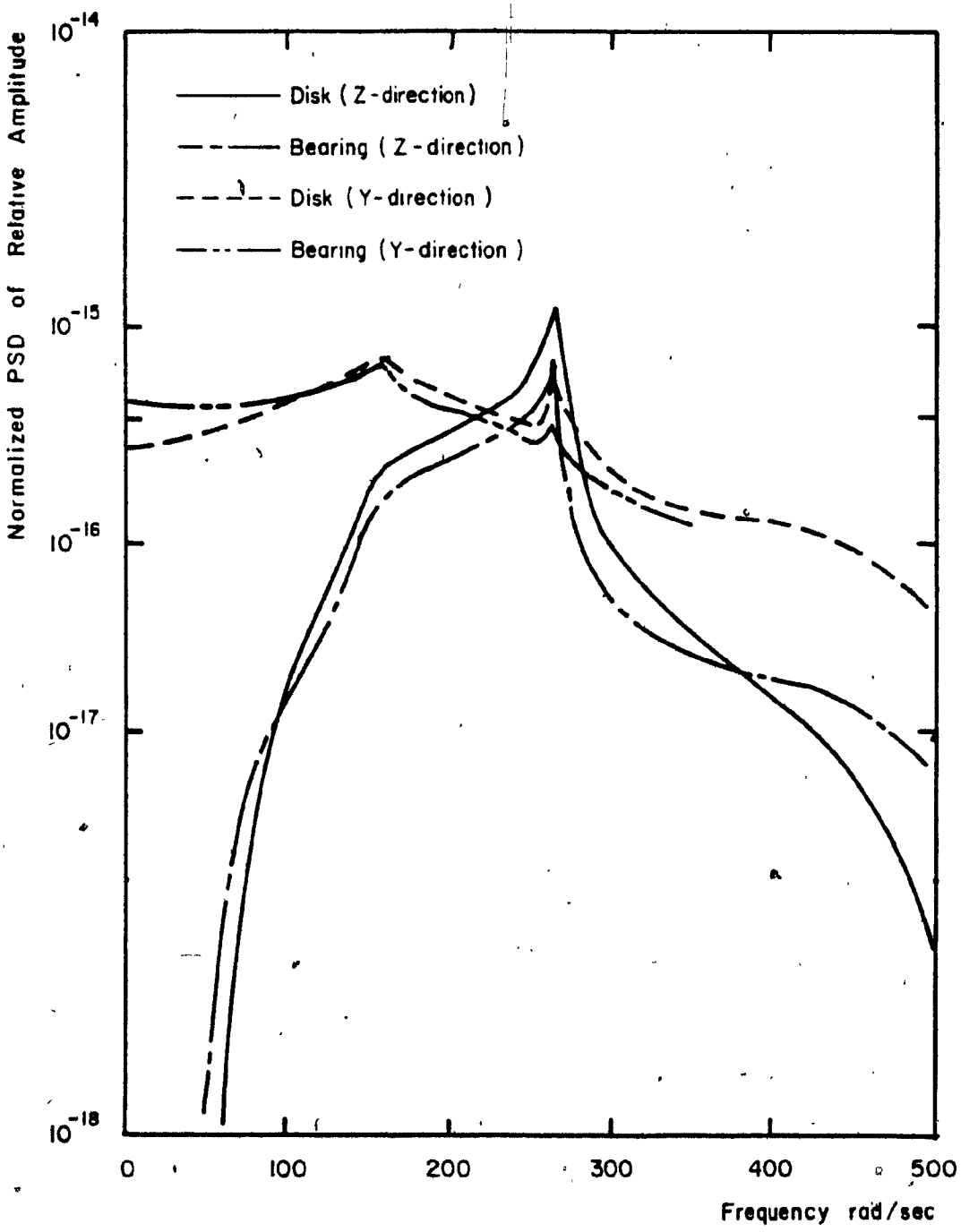

Figure 6.3 Amplitude Spectral Density Distribution Due to Excitations (Y-direction) at the Bearings of Rotor I.

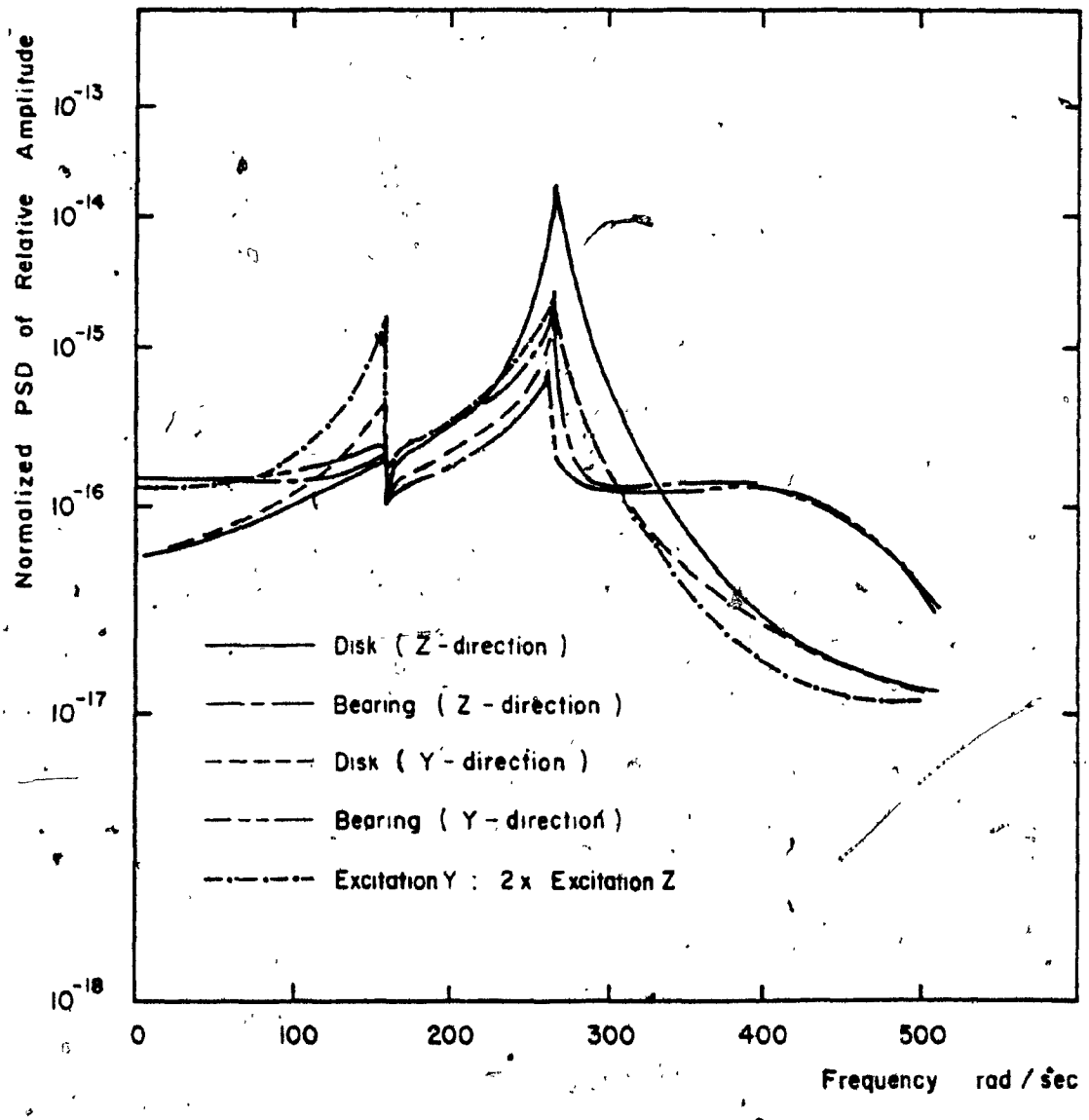

Figure 6.4 Amplitude Spectral Density Distribution Due to Support Excitations (both Z and Y directions) at the Bearings of Rotor I .

magnitude simultaneously in both Z and Y directions. This plot corresponds to the severity condition that can be simulated for the seismic type of excitations.

In practice, the base motions due to earthquake excitations are expected to be larger in the Y-direction because the support structure is comparatively more stiff in the Z-direction than in the Y-direction. Hence, it is reasonable to consider the base excitations along the Y-direction to be larger than the base motion that is expected along Z-directions, to simulate close to real conditions of the machine. As such, the relative power spectral densities of the machine due to base excitation which is 2 times larger in the Y-direction than the base motion along the Z-direction is plotted in chain lines at the disk location only as shown in Fig. 6.4. It is seen that the magnitude of the response of the rotor at disk location along Y-direction is larger in this case than those observed for the corresponding position before.

When such a rotor system (Rotor 1) is supported on a floating base, for example, on board a ship, the support excitations are felt not only in Z and Y directions, but also in their corresponding rotational directions, θ and ϕ respectively. Under severe wave motions arising out of rough sea conditions, a ship undergoes motions like pitch, roll and yaw. Under these conditions, it is important to study the influence of the base excitations due to rotational degrees of freedom on the relative amplitude PSDs in Z and Y directions of the rotor system.

The vertical and horizontal amplitude response spectrum due to rotational excitations about the Y axis at the two supports are shown in Figs. 6.5 and 6.6 respectively. It is observed from these plots that the

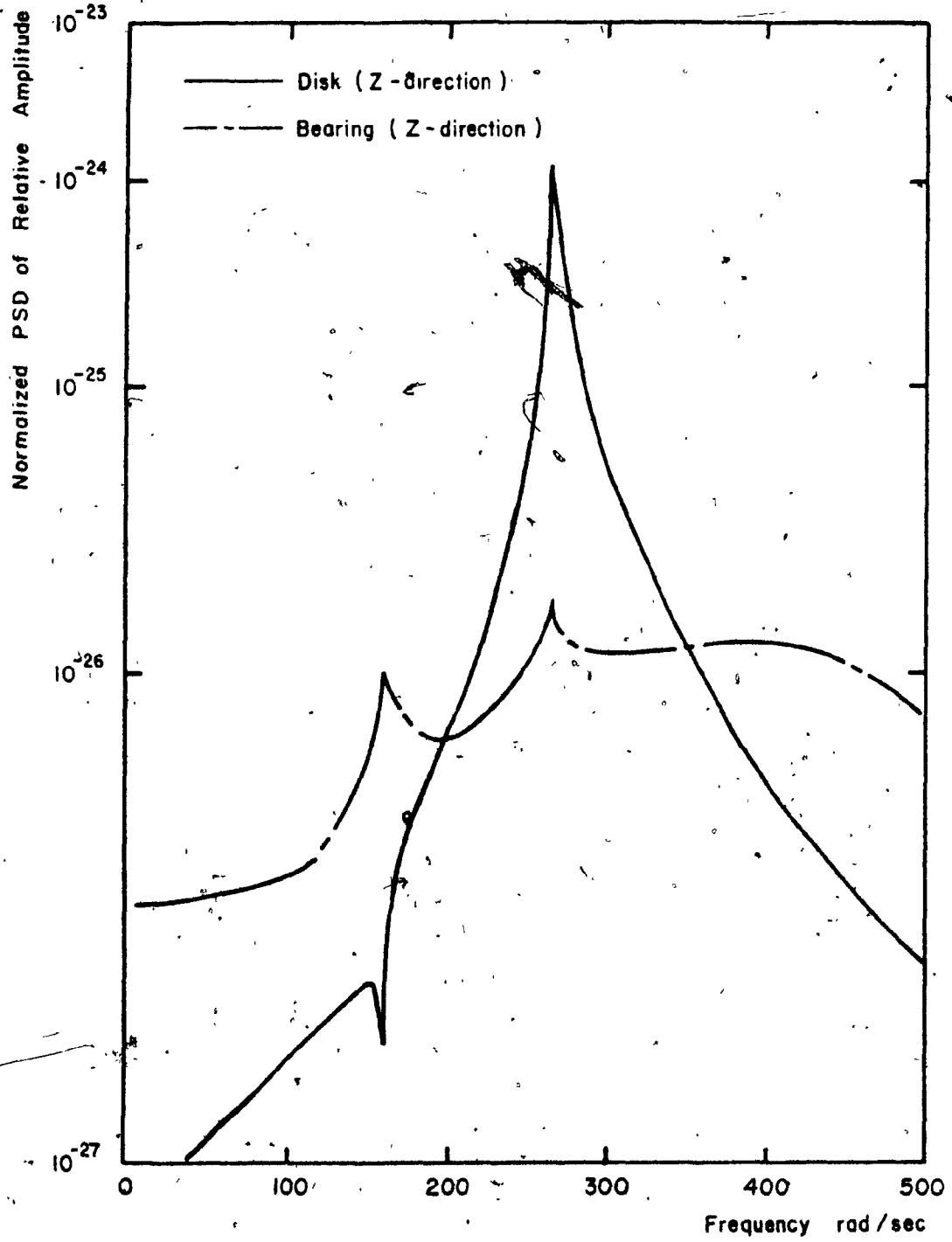

Figure 6.5 Amplitude Spectral Density Distribution Due to Rotational Support Excitation (θ – direction) at the Bearings of Rotor I.

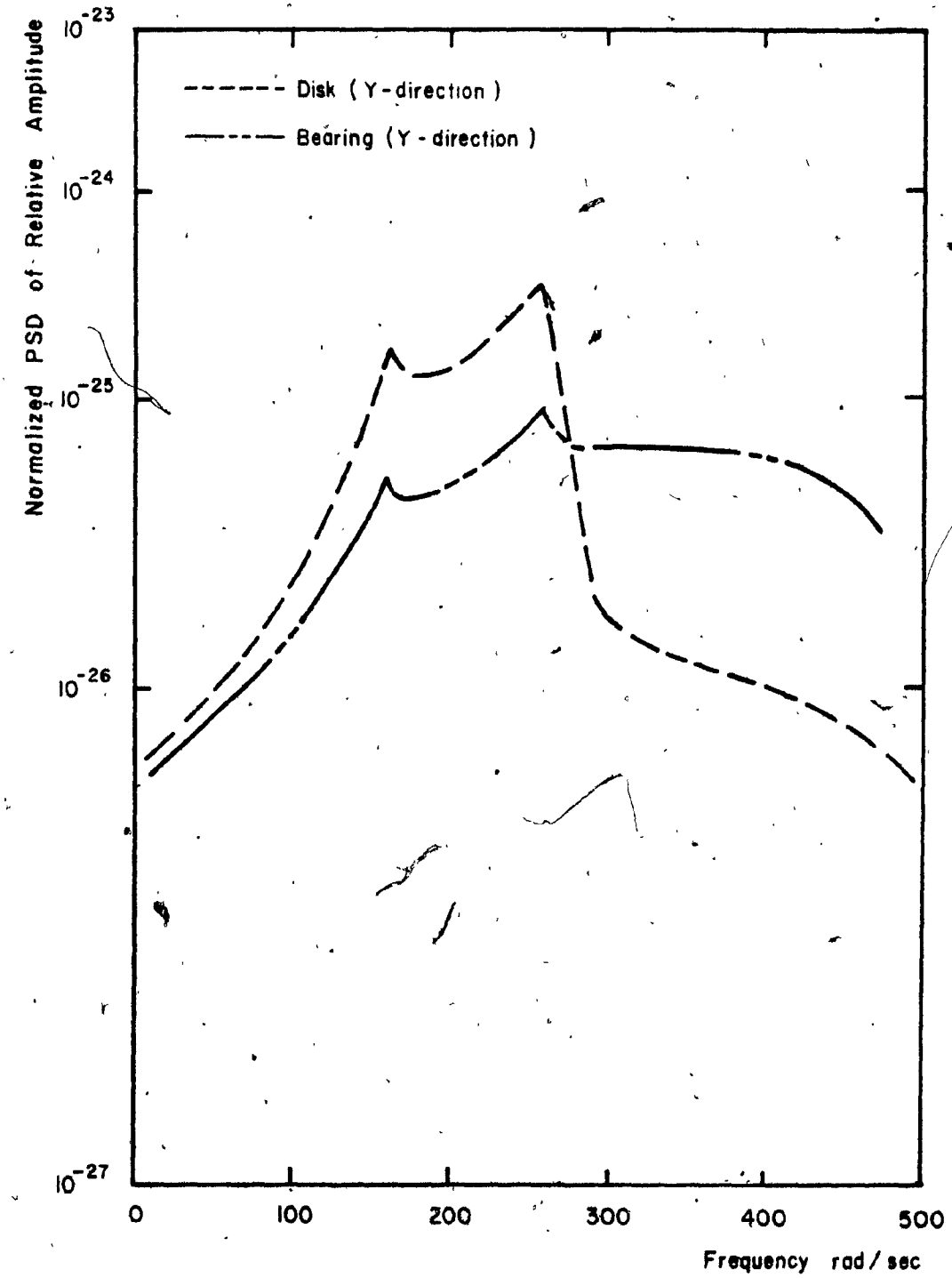

Figure 6.6 Amplitude Spectral Density Distribution Due to Rotational Support Excitations (θ -direction) at the Bearings of Rotor I.

response due to the rotational excitations are less than that due to translational base excitations. A similar trend in the response spectrum is observed due to rotational excitations about Z-axis.

For this configuration of rotor, the normalized unbalance response is also shown in Fig. 6.7 to have an ideal of the deterministic response pattern.

Thus far, a simple rotor system (Rotor 1) was studied for its response due to random support excitations. In practice, large rotor systems like turbine rotors consist of different components along the shaft and also have larger span between supports. Such a large rotor system is considered and it is called Rotor 2. The details of this rotor system are given in Table 6.2. This rotor consists of two overhung disks at the two ends and a rigid flange coupling connecting the two ends of the shaft at the center. This rotor is mounted on fluid film bearings at two points and in turn is supported by pedestals as shown in Fig. 6.8. The mechanical rigid coupling is designed as shown by Bannister [96]. It is assumed that the structure gets excitation through one support point only whereas the other support point does not get excited. Under this condition, the effect of the random support excitation on the response of the structure at the vulnerable points like bearings, mechanical coupling etc., is studied.

Base excitations are provided in the form of translational motion along Z and Y directions. The power spectral densities of relative amplitude of this rotor system at the two disks and coupling locations due to base excitations along Z and Y directions are plotted as shown in Figs. 6.9 through 6.12. The effect of moment stiffness and damping

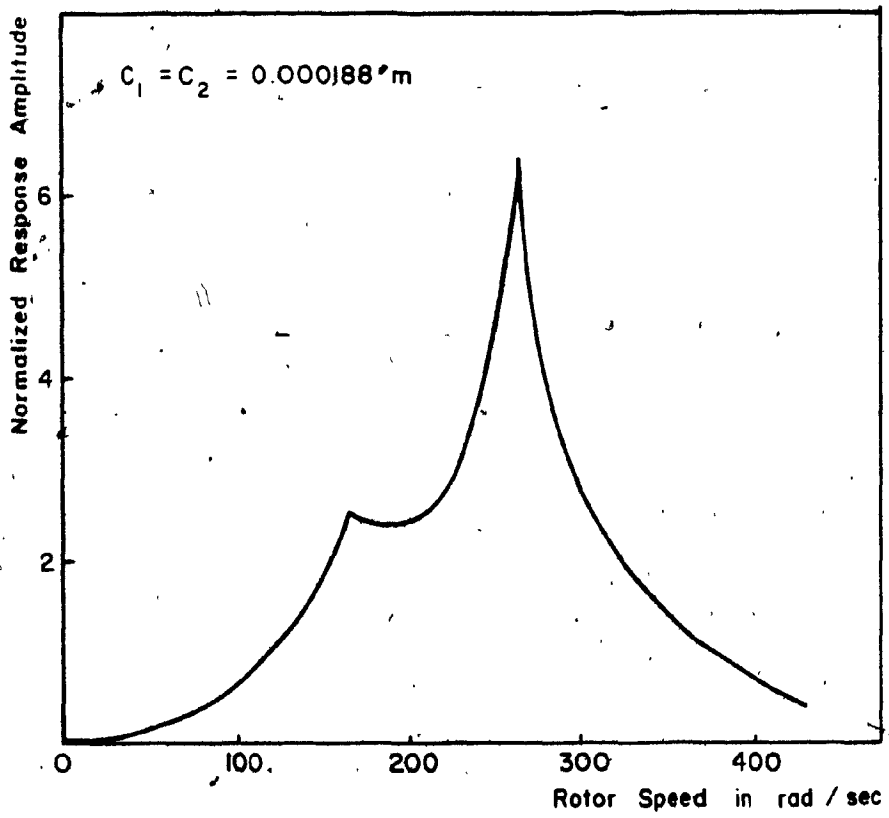

Figure 6.7 Normalized Unbalance Response of Rotor I.

TABLE 6.2: Details of Rotor 2

Diameter of shaft	:	0.127 m
Total length of the shaft	:	3 m
Mass of disk 1	:	240 kg
Mass of disk 2	:	661.2 kg
Diameter of disk 1	:	0.3048 m
Diameter of disk 2	:	0.3048 m
Thickness of disk 1	:	0.043 m
Thickness of disk 2	:	0.118 m

Transverse mass M.I. of disk 1,

$$I_{zz} = I_{yy} = 1.21666 \text{ kg.m}^2$$

Transverse mass M.I. of disk 2,

$$I_{zz} = I_{yy} = 4.6064 \text{ kg.m}^2$$

Pedestal data:

Mass of the pedestal 1	:	204.12 kg
Mass of the pedestal 2	:	226.8 kg

Stiffness of pedestals:

$$k_{p_{z1}} = 0.23642 \times 10^{10} \text{ N/m}$$

$$k_{p_{y1}} = 0.355 \times 10^{9} \text{ N/m}$$

$$k_{p_{\theta 1}} = 0.23642 \times 10^{10} \text{ N.m/rad}$$

$$k_{p_{\phi 1}} = 0.742 \times 10^{8} \text{ N.m/rad}$$

$$k_{p_{z2}} = 0.122588 \times 10^{10} \text{ N/m}$$

$$k_{p_{y2}} = 0.184 \times 10^{9} \text{ N/m}$$

$$k_{p_{\theta 2}} = 0.122588 \times 10^{10} \text{ N.m/rad}$$

$$k_{p_{\phi 2}} = 0.380 \times 10^{8} \text{ N.m/rad}$$

...2/

TABLE 6.2: Details of Rotor 2 (continued)

Bearing details:

Weight on bearing 1	:	17747.52 N
Weight on bearing 2	:	23930.24 N
Bearing L/D ratio	:	1
Viscosity of oil at 25.5°C	:	0.0138 N.sec/m^2
Bearing clearance	:	0.0001524 m

Rigid coupling details:

Mass of the coupling	:	448.82 kg
Diameter of the hub	:	0.020285 m
Young's modulus for the material of coupling	:	1.9718×10^{11} N/m^2
Equivalent second moment of area of coupling	:	7.357×10^{-5} m^4
Bolt circle of diameter of coupling	:	0.2811 m

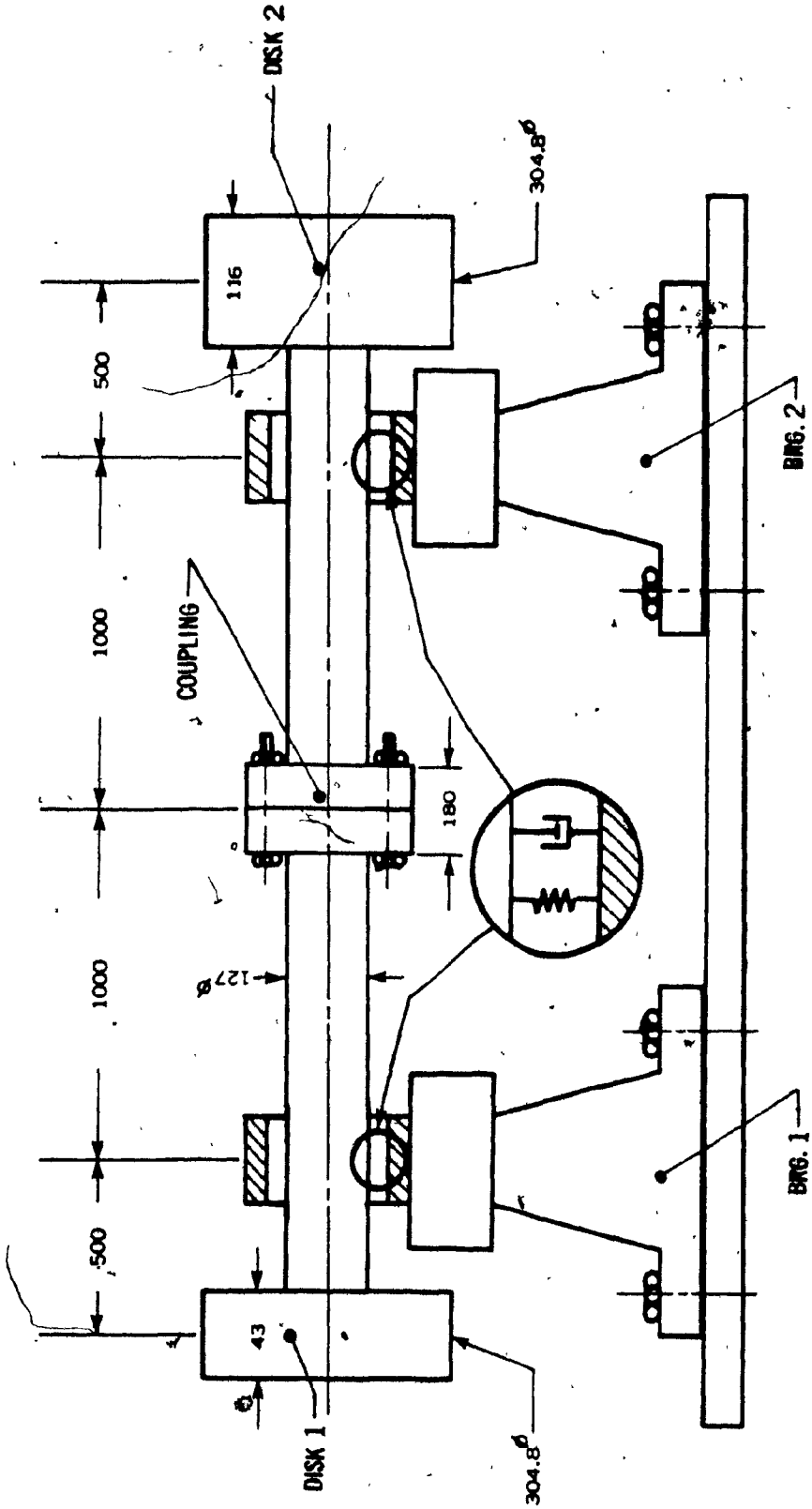

Figure -6.8 - Two Disk Rotor - Bearing System (Rotor 2).

offered by the fluid film is considered. The power spectral densities of resulting amplitudes for base excitations which are predominant at specific locations and directions are determined and plotted for a constant rotor speed of 2400 rpm and for the frequency range of 0 to 1000 rad/sec.

The power spectral density of relative amplitude of the rotor due to base excitations only in Z-direction at the left support is shown in Fig. 6.9. The system exhibits six eigenvalues at the range of frequencies of interest. The six eigenvalues are 278.63, 346.65, 395.8, 544.74, 672.54 and 934.43 rad/sec. The response power spectral densities are calculated at the locations of the disk and the coupling. It is seen from these plots that the power spectral density of amplitude of the rotor system along the Z-direction has a prominent peak at the disk 1 location.

The power spectral density of relative amplitude due to base excitations in Z-direction only at the right end support are shown in Fig. 6.10. It is again seen that the peak amplitude response is larger at disk 2 location compared to the responses at all other locations. However, the peak response at the coupling location is predominant at one of the eigenvalues which match with the running speed of the rotor at the frequency and this trend is the same as was observed in the plot of Fig. 6.9.

Similar plots are obtained for the horizontal excitations at the support point considered one at a time and are shown in Figs. 6.11 and 6.12. They again show the peak responses are predominant at one or more natural frequencies of the system.

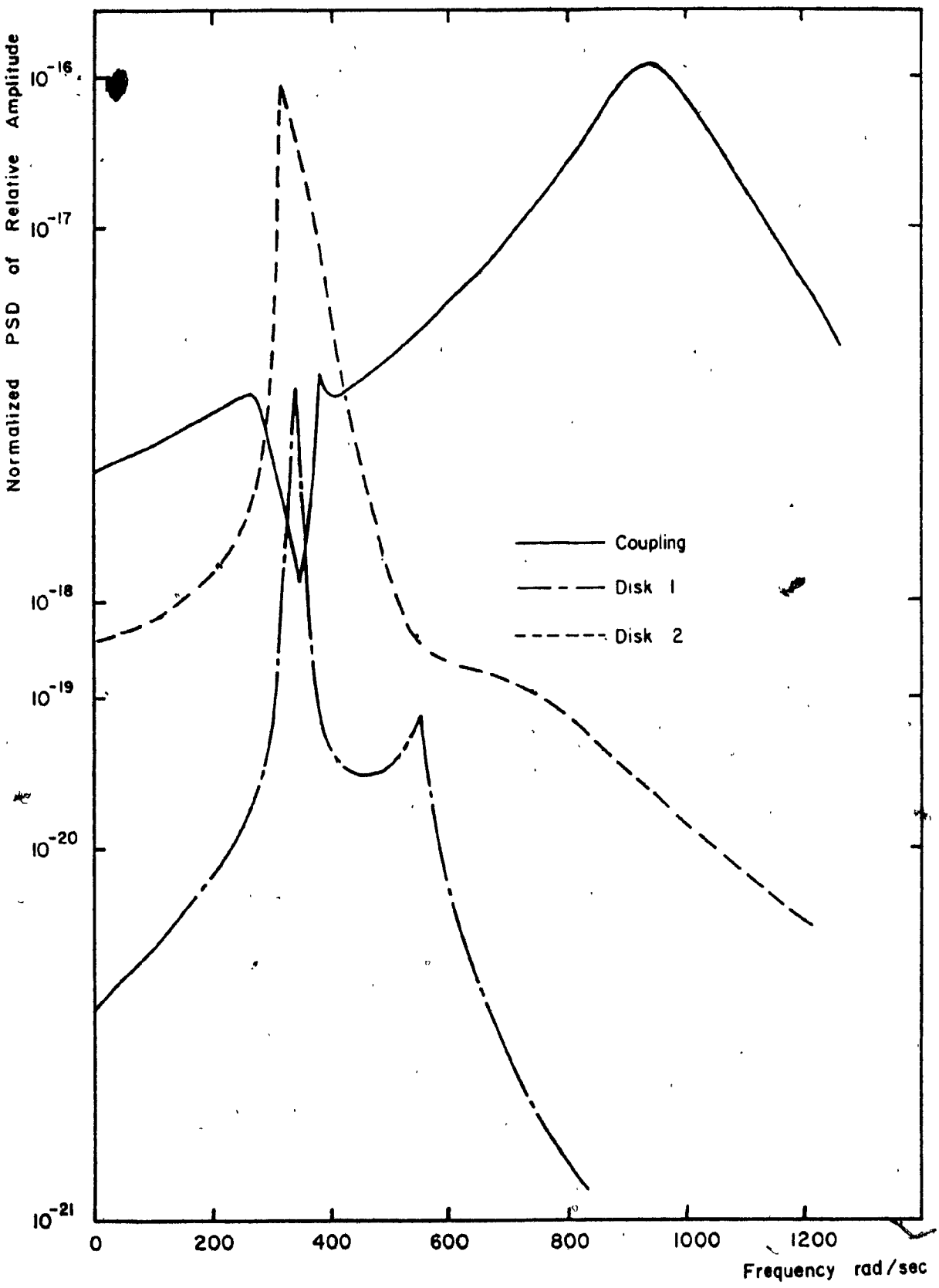

Figure 6.9 Amplitude Spectral Density Distribution Due to Support Excitations (Z - direction) at Bearing 1 .

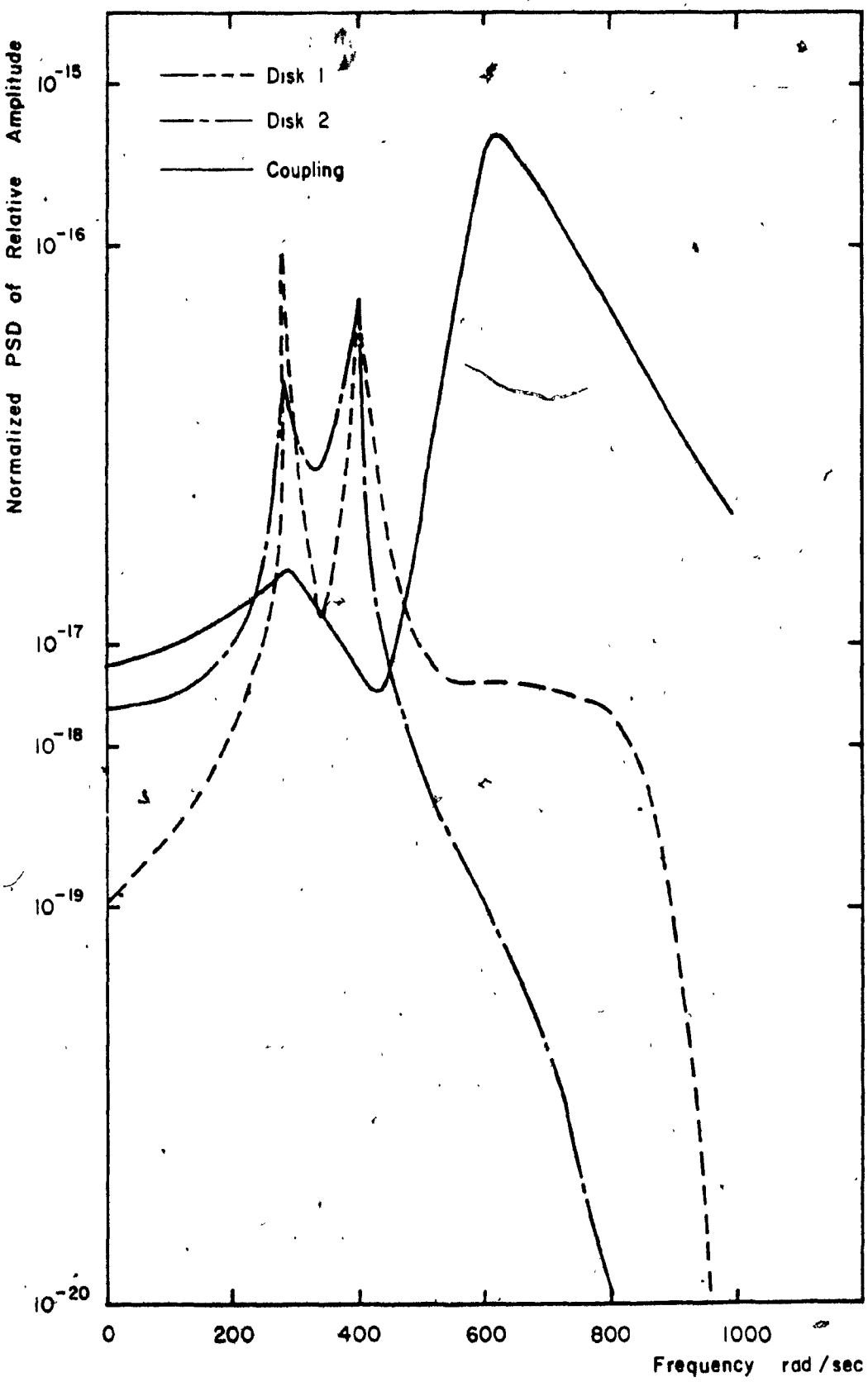

Figure 6.10 Amplitude Spectral Density Distribution Due to Support Excitations (Z-direction) at Bearing 2.

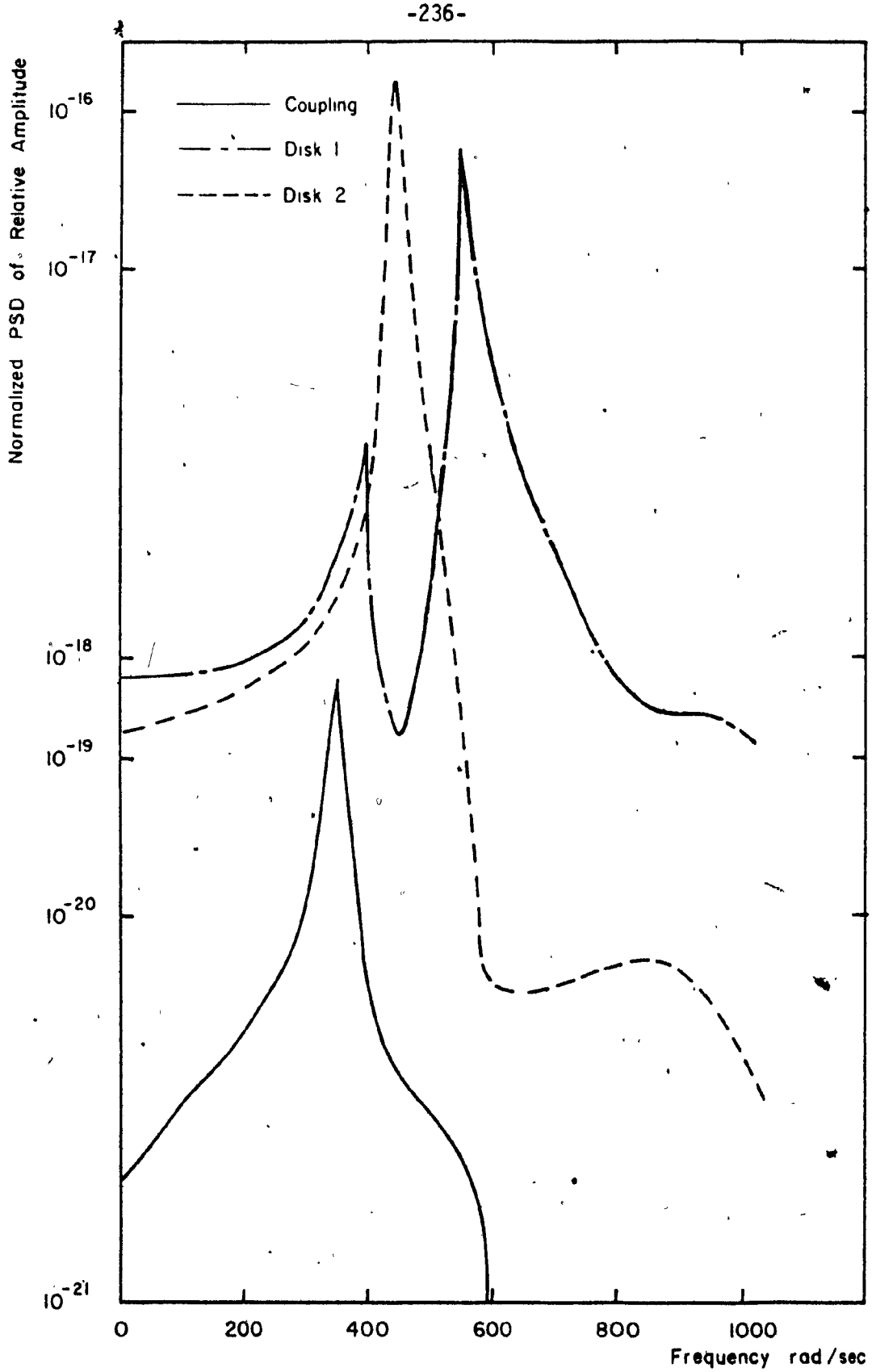

Figure 6.11 Amplitude Spectral Density Distribution Due to Support Excitations (Y-direction) at Bearing 1.

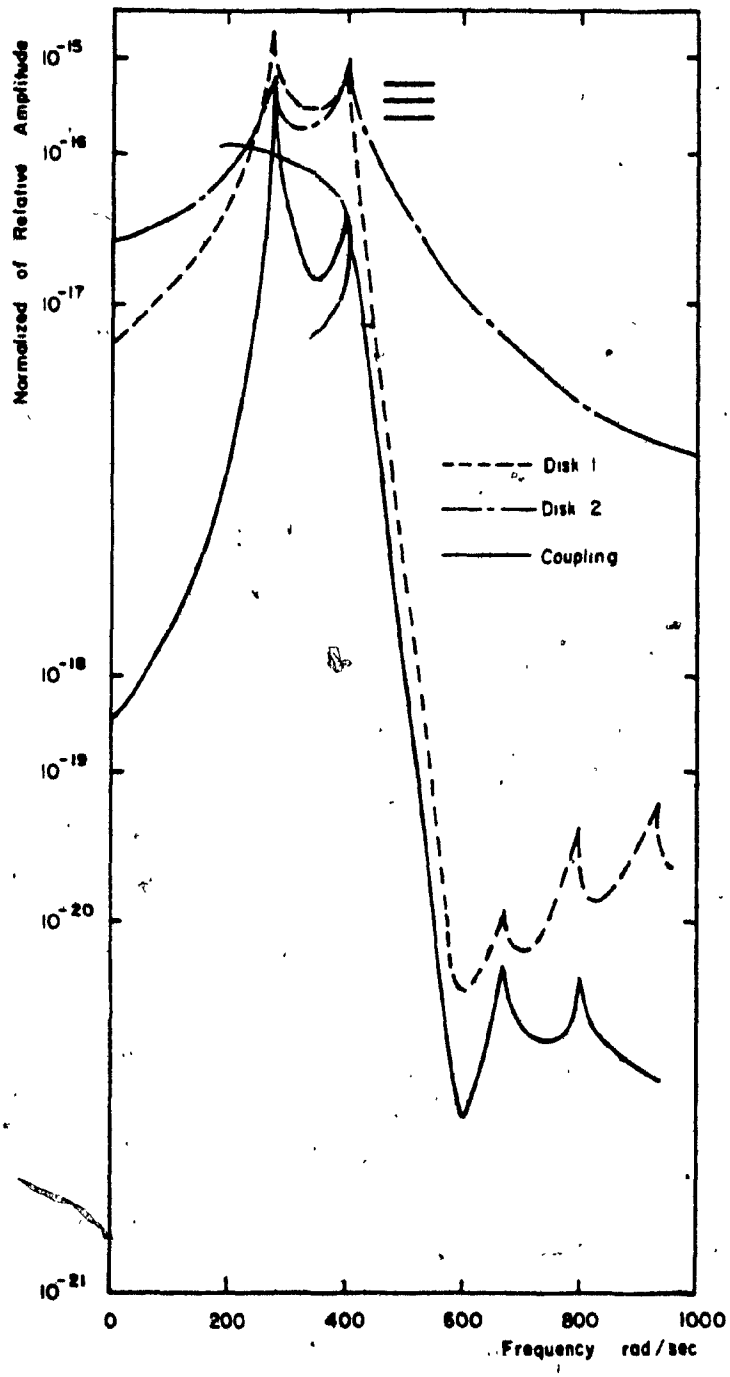

Figure 6.12 Amplitude Spectral Density Distribution Due to Support Excitations (Y-direction) at Bearing 2.

6.6 Conclusions

The support structure of a rotor system is modelled. The response power spectral density of the rotor system subjected to support random excitations in different degrees of freedom is studied using modal analysis. The power spectral densities of relative amplitudes are obtained at different locations of two different rotor systems (Rotor 1 and Rotor 2) and are presented. It was observed that,

(i) Significant response in the vertical direction can occur when the rotor experiences support excitations in the horizontal direction and vice versa because of coupling in the oil film co-efficients.

(ii) Translational response resulting from support excitations in the rotational directions is not significant.

In this analysis only fluid film translational and rotational co-efficients are considered. However, for a large rotor system, the inclusion of coupling effect of these co-efficients will improve the model and provide better response values. Moreover, the pedestal coupling motions in Z and Y directions are not taken into account. An improved model of the rotor system can be obtained by including the above mentioned coupling effects both in the fluid film bearing and support structure.

CHAPTER 7

CONCLUSIONS AND RECOMMENDATIONS

The dynamic behavior of a simple rotor system supported on hydrodynamic bearings is studied. Orbit diagrams at the disk as well as at the bearing locations are obtained for various configurations of the rotor and the conditions for the occurrence of backward whirl are derived.

Modal analysis is used to obtain all the required rotor system behavior such as unbalance response, critical speeds, individual system modes and the threshold speed of instability etc. The above dynamic behavior of the simple rotor system is verified by experiments. Also, the modal parameters of the rotor are identified through modal testing. The support structure and suspension are modelled in a comprehensive manner and included in the analysis. Accordingly, the rotational springs and dampers are introduced in the model for the fluid film in the finite cylindrical bearing in addition to the translational springs and dampers. The rotational stiffness and damping co-efficients for the fluid film are obtained by solving the Reynolds equations governing the fluid film behavior and are graphically presented in a nondimensional form against Sommerfeld number. However, the properties of support pedestals for the bearings have also been considered in this study and, as a result, an overall rotor-bearing pedestal system is developed using finite element model. Large size matrices, arising out of the finite element assembly for the several elements considered, are reduced using a modal condensation technique. The dynamic behavior of such a rotor system is obtained for specified unbalance conditions at the disk and also due to

stochastically varying base excitations.

7.1 Conclusions

The conclusions arrived on the basis of the results of this investigation described in the different chapters of the thesis are summarized and given below:

(i) A proper design of the rotor system must consider the response at the bearings also, in addition to the response at other important locations, such as those where disks are mounted. This is because when the response at the bearings are of the order of magnitude of bearing clearance, a linear analysis is not sufficient to study the rotor behavior and also the operating range cannot be chosen at the critical region.

(ii) The configuration of a single disk rotor supported on hydrodynamic bearings at the two ends, can be altered by adjusting the bearing clearances in the two bearings and also by adjusting the location of the disk so as to have a specific load distribution on the two bearings. Consequently, the response pattern of the rotor changes, depending upon the rotor configurations.

(iii) For a particular configuration of a simple rotor which exhibits split criticals, a backward whirl condition is obtained in between the criticals, depending upon the bearing parameters and the operating speed. Since, backward whirl provides stress reversals in the rotor, it can be avoided by suitably changing the configuration of the rotor.

(iv) Since modal analysis provides all the system information such as unbalance response, critical speeds, the modal behavior and also the stability of the system in a single procedure, this is preferred over

other direct methods. The discrepancy between the dynamic responses obtained by modal analysis and those by other direct methods, in most cases is negligible and in some cases it is less than 1%.

(v) The modal testing is normally performed for stationary structures in order to identify the modal parameters of the structure. For a simple rotor system, the method provides the critical frequencies which are found closer to those obtained by analysis. This forms a sound basis that the modal testing technique can be extended to more complex structures in order to obtain their modal parameters.

(vi) The predicted dynamic behavior of a simple rotor system, due to specified unbalance in the disk, achieved using the rotational dynamic film properties along with the translational film properties in the comprehensive model of the bearing does not change significantly when compared with that obtained using only translational fluid film co-efficients in the simple model of the bearing. However, for a large rotor system such as a three disk rotor model used by Kikuchi [14], the dynamic characteristics obtained using the comprehensive model of the finite bearing provide results which are closer to those obtained by experiments.

(vii) Significant response in the vertical plane can occur when the rotor experiences support excitations in the horizontal plane and vice versa due to the coupling in the fluid film co-efficients.

(viii) Translational response resulting from support excitations in the rotational directions, which are considered to be random stationary Gaussian process, is not significant.

7.2 Recommendations for Future Work

Some suggestions for the possible future work are given below:

1. The rotational fluid film properties can be evaluated for different types of bearings such as elliptical, tilted pad bearings etc., with different L/D ratios so that they can be used as design charts in the nondimensional form for the analysis of large and complex rotor systems.

2. In the present investigation, the rotational stiffness and damping fluid film co-efficients are obtained for small perturbations around the mean position of the journal. This work can be extended for larger tilt angles and displacements of the journal and the resulting non-linear fluid film properties can be obtained.

3. In the transfer matrix procedure, the mass matrix is a diagonal matrix and the stiffness properties are obtained assuming cantilever beam theory. These matrices can be obtained based on a consistant formulation of properties so that the accuracy and the computational complexity of this method can be compared with those obtained by the finite element method.

4. With the comprehensive support model achieved in the present investigation, the response behavior of rotor systems can be analyzed with the non-stationary base motions.

5. Fluid filled disks can be introduced in the rotor system and they can be modelled to study their influence on the stability of system with a view to limiting the unstable regions which are obtained in the case of rotors supported on hydrodynamic bearings.

6. The dynamic characteristics obtained by the variation of different clearance values at the bearing supports show a certain pattern; hence this study may be undertaken for a whole range of clearance parameters for completion.

7. In the case of transient vibration of rotors, coupled torsional-bending motions are possible, and hence this coupled effect is important and that kind of study is recommended for rotor systems.

8. A trend analysis can be carried out with nonlinear bearings in order to compare all the dynamic information of the system with those obtained using linear bearing theory.

REFERENCES

1. Jeffcott, H.H., "The Lateral Vibrations of Loaded Shafts in the Neighbourhood of a Whirling Speed - The Effect of Want of Balance", Phil. Mag., Series 6, Vol. 37, 1919, p. 304.

2. Prohl, M.A., "A General Method for Calculating Critical Speeds of Flexible Rotors", Transactions of ASME, Journal of Applied Mechanics, Vol. 12, 1945, pp. A-142 to A-148.

3. Myklestad, N.O., "A New Method of Calculating Natural Modes of Uncoupled Bending Vibration of Airplane Wings and Other Types of Beams", Journal of Aeronautical Science, April 1944, pp. 153-162.

4. Bishop, R.E.D. and Gladwell, G.M.L., "The Receptances of Uniform and Non-uniform Rotating Shafts", Journal of Mechanical Engineering Science, Vol. 1, No. 1, 1959, pp. 78-91.

5. Green, R.B., "Gyroscopic Effects on the Critical Speeds of Flexible Rotors", Journal of Applied Mechanics, December, 1948, pp. 369-376.

6. Eshleman, R.L. and Eubanks, R.A., "On the Critical Speeds of a Continuous Rotor", Journal of Engg. for Industry, Trans. ASME, 91(4B), November 1969, pp. 1180-1188.

7. Tondl, A., Some Problems of Rotor Dynamics, Chapman Hall, London, 1965.

8. Yamamoto, T., Ota, H. and Kono, K., "On the Unstable Vibrations of a Shaft with Unsymmetrical Rotor", Applied Mechanics, June 1968, p. 313.

9. Ardayfio, D. and Frohrib, D.A., "Vibration of an Asymmetrically Mounted Rotor with Gyroscopic Effects", Journal of Engg. for Industry, Trans. ASME, February 1976, pp. 327-331.

10. Rao, J.S., "Out of Balance Response of Turbo-Alternator Rotors", Bharat Heavy Electricals Limited, Hyderabad, India, 1980.

11. Rao, J.S., Bhat, R.B. and Sankar, T.S., "Effect of Damping on the Synchronous Whirl of a Rotor in Hydrodynamic Bearings", Trans. CSME, Vol. 6, No. 3, 1981.

12. Kramer, E., "Computation of Unbalance Vibrations of Turbo-rotors", ASME Publication, Paper No. 77-DET-13.

13. Lund, J.W., "Rotor Bearings Dynamics Design Technology, Part V: Computer Program Manual for Rotor Response and Stability", Mechanical Technology Inc., Latham, N.Y., AFAPL-Tr-65-45, 1965.

14. Kikuchi, K., "Analysis of Unbalance Vibration of Rotating Shaft System with many Bearings and Disks", Bulletin of JSME, 13, 61 (1970).

15. Rao, J.S., "Time Marching Transfer Matrix Techniques for Transient Analysis of Rotors", Proceedings of 1985 Bently Rotor Dynamics Research Corporation Symposium, June 1985, Carson City, Nevada.

16. Gunter, E.J., Choy, K.C. and Allaire, P.E., "Modal Analysis of Turbo-rotors using Planar Modes-Theory", Journal of the Franklin Institute, Vol. 305, No. 4, April 1978.

17. Berthier, P., Ferraris, G. and Lalanne, M., "Prediction of Critical Speed, Unbalance and Non-Synchronous Forced Response of Rotor", Shock and Vibration Bulletin, 53, Part 4, May 1983, pp. 103-111.

18. Lund, J.W., "Modal Response of a Flexible Rotor in Fluid Film Bearings", Journal of Engg. for Industry, Trans. ASME, Vol. 96, 1974, p. 525.

19. Saito, S. and Azuma, T., "Balancing of Flexible Rotors by the Complex Modal Method", Paper No. 81-DET-46, ASME Design Engineering Conference, Hartford, 1981.

20. Childs, D.W., "Two Jeffcott-Based Modal Simulation Models for Flexible Rotating Equipment", Journal of Engineering for Industry, Trans. ASME, Vol. 97, No. 3, August 1975, pp. 1000-1014.

21. Childs, D.W., "A Modal Transient Simulation Model for Flexible Asymmetric Rotors", Journal of Engineering for Industry, Trans. ASME, Vol. 98, No. 1, February 1976, pp. 312-319.

22. Glasgow, D.A. and Nelson, H.D., "Stability Analysis of Rotor-Bearing Systems Using Component Mode Synthesis", Journal of Mechanical Design, Trans. ASME, Vol. 102, April 1980, pp. 352-359.

23. Bhat, R.B., "Unbalance Response of a Single Mass Rotor on Fluid Film Bearings Using Modal Analysis", Proceedings of the Ist International Modal Analysis Conference held at Orlando, 1982, p. 648.

24. Bhat, R.B., Subbiah, R. and Sankar, T.S., "Dynamic Behavior of a Simple Rotor With Dissimilar Hydrodynamic Bearings by Modal Analysis", Journal of Vibration, Acoustics, Stress and Reliability in Design, Trans. ASME, April 1985, Vol. 107, No. 2, pp. 267-269.

25. Ruhl, R.L. and Booker, J.F., "A Finite Element Model for Distributed Parameter Turborotor Systems", Journal of Engg. for Industry, Trans. ASME, February 1972, pp. 126-132.

26. Nelson, H.D. and McVaugh, J.N., "The Dynamics of Rotor-Bearing Systems Using Finite Elements", Journal of Engineering for Industry, Trans. ASME, Vol. 98, No. 2, May 1976, pp. 593-600.

27. Zorzi, E.S. and Nelson, H.D., "Finite Element Simulation of Rotor-Bearing Systems with Internal Damping", Journal of Engineering for Power, Trans. ASME, Vol. 99, No. 1, January 1977, pp. 71-76.

28. Zorzi, E.S. and Nelson, H.D., "The Dynamics of Rotor-Bearing Systems with Axial Torque-A Finite Element Approach", Journal of Mechanical Design, Trans. ASME, Vol. 102, January 1980, pp. 158-161.

29. Nelson, H.D., "A Finite Rotating Shaft Element Using Timoshenko Beam Theory", Journal of Mechanical Design, Trans. ASME, Vol. 102, October 1980, pp. 793-803.

30. Craig, R.R. and Bampton, M.C.C., "Coupling of Substructures for Dynamic Analyses", AIAA Journal, Vol. 6, July 1968, pp. 1313-1319.

31. Rouch, K.E. and Kao, J.S., "Dynamic Reduction in Rotor Dynamics by the Finite Element Method", Journal of Mechanical Design, Trans. ASME, Vol. 102, April 1980, pp. 360-368.

32. Guyan, R.J., "On the Reduction of Stiffness and Mass Matrices", American Institute of Aeronautics and Astronautics Journal 3, 380, 1965.

33. Ookuma, M. and Nagamatsu, A., "Vibration Analysis by Multiple Component Mode Synthesis Method", Bull. JSME, Vol. 27, No. 228, June 1984, pp. 1288-1293.

34. Yamamoto, T., "On the Critical Speeds of a Shaft", Memoirs of the Faculty of Engineering, Nagoya University, Japan, Vol. 6, No. 2, November 1954, pp. 106-174.

35. Wehrli, Ch., "On the Stability of Periodic Systems in Connection with Rotating Shafts", IUTAM Symposium on Dynamics of Rotors, August 12-16, 1974, Springer-Verlag, 1975, pp. 546-563.

36. Carnegie, W. and Thomas, J., "The Effects of Shear Deformation and Rotary Inertia on the Lateral Frequencies of Cantilever Beams in Bending", ASME Paper 71-Vibr-79.

37. Wojnowski, R.F. and Fancett, "Critical Speeds of Two Bearing Machines with Overhung Weight", Journal of Engineering for Industry, Trans. ASME, Vol. 83, Series B, No. 4, November 1961, pp. 377-382.

38. Glienicke, J., "Experimental Investigation of the Stiffness and Damping Coefficients of Turbine Bearings and Their Application to Instability Prediction", Proc. I.Mech.E., Vol. 181, Part 3B, Paper 13, 1966-67, pp. 116-129.

39. Kellenberger, W., "Double-Frequency Accelerations in Turbogenerator Rotors Resulting From Anisotrophy in the Bearings", Proc. I.Mech.E. Paper No. C312/80, 1980, pp. 415-420.

40. Rao, J.S., "Conditions for Backward Synchronous Whirl of a Flexible Rotor in Hydrodynamic Bearings", Mechanism and Machine Theory Journal, Vol. 17, No. 2, 1982, pp. 143-152.

41. Den Hartog, J.P., Mechanical Vibrations, McGraw-Hill Book Co., 1956.

42. Newkirk, B.L., "Varities of Shaft Disturbances Due to Fluid Films in Journal Bearings", Trans. ASME, Vol. 78, 1956, p. 985.

43. Morrison, D. and Patterson, A.N., "Criteria for Unstable Oil-Whirl of Flexible Rotors", The Institute of Mech. Eng. Proceedings, Vol. 179, Part 3J, 1964-65, p. 45.

44. Hagg, A.C., "The Influence of Oil Film Journal Bearings on the Stability of Rotating Machines", Journal of Applied Mechanics, Vol. 68, 1946, p. 211.

45. Robertson, D., "Whirling of Journal in Sleeve Bearings", Phil. Mag., Vol. 15, 1933, p. 113.

46. Gunter, E.J., Dynamic Stability of Rotor Bearing Systems, NASA Report SP-113, 1966.

47. Rao, J.S., "Instability of Rotors in Fluid Film Bearings", ASME Design Engineering Conference, April 1981, 81-DE-06.

48. Reiger, N.F., "Comparison of Instability Threshold Speed Predictions with Laboratory and Field Test Data", Proceedings of Eighth Machinery Dynamics Seminar, Halifax, October 1984.

49. Lund, J.W., 'Rotor-Bearings Dynamics Design Technology, Part III: Design Handbook for Fluid Film Bearings, Mechanical Technology Inc., Latham, N.Y., AFAPL-Tr-65-45, 1965.

50. Iwatsubo, T. and Kawai, R., "Stability Analysis of Multi Span Rotor System and its Application", Bull. JSME, Vol. 24, No. 196, October 1981, pp. 1853-1858.

51. Glienicke, J., Han, D.C. and Leonhard, M., "Practical Determination and Use of Bearing Dynamic Co-efficients", Tribology International, December 1980, pp. 197-207.

52. Lund, J.W., "Spring and Damping Co-efficients for the Tilting Pad Journal Bearings", Trans. ASLE, 1964, 7(4), pp. 342-352.

53. Smith, D., Journal Bearings in Turbomachinery, Chapman and Hall Ltd., 1969.

54. Cameron, A., Principles of Lubrication, Longmans, 1966.

55. Pinkus, O. and Sternlicht, B., Theory of Hydrodynamic Lubrication, McGraw Hill Book Co., 1961.

56. Bannister, R.H., "A Theoretical and Experimental Investigation Illustrating the Influence of Nonlinearity and Misalignment on the Eight Oil Film Force Co-efficients", Vibrations in Rotating Machinery, I.Mech.E. Conference, C219/76, 1976, p. 271.

57. Hashish, E.A., "Improved Mathematical Models and Dynamic Analysis of Light Rotor-Bearing Systems Under Unbalance and Stochastic Excitation", Ph.D. Dissertation, Concordia University, February 1981.

58. Black, H.F. and Brown, R.D. "Model Dynamic Simulation of Flexible Shafts in Hydrodynamic Bearings", Second International Conference of Vibrations in Rotating Machinery, Mechanical Engineering Conference Publications, C266/80, 1980, pp. 1980-84.

59. Mukherjee, A. and Rao, J.S., "Stiffness and Damping Co-efficients of an Inclined Journal Bearing", Journal of Mechanism and Machine Theory, 12, 1977, pp. 339-355.

60. Capriz, G., "On Some Dynamic Problems Arising in the Theory of Lubrication", Nelson Research Lab., English Electric Co. Ltd., Stafford, England, Research Report - Part 1, Riv. Mat. Univ. Parma (2) 1, 1-20 (1960).

61. Pafelias, T.A., "Solution of Certain Problems of Viscous Laminar Flow with Application in Engineering Problems", Ph.D. Thesis, Rensselaer Polytechnic Institute, 1974.

62. Heshmat, H., Walowit, J.A. and Pinkus, O., "Analysis of Gas-Lubricated Foil Journal Bearings", Journal of Lubrication Technology, Trans. ASME, October 1983, Vol. 105, pp. 647-655.

63. Grass, W.A., Matsch, L.A., Castelli, V., Eshel, A., Vohr, J.H. and Wildmann, M., Fluid Film Lubrication, John Wiley & Sons, p. 621.

64. Downham, E., "Theory of Shaft Whirling, A Fundamental Approach to Shaft Whirling", The Engineer, 1957, 518-522, 552-555 and 660-665.

65. Hull, E.H., "Shaft Whirling as Influenced by Stiffness Asymmetry", Journal of Engineering for Industry, 83, 219 (1961).

66. Lund, J.W. and Orcutt, F.K., "Calculations and Experiments on the Unbalance Response of a Flexible Rotor", Journal of Engineering for Industry, Trans. ASME, 89, No. 4, November 1967, pp. 785-796.

67. Cunningham, R.E., "Steady-State Unbalance Response of a Three-Disk Flexible Rotor on Flexible Damped Supports", Journal of Mechanical Design, Trans. ASME, Vol. 100, July 1978, pp. 563-573.

68. Klosterman, A.L., "On the Experimental Determination and Use of Modal Representation of Dynamic Characteristics", Ph.D. Dissertation, University of Cincinnati, 1971.

69. Nordmann, R., "Modal Parameter Identification and Sensitivity Analysis in Rotating Machinery", International Conference in Rotordynamic Problems in Power Plants, Proceedings of the IFToMM Conference, Rome, Italy, Sept. 29-Oct. 1, 1982, pp. 95-102.

70. Nordmann, R. "Identification of Modal Parameters of an Elastic Rotor with Oil Film Bearings", Trans. ASME, Paper No. 83-DET-11.

71. Ruhl, R.L., Conry, T.F. and Steger, R.L., "Unbalanced Response of a Large Rotor-Pedestal-Foundation System Using an Elastic Half-Space Soil Model", Journal of Mechanical Design, Vol. 102, April 1980, pp. 311-319.

72. Armentrout, R.W., Gunter, J.E. and Humphris, R.R., "Dynamic Characteristics of a Jeffcott Rotor Including Foundation Effects", ASME Paper No. 83-DET-98, Presented at the Design Engineering Conference held in Dearborn, September 1983.

73. Adams, M.L., "Non-Linear Dynamics of Flexible Multi-Bearing Rotors", Journal of Sound and Vibration, 1980, pp. 129-144.

74. Asmis, G.J.K., "Response of Rotating Machinery Subjected to Seismic Excitation", I.Mech.E. Conference Publications, Engineering Design For Earthquake Environments, C192/78, 1978, pp. 215-226.

75. Hadjian, A.H., "Support Motions for Mechanical Components During Earthquakes", I.Mech.E., Conference Publications, Engineering Design for Earthquake Environments, C173/78, 1978, pp. 27-46.

76. Boyce, L., Kozik, T.J. and Parzen, E., "Probabilistic Design and Analysis of Foundation Forces for a Class of Unbalanced Rotating Machines", Journal of Vibration, Acoustics, Stress and Reliability in Design, Paper No. 83-DET-26.

77. Lund, J.W., "Response Characteristics of a Rotor with Flexible Damped Supports", Symposium of International Union of Theoretical and Applied Mechanics, Lyngby, August 12-16, 1974, pp. 319-349.

78. Tessarzik, J.M., Chiang, T. and Badgley, R.H., "The Response of Rotating Machinery to External Random Vibration", Journal of Engg. for Industry, Trans. ASME, Series B, Vol. 96, No. 2, May 1974, pp. 477-489.

79. Subbiah, R., Bhat, R.B. and Sankar, T.S., "Experimental Study of Unbalance Response of Rotor Mounted on Dissimilar Hydrodynamic Bearings", Proceedings of IFToMM Conference held in New Delhi, 1983, pp. 697-700.

80. Subbiah, R., Bhat, R.B. and Sankar, T.S., "Rotational Stiffness and Damping Co-efficients of Fluid Film in a Finite Cylindrical Bearing", Trans. ASLE, Paper No. 85-AM-2E-2, Presented at the 40th Annual Meeting in Las Vegas, May 6-9, 1985.

81. Subbiah, R., Bhat, R.B. and Sankar, T.S., "Response of Rotors Subjected to Random Support Excitations", To appear in the Journal of Vibration, Acoustics, Stress and Reliability in Design, Trans. ASME, Also to be presented at the ASME Design Engg. Conference, Cincinnati, Sept. 10-13, 1985.

82. Kennedy, C.C. and Pancu, C.D.P., "Use of Vectors in Vibration Measurement and Analysis", Journal of Aeronautical Sciences, Vol. 14, No. 11, 1947, pp. 603-625.

83. Beatty, R.F., "Differentiating Rotor Response Due to Radial Rubbing", Journal of Vibration, Acoustics, Stress and Reliability in Design", Trans. ASME, Vol. 107, April 1985, pp. 151-160.

84. Archer, J.S., "Consistent Mass-Matrix for Distributed Mass Systems", Journal of the Structural Division, Proceedings of the ASCE, Vol. 89, ST4, 1963, p. 161.

85. Nezat Özgüven, H. and Levent Özkan, Z., "Whirl Speeds and Unbalance Response of Multibearing Rotors Using Finite Elements", Presented at the Design and Production Engg. Conference, Dearborn, Sept. 11-14, 1983, ASME Paper No. 83-DET-89.

86. Someya, T., "Stabilität einer in zylindrischen Gleitlagern laugenden, unwuchtfreien Welle", Dissertation, Technical University, Karlsruhe, 1962.

87. Sassenfeld, H. and Walther, A., "Gleitlagerberechnungen", VDI ForschHft 1954, p. 441.

88. Kollmann, K. and Glienicke, J., "The Behaviour of Turbine Bearings with Respect to Instability Prediction", JSME 1967 Semi-International Symposium, 4-8 September 1967, Tokyo, pp. 195-205.

89. Morton, P.G., "The Derivation of Bearing Characteristics by Means of Transient Excitation Applied Directly to a Rotating Shaft", IUTAM Symposium, Dynamics of Rotors, Lyngby, 1974, pp. 350-379.

90. Prabhu, B.S. and Rao, B.V.A., "Bearing Influenced Rotor Dynamics", Tribology International, Vol. 14, No. 2, 1981, pp. 107-111.

91. Prabhu, B.S., "Steady-State and Dynamic Characteristics of Partial Journal Bearings", Wear, Vol. 40, No. 1, 1976, pp. 1-8.

92. Hagg, A.C. and Sankey, G.O., "Elastic and Damping Properties of Oil-Film Journal Bearings for Application to Unbalance Vibration Calculations", Journal of Applied Mechanics, Vol. 25, 1958, pp. 141-143.

93. Lund, J.W. and Thomson, K.K., "A Calculation Method and Data for the Dynamic Co-efficients of Oil Lubricated Journal Bearings", Presented at the Design Engg. Conference, Chicago, Illinois, April 17-20, 1978, pp. 1-28.

94. Smith, D.M., "Dynamic Characteristics of Turbine Journal Bearings", Proc. Lubrication and Wear Convention, Bournemouth, 1963, Paper 8, 72, I.Mech.E. (London).

95. Kana, D.D. and Pomerening, D.J., "Suitability of Synthesized Waveforms of Seismic Qualification of Equipment", Journal of Pressure Vessel Technology, Trans. ASME, Vol. 106, February 1984, pp. 63-68.

96. Bannister, R.H., "Methods for Modelling Flanged and Curvic Couplings for Dynamic Analysis of Complex Rotor Constructions", Journal of Mechanical Design, Trans. ASME, Vol. 102, January 1980, pp. 130-139.

97. Caughey, T.K., "Classical Norman Modes in Damped Linear Dynamic Systems", Journal of Applied Mechanics, Trans. ASME, June 1960, pp. 269-271.

APPENDIX A
BEAM ELEMENT MATRICES

$$[m_t^e] = \frac{\mu_1 \ell}{420}\begin{bmatrix} 156 & & & & & & & \\ 0 & 156 & & & & \text{Symmetric} & & \\ 0 & 22\ell & 4\ell^2 & & & & & \\ 22\ell & 0 & 0 & 4\ell^2 & & & & \\ 54 & 0 & 0 & 13\ell & 156 & & & \\ 0 & 54 & -13\ell & 0 & 0 & 156 & & \\ 0 & 13\ell & -13\ell^2 & 0 & 0 & 22\ell & 4\ell^2 & \\ -13\ell & 0 & 0 & -3\ell^2 & -22\ell & 0 & 0 & 4\ell^2 \end{bmatrix}$$

$$[m_r^e] = \frac{\mu_1 R_e^2}{120\ell}\begin{bmatrix} 36 & & & & & & & \\ 0 & 36 & & & & \text{Symmetric} & & \\ 0 & -3\ell & 4\ell^2 & & & & & \\ 3\ell & 0 & 0 & 4\ell^2 & & & & \\ -36 & 0 & 0 & -3\ell & 36 & & & \\ 0 & -36 & 3\ell & 0 & 0 & 36 & & \\ 0 & -3\ell & -\ell^2 & 0 & 0 & 3\ell & 4\ell^2 & \\ 3\ell & 0 & 0 & -\ell^2 & -3\ell & 0 & 0 & 4\ell^2 \end{bmatrix}$$

$$[g^e] = \frac{\mu_1 R_e^2}{120\ell}\begin{bmatrix} 0 & -36 & 3\ell & 0 & 0 & 36 & 3\ell & 0 \\ 36 & 0 & 0 & 3\ell & -36 & 0 & 0 & 3\ell \\ -3\ell & 0 & 0 & -4\ell^2 & 3\ell & 0 & 0 & \ell^2 \\ 0 & -3\ell & 4\ell^2 & 0 & 0 & 3\ell & -\ell^2 & 0 \\ 0 & 36 & -3\ell & 0 & 0 & -36 & -3\ell & 0 \\ -36 & 0 & 0 & -3\ell & 36 & 0 & 0 & -3\ell \\ -3\ell & 0 & 0 & \ell^2 & 3\ell & 0 & 0 & -4\ell^2 \\ 0 & -3\ell & -\ell^2 & 0 & 0 & -3\ell & 4\ell^2 & 0 \end{bmatrix}$$

$$[k_B^e] = \frac{EI_0}{\ell^3}\begin{bmatrix} 12 & & & & & & & \\ 0 & 12 & & & & \text{Symmetric} & & \\ 0 & -6\ell & 4\ell^2 & & & & & \\ 6\ell & 0 & 0 & 4\ell^2 & & & & \\ -12 & 0 & 0 & -6\ell & 12 & & & \\ 0 & -12 & 6\ell & 0 & 0 & 12 & & \\ 0 & -6\ell & 2\ell^2 & 0 & 0 & 6\ell & 4\ell^2 & \\ 6\ell & 0 & 0 & 2\ell^2 & -6\ell & 0 & 0 & 4\ell^2 \end{bmatrix}$$

APPENDIX B

REYNOLDS EQUATIONS FOR FLUID FILM

Substitution of equations (5.2) and (5.3) in equation (5.1) result in the following nine equations:

$$\frac{1}{R^2}\frac{\partial}{\partial\bar{\beta}}\left\{\frac{h_o^3}{12\Omega}\frac{\partial p_o}{\partial\bar{\beta}}\right\}+\frac{\partial}{\partial x}\left\{\frac{h_o^3}{12\Omega}\frac{\partial p_o}{\partial x}\right\}=\frac{1}{2}\omega\frac{\partial h_o}{\partial\bar{\beta}} \qquad (B.1)$$

$$\frac{1}{R^2}\frac{\partial}{\partial\bar{\beta}}\left\{\frac{h_o^3}{12\Omega}\frac{\partial p_z}{\partial\bar{\beta}}\right\}+\frac{\partial}{\partial x}\left\{\frac{h_o^3}{12\Omega}\frac{\partial p_z}{\partial x}\right\}=\frac{1}{2}\omega\frac{\partial}{\partial\bar{\beta}}(\cos\bar{\beta})$$

$$-\frac{1}{R^2}\frac{\partial}{\partial\bar{\beta}}\left(3h_o^2\cos\bar{\beta}\frac{\partial p_o}{\partial\bar{\beta}}-\frac{\partial}{\partial x}\right)\left(3h_o^2\cos\bar{\beta}\frac{\partial p_o}{\partial x}\right) \qquad (B.2)$$

$$\frac{1}{R^2}\frac{\partial}{\partial\bar{\beta}}\left\{\frac{h_o^3}{12\Omega}\frac{\partial p_y}{\partial\bar{\beta}}\right\}+\frac{\partial}{\partial x}\left\{\frac{h_o^3}{12\Omega}\frac{\partial p_y}{\partial x}\right\}=\frac{1}{2}\omega\frac{\partial}{\partial\bar{\beta}}(\sin\bar{\beta})$$

$$-\frac{1}{R}\frac{\partial}{\partial\bar{\beta}}\left(3h_o^2\sin\bar{\beta}\frac{\partial p_o}{\partial\bar{\beta}}\right)-\frac{\partial}{\partial x}\left(3h_o^2\sin\bar{\beta}\frac{\partial p_o}{\partial x}\right) \qquad (B.3)$$

$$\frac{1}{R^2}\frac{\partial}{\partial\bar{\beta}}\left\{\frac{h_o^3}{12\Omega}\frac{\partial p_z^*}{\partial\bar{\beta}}\right\}+\frac{\partial}{\partial x}\left\{\frac{h_o^3}{12\Omega}\frac{\partial p_z^*}{\partial x}\right\}=\cos\bar{\beta} \qquad (B.4)$$

$$\frac{1}{R^2}\frac{\partial}{\partial\bar{\beta}}\left\{\frac{h_o^3}{12\Omega}\frac{\partial p_y^*}{\partial\bar{\beta}}\right\}+\frac{\partial}{\partial x}\left\{\frac{h_o^3}{12\Omega}\frac{\partial p_y^*}{\partial x}\right\}=\sin\bar{\beta} \qquad (B.5)$$

$$\frac{1}{R^2}\frac{\partial}{\partial\bar{\beta}}\left\{\frac{h_o^3}{12\Omega}\frac{\partial q_z}{\partial\bar{\beta}}\right\}+\frac{\partial}{\partial x}\left\{\frac{h_o^3}{12\Omega}\frac{\partial q_z}{\partial x}\right\}=\frac{1}{2}\omega\frac{\partial}{\partial\bar{\beta}}(x\cos\bar{\beta})$$

$$-\frac{1}{R^2}\frac{\partial}{\partial\bar{\beta}}\left(3h_o^2 x\cos\bar{\beta}\frac{\partial p_o}{\partial\bar{\beta}}\right)-\frac{\partial}{\partial x}\left(3h_o^2 x\cos\beta\frac{\partial p_o}{\partial x}\right) \qquad (B.6)$$

$$\frac{1}{R^2}\frac{\partial}{\partial\bar{\beta}}\left\{\frac{h_o^3}{12\Omega}\frac{\partial q_y}{\partial\bar{\beta}}\right\}+\frac{\partial}{\partial x}\left\{\frac{h_o^3}{12\Omega}\frac{\partial q_y}{\partial x}\right\}=\frac{1}{2}\omega\frac{\partial}{\partial\bar{\beta}}(x\sin\bar{\beta})$$

$$-\frac{1}{R^2}\frac{\partial}{\partial\bar{\beta}}\left(3h_o^2 x-\sin\bar{\beta}\frac{\partial p_o}{\partial\bar{\beta}}\right)+\frac{\partial}{\partial x}\left(3h_o^2 x\sin\bar{\beta}\frac{\partial p_o}{\partial x}\right) \qquad (B.7)$$

$$\frac{1}{R^2}\frac{\partial}{\partial\bar{\beta}}\left\{\frac{h_o^3}{12\Omega}\frac{\partial q_z^*}{\partial\bar{\beta}}\right\}+\frac{\partial}{\partial x}\left\{\frac{h_o^3}{12\Omega}\frac{\partial q_z^*}{\partial x}\right\}=x\cos\bar{\beta} \qquad (B.8)$$

$$\frac{1}{R^2}\frac{\partial}{\partial\bar{\beta}}\left\{\frac{h_o^3}{12\Omega}\frac{\partial q_y^*}{\partial\bar{\beta}}\right\}+\frac{\partial}{\partial x}\left\{\frac{h_o^3}{12\Omega}\frac{\partial q_y^*}{\partial x}\right\}=x\sin\bar{\beta} \qquad (B.9)$$

Introducing the non-dimensional quantities,

$$H_o=\frac{h_o}{c}\ ;\ x=\frac{L}{2}\bar{x}\ ;\ p_o=\Omega N\left(\frac{R}{c}\right)^2\bar{p}_o$$

$$p_z,\ p_y=\left\{\Omega\frac{N}{c}\left(\frac{R}{c}\right)^2\right\}\bar{p}_z^*,\ \bar{p}_y^*$$

$$p_z^*,\ p_y^*=\left\{\frac{\Omega}{c}\left(\frac{R}{c}\right)^2\right\}\bar{p}_z^*,\ \bar{p}_y^*$$

$$q_z,\ q_y=\left\{\Omega\frac{N}{c}\left(\frac{R}{c}\right)^2 L\right\}\bar{q}_z,\ \bar{q}_y$$

$$q_z^*,\ q_y^* = \left\{\frac{\Omega}{c}\ \left(\frac{R}{c}\right)^2 L\right\}\ \bar{q}_z^*,\ \bar{q}_y^*$$

and substituting then in the above nine equations (B.1 through B.9) result in the nondimensional form of Reynold's equations which are shown in equations (5.4).

APPENDIX C

STIFFNESS AND DAMPING MATRICES OF THE FLUID FILM IN FINITE BEARING

The bearing element stiffness matrix is given by:

$$\begin{bmatrix} k_{zz}^{tt} & k_{zy}^{tt} & k_{zz}^{tr} & k_{zy}^{tr} \\ k_{yz}^{tt} & k_{yy}^{tt} & k_{yz}^{tr} & k_{yy}^{tr} \\ k_{zz}^{rt} & k_{zy}^{rt} & k_{zz}^{rr} & k_{zy}^{rr} \\ k_{yz}^{rt} & k_{yy}^{rt} & k_{yz}^{rr} & k_{yy}^{rr} \end{bmatrix}$$

and the corresponding vector of displacements is

$$\begin{Bmatrix} z \\ y \\ \psi \\ \varphi \end{Bmatrix}$$

Similarly the bearing element damping matrix is given as:

$$\begin{bmatrix} c_{zz}^{tt} & c_{zy}^{tt} & c_{zz}^{tr} & c_{zy}^{tr} \\ c_{yz}^{tt} & c_{yy}^{tt} & c_{yz}^{tr} & c_{yy}^{tr} \\ c_{zz}^{rt} & c_{zy}^{rt} & c_{zz}^{rr} & c_{zy}^{rr} \\ c_{yz}^{rt} & c_{yy}^{rt} & c_{yz}^{rr} & c_{yy}^{rr} \end{bmatrix}$$

and the corresponding velocity vector is

$$\begin{Bmatrix} \dot{z} \\ \dot{y} \\ \dot{\psi} \\ \dot{\varphi} \end{Bmatrix}$$

APPENDIX D

SUPPORT MASS AND STIFFNESS MATRICES OF A ROTOR SYSTEM

The support mass matrix becomes, $M = \left[\begin{array}{c|c} 0 & 0 \\ \hline 0 & M_p \end{array}\right]$

where

$$[M_p] = \begin{bmatrix} m_p & 0 & 0 & 0 \\ 0 & m_p & 0 & 0 \\ 0 & 0 & I_{p_{yy}} & 0 \\ 0 & 0 & 0 & I_{p_{zz}} \end{bmatrix}$$

The support stiffness matrix becomes, $[K] = \left[\begin{array}{c|c} K_{bb} & K_{bp} \\ \hline K_{pb} & k_{pp} \end{array}\right]$

$$k_{bb} = \begin{bmatrix} k_{zz}^{tt} & k_{zy}^{tt} & 0 & 0 \\ k_{yz}^{tt} & k_{yy}^{tt} & 0 & 0 \\ 0 & 0 & k_{zz}^{rr} & k_{zy}^{rr} \\ 0 & 0 & k_{yz}^{rr} & k_{yy}^{rr} \end{bmatrix}$$

$$k_{pb} = \begin{bmatrix} -k_{zz}^{tt} & -k_{zy}^{tt} & 0 & 0 \\ -k_{yz}^{tt} & -k_{yy}^{tt} & 0 & 0 \\ 0 & 0 & -k_{zz}^{rr} & -k_{zy}^{rr} \\ 0 & 0 & -k_{yz}^{rr} & -k_{yy}^{rr} \end{bmatrix}$$

$$k_{bp} = \begin{bmatrix} -k_{zz}^{tt} & -k_{zy}^{tt} & 0 & 0 \\ -k_{yz}^{tt} & -k_{yy}^{tt} & 0 & 0 \\ 0 & 0 & -k_{zz}^{rr} & -k_{zy} \\ 0 & 0 & -k_{yz}^{rr} & -k_{yy}^{rr} \end{bmatrix}$$

$$k_{pp} = \begin{bmatrix} \left(k_{zz}^{tt} + k_{p_z}\right) & k_{zy}^{tt} & 0 & 0 \\ k_{yz}^{tt} & \left(k_{yy}^{tt} + k_{p_y}\right) & 0 & 0 \\ 0 & 0 & \left(k_{p\theta}^{rr} + k_{zz}^{rr}\right) & k_{zy}^{rr} \\ 0 & 0 & k_{yz}^{rr} & \left(k_{p\phi} + k_{yy}^{rr}\right) \end{bmatrix}$$

The corresponding generalized displacement vector is

$$[w_1, v_1, \bar{\theta}_1, \bar{\phi}_1, w_0, v_0, \bar{\theta}_0, \bar{\phi}_0]^T$$

The support damping matrix can be written analogously.